KERNFORSCHUNGSANLAGE JÜLICH GmbH
Institut für Festkörperforschung

Numerical Simulation of Convective Flow of the Melt in the Classical Czochralski Method, in ACRT and CACRT

Part 1: Simulation of Forced Convection

by

Mihelčič, M., Schröck-Pauli, C., Wingerath, K., Wenzl, H.,
Uelhoff, W., van der Hart, A.

Jül - 1682
Oktober 1980
ISSN 0366 - 0885

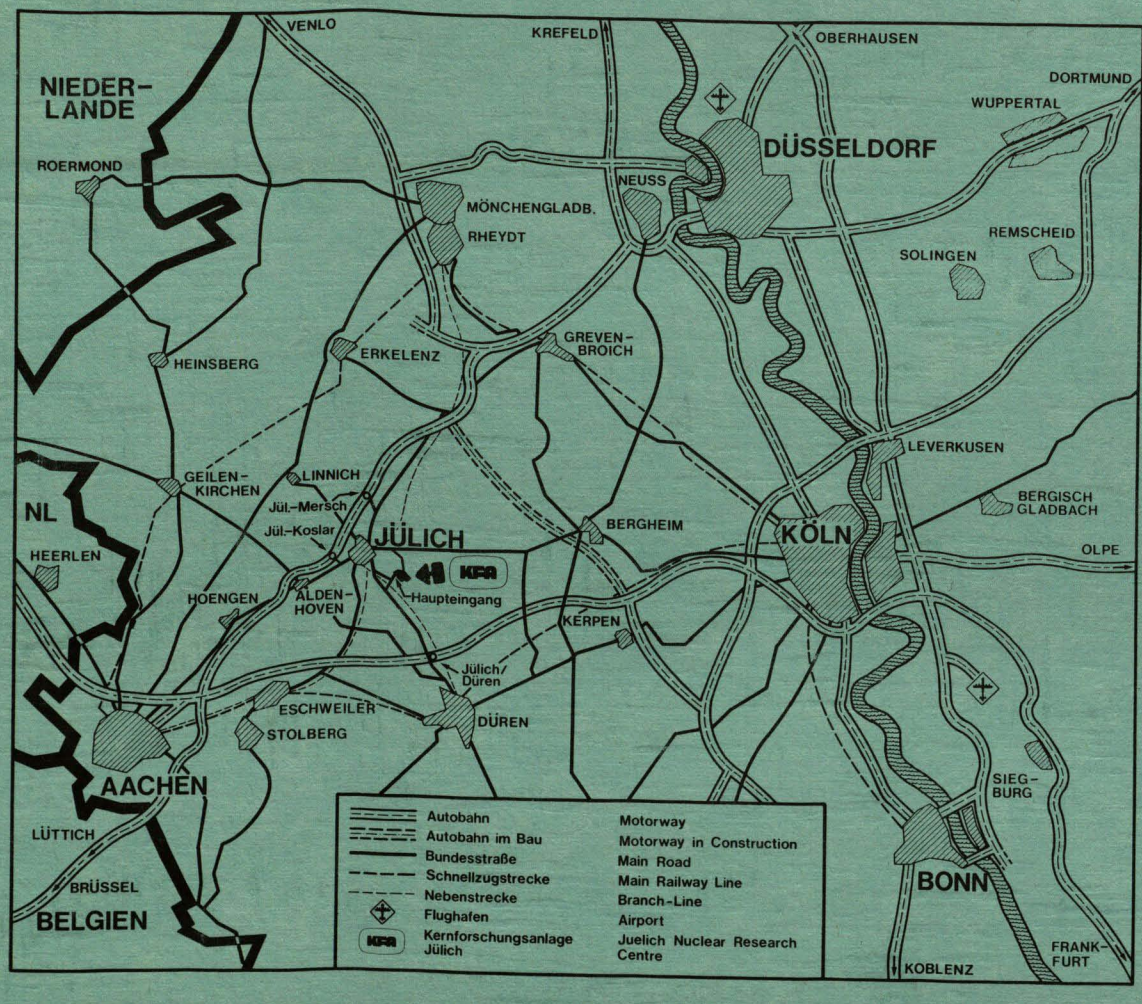

Als Manuskript gedruckt

Berichte der Kernforschungsanlage Jülich - Nr. 1682

Institut für Festkörperforschung Jül - 1682

Zu beziehen durch: ZENTRALBIBLIOTHEK der Kernforschungsanlage Jülich GmbH

Postfach 1913 · D-5170 Jülich (Bundesrepublik Deutschland)

Telefon: 02461/611 · Telex: 833556 kfa d

Numerical Simulation of Convective Flow of the Melt in the Classical Czochralski Method, in ACRT and CACRT

Part 1: Simulation of Forced Convection

by

Mihelčič, M., Schröck-Pauli, C., Wingerath, K., Wenzl, H.,
Uelhoff, W., van der Hart, A.

Abstract

In part 1 of this report, a procedure is described for the numerical solution of the time-dependent Navier-Stokes equations governing the forced convective flow in a crystal-growth crucible. By means of five digital simulations of the classical Czochralski crystal-pulling process, we show the excellent agreement of our calculations with the experimental data of Carruthers and Nassau [3], not only qualitatively but quantitatively, too. Moreover, for the Accelerated Crucible-Rotation Technique (ACRT) and its application to the Czochralski method (CACRT), the first numerical simulations are presented assuming the fluid model to be the same 1:1 glycerine-water mixture of moderate kinematic viscosities as in [3]. But our programme can also deal with low viscosities typical for semi-conductors and liquid metals: This is demonstrated by our simulations of the classical Czochralski, the ACRT and the CACRT arrangements with the viscosity of liquid copper.

The influence of the temperature distribution on these flow phenomena will be studied in part 2.

Contents

1. Introduction

In all crystal growth processes from the liquid phase, convection of the melt strongly influences the chemical and physical properties of the grown crystal. In the well-known Czochralski crystal-pulling process as well as in the Accelerated Crucible-Rotation Technique (ACRT) proposed by Scheel and Schulz-Dubois [15,17,18] (see fig. 1a and fig. 1b), there exist two kinds of convection: natural convection driven by density fluctuations that are induced by inhomogeneous temperature distribution or different impurity concentration, and forced convection due to crystal and crucible rotation. Both crystal-growth methods are performed with uniformly resp. non-uniformly rotating crucible and, in the Czochralski case, with revolving crystal, too, in order to obtain adequate mixing of the melt. The stirring of the liquid is done most effectively, if all parts of the solution are in motion and if the highest flow velocity occurs close to the surface of the growing crystal. In this case, optimum temperature balance and low impurity concentration can be expected in the vicinity of the solid-liquid interface preventing striations and spontaneous nucleation followed by polycristalline growth.

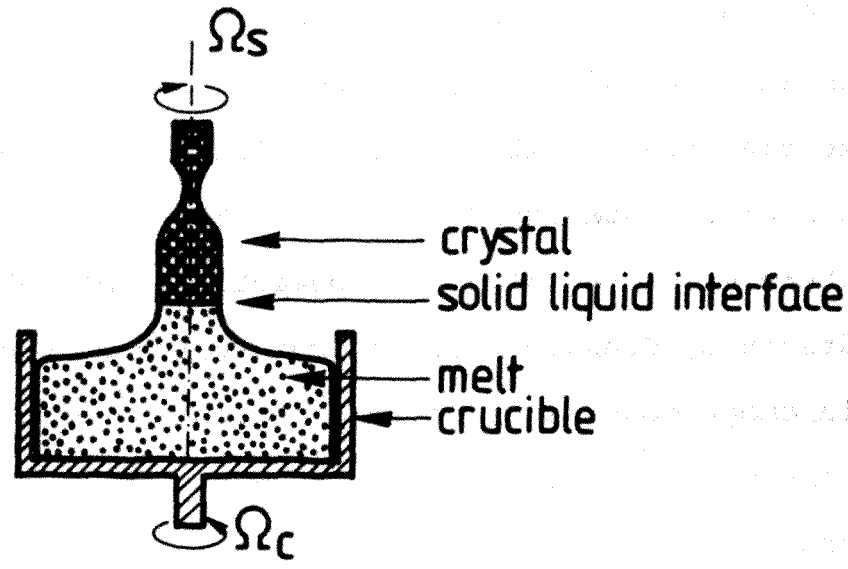

Fig. 1a : Principle of Czochralski Pulling Process

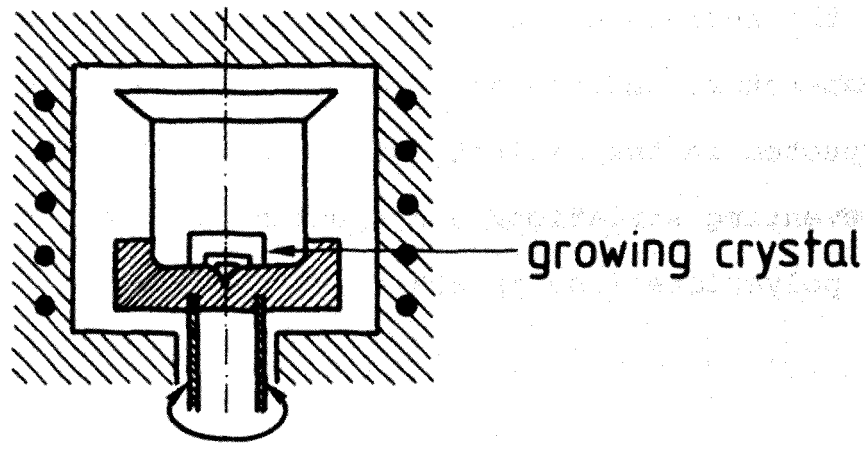

Fig. 1b : Principle of Accelerated Crucible-Rotation Technique (ACRT).

The aim of part 1 of this report is to investigate the isothermal time-dependent flow patterns of the forced convection in the Czochralski and the ACRT arrangement numerically.[1] In section 2, we start with the time-dependent Navier-Stokes and continuity equations in primitive variables (pressure and velocity) for the axisymmetric case. In order to obtain digital simulations closely related to the real physical system (e.g. ability for comparison with experimental data of Carruthers and Nassau [3]), we do not introduce dimensionless variables. Contrary to other flow computations by Kobayashi and Arizumi [8,9] and Langlois [11], Langlois and Shir [12], we avoid the stream function and vorticity formulation, as we are interested in the transient pressure distribution, which has to be evaluated iteratively. The performance of these calculations works faster in the primitive variables of the equations (see [14]). Moreover, the primitive variable formulation seems to be advantageous with regard to the possibility of extension to three-dimensional flow simulations.[2]

---

[1] The influence of the temperature distribution on the convective flow in the melt will be considered in part 2 of this report.

[2] We shall investigate the three-dimensional fluid flow, in the near future, in order to examine if there are similar asymmetric flow patterns as seen in the experiments of Hide and Titman [6].

As is well-known (see [1,1o,14]), the mathematical problems of existence and uniqueness of the solution of the Navier-Stokes and continuity equations and their finite-difference analogues are far from settled. In the case of incompressible viscous flow, one conjectures that a unique steady solution exists only below an undefined Reynolds-number limit, that several solutions exist for a range of Reynolds-numbers above this limit, and that no solutions exist above a second undefined Reynolds-number. Concerning the solution of the unsteady equations, the situation seems to be less stringent: Since the time-dependent equations are believed to be physically reliable, one can assume that a numerical solution which proceeds from a physically reasonable initial condition has validity. Therefore, such non-stationary simulations should also enable to detect whether a steady-state solution exists or not. Nevertheless, one cannot predict towards which solution the numerical scheme will converge, if non-uniqueness exists. Therefore hydrodynamic experiments are indispensable to check if the numerically computed solution is physically reasonable (see [14]). For these reasons, we solve numerically the discrete analogues of the time-dependent equations of forced convective motion in the melt for a consecutive sequence of time-steps until an approximate steady-state solution is reached. Our discretization procedure consists in the difference schemes of the well-known MAC-method of Welch and Harlow (et al.) (see [19] and [5]), which was especially developed for solving flow problems with a free surface. However, in our cases the original version of the MAC-method as well as all improved

versions of it, proposed by the authors of [2,4,7,13], were not able to produce the correct pressure distribution at the free surface of the melt. Therefore, we had to make some essential modifications concerning the free surface handling (see section 2.4.).

At the beginning of section 3, we present the numerical simulation of the Czochralski crystal-growth arrangement for both cases of isorotation and counterrotation choosing essentially the same physical and geometrical parameters as Carruthers and Nassau [3] did in their experiments (esp. kinematic viscosity $\nu = 0.06 \frac{cm^2}{s}$). These authors determined the number and size of the non-mixing Taylor-Proudman cells in the steady -state flow emerging from the relative rotary motion of crystal and crucible. Moreover, they studied the flow patterns in each of the cells and measured the flow velocity therein. In all simulated cases with angular velocities typical for practical applications of the Czochralski method in crystal growth, our numerical results show large agreement with the experimental data, not only qualitatively but quantitatively, too. This lends credibility to our hydrodynamic simulation technique and gives valuable information on the region of maximum flow velocity.

Next we consider the ACRT arrangement of Scheel and Schulz-Dubois [15,17,18] maintaining the moderate kinematic viscosity of [3], and, in the first, we determine the progress in time of the forced convective bulk flow for periodic switching on and off of the crucible rotation, numerically. Furthermore, Scheel and Müller-Krumbhaar [16] propose to perform the

Czochralski crystal-pulling process with non-uniform iso- and counterrotation of crystal and crucible (CACRT) in order to eliminate the non-mixing Taylor-Proudman cells thereby getting optimum stirring of the melt. In the case of the moderate kinematic viscosity of [3], our computer simulations of such arrangements show that in the periodically accelerated and decelerated counterrotational case only a pulsation effect of the original cell beneath the crystal occurs. In the periodically accelerated and decelerated isorotational case, however, it can be achieved that the non-mixing Taylor-Proudman cells vanish periodically.

In the second part of section 3, we repeat our digital simulations of the classical Czochralski, the ACRT and the CACRT arrangements with the kinematic viscosity $\nu = 0.005 \frac{cm^2}{s}$ of liquid copper. Here it is noteworthy that the transition time needed for reaching the steady-state of the flow is remarkably longer than in the previous calculations with a twelve times larger kinematic viscosity.
Moreover, for the low kinematic viscosity the particular flow patterns during this non-stationary transition phase are quite distinct from those in the moderate viscosity case. In the CACRT arrangement, especially, the flow patterns in the counterrotational and the isorotational cases do not differ as significantly as in the moderate viscosity simulations before.

In section 4, we draw some comprehensive conclusions with regards to experimental design of the crystal-growth process by the classical Czochralski method, the ACRT, and the CACRT arrangements, respectively.

Finally, in section 5, an outlook on our forthcoming calculations and experiments is given.

2. The mathematical model

2.1. *The continuous equations of motion*

Our calculations are based on the simplified geometrical model for the Czochralski process and the ACR Technique shown in fig. 2a and fig. 2b, respectively. For the basic field variables we use the fluid velocity $\vec{u} = (u,v,w)$ with radial component u, zonal component v and vertical component w, and the ratio $\phi = p/\rho$ of pressure p to (constant) density ρ. In addition, t denotes the elapsed time, and $\vec{r} = (r,\Theta,z)$ is the Eulerian (laboratory frame) coordinate in cylindrical components. Like the density ρ, the kinematic viscosity ν of the melt is taken to be constant all the time. With these definitions, the equations governing the time-dependent incompressible viscous flow in the crucible are

$$\nabla \cdot \vec{u} = 0 \,, \tag{2.1}$$

$$\frac{\partial \vec{u}}{\partial t} = -(\vec{u}\cdot\nabla)\vec{u} - \nabla\phi + \nu\Delta\vec{u} + \vec{g} \,. \tag{2.2}$$

Eq. (2.1) is the *continuity equation* expressing the conservation of mass for an incompressible fluid. (2.2) represent the well-known *Navier-Stokes equations* describing the local production of momentum in terms of the following sources: the convection of momentum by fluid motion, $-(\vec{u}\cdot\nabla)\vec{u}$, the momentum change arising from normal pressure forces, $-\nabla\phi$, the diffusion of momentum by viscous processes, $\nu\Delta\vec{u}$, and the momentum portion produced by gravitational forces, $\vec{g}$.
With the help of (2.1), we rewrite eq. (2.2) in the *con-*

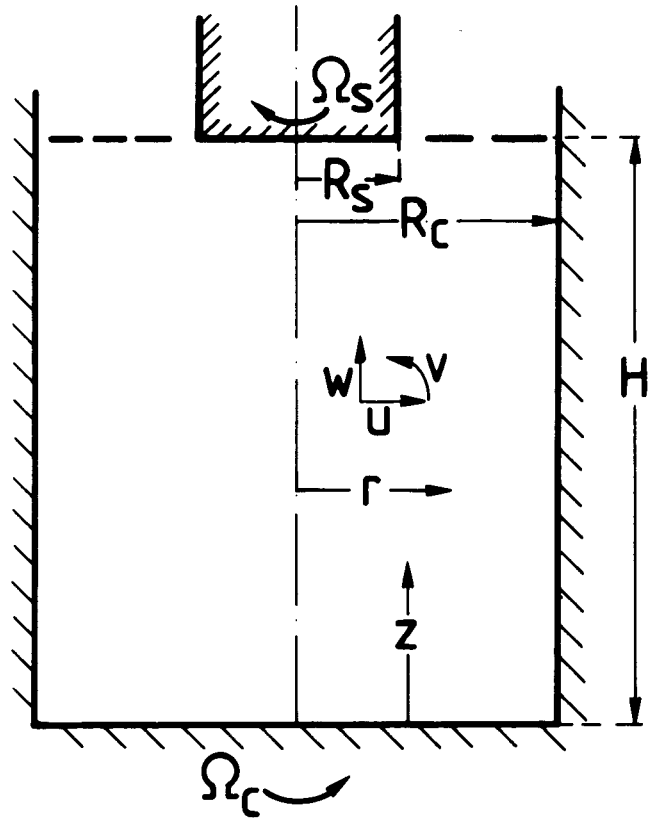

Fig. 2a : Geometry of the Czochralski Technique.

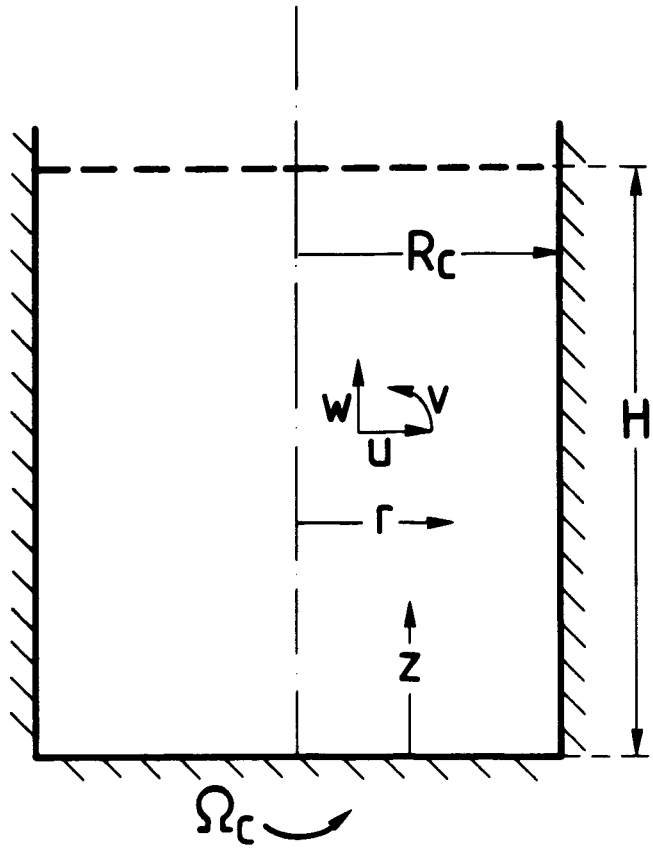

Fig. 2b : Geometry of the ACRT.

servative form

$$\frac{\partial \vec{u}}{\partial t} = - \nabla\cdot(\vec{u}\vec{u}) - \nabla\phi - \nu\nabla\times(\nabla\times\vec{u}) + \vec{g} \quad . \tag{2.3}$$

The reason for the change in the convective and diffusive terms of (2.2) is that in a cylindrical coordinate system (2.3) is the only differential form the finite difference analogue of which retains rigorous momentum conservation (see [5,19] and section 2.2. below). In order to satisfy the continuity equation (2.1) , it is convenient to derive an equation for the pressure ϕ : Applying the divergence operator on eq.(2.3) and taking account of (2.1), we obtain the well-known *Poisson-equation*

$$\Delta\phi = - \frac{\partial}{\partial t} (\nabla\cdot\vec{u}) - \nabla\cdot(\nabla\cdot(\vec{u}\vec{u})) \quad . \tag{2.4}$$

Obviously, in the continuous case, the first term on the right side of eq. (2.4) vanishes by the continuity equation (2.1), but during the discretization process we have to pay regard to $\frac{\partial}{\partial t} (\nabla\cdot\vec{u})$ in order to fulfill the discrete version of the mass conservation (i.e. volume conservation). Eq. (2.4) shows another advantage of the use of eq. (2.3) instead of (2.2): In (2.4) only advective and no viscous terms appear simplifying the difference analogue, too, and thereby preventing needless accumulation of round-off errors later on.

In our special Czochralski and ACRT arrangements in the configuration of figs. 3 and 4, we may assume *rotational symmetry* of the flow, so that eqs. (2.3-4) read as follows:

$$u_t = -\frac{1}{r}(ru^2)_r - (uw)_z + \nu\left\{u_{zz} - w_{rz}\right\} - \phi_r + \frac{v^2}{r} \tag{2.5}$$

$$v_t = -\frac{1}{r}(ruv)_r - (vw)_z + \nu\left\{v_{zz} + \left(\frac{1}{r}(rv)_r\right)_r\right\} - \frac{uv}{r} \tag{2.6}$$

$$w_t = -\frac{1}{r}(ruw)_r - (w^2)_z + \nu\left\{\frac{1}{r}(rw_r)_r - \frac{1}{r}(ru_z)_r\right\} - \phi_z - g \tag{2.7}$$

$$\mathcal{D}_t = -\frac{1}{r}(r\phi_r)_r - \phi_{zz} - \frac{1}{r}(ru^2)_{rr} - (w^2)_{zz} - 2(uw)_{rz} + \frac{1}{r}(v^2)_r - \frac{2}{r}(uw)_z \tag{2.8}$$

Here subscripts denote partial derivatives, g is the gravity acceleration, and $\mathcal{D}$ is the abbreviation for $\nabla\cdot\vec{u}$, so that

$$\mathcal{D} = \frac{1}{r}(ru)_r + w_z \ . \tag{2.9}$$

2.2. *The grid system*

To turn the above equations into a practical scheme of computation, they are expressed in finite difference form on the following grid arrangement, which is a simplification of the one used in [20]. First, in our current simulations presented in section 3, we assume rotational symmetry of the flow so that it is sufficient to consider a vertical cross-section of the melt. There we have a basic grid formed by points where the pressure ϕ and the zonal velocity component v are defined. The velocity components u and w are both evaluated at different points interlacing with the basic grid (see fig. 3). The u points lie on vertical lines and the w points on horizontal lines of the basic grid, both midway between the ϕ points, in each case. The physical boundaries are placed so that they fall halfway between two

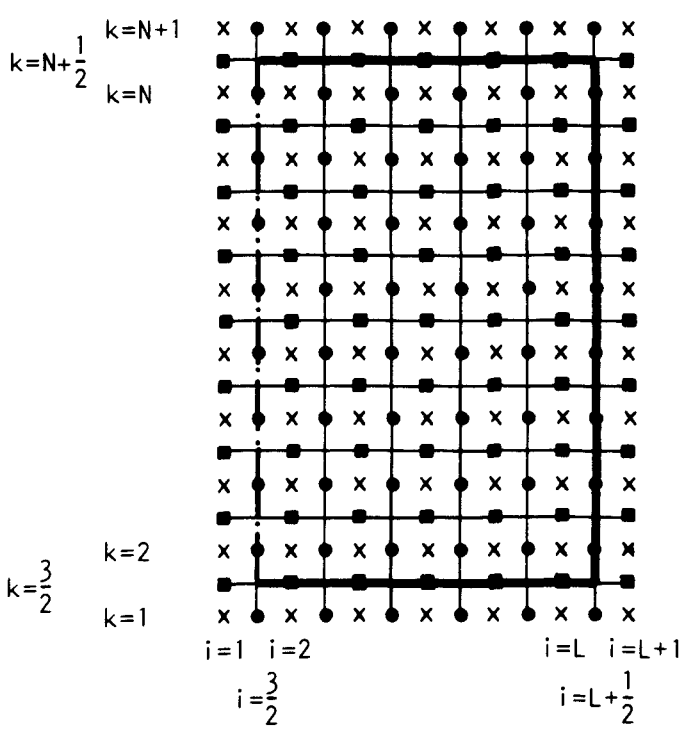

Fig. 3 :

Grid arrangement in a vertical cross section:

x, pressure and zonal velocity points;

●, radial velocity points;

■, vertical velocity points.

The broken line indicates the axis of symmetry; the heavy lines denote crucible walls and the free surface (possibly with the crystal), respectively.

ϕ points. The continuous cylindrical coordinates (r,z) are thus replaced by the discrete grid system $(r_i,z_k) = (i,k)$ such that

$$r_i = (i-\tfrac{3}{2})\Delta r,\ 1 \le i \le L+1;\ z_k = (k-\tfrac{3}{2})\Delta z,\ 1 \le k \le N+1, \qquad (2.10)$$

give the coordinates of the pressure points $\phi(i,k)$ and the zonal velocity points $v(i,k)$.

The mesh widths of the basic grid are

$$\Delta r = R_c / (L-1)\ ; \qquad \Delta z = H / (N-1)\ , \qquad (2.11)$$

where R_c and H denote the radius of the crucible and the melt height in it, respectively. The interlacing grids of the velocity points are similarly indexed, leading to discrete velocity values $u(i+\frac{1}{2},k)$ and $w(i,k+\frac{1}{2})$. The discrete fluid element centered on a ϕ resp. v point and bounded by the u, w points will be called a cell. For each of these cells the conservation of mass and momentum will apply.
In our calculations in section 3 for a crucible of radius $R_c = 3.4$ cm and a melt height $H = 4$ cm we choose

$$\Delta r \equiv \Delta z \equiv h = \begin{cases} 0.2 \text{ cm} & \text{for } \nu = 0.06\ \frac{\text{cm}^2}{\text{s}} \\ 0.1 \text{ cm} & \text{for } \nu = 0.005\ \frac{\text{cm}^2}{\text{s}} \end{cases} \qquad (2.12)$$

Additionally, our discrete time step length $\Delta t = 0.001$ s is taken small enough to satisfy the necessary stability condition of Courant, Lewy and Friedrichs, i.e.

$$\Delta t < \frac{\Delta r^2 \Delta z^2}{2\nu(\Delta r^2+\Delta z^2)} = \frac{h^2}{4\nu}\ . \qquad (2.13)$$

2.3. *The finite difference scheme*

Our discretization procedure consists in the well-known "Marker-and-Cell" - (MAC-) method originally developed by Welch and Harlow [5,19] (see also [2,4,7,13]), which was especially designed for free-surface problems in fluid dynamics. In applying the MAC-method, we replace all partial derivatives of equations (2.5-8) by difference quotients, where we use forward difference schemes for first order derivatives in time and central differencing for the spatial derivatives maintaining the order of differentiation.
In these difference equations several undefined quantities appear, as velocity and pressure values are demanded at interim mesh points of our grid in section 2.2. These terms are subsequently replaced by simple averages of the two adjacent grid point values. Now the MAC-method works as follows: Starting with a certain initial state of the pressure and velocity field, a new velocity and pressure distribution is computed for a consecutive sequence of time-steps, whereby the last velocity field and a time-extrapolated pressure distribution of the last time-cycle act as initial state for the following calculations at the next time-step.
Within each time-cycle the new pressure distribution is determined from the discrete version of equation (2.8) by the requirement of discrete conservation of mass for the next time-step. The resulting implicit difference equation - the discrete Poisson equation - is solved iteratively by the SOR method combined with an extrapolation technique. From this new pressure distribution and the old velocity values of the

last time-cycle, the new velocity distribution is evaluated with the aid of the discrete analogue of equations (2.5-7).

Now, a special facility of the MAC-method consists in some massless particles - called marker -, which are located in the cells and move with the corresponding cell velocity computed above. These markers contribute nothing to the dynamics of the system, and enter into the calculations only in so far as they designate which are the surface cells and visualize changes in the flow configuration of the system. At the end of every time-cycle, the markers are moved to their new positions according to the updated velocity distribution [1)].
Here, we use vector velocity plots for showing the direction of flow and the velocity field of the fluid at the end of every time-cycle. For each cell in the system we draw one velocity vector starting at the cell center, with a length proportional to the averaged cell velocities u,w and in the direction of the local flow.

[1)] For the present confined flow simulations (see also section 2.4 below), we need not to make use of the markers. The marker facility will be of importance lateron, as we intend to visualize the fluid motion in a film.

Finally, we emphasize the great significance and advantage of the discrete conservation of mass and momentum in the MAC-method, where the former is obtained by construction of the calculation process and the latter by the choice of the conservative form of the continuous momentum equations and the particular difference scheme. It is well-known (see e.g. [14]) that finite-difference methods possessing similar conservative properties as the continuous equations generally produce more accurate approximations than others. Moreover, those discrete systems seem to be physically more reasonable.

2.4. *The boundary conditions*

A rigid wall may be either of two types, no-slip or free-slip. The latter may be considered to represent a plane or line of symmetry, or if the fluid is viscous, it may represent a non-adhering ("greased") surface. The basic boundary conditions are simply that the normal velocity component vanishes and, in addition, that the tangential component vanishes if no slippage is to be allowed. The decision whether to take free-slip or no-slip boundary conditions depends upon the relation between the spatial discretization parameter and the thickness of the boundary layer that would be expected to develop in the true fluid.

In our special arrangements (see figs. 2a, 2b, 3) there are the following boundaries: the rotational axis being a vertical line of symmetry; the ground and side wall of the crucible, both rigid walls in the horizontal and the vertical, respectively; in the Czochralski simulations, a third horizontal rigid wall appears representing the crystal surface, which is continued by the free surface of the melt. Due to our coarse spatial discretization (see (2.12)) we choose free-slip boundary conditions for u and w at all rigid walls.

The basic boundary conditions for a free surface are the vanishing of the stress tangential to the surface and the balance between the externally applied normal stress and the stress normal to the surface. In the original MAC-method,

the location of the free surface determined by the marker positions and the discretized version of the above boundary conditions is implemented using a special interpolation technique. As these pressure boundary conditions at the free surface strongly influence the whole numerical computation, several authors proposed improvements for the free surface handling in the MAC-method (see [2,4,7,13]). We tried all these methods with our special arrangements, but none of the proposed procedures was able to produce the correct pressure distribution at the free surface. Only when performing confined flow calculations by taking free-slip rigid wall boundary conditions for u and w at the free surface, too, our numerical simulations yielded correct flow patterns in the fluid. This assumption is permitted as long as the ratio between centrifugal and gravitational forces is small as it is the case in the present study. As the normal velocity component has to vanish at all boundaries, the boundary condition for the pressure can be determined from the equation of momentum. In the discrete formulation, this means that the normal velocity in the "virtual" cell outside of the physical boundary has to be the negative of the corresponding velocity value in the adjacent "fluid cell", while the tangential velocity values remain the same. The pressure values of the virtual cells are determined such that the discrete versions of the equations of momentum are satisfied.

The boundary conditions for the zonal velocity component v include the angular velocities Ω_c and Ω_s of the rotation of crucible and crystal: The zonal velocity component v in the i^{th} crystal and crucible boundary cell is defined as $r_i\Omega_s$ and $r_i\Omega_c$, respectively.

3. Numerical results

3.1. *The case of moderate kinematic viscosity*

3.1.1. *Classical Czochralski Method*

As is well-known (see e.g. [3]), the phenomena of hydrodynamic flow in rotating systems are complex and often fail to confirm intuitive predictions. Classification of these phenomena is assisted by the Taylor-Proudman theorem, which is stricly valid only for inviscid fluids, but true as an approximation as long as the Ekman number $Ek = 2\nu/[R_s^2(\Omega_s+\Omega_c)]$ is small (e.g. [6]). In the case of a vertical rotation axis, the theorem states that all three components of the fluid velocity $\vec{u}$ and the dynamic pressure Δp (i.e. pressure difference between the rotating and non-rotating system) do not depend on the vertical coordinate, so that

$$\frac{\partial \Delta p}{\partial z} \equiv \frac{\partial u}{\partial z} \equiv \frac{\partial v}{\partial z} \equiv \frac{\partial w}{\partial z} \equiv 0 \ . \qquad (3.1)$$

For finite Ekman numbers, one observes the set-up of flow patterns where the theorem is obeyed in the major fraction of the fluid volume. To compensate, there are small liquid regions, i.e. boundary layers, where the theorem does not hold. Therefore bulk flow simulations should confirm the Taylor-Proudman statement.

If an object is immersed in a rotating liquid which has a different angular velocity, the Taylor-Proudman theorem implies that the fluid isolates this obstacle by the formation of a liquid column in its vicinity where no mixing

with the outer fluid regions occurs. Such liquid columns are called Taylor-Proudman cells. In the case of a cylindrical crystal contacting the upper free surface of the melt in the rotating crucible, as in the Czochralski crystal-growth arrangement, the Taylor-Proudman cell is bounded by a cylindrical stagnation surface in the liquid beneath and concentric with the crystal. Outside of this stagnation surface the liquid rotates essentially as a solid body provided the crucible rotation is fast enough. If the crystal as well as the crucible rotate in the same direction ("isorotation") only a single Taylor-Proudman cell develops, whereas in the case of opposite rotational directions of crystal and crucible ("counterrotation") the liquid column beneath the crystal divides into two Taylor-Proudman cells seperated by another horizontal stagnation surface ([3],[6]).

In tables 1 and 2, we compare the experimental data of Carruthers and Nassau [3] with our computer simulations for a crucible of radius $R_c = 3.4$ cm [1], a crystal of radius $R_s = 1.2$ cm [1], a melt height $H = 4$ cm, and with discretization parameters $\Delta r = \Delta z = 0.2$ cm in space and $\Delta t = 0.001$ s in time. Only in the counterrotational case with high angular

(continued p. 23)

---

[1] These are essentially the same parameters as in [3]. The exact values $R_c = 3.5$ cm and $R_s = 1.25$ cm of [3] could not be chosen for the coarser mesh width $\Delta r = \Delta z = 0.2$ cm because of technical reasons in the computer programme.

Table 1: Comparison between experiment ([3]) and simulation (isorotation)

Crystal rotation (rpm)	Crucible rotation (rpm)	Cell diameter at top surface (cm)		Cell diameter at bottom of crucible (cm)		Rotation at center of cell (rpm)		Vertical flow at center of cell (cm/s)		Vertical flow near boundary of cell (cm/s)	
		A	B	A	B	A	B	A	B	A	B
o[1)]	15[1)]	3	3,4	2	4,6	12	12,7	-o,3	-o,28	o,1	o,o6
15	15	...	...	...	...	15	15	o	$<5 \cdot 1o^{-5}$	o	$<7 \cdot 1o^{-6}$
25	15	4	3,8	4	4,6	15	16,2	o,1	o,13	-o,1	-o,o1
6o[2)]	15[2)]	3	3,8	4	5,o	2o	19,2	o,4	o,49	-o,1	-o,o4
25	o	...	...	...	...	2	o,82	o,25	o,32	-o,25	-o,11
5o[3)]	o[3)]	...	...	...	...	3	1,1	o,5	o,45	-o,5	-o,27

A, parameters and results from J.R. Carruthers and K. Nassau [3]; B, simulated results from the present study; ..., no formation of the cell; [1)] see fig. 4; [2)] see fig. 5; [3)] see fig. 6

Table 2: Comparison between experiment ([3]) and simulation (counterrotation)

Crystal rotation (rpm)	Crucible rotation (rpm)	upper cell diameter at top surface (cm)		lower cell diameter at bottom of crucible (cm)		Thickness of upper cell (cm)		Rotation at center of lower cell (rpm)		Downward flow rate at center of lower cell (cm/s)	
		A	B	A	B	A	B	A	B	A	B
o	-25	2,5	3,o	2,5	3,8	...	...	-25	-23,9	o,4	o,36
7	-25	3	3,o	3	3,8	<o,2	<o,2	-2o	-21,3	o,5	o,46
25	-25	4	3,o	4,5	4,o	o,2	<o,2	-15	-16,7	...	o,73
5o	-25	4	3,o	5	4,o	o,2	o,3	-15	-15,4	o,4	o,66
5o *)	-5o *)	2,5	2,6	4	4,2	<o,2	<o,1	-3o	-28,6	1,3	1,7o
5o 1)	-1o 1)	4	4,6	b	6,6	1,5	o,6	∿o	- 7,8	...	o,25
5o 2)	- 2 2)	6	6,8	b	4,4	d	d	...	...	...	...

A, parameters and results from J.R. Carruthers and K. Nassau [3]; B, simulated results from the present study; ..., no formation of the cell; b, could not be measured satisfactorily; d, penetration has occurred, one single circulation only; *), in this case, a smaller discretization parameter h = o.1 cm had to be chosen; 1) see fig. 7; 2) see fig. 8

velocities of 5o rpm and -5o rpm of crystal and crucible, respectively, we had to refine the spatial mesh width in order to get better agreement with [3]. The liquid used in our simulations has the kinematic viscosity ν = o.o6 $\frac{cm^2}{s}$ as the 1:1 glycerine-water mixture in [3]. The computing time needed for one simulation has been less than one hour on the IBM 3o33 in Jülich.

Within the scope of measuring and computational accuracy, tables 1 and 2 show in both cases of isorotation and counterrotation, respectively, that our digital simulations eminently agree with the experimental results of [3] not only qualitatively but quantitatively, too. Furthermore, we remark that our simulated flow patterns are quite similar to those obtained by Langlois [11], Langlois and Shir [12], and Kobayashi and Arizumi [8,9]. However, we do not agree with Kobayashi and Arizumi [9, page 182] who state: "Carruthers and Nassau who studied flow patterns in a crucible showed that the stirring occurs when there is no stagnation surface. This condition was realized in practice when the crucible rotation rate was very small compared with the crystal rotation rate. According to the present analyses, however, the same condition is satisfied only when the crystal and the crucible rotate in the same direction." Our digital simulations with Ω_s = 5o and Ω_c = -2 of table 2 clearly disprove the cited statement of Kobayashi and Arizumi (see also fig. 8).

In figs. 4,5,6 and figs. 7,8 we present some characteristic flow patterns of our classical Czochralski simulations in the isorotational and the counterrotational case, respectively. Although our numerical calculations are performed in the Eulerian coordinate system, the plots show the momentary state of the rotational melt flow in the right half of a vertical (symmetric) cross section of the crucible in view of the Lagrangian frame (i.e. in a corotational coordinate system). In all cases, we have started our simulations from the liquid at rest, switching on the appropriate crystal and crucible rotation at the time t=o . The figures show the flow patterns at the time indicated, and v_{max} designates the absolute value of the maximum cell velocity whose calculation has been described in section 2.3. The last plots always reveal nearly steady-state flow situations.

Fig. 4 shows the typical flow patterns during the formation of the Taylor-Proudman cell around a stationary obstacle (i.e. the non-rotating crystal) immersed in a rotating liquid, with the fluid motion starting at the lower edge of the crucible because of adhesion ("spin-up effect"). In the steady state, the Taylor-Proudman cell has emerged, and maximum flow velocities occur beneath the crystal.

When the crystal as well as the crucible rotate in the same direction but with different angular velocities, as shown in fig. 5, two vortices set up in the beginning, one below the crystal and another in the lower edge of the crucible. But gradually, the crystal draws more and more fluid upwards

(continued p. 27)

Fig. 4 :

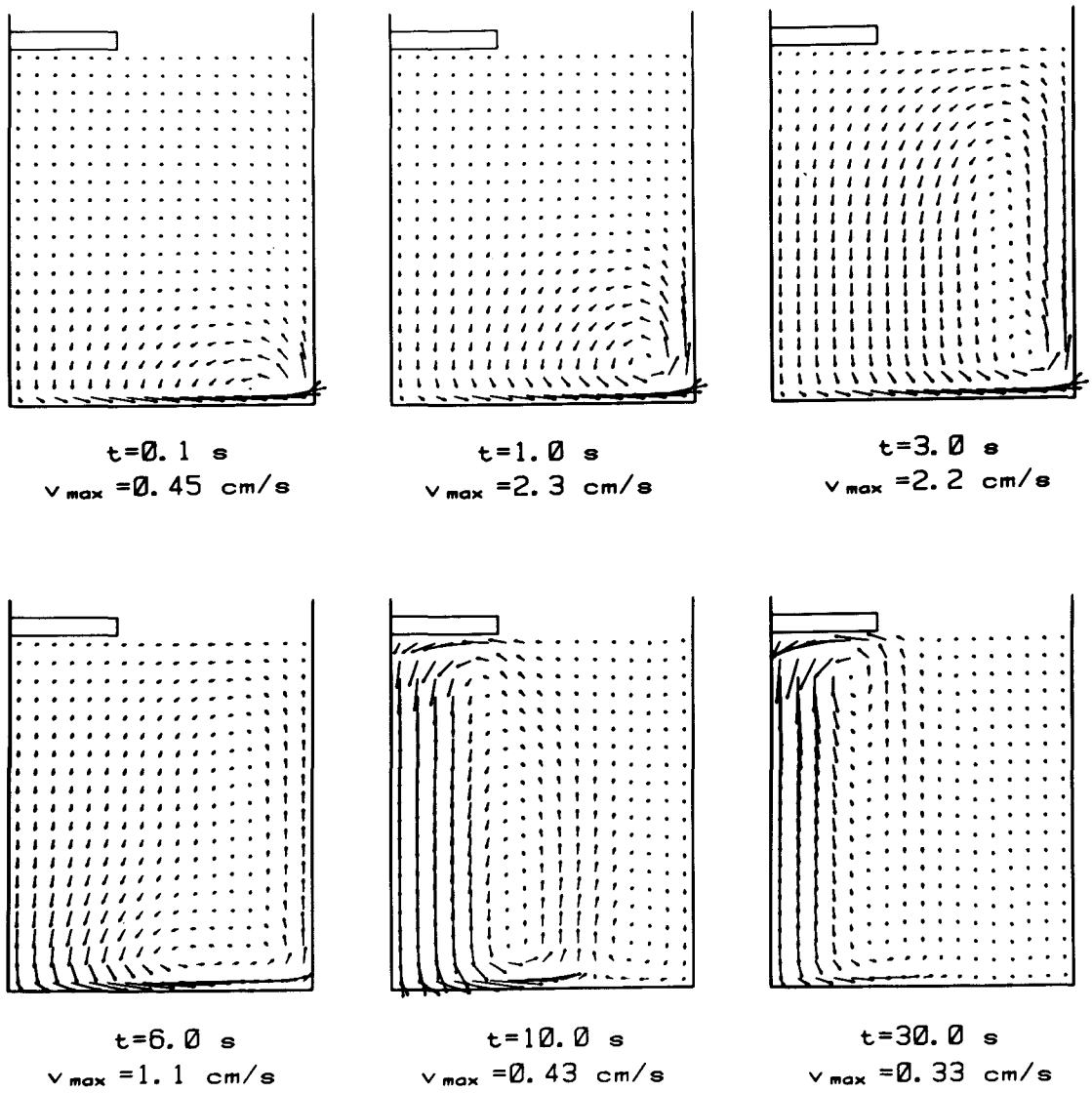

CRUCIBLE ROTATION: 15 RPM

CRYSTAL ROTATION : 0 RPM

Fig. 5 :

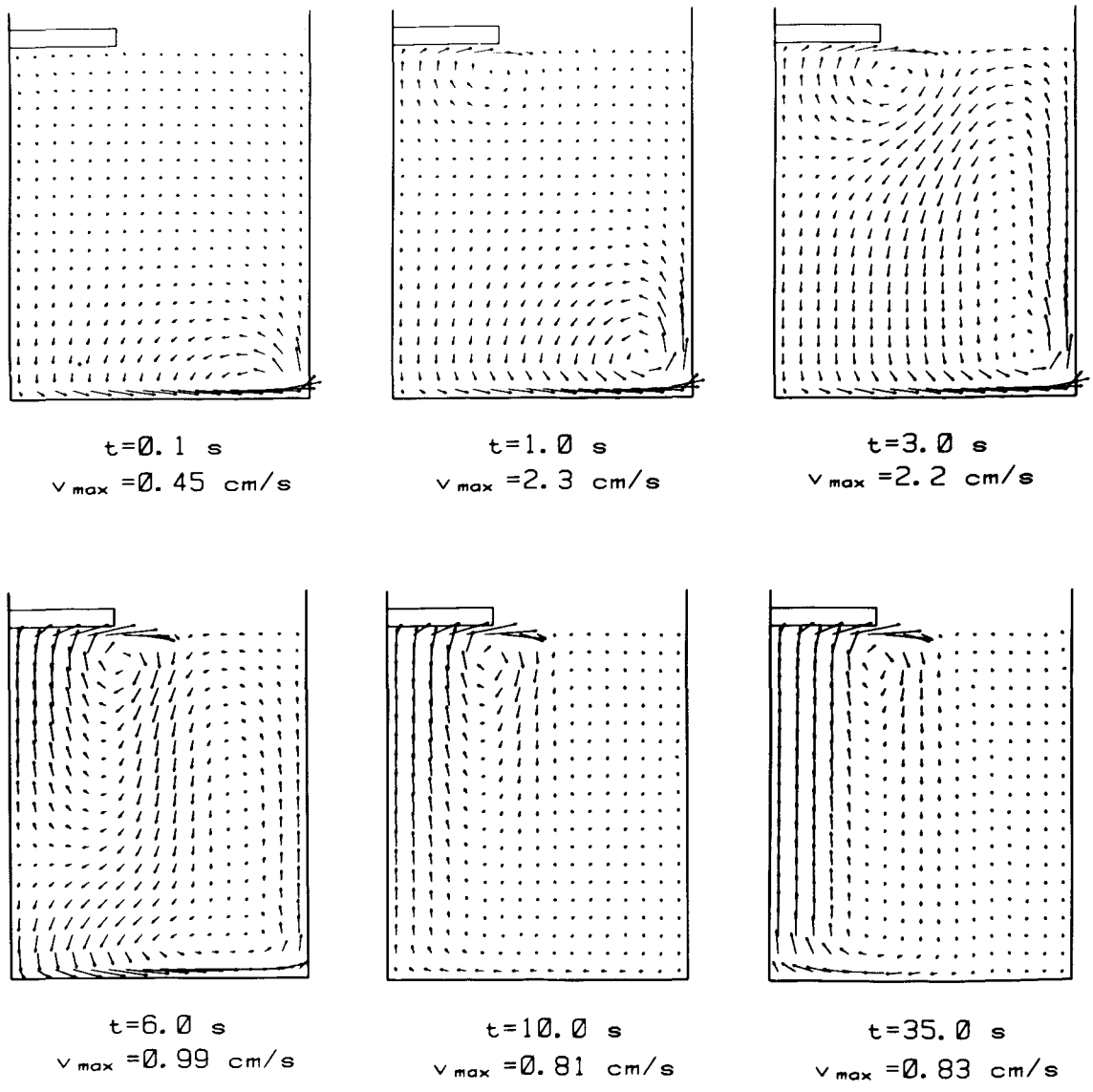
t=Ø.1 s
v max =Ø.45 cm/s
t=1.Ø s
v max =2.3 cm/s
t=3.Ø s
v max =2.2 cm/s
t=6.Ø s
v max =Ø.99 cm/s
t=1Ø.Ø s
v max =Ø.81 cm/s
t=35.Ø s
v max =Ø.83 cm/s
CRUCIBLE ROTATION: 15 RPM
CRYSTAL ROTATION : 6Ø RPM

($\Omega_s > \Omega_c$), so that a Taylor-Proudman cell develops reaching right to the bottom of the crucible. The highest cell velocities occur where the crystal throws the fluid aside.

In fig. 6, the crucible stays at rest and the fluid motion is induced by the crystal rotation. In the course of time, the crystal spins up the whole liquid volume, and no stagnation surface is formed. Therefore the entire melt in the crucible is stirred.

Fig. 7 shows the evolution in time of the flow patterns, where crystal and crucible rotate in opposite directions with different (but not too small) angular velocities. Again two vortices occur beneath the crystal and in the lower edge of the crucible, respectively, which gradually devolve in the two expected Taylor-Proudman cells. The size of the one beneath the crystal obviously depends on the relative angular velocity between crystal and crucible. Additionally, in this cell the maximum flow velocities appear.

Finally, in fig. 8 we present the flow patterns of a counterrotational case, where in the steady state situation the crystal rotation dominates over the crucible rotation. In time, the crystal draws most of the liquid volume upwards and throws the fluid aside, the latter with the maximum flow velocity. This prevents the formation of the Taylor-Proudman cells.

Fig. 6 :

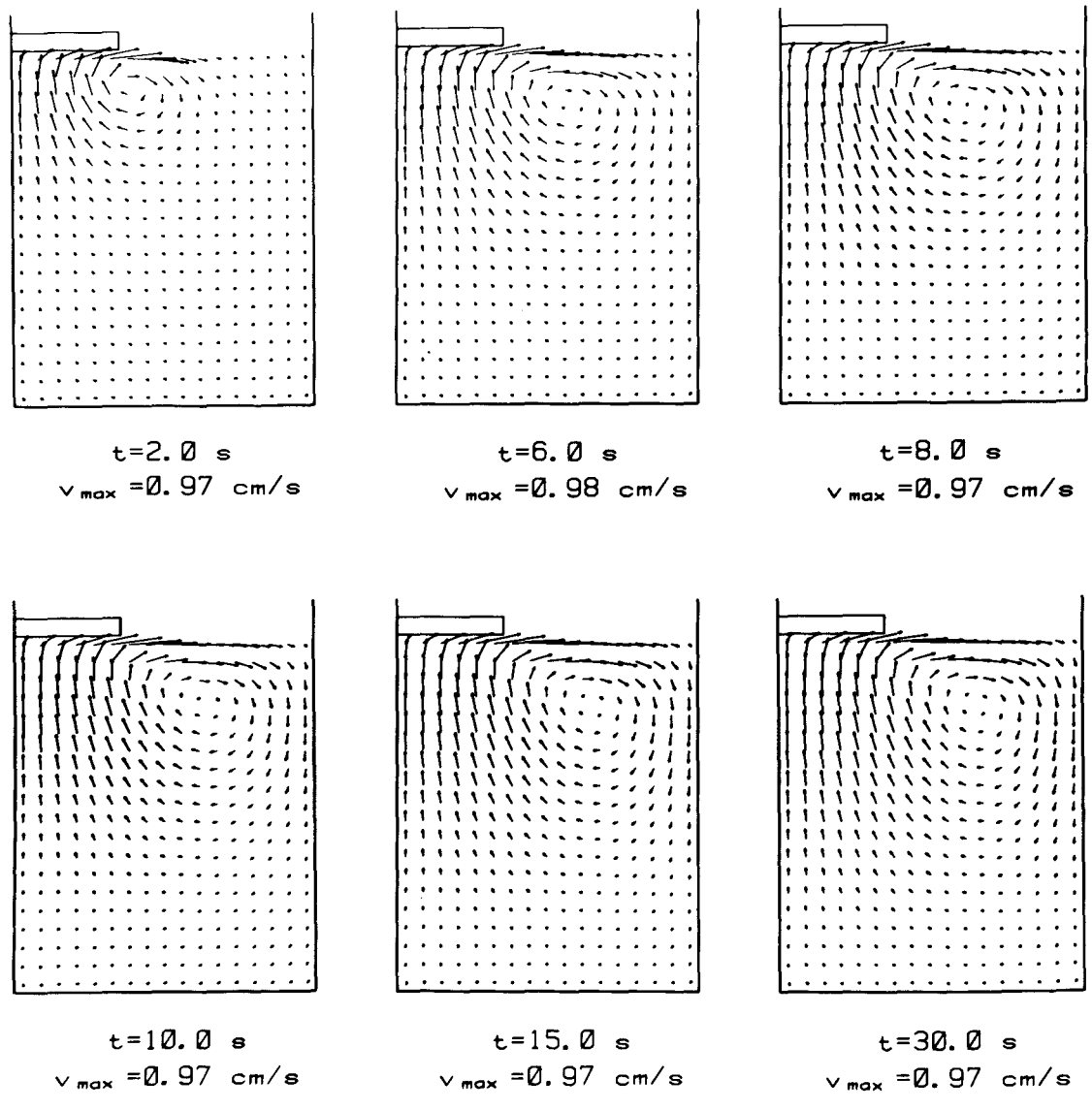
t=2.Ø s
v max =Ø.97 cm/s
t=6.Ø s
v max =Ø.98 cm/s
t=8.Ø s
v max =Ø.97 cm/s
t=1Ø.Ø s
v max =Ø.97 cm/s
t=15.Ø s
v max =Ø.97 cm/s
t=3Ø.Ø s
v max =Ø.97 cm/s
CRUCIBLE ROTATION: Ø RPM
CRYSTAL ROTATION : 5Ø RPM

Fig. 7 :

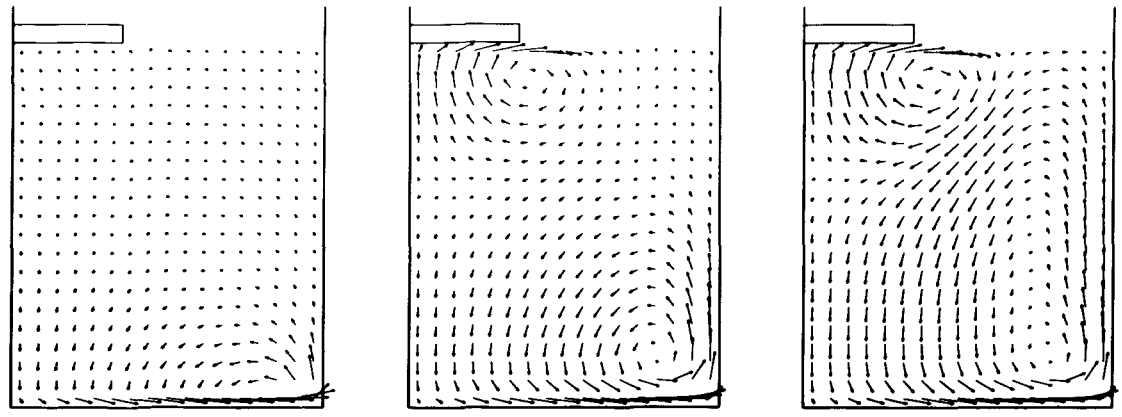

t=Ø.1 s
v_{max} =Ø.2Ø cm/s

t=2.Ø s
v_{max} =1.4 cm/s

t=4.Ø s
v_{max} =1.3 cm/s

t=8.Ø s
v_{max} =Ø.86 cm/s

t=15.Ø s
v_{max} =Ø.66 cm/s

t=3Ø.Ø s
v_{max} =Ø.64 cm/s

CRUCIBLE ROTATION: 1Ø RPM
CRYSTAL ROTATION : -5Ø RPM

Fig. 8 :

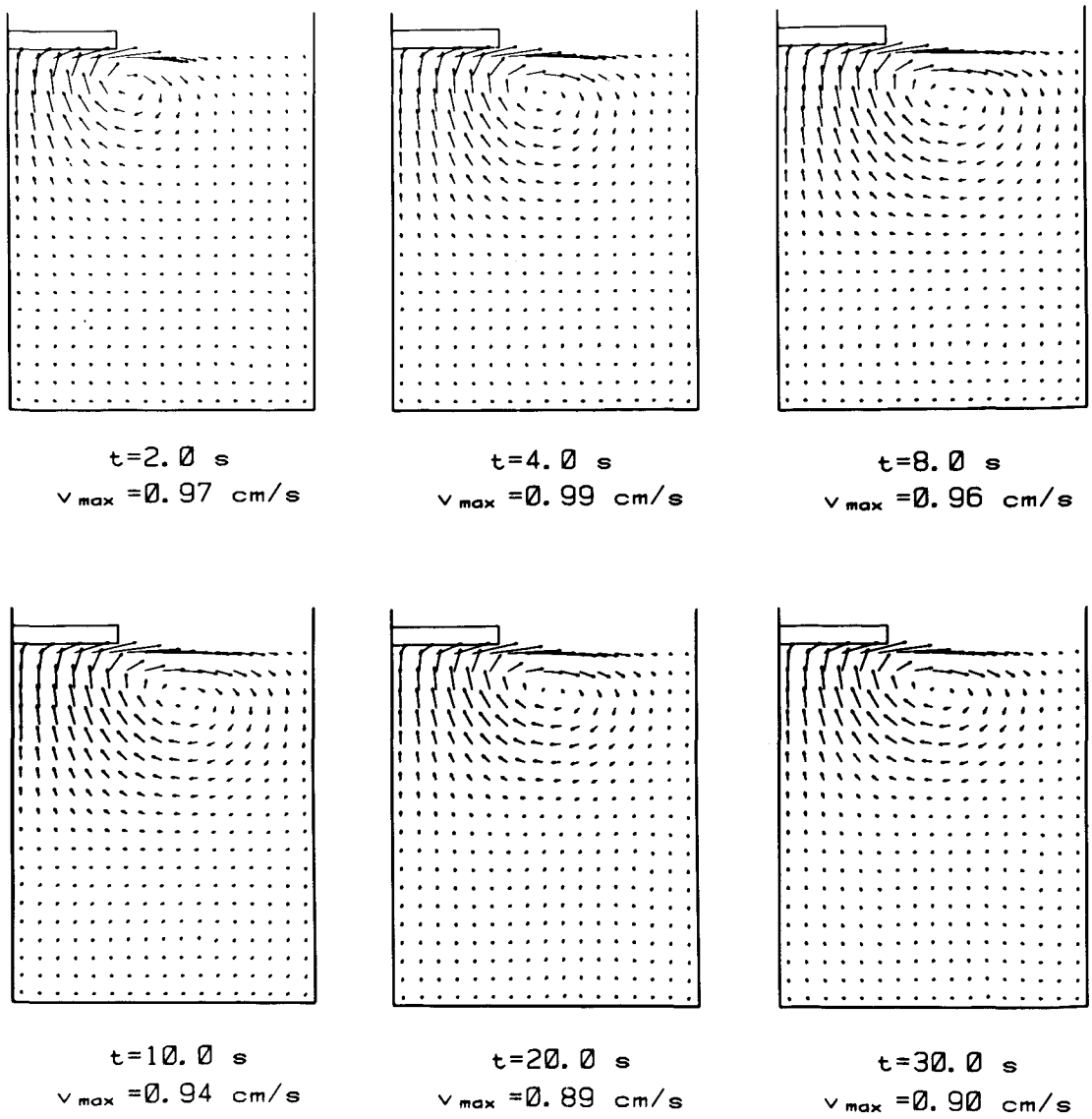

CRUCIBLE ROTATION: 2 RPM

CRYSTAL ROTATION : -5Ø RPM

3.1.2. ACRT Flux Growth

In this section we present the first digital simulations for the Accelerated Crucible-Rotation Technique proposed by Scheel and Schulz-Dubois [15,17,18] (see fig. 1b and fig. 2b). All geometrical, physical and numerical parameters are identical to those in section 3.1.1 disregarding the absence of the crystal. With a period of 1o s , we alternate the crucible rotation between constant rotary motion of 2o rpm and stoppage. Fig. 9 shows the flow patterns exhibited in the two acceleration modes. Obviously, our calculations confirm the presumptions in [15,17,18] that total stirring of the melt is achieved by applying ACRT and that the maximum flow velocities occur at the bottom of the crucible as desired[1].

3.1.3. CACRT Czochralski Growth

Scheel and Müller-Krumbhaar [16] have proposed to apply the Accelerated Crucible (and Crystal) Rotation Technique to the Czochralski crystal-pulling process (CACRT) in order to avoid the formation of stationary Taylor-Proudman cells (see section 3.1) and to achieve smooth stirring of the melt, thereby producing crystals of improved homogeneity. On the same geometrical, physical and numerical conditions as in section 3.1.1, we study CACRT in a counterrotational as well as in an isorotational arrangement numerically. In both cases,

(continued p. 33)

---

[1] For the corresponding simulations with h = o.1 cm (see (2.12)) see figs. 23a-k in the appendix.

Fig. 9 :

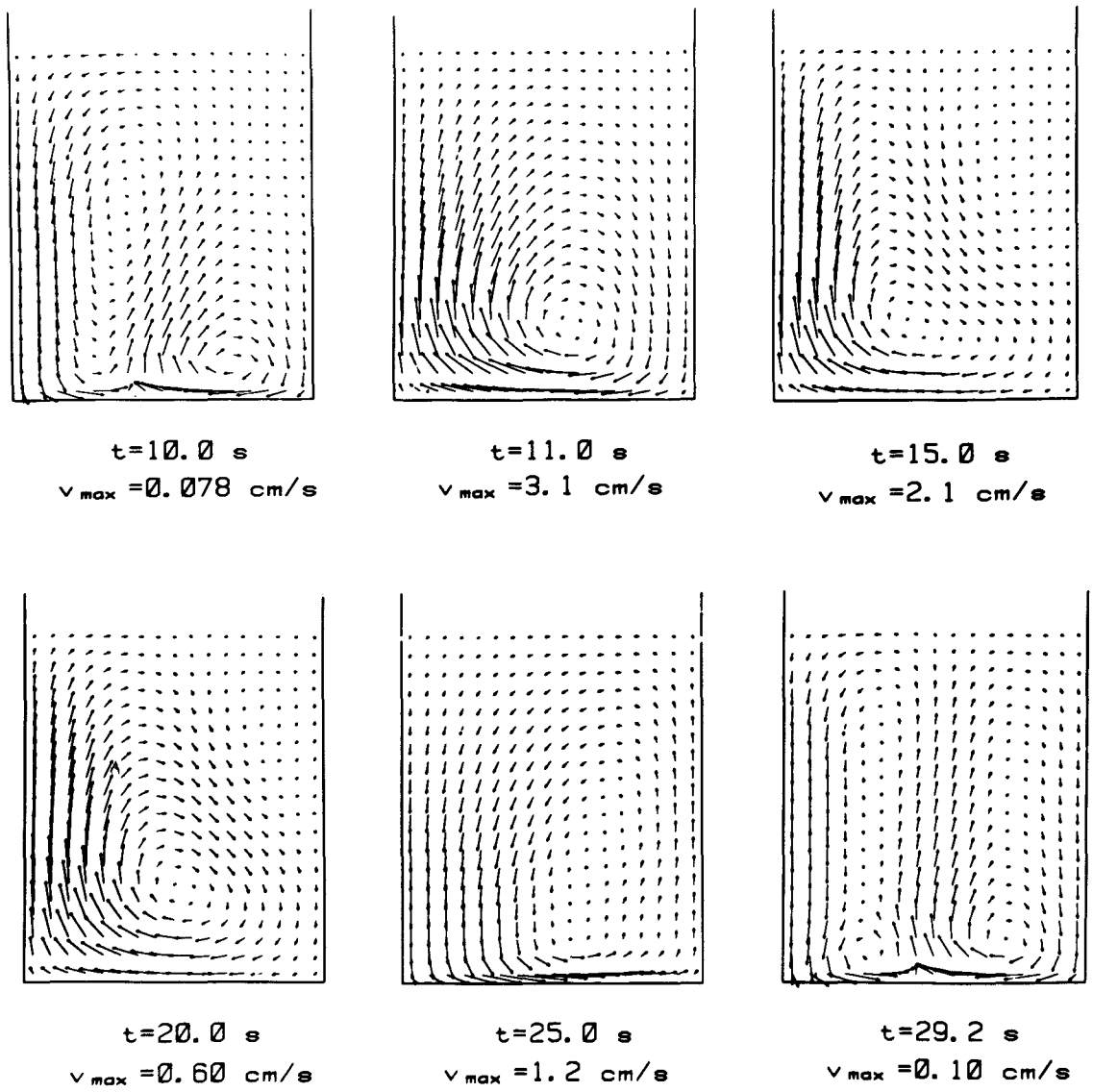
t=10.0 s
v max =0.078 cm/s
t=11.0 s
v max =3.1 cm/s
t=15.0 s
v max =2.1 cm/s
t=20.0 s
v max =0.60 cm/s
t=25.0 s
v max =1.2 cm/s
t=29.2 s
v max =0.10 cm/s
CRUCIBLE ROTATION: 20 : 0 RPM
TIME PERIOD : 10 s

apart from different crystal rotational directions, we vary the crystal and the crucible rotation with a time period of 1o s by a constant acceleration from ±4o rpm to ±8o rpm and 1o rpm to 3o rpm , respectively, followed by a constant deceleration from ±8o rpm to ±4o rpm of the crystal and 3o rpm to 1o rpm of the crucible (see [16]). In fig. 1o and fig. 11, we present, for the first time, the results of our digital simulations for the counterrotational and the isorotational CACRT arrangements, respectively.
In the case of counterrotation, fig. 1o shows that the originally developed Taylor-Proudman cell beneath the crystal certainly changes its size nearly periodically, but still cannot be destroyed. For equally directed crystal and crucible rotation, however, the flow patterns in fig. 11 are completely different from the ones before. Namely, in this arrangement, the Taylor-Proudman cell beneath the crystal is only formed during the acceleration phase, while deceleration causes the disappearance of the cell. Additionally, the size of the cell is in any case greater than before. For these reasons, the isorotational CACRT arrangement seems to be more advantageous in view of optimum stirring of the melt [1].

---

[1] For the analogous simulations with h = o.1 cm (see (2.12)) see figs. 24-25 in the appendix. Figs. 26-27 of the appendix present the corresponding flow patterns for a time period of 2o s .

Fig. 1o :

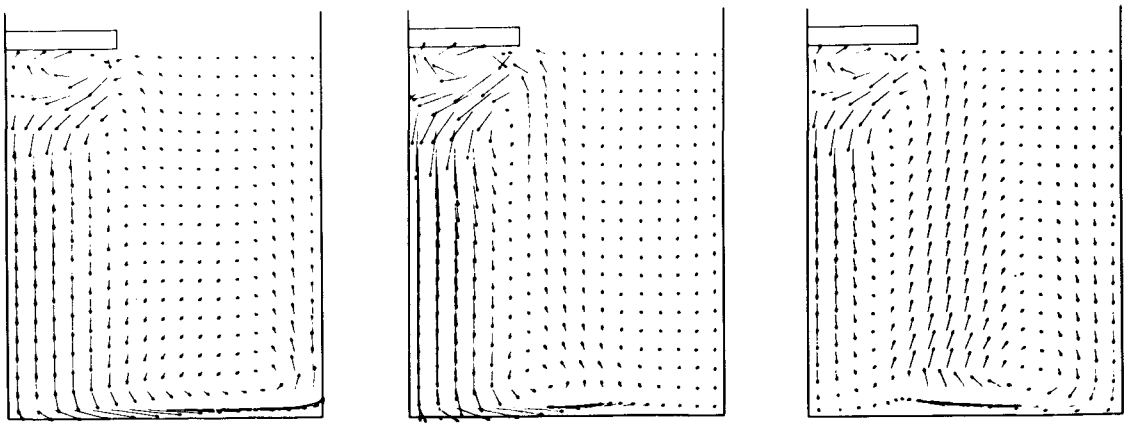

t=10.0 s
v_{max} =1.6 cm/s

t=11.0 s
v_{max} =0.92 cm/s

t=15.0 s
v_{max} =1.2 cm/s

t=20.0 s
v_{max} =1.3 cm/s

t=21.0 s
v_{max} =0.82 cm/s

t=25.0 s
v_{max} =1.7 cm/s

CRUCIBLE ROTATION: 10 : 30 RPM
CRYSTAL ROTATION : -40 : -80 RPM
TIME PERIOD : 10 s

Fig. 11 :

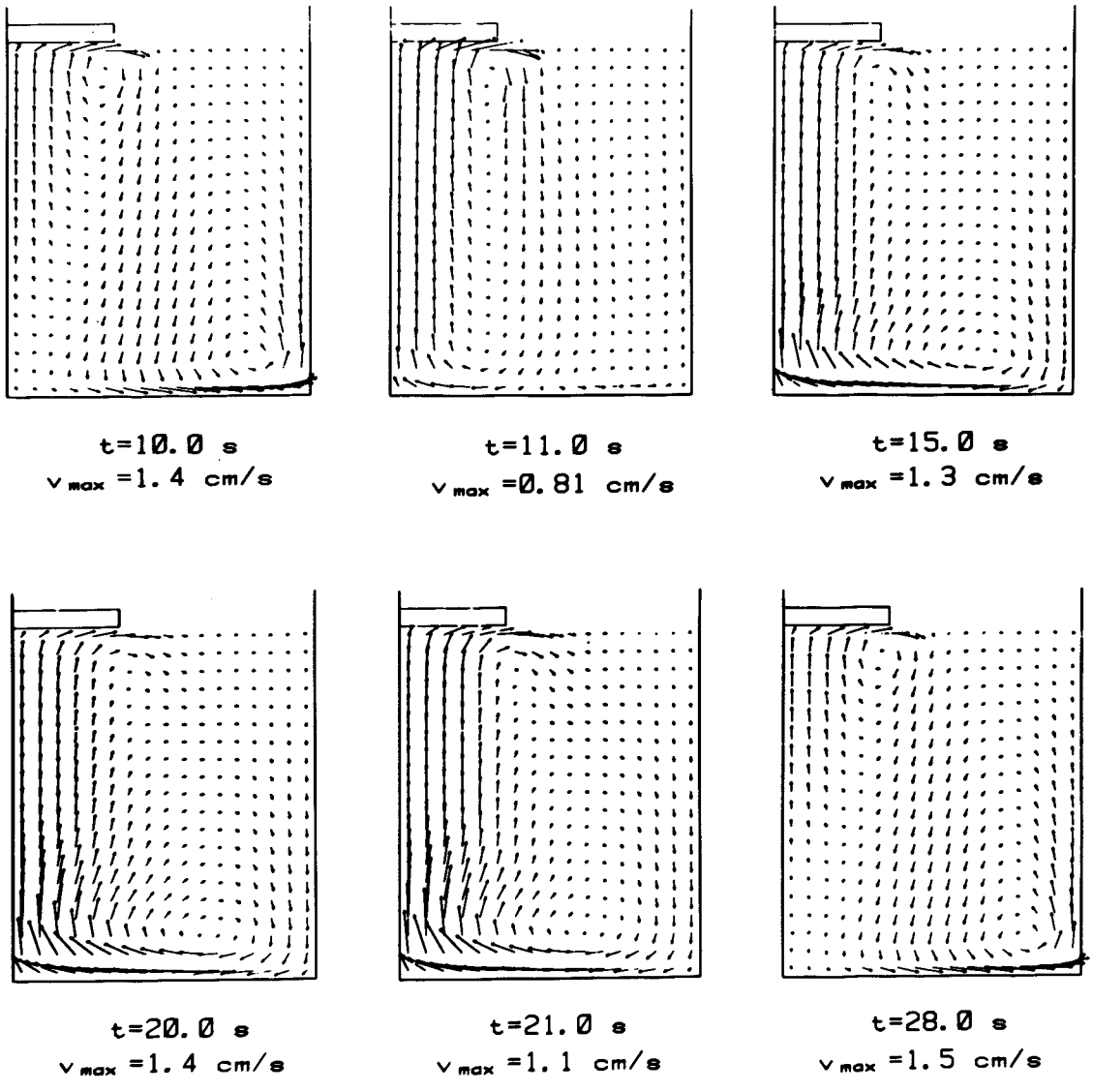

CRUCIBLE ROTATION: 10 : 30 RPM
CRYSTAL ROTATION : 40 : 80 RPM
TIME PERIOD : 10 s

3.2. The case of low kinematic viscosity

3.2.1. Classical Czochralski Method

In this section, we present the flow patterns of the classical Czochralski simulations with the kinematic viscosity $\nu = 0.005 \frac{cm^2}{s}$ of liquid copper. Although the steady state flow configurations must be essentially the same as in section 3.1.1, the transition time needed to reach the steady-state in this case is much longer than before. Moreover, for the low kinematic viscosity, the particular flow patterns during this non-stationary transition phase are completely different from those for the moderate viscosity in section 3.1.1.

All physical (except ν), geometrical and numerical parameters are identical to those in section 3.1.1, only the mesh width h of the spatial grid system had to be refined for the low viscosity simulations (see (2.12)). Figs. 12-16 show the flow patterns of the low viscosity analogues to figs. 4-8, where the last plots are very similar to the expected steady-state configuration. The computing time needed to perform one of these simulations was about six hours on the IBM 3033 in Jülich.

However, the true analogues of the nearly steady-state configurations in figs. 4-8 would only have been reached after approximately 150 s , i.e. 150 000 time-cycles, the calculation of which would have taken about ten and more hours CPU time. Therefore we stopped our simulations earlier (maximum CPU time: 8 hours).

Figs. 12a-f, corresponding to fig. 4 in section 3.1.1, show the typical flow patterns during the formation of the Taylor-Proudman cell beneath the stationary crystal immersed into the rotating crucible. First the fluid exhibits the so-called "spin-up effect" at the lower edge of the crucible, and in the course of time the Taylor-Proudman cell emerges.

Figs. 13a-f are the analogues to fig. 5 for the isorotational case with $\Omega_s > \Omega_c$. The flow patterns of fig. 5 and figs. 13a-f are quite similar, disregarding the pulsation effect of the Taylor-Proudman cell beneath the crystal during its formation in the low viscosity case.

If the crucible stays at rest, while the fluid motion is merely induced by the crystal rotation, as it is the case in figs. 14a-f, no stagnation surface develops and the whole melt is stirred. As in fig. 6, a vortex appears beneath the rotating crystal which gradually enlarges moving to the outer region of the crucible. Finally, the crystal spins up the whole liquid volume.

Figs. 15a-f show the evolution in time of the flow patterns in a counterrotational case with different but not too small angular velocities of the crystal and crucible rotation. As in fig. 7, two vortices occur beneath the crystal and in the lower edge of the crucible, respectively, which gradually devolve in the two expected Taylor-Proudman cells. Moreover, we note that in contrast to fig. 7 the formation of the Taylor-Proudman cell beneath the crystal does not proceed monotonously but exhibits the same pulsation effect as in figs. 13a-f.

Figs. 16a-f are concerned with the counterrotational Czochralski case of a much faster crystal than crucible rotation. In the beginning, the flow patterns are quite similar to those of figs. 15a-f, but in time the crystal throws the fluid aside up to the crucible wall and a large vortex develops in the upper part of the melt. Nevertheless, contrary to the moderate viscosity analogue in fig. 8, the rotating crystal is not yet able to draw a whole column of liquid from the bottom of the crucible upwards. We therefore present the simulation of this case with a still lower crucible rotation rate (see figs. 17a-f). Here, the flow patterns are very similar to those before, but gradually the crystal rotation dominates over the crucible rotation, thereby preventing the formation of Taylor-Proudman cells.

Fig. 12a : t = 1.o s , v_{max} = 3.1EO cm/s

NUE : 0.005 cm^2/s

CRUCIBLE ROTATION : 15 rpm

CRYSTAL ROTATION : O rpm

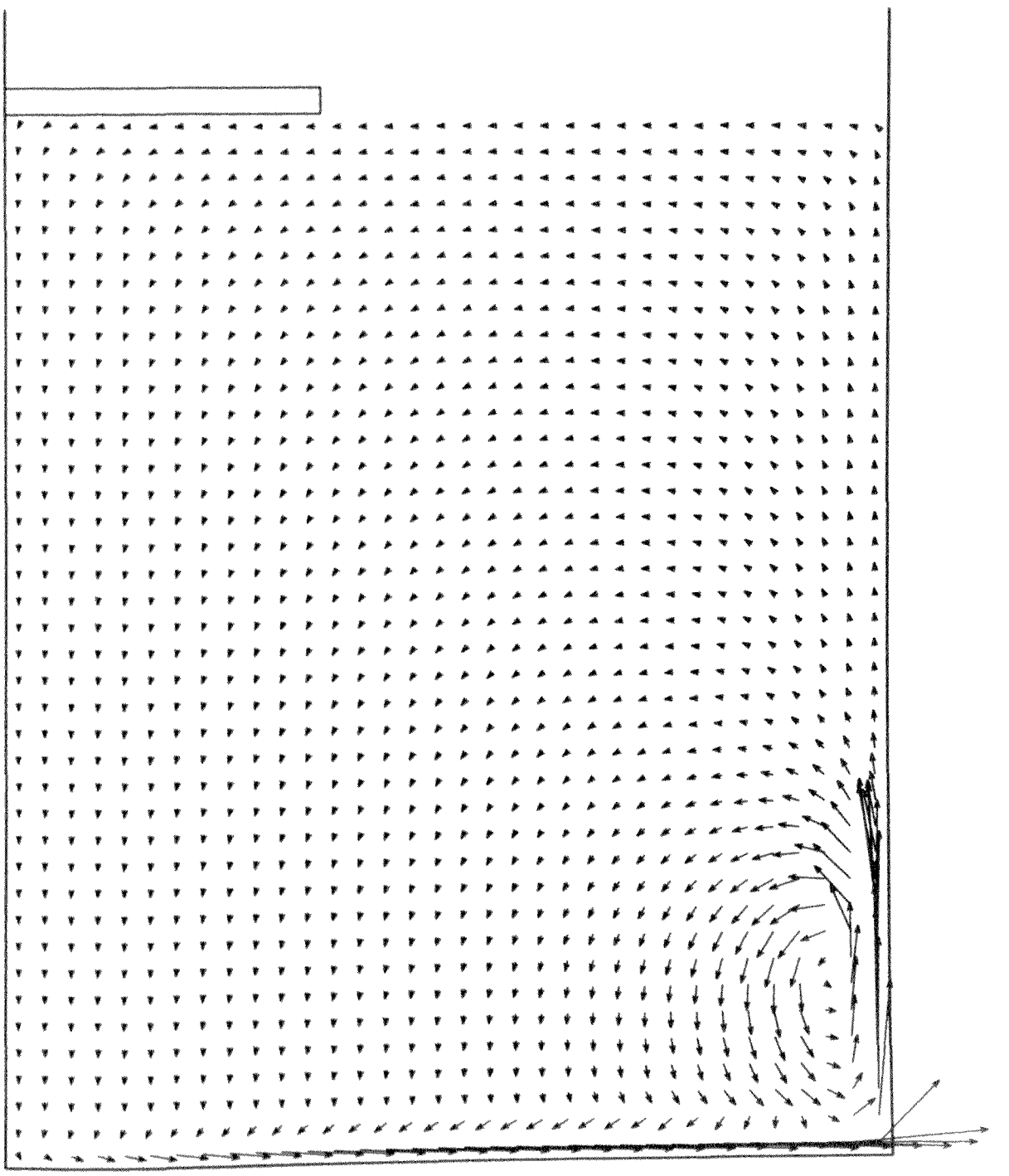

Fig. 12b : t = 5.0 s , v_{max} = 2.9EO cm/s

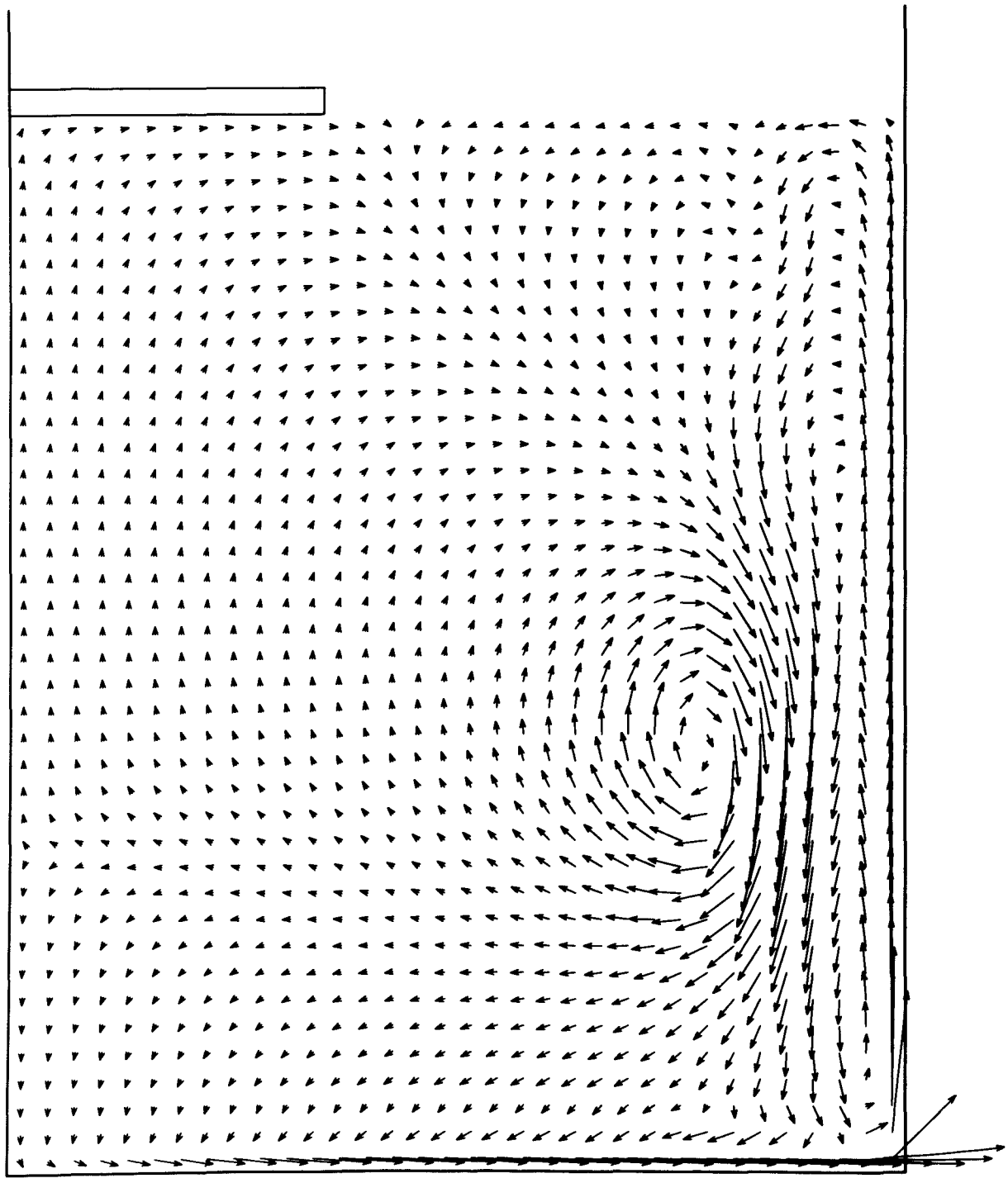

Fig. 12c : t = 18.0 s , v_{max} = 1.6E0 cm/s

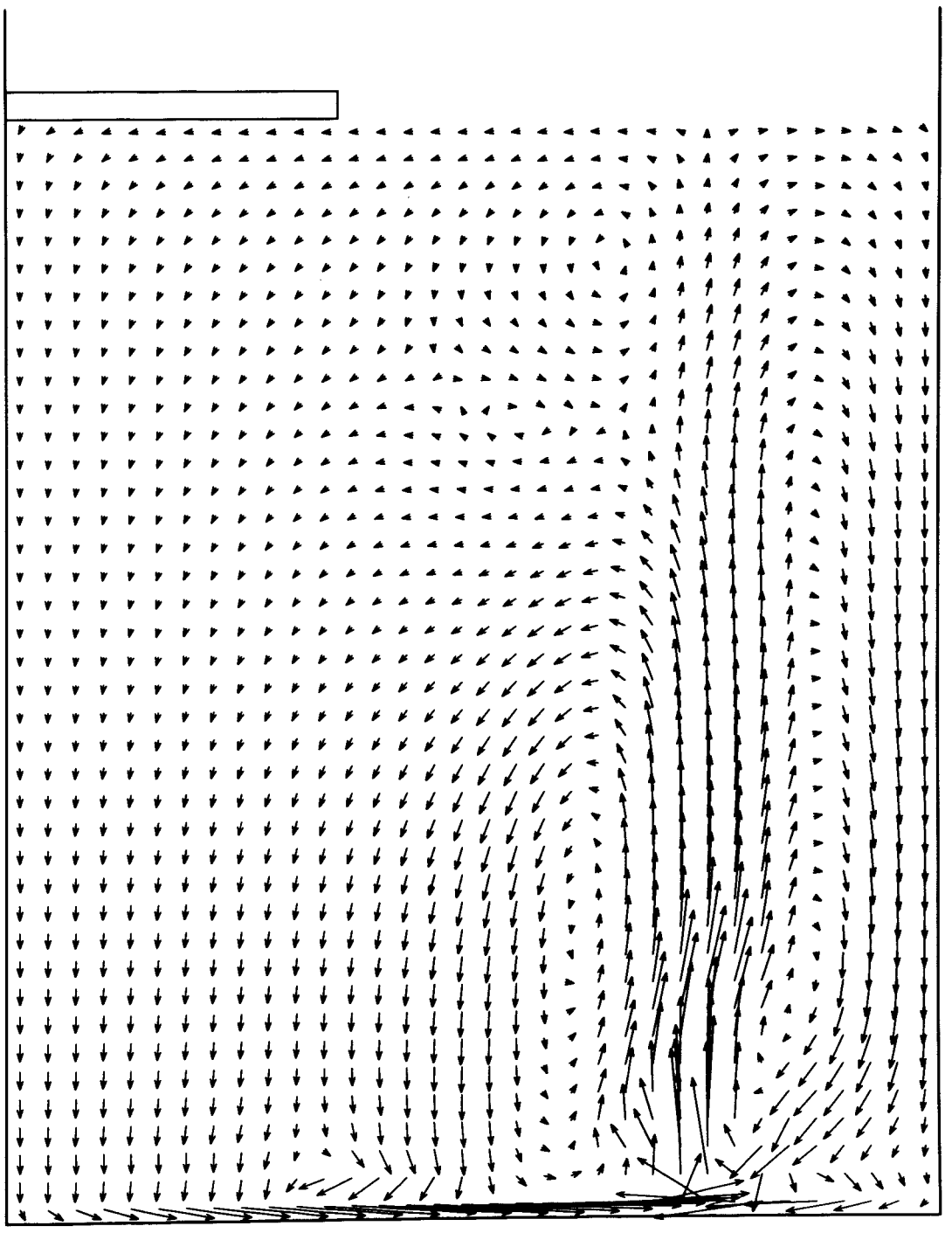

Fig. 12d : t = 25.0 s , v_{max} = 1.2E0 cm/s

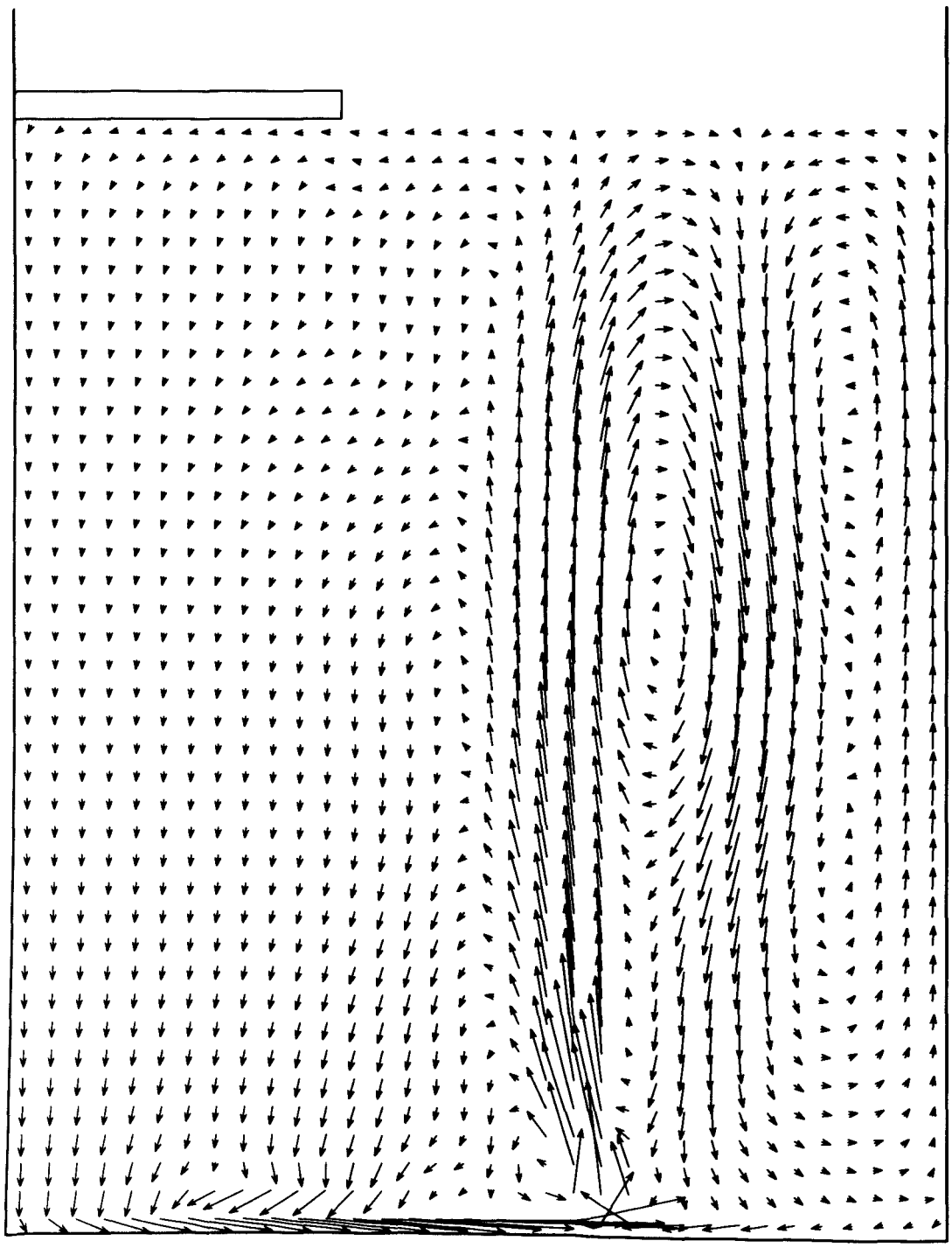

Fig. 12e : t = 35.0 s , v_{max} = 8.5E-1 cm/s

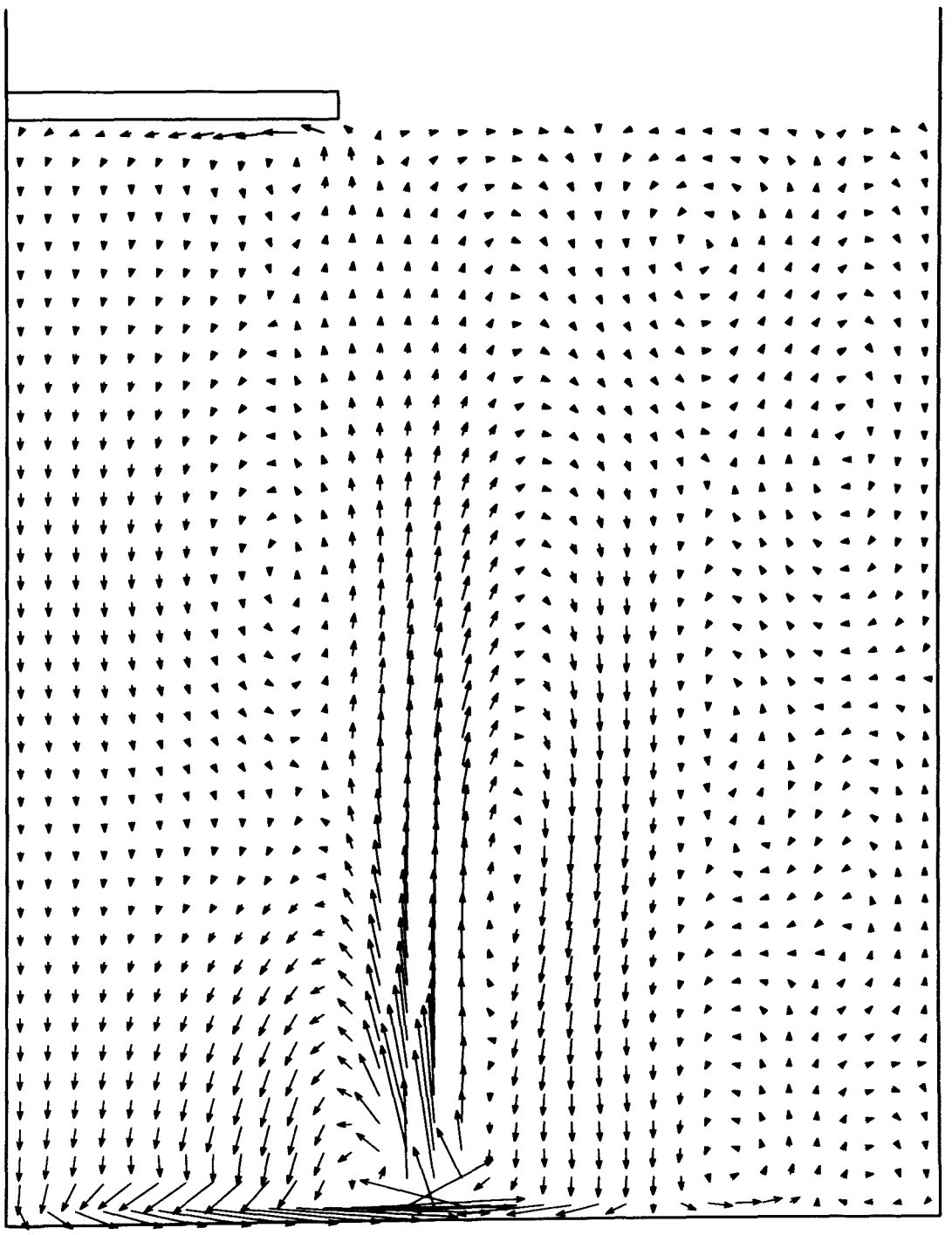

Fig. 12f : t = 48.677 s , v_{max} = 2.6E-1 cm/s

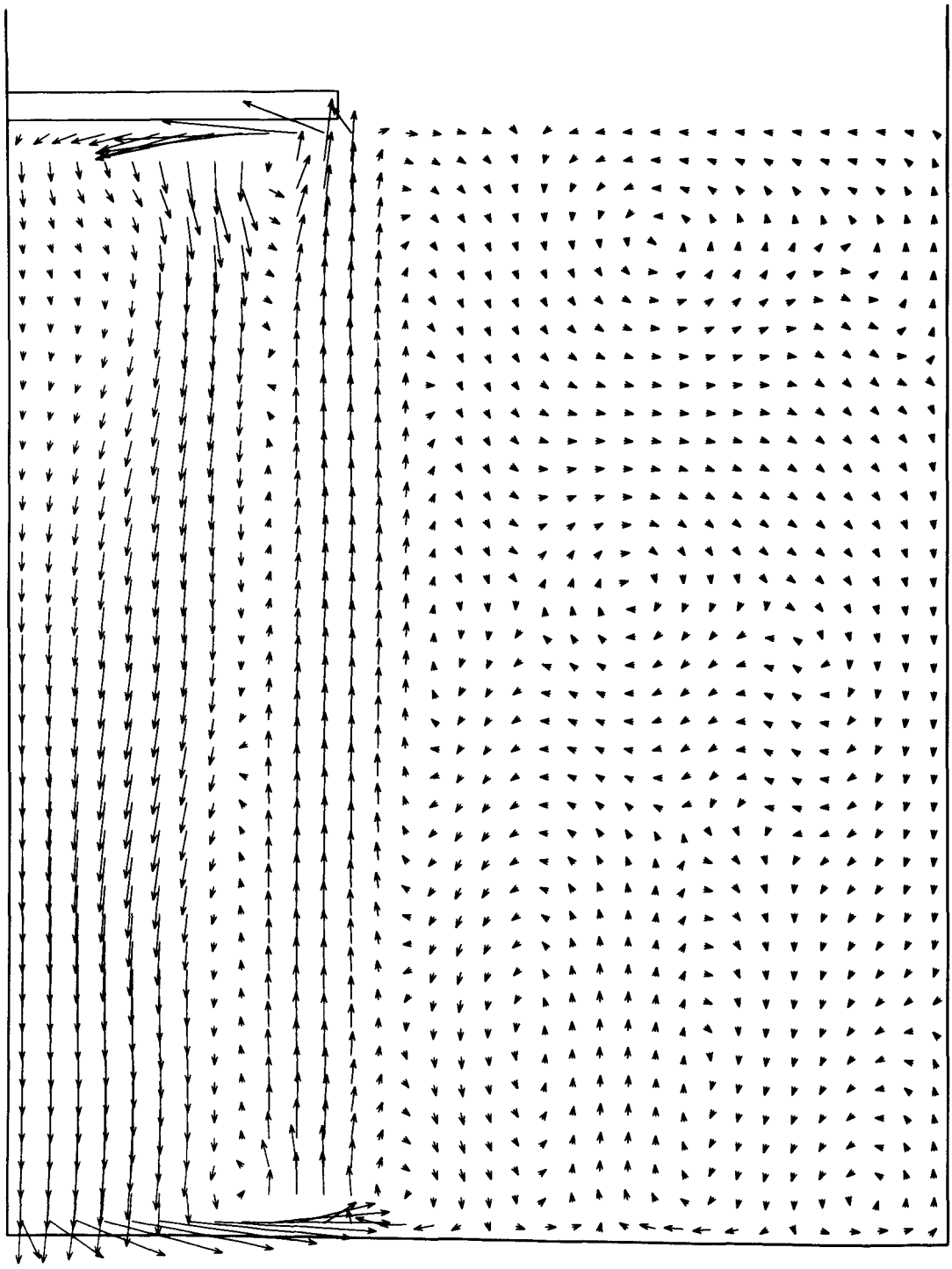

Fig. 13a : t = 1.0 s , v_{max} = 3.1E0 cm/s

NUE : 0.005 cm^2/s

CRUCIBLE ROTATION : 15 rpm

CRYSTAL ROTATION : 60 rpm

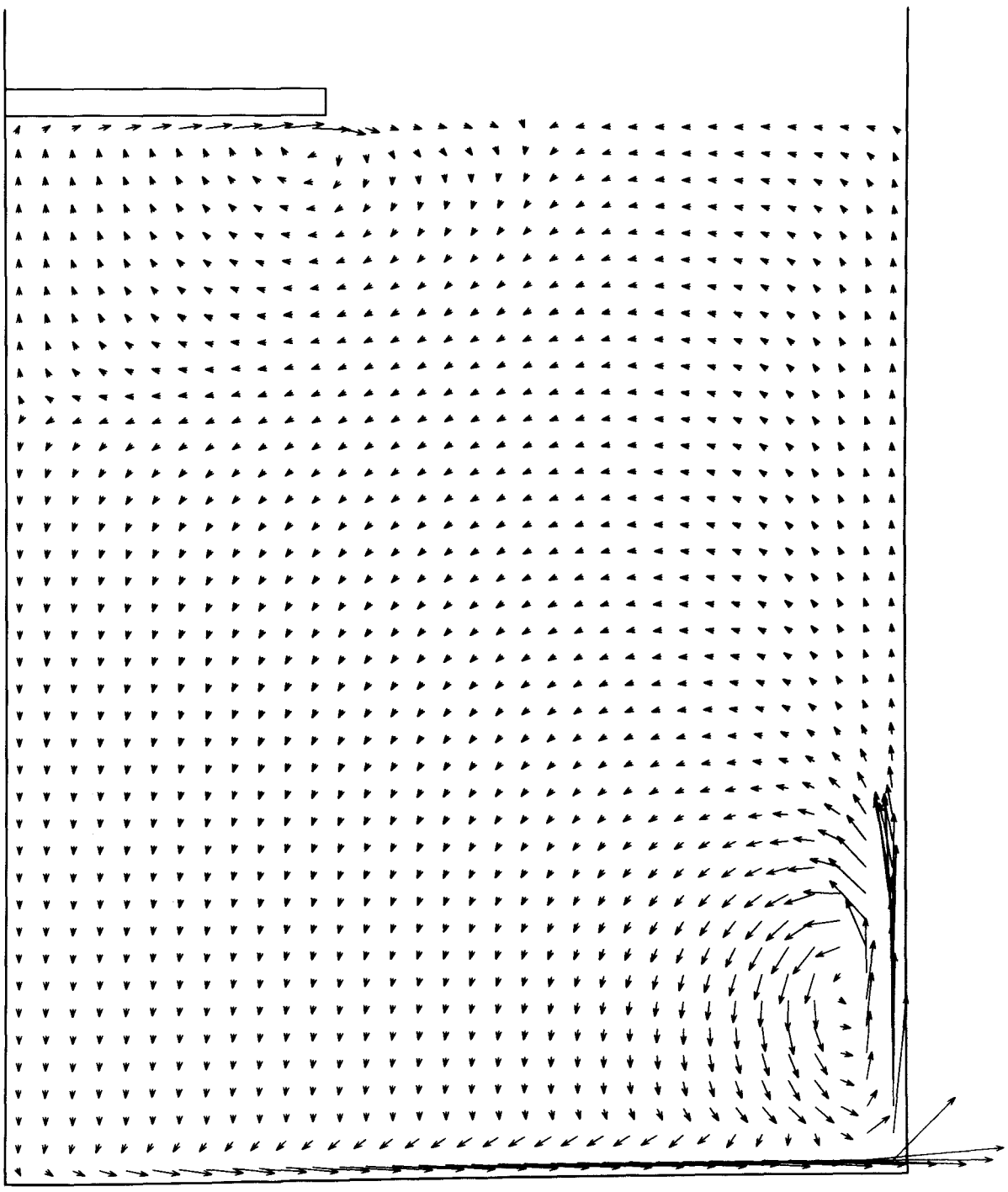

Fig. 13b : t = 5.0 s , v_{max} = 2.9E0 cm/s

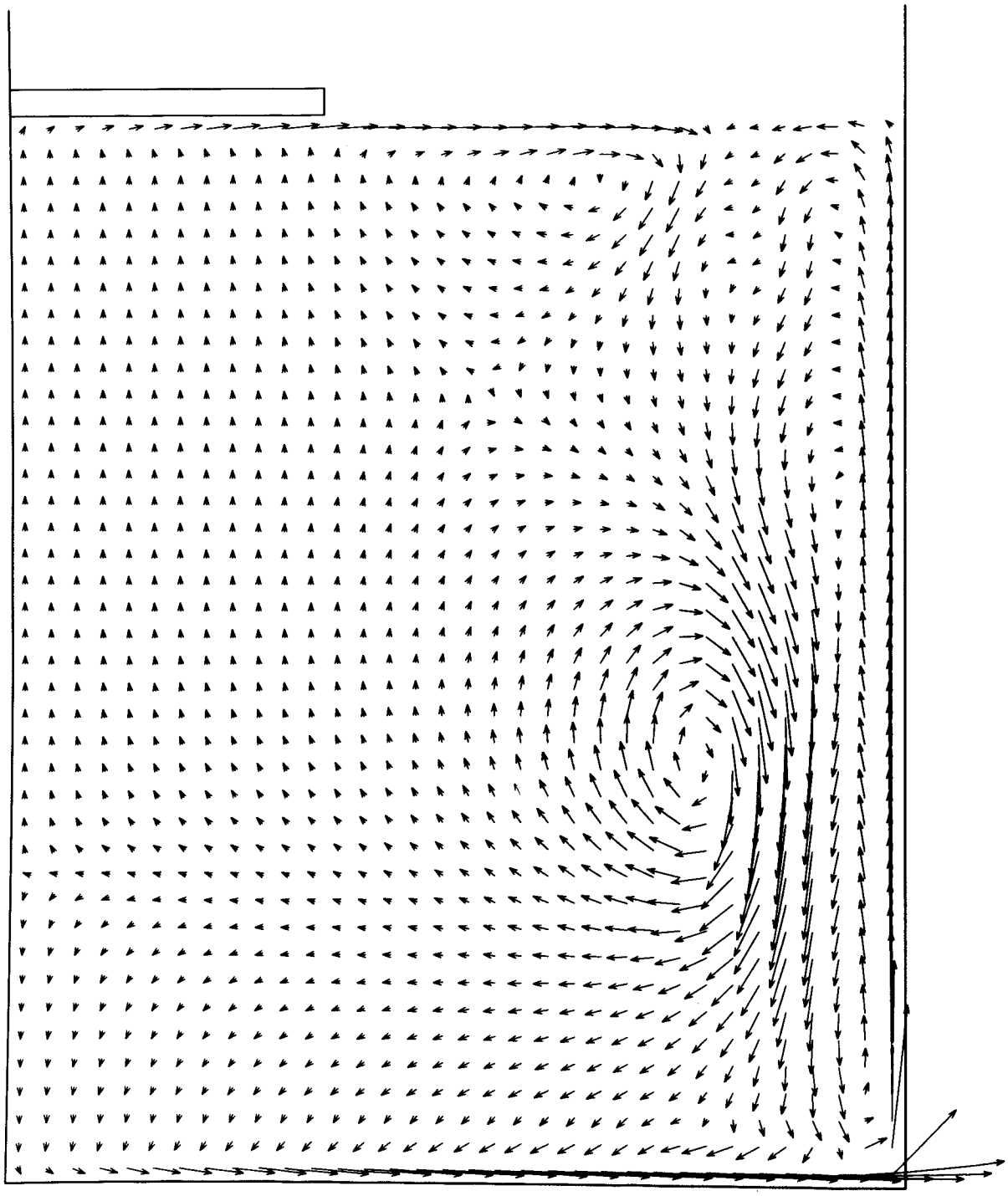

Fig. 13c : t = 18.0 s , v_{max} = 1.5EO cm/s

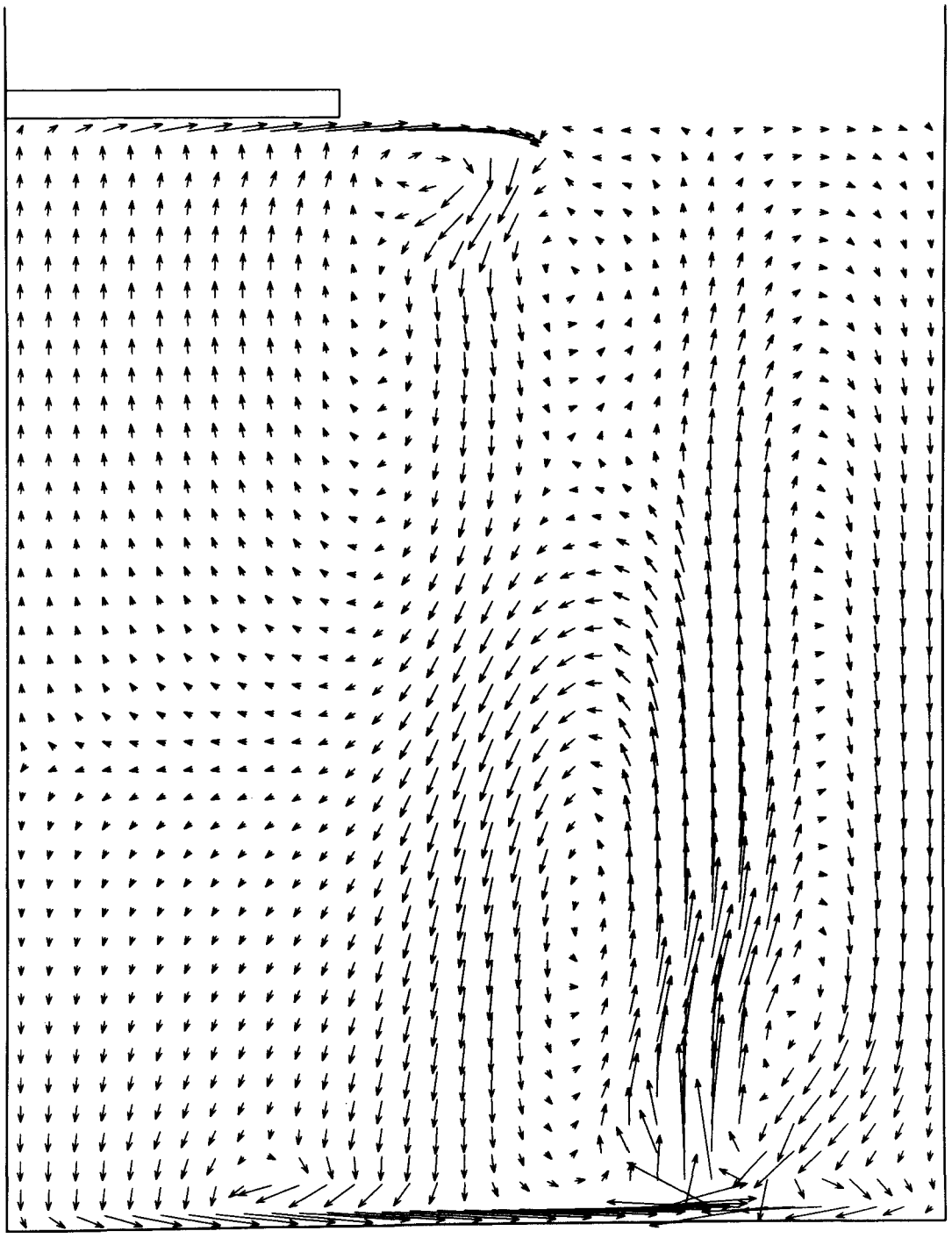

Fig. 13d : t = 25.0 s , v_{max} = 1.0E0 cm/s

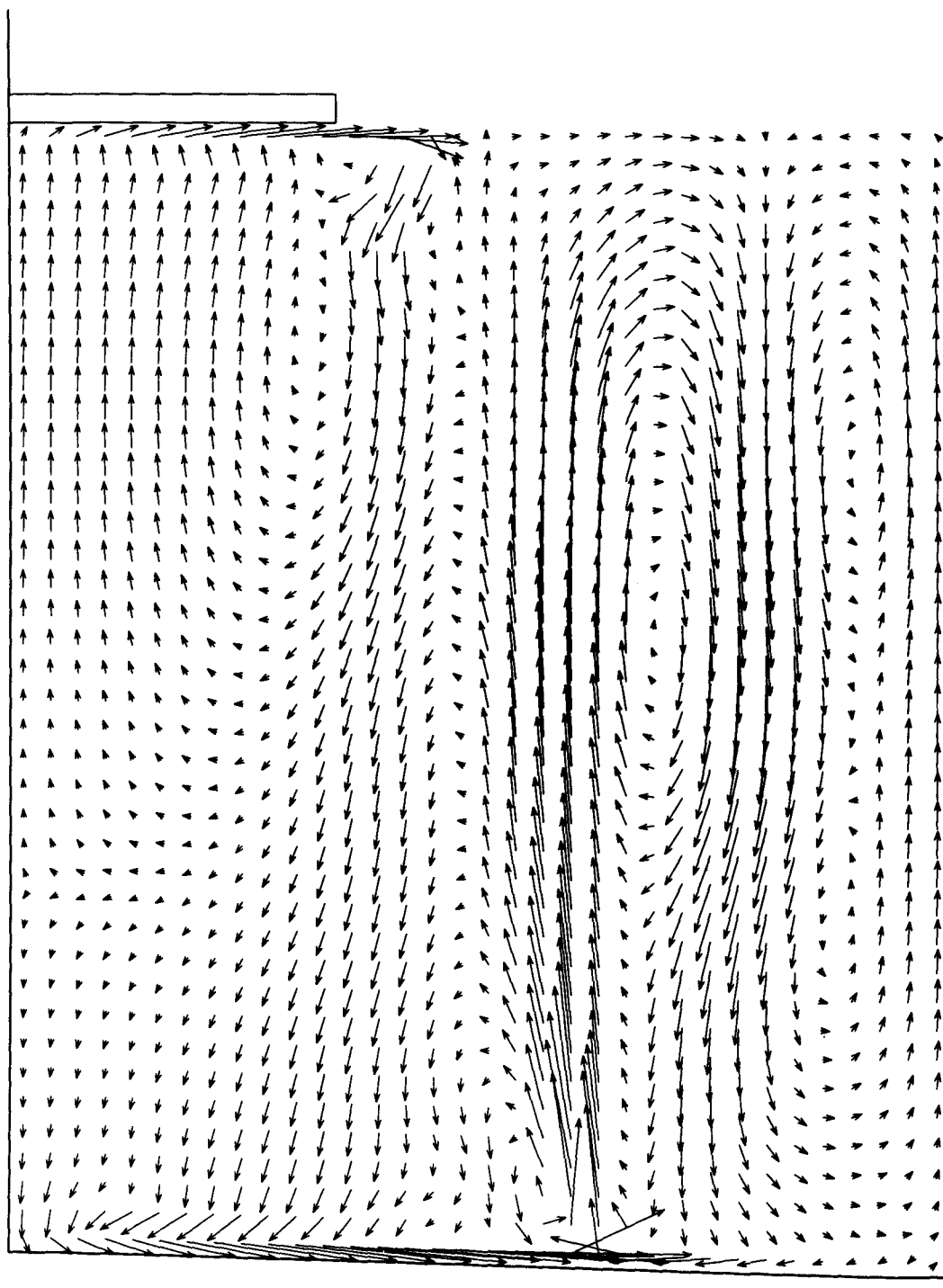

Fig. 13e : t = 35.0 s , v_{max} = 5.9E-1 cm/s

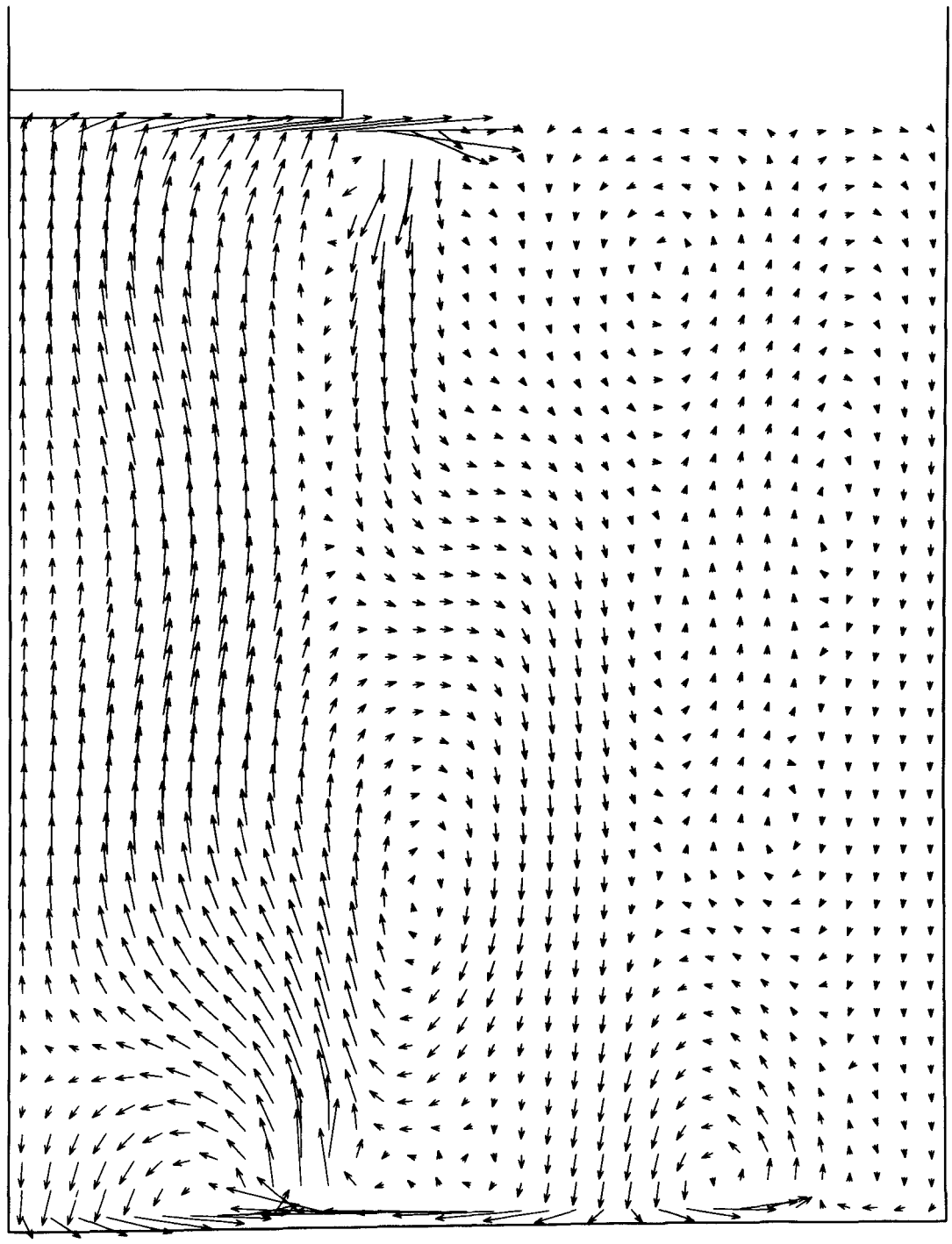

Fig. 13f : t = 48.659 s , v_{max} = 5.7E-1 cm/s

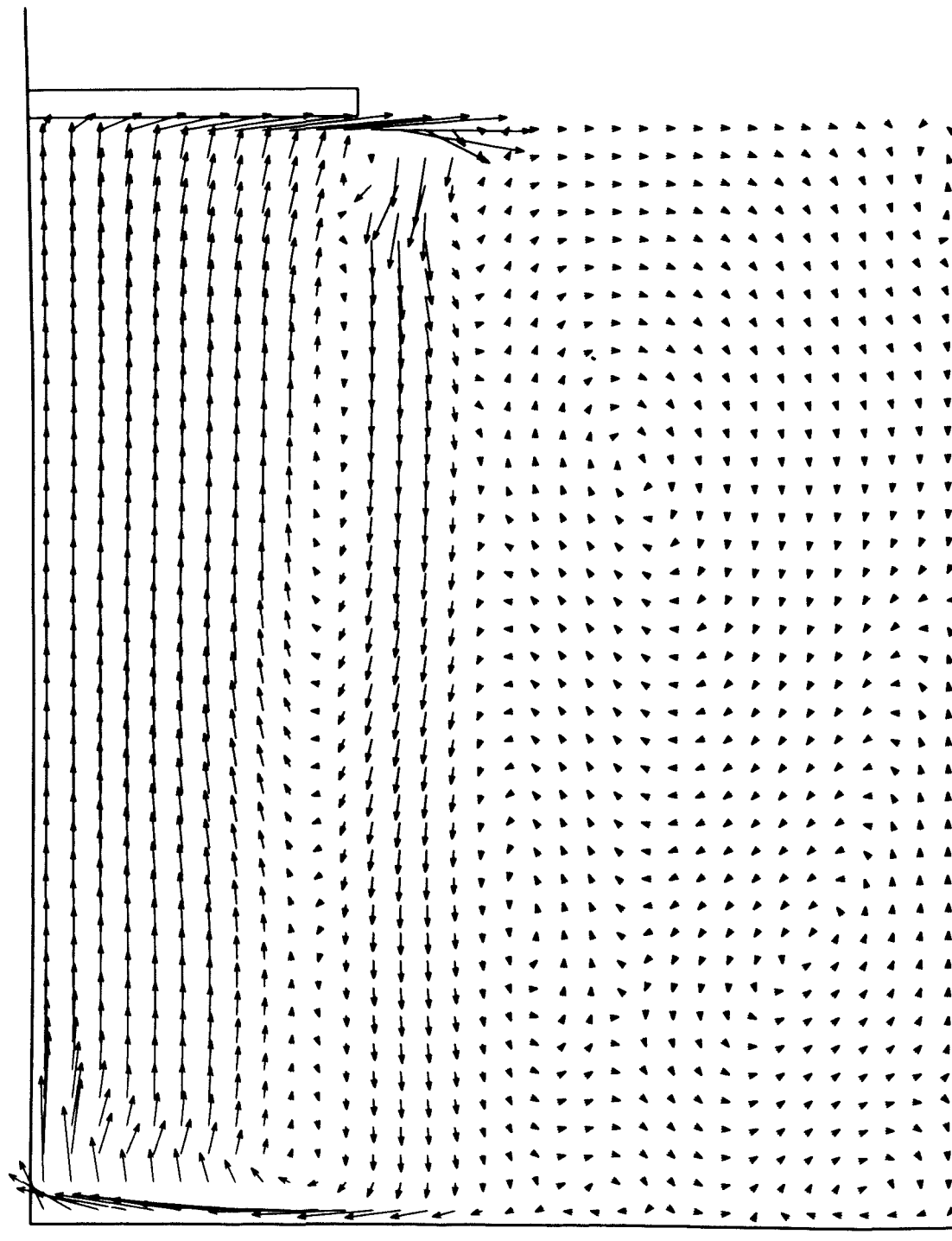

Fig. 14a : t = 2.0 s , v_{max} = 9.2E-1 cm/s

NUE : 0.005 cm^2/s

CRUCIBLE ROTATION : 0 rpm

CRYSTAL ROTATION : 50 rpm

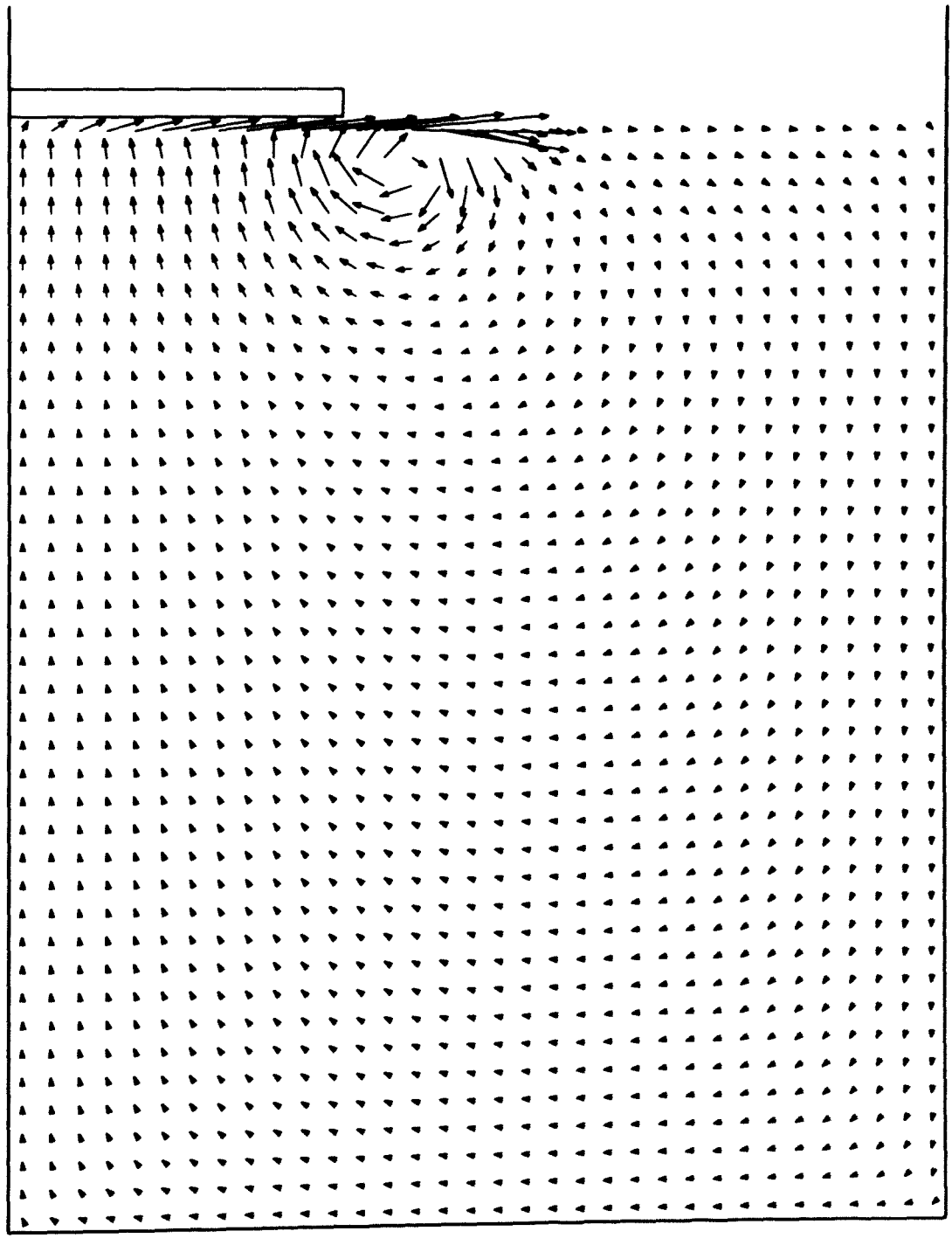

Fig. 14b : t = 5.0 s , v_{max} = 7.0 E-1 cm/s

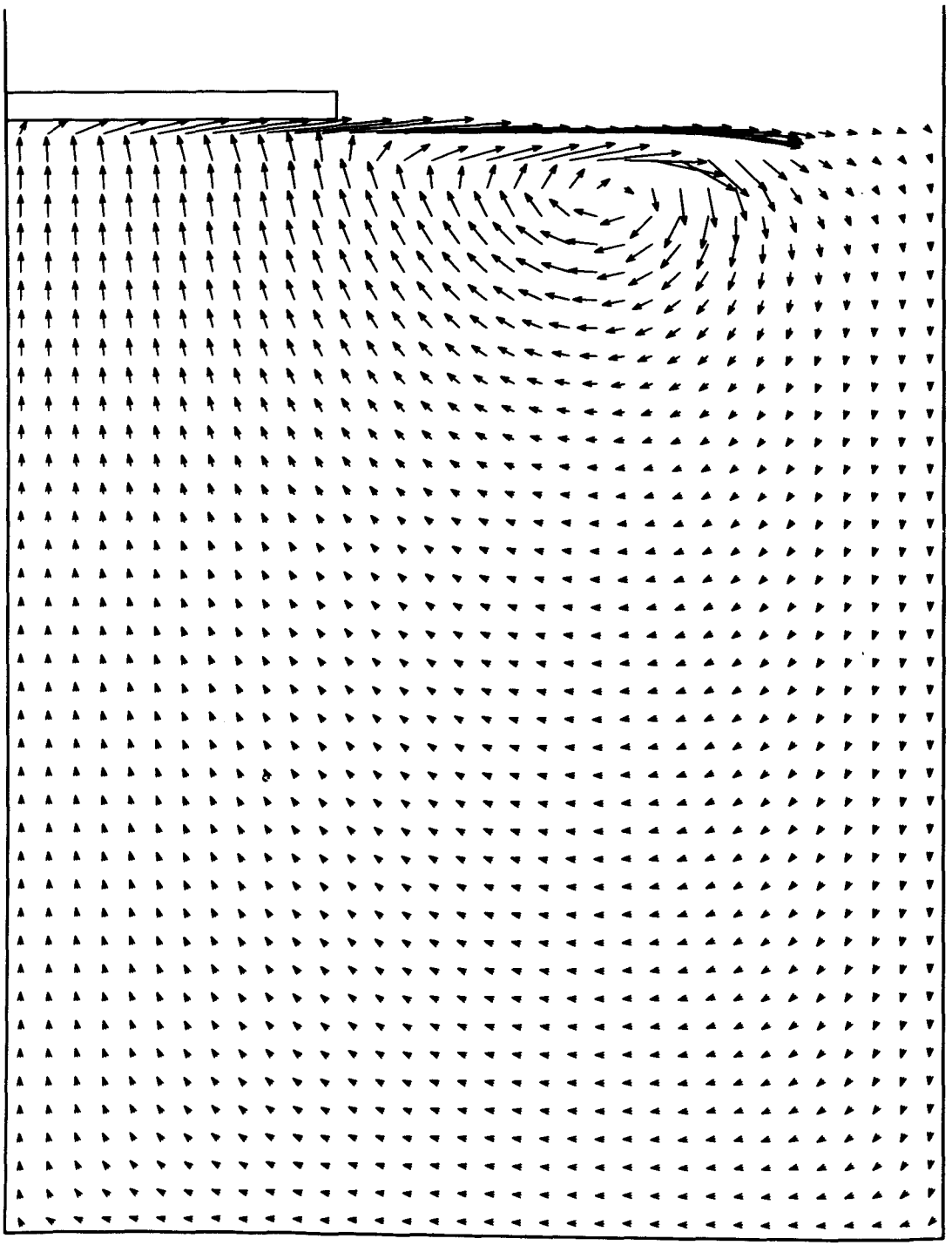

Fig. 14c : t = 10.0 s , v_{max} = 6.9E-1 cm/s

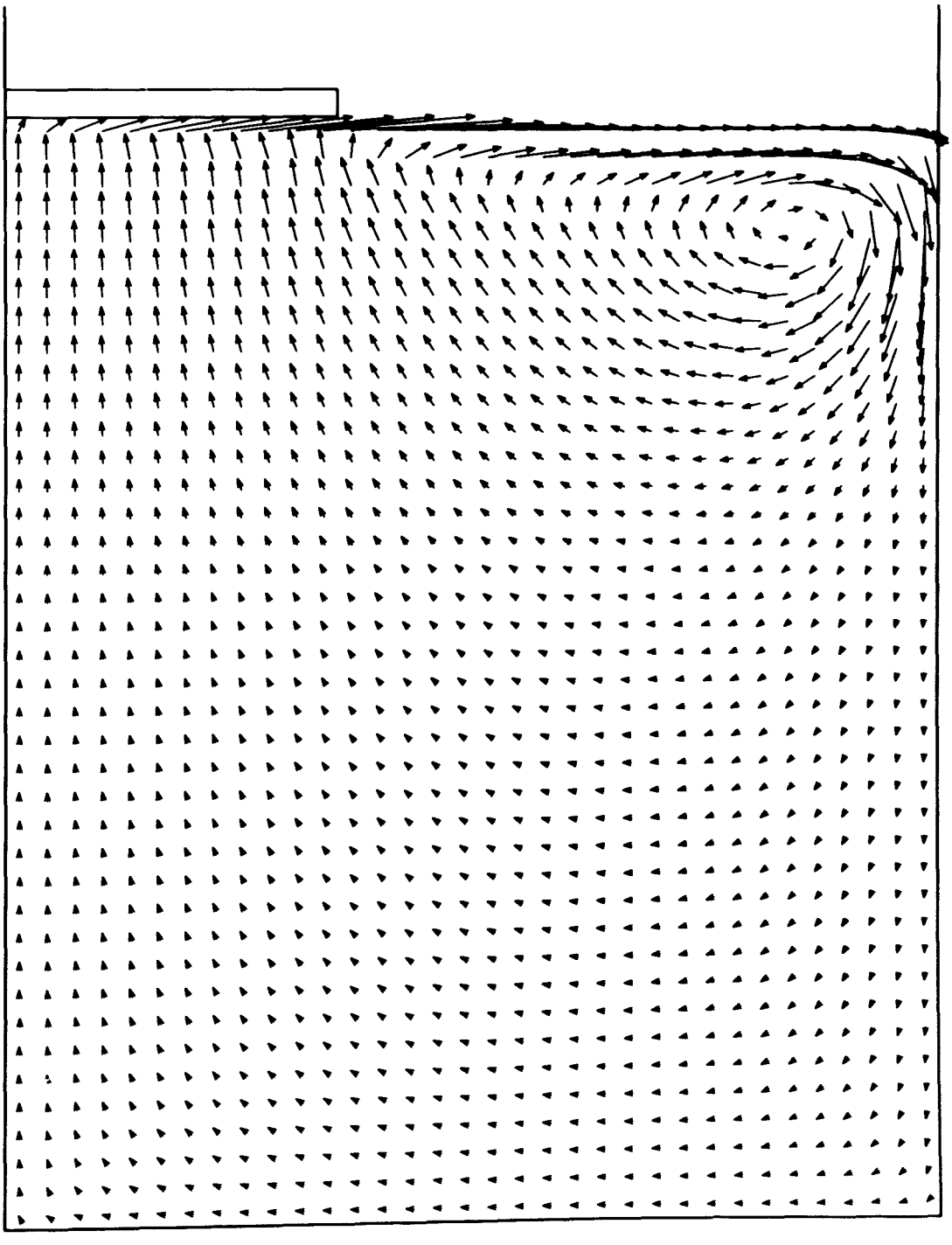

Fig. 14d : t = 20.0 s , v_{max} = 7.0E-1 cm/s

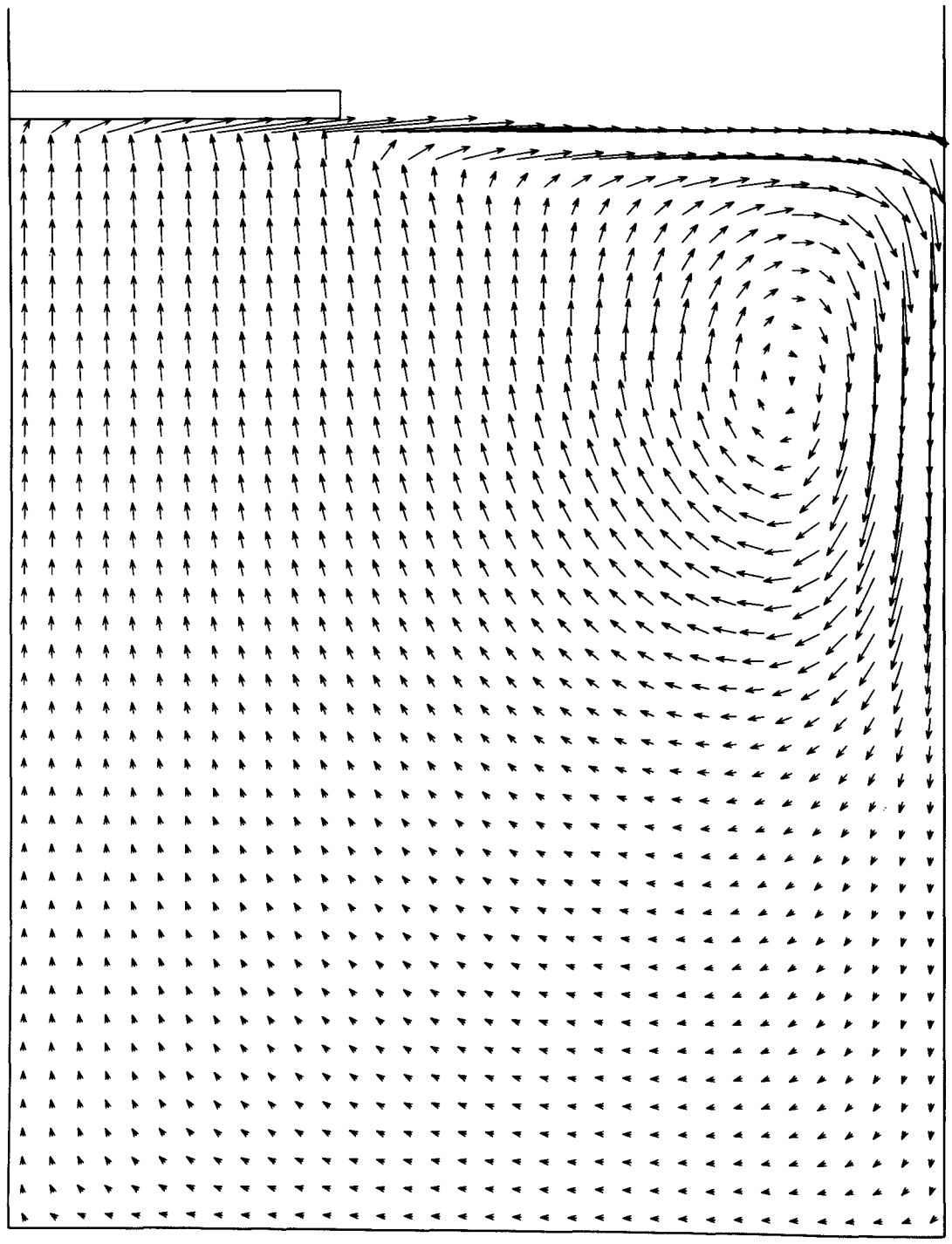

Fig. 14e : t = 30.0 s , v_{max} = 7.0E-1 cm/s

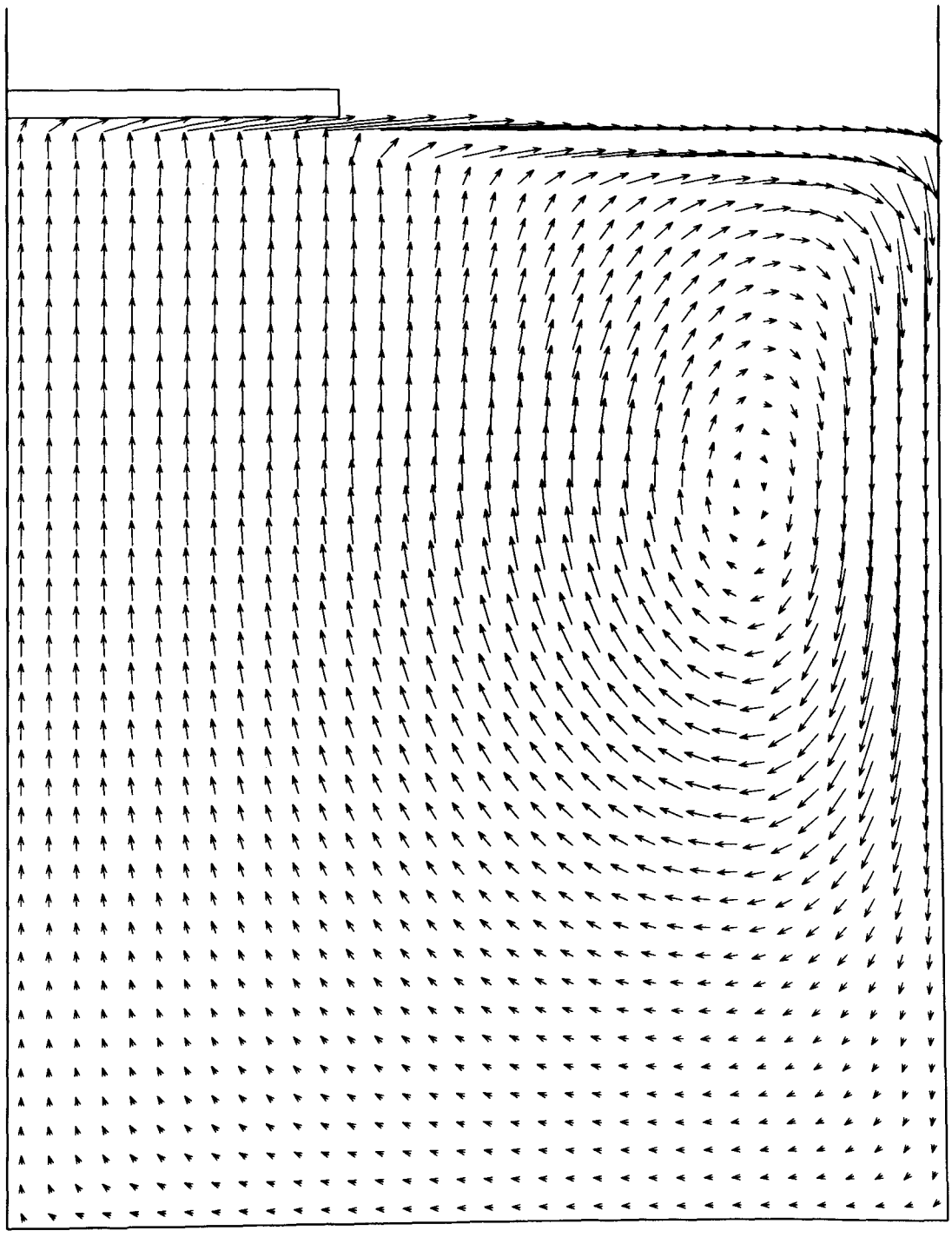

Fig. 14f : t = 48.681 s , v_{max} = 7.OE-1 cm/s

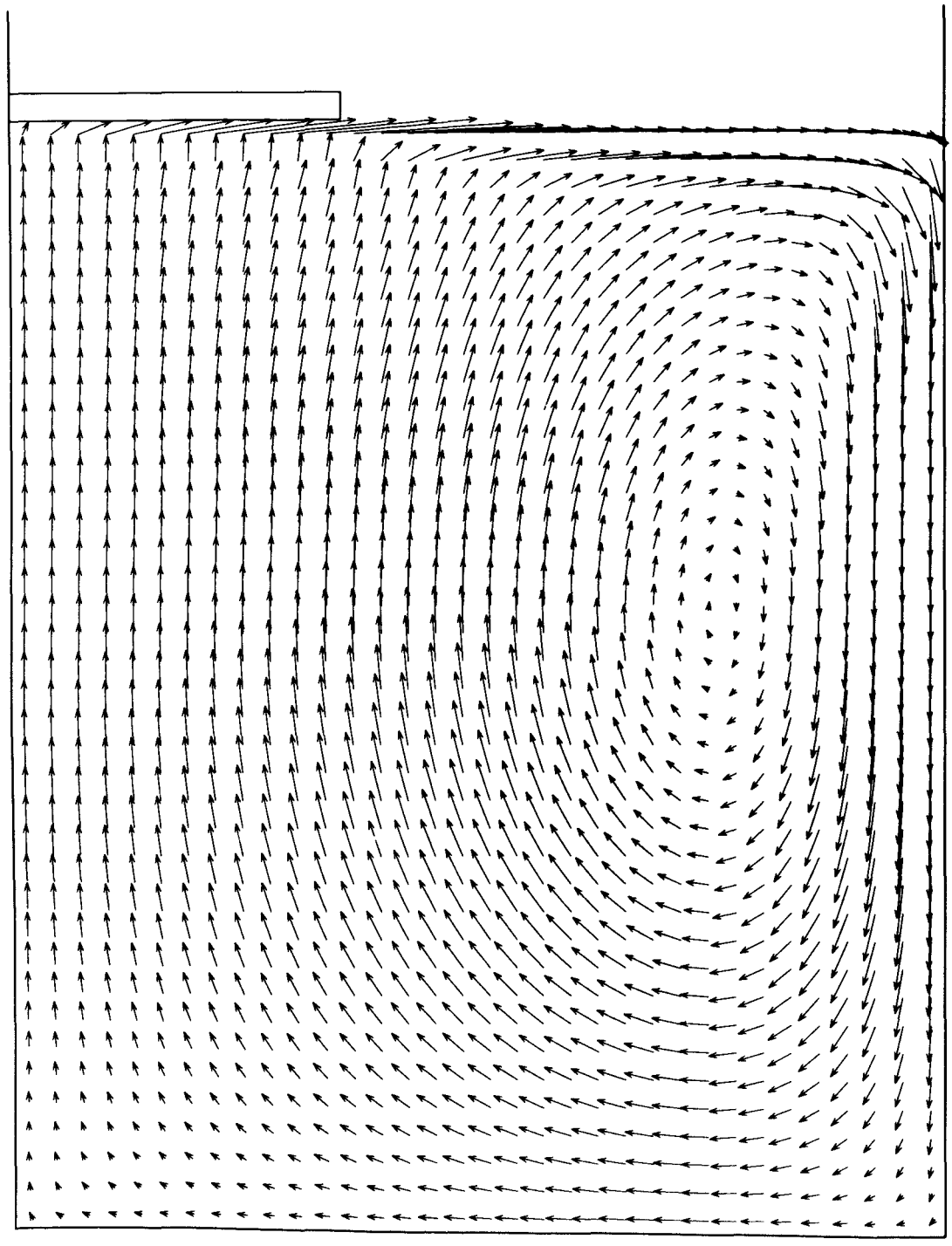

Fig. 15a : t = 2.0 s , v_{max} = 1.9E0 cm/s

NUE : 0.005 cm^2/s

CRUCIBLE ROTATION : 10 rpm

CRYSTAL ROTATION : -50 rpm

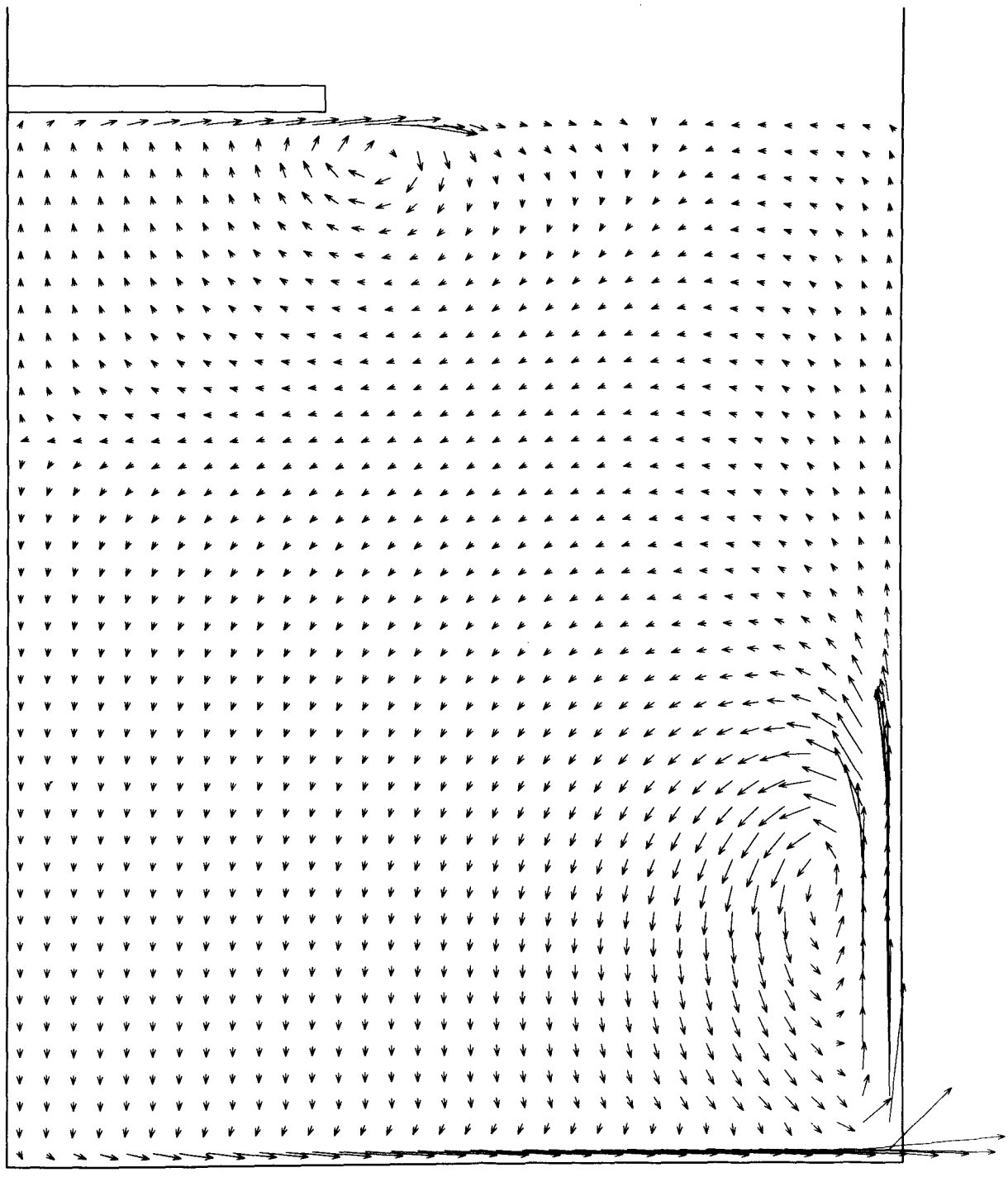

Fig. 15b : t = 5.0 s , v_{max} = 1.9EO cm/s

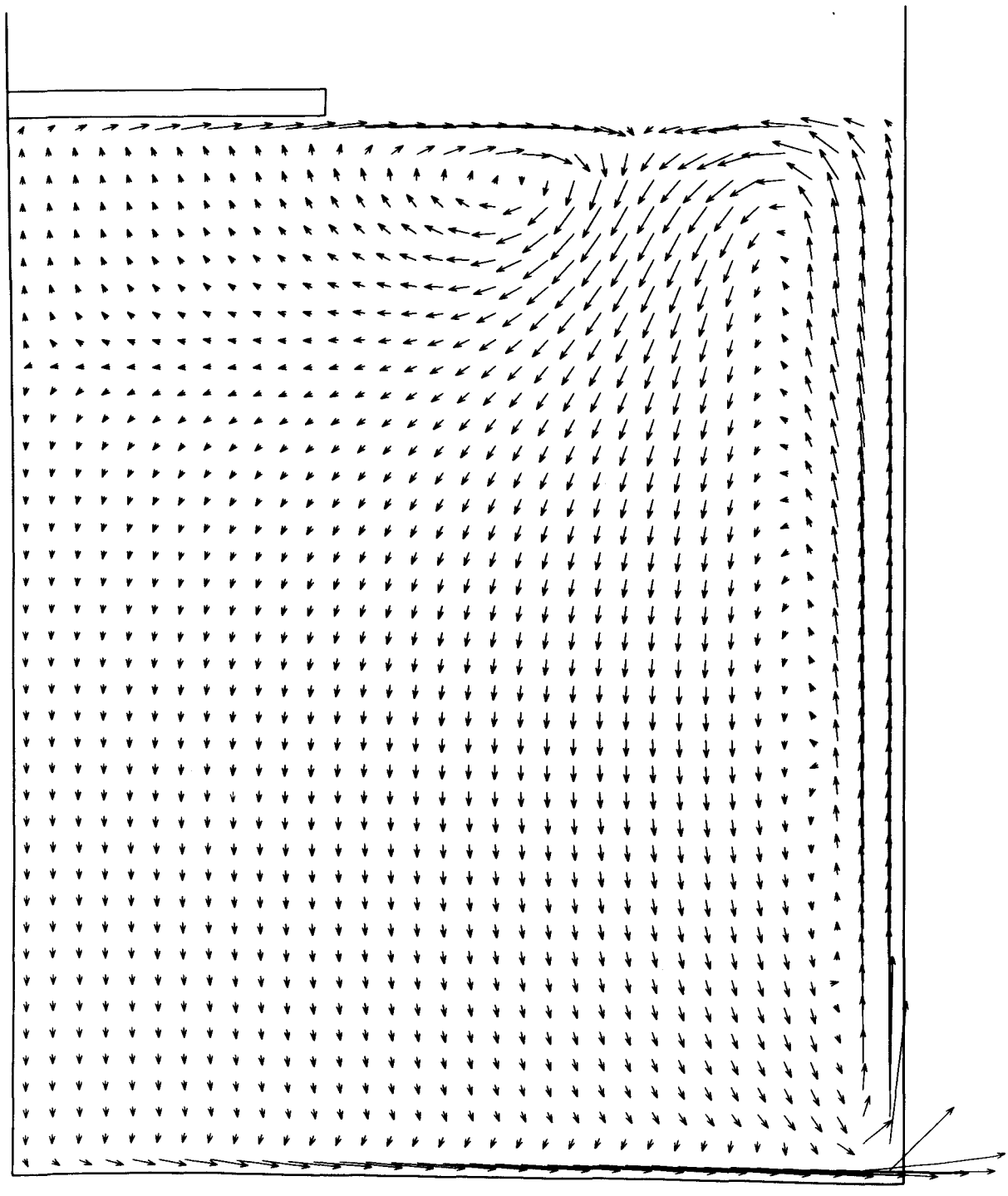

Fig. 15c : t = 15.0 s , v_{max} = 1.3E0 cm/s

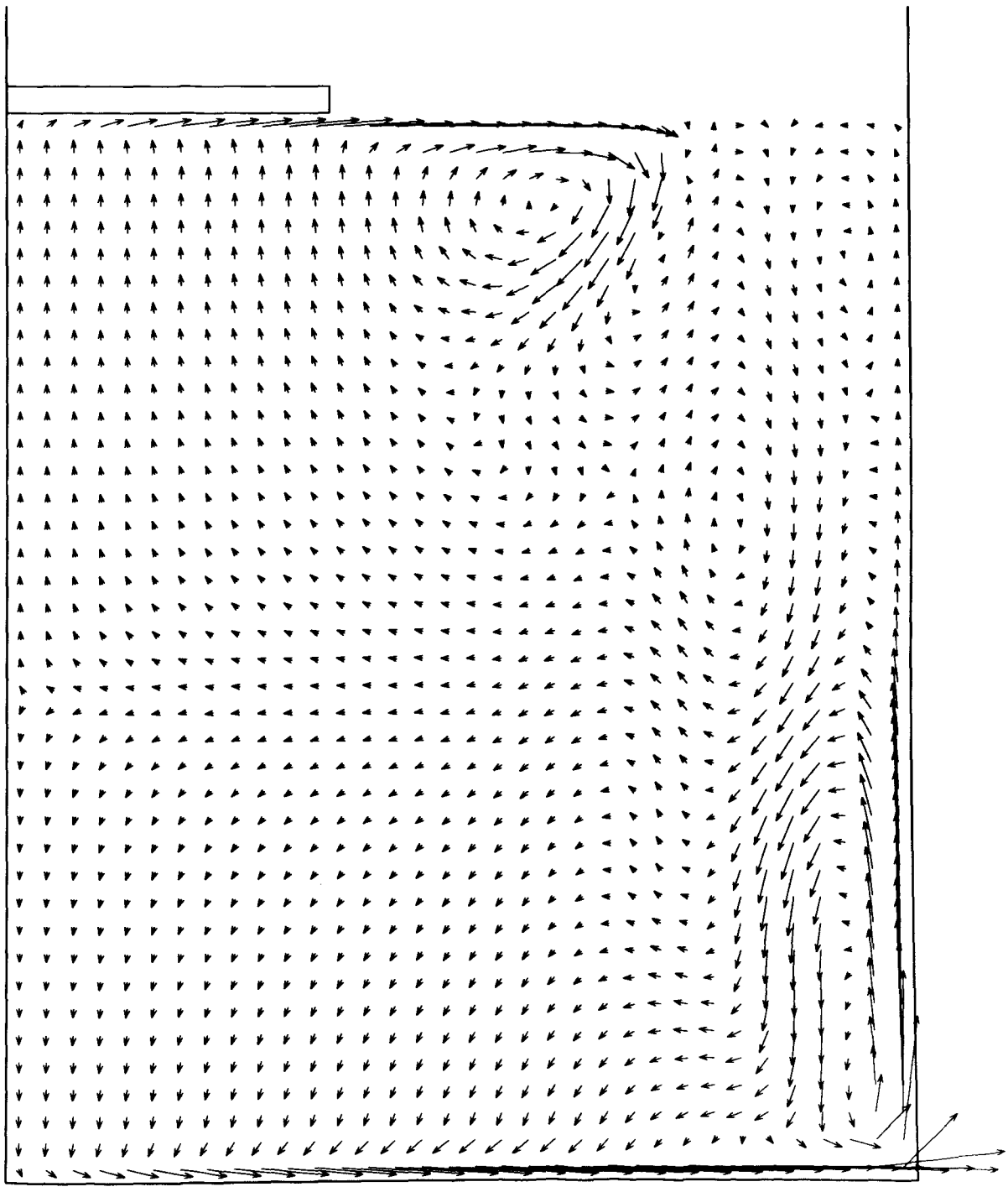

Fig. 15d : t = 30.0 s , v_{max} = 9.6E-1 cm/s

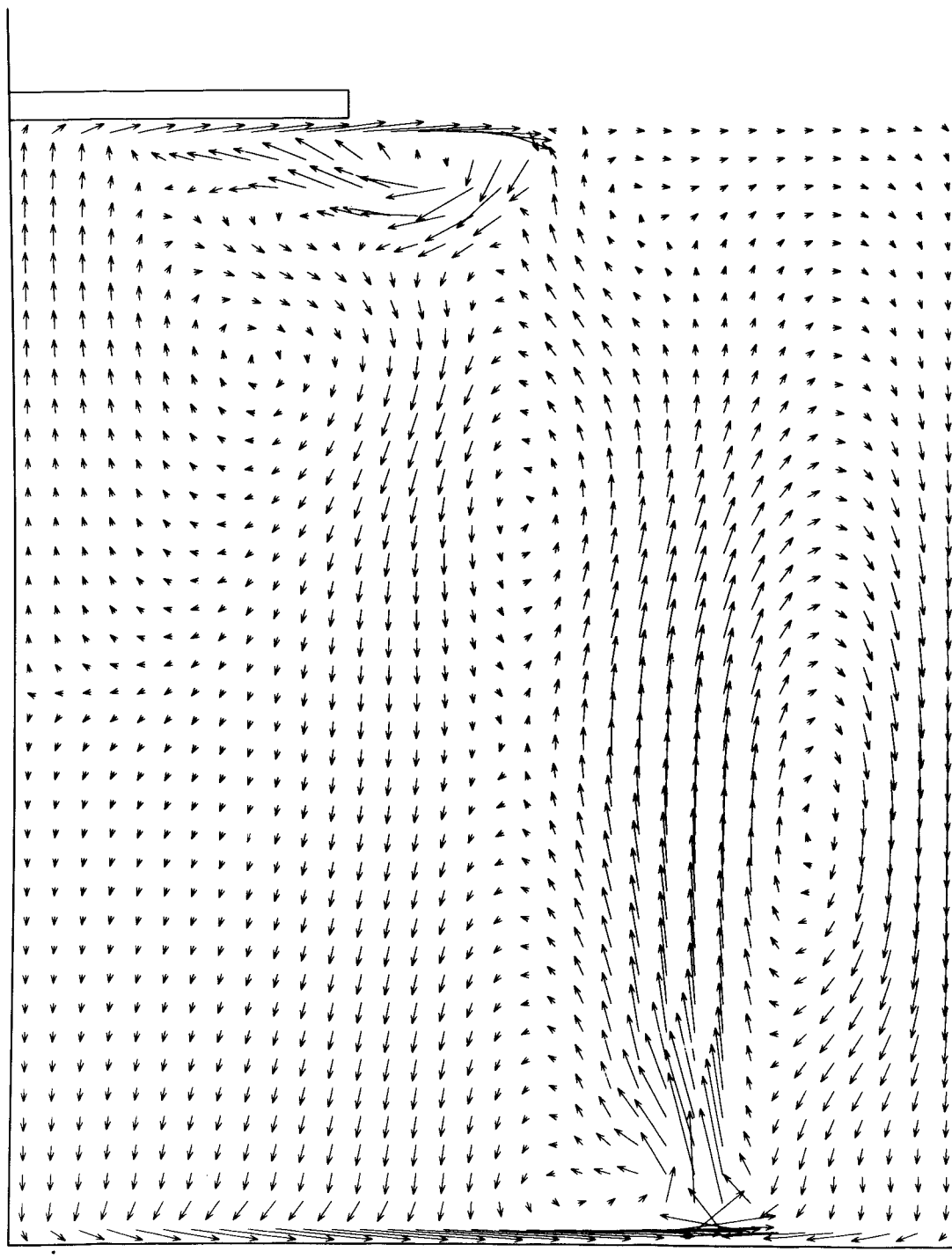

Fig. 15e : t = 40.0 s , v_{max} = 7.4E-1 cm/s

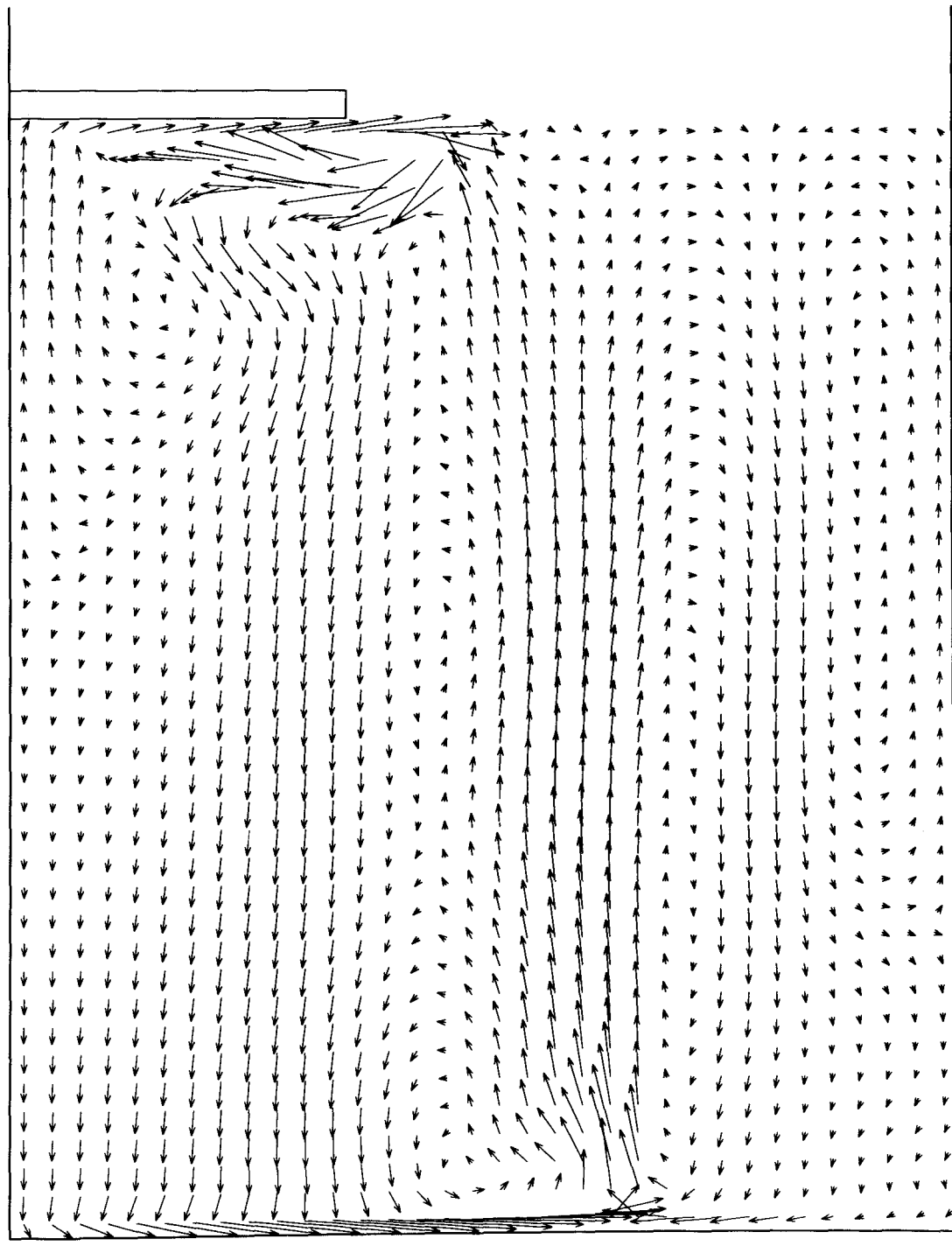

Fig. 15f : t = 56.975 s , v_{max} = 5.8E-1 cm/s

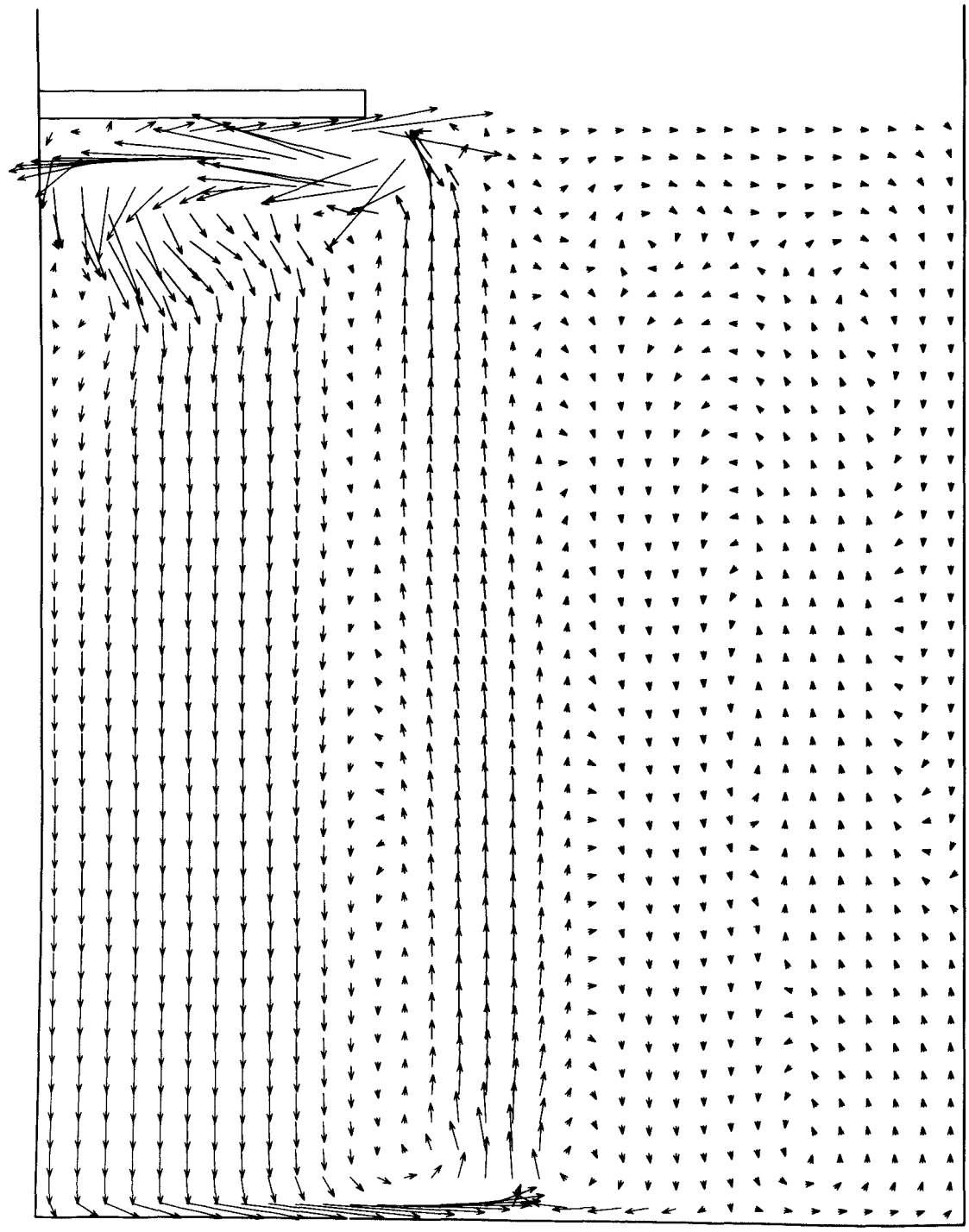

Fig. 16a : t = 2.0 s , v_{max} = 9.2E-1 cm/s

NUE : 0.005 cm^2/s
CRUCIBLE ROTATION : 2 rpm
CRYSTAL ROTATION : -50 rpm

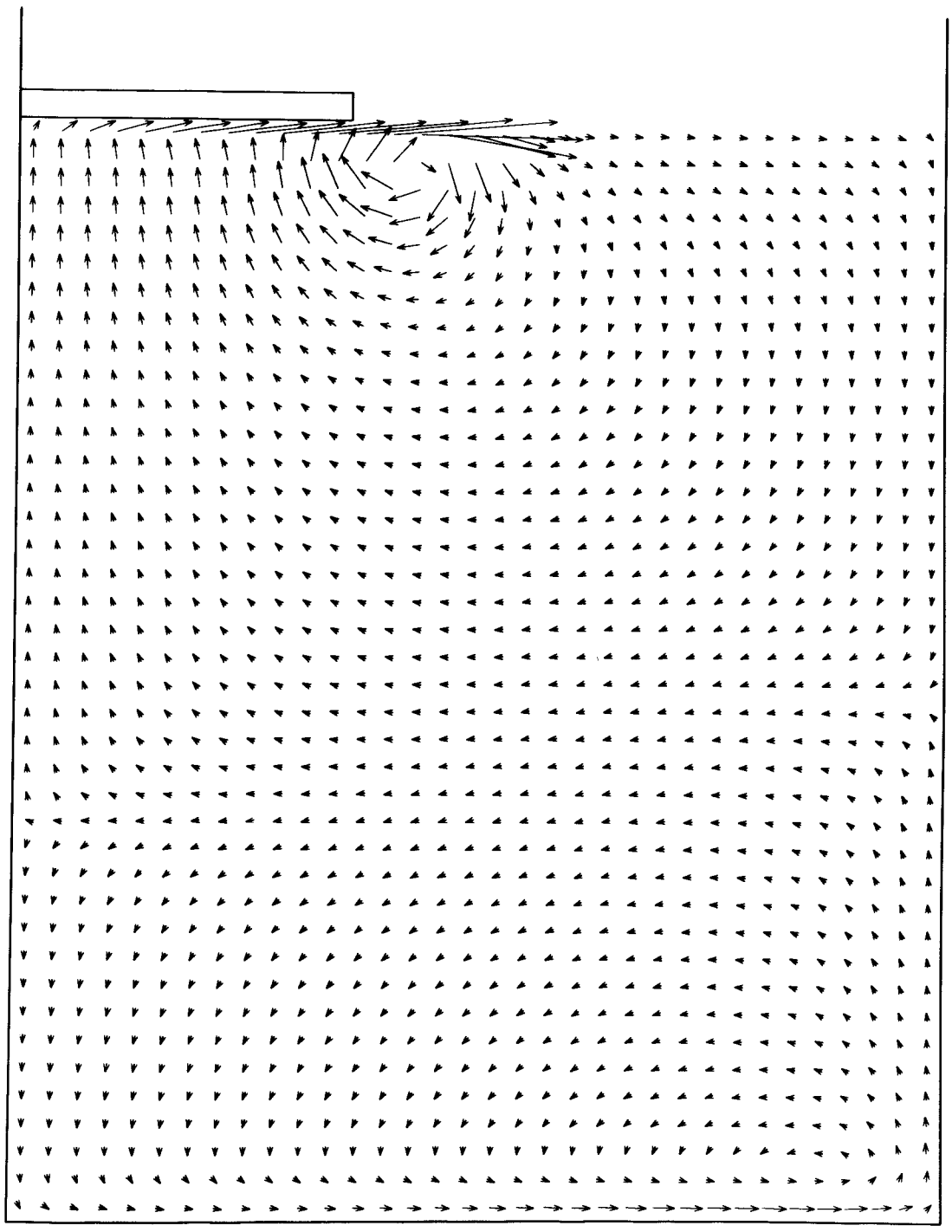

Fig. 16b : t = 10.0 s , v_{max} = 6.9E-1 cm/s

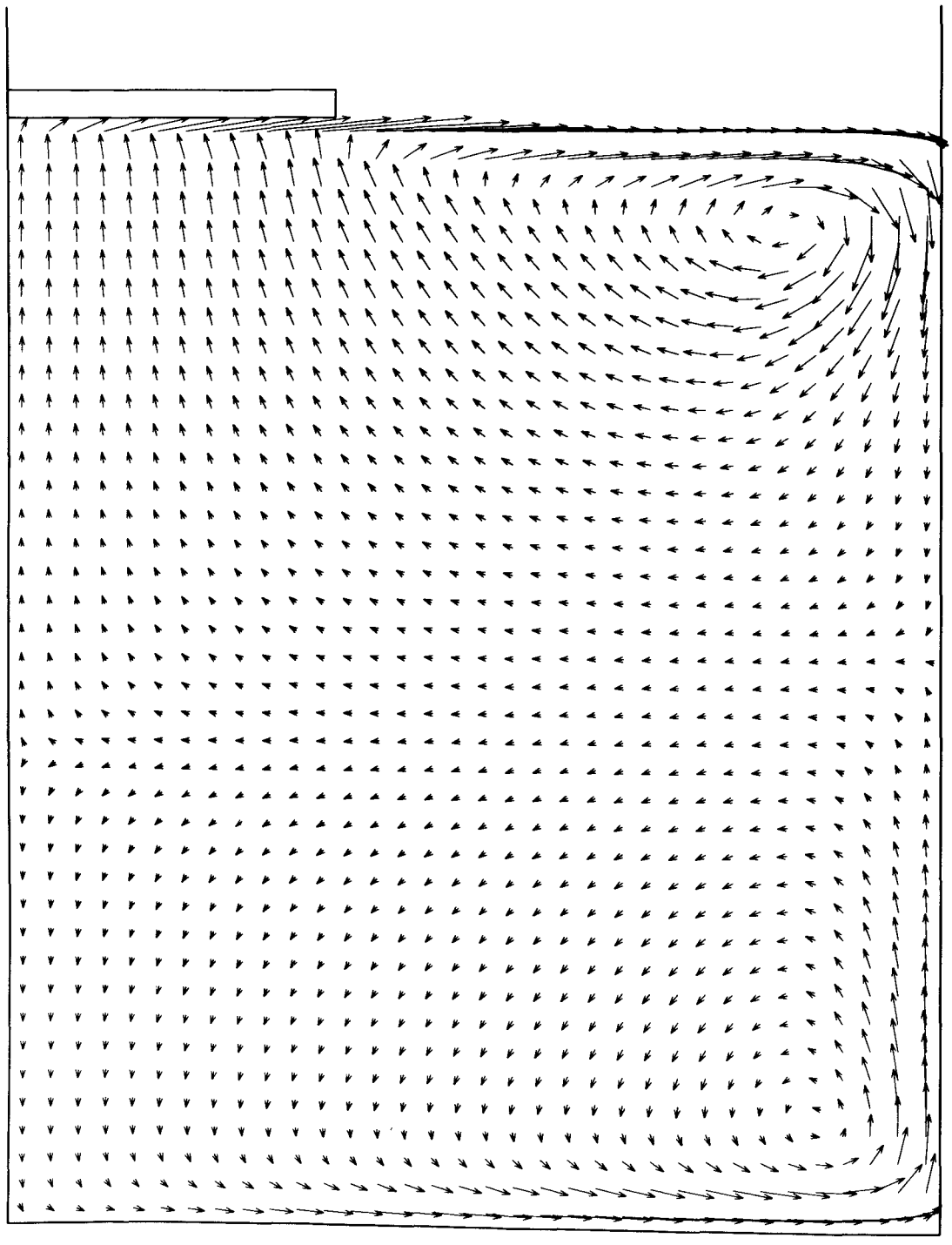

Fig. 16c : t = 20.0 s , v_{max} = 6.9E-1 cm/s

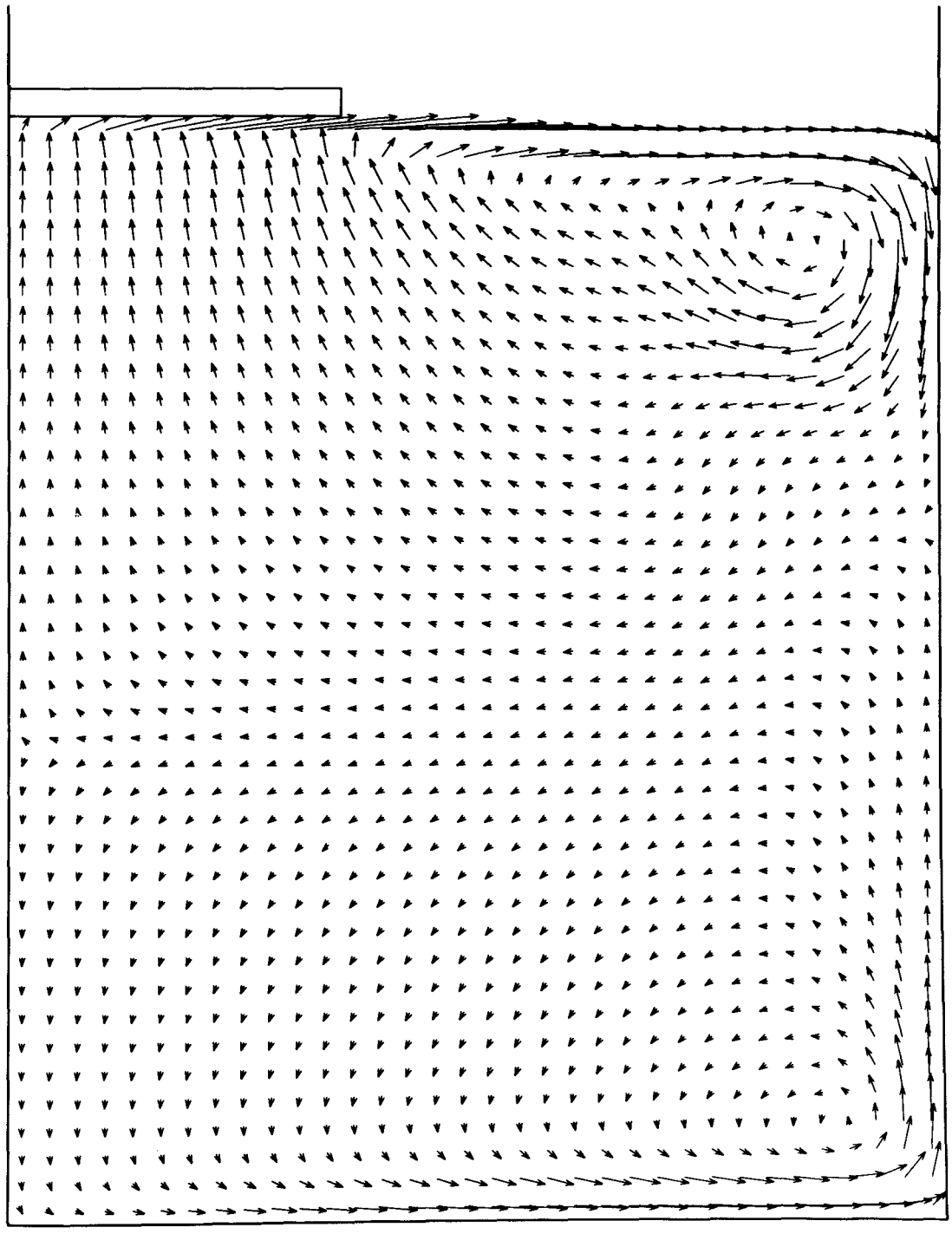

Fig. 16d : t = 35.0 s , v_{max} = 6.7E-1 cm/s

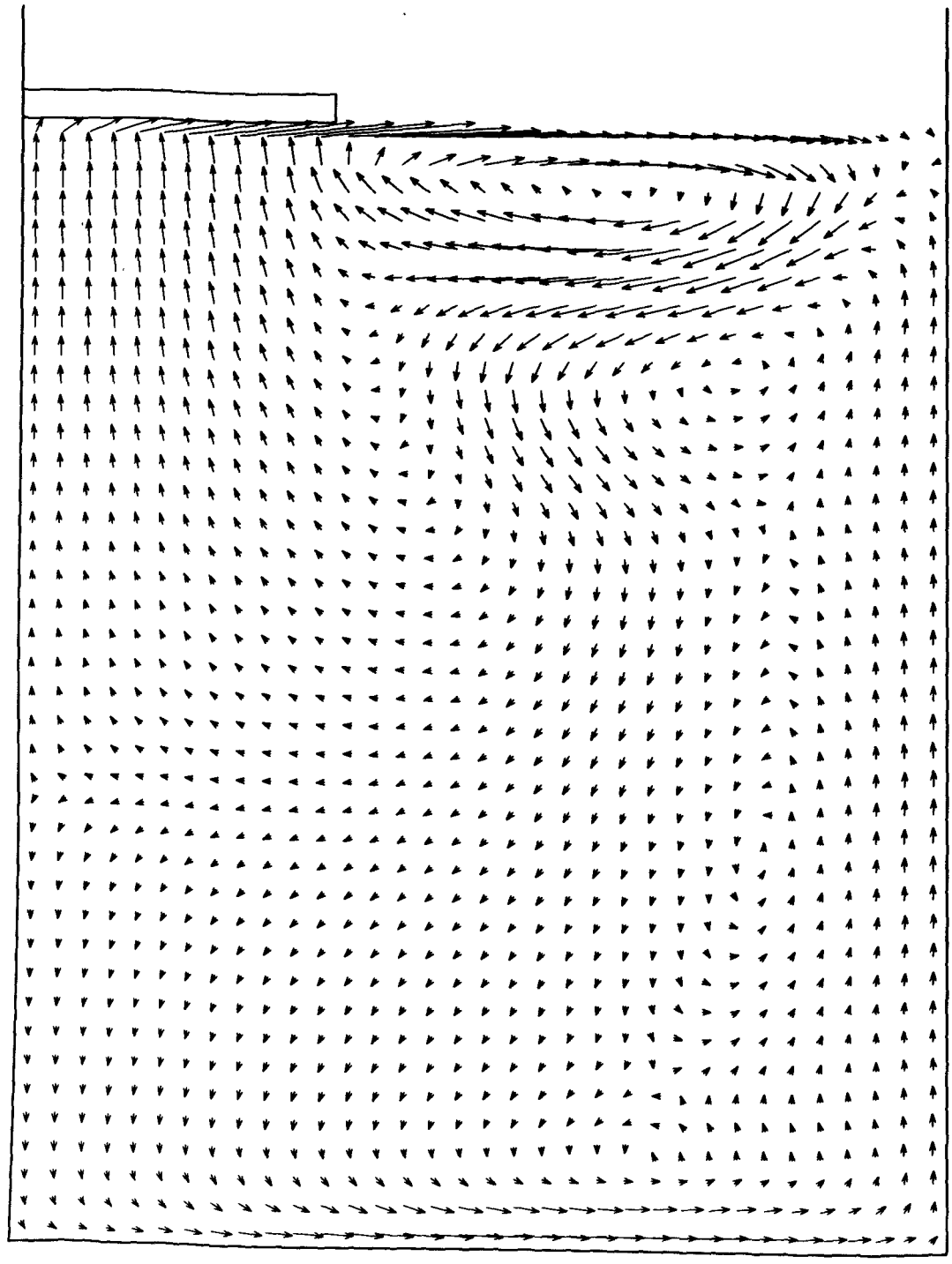

Fig. 16e : t = 45.0 s , v_{max} = 6.5E-1 cm/s

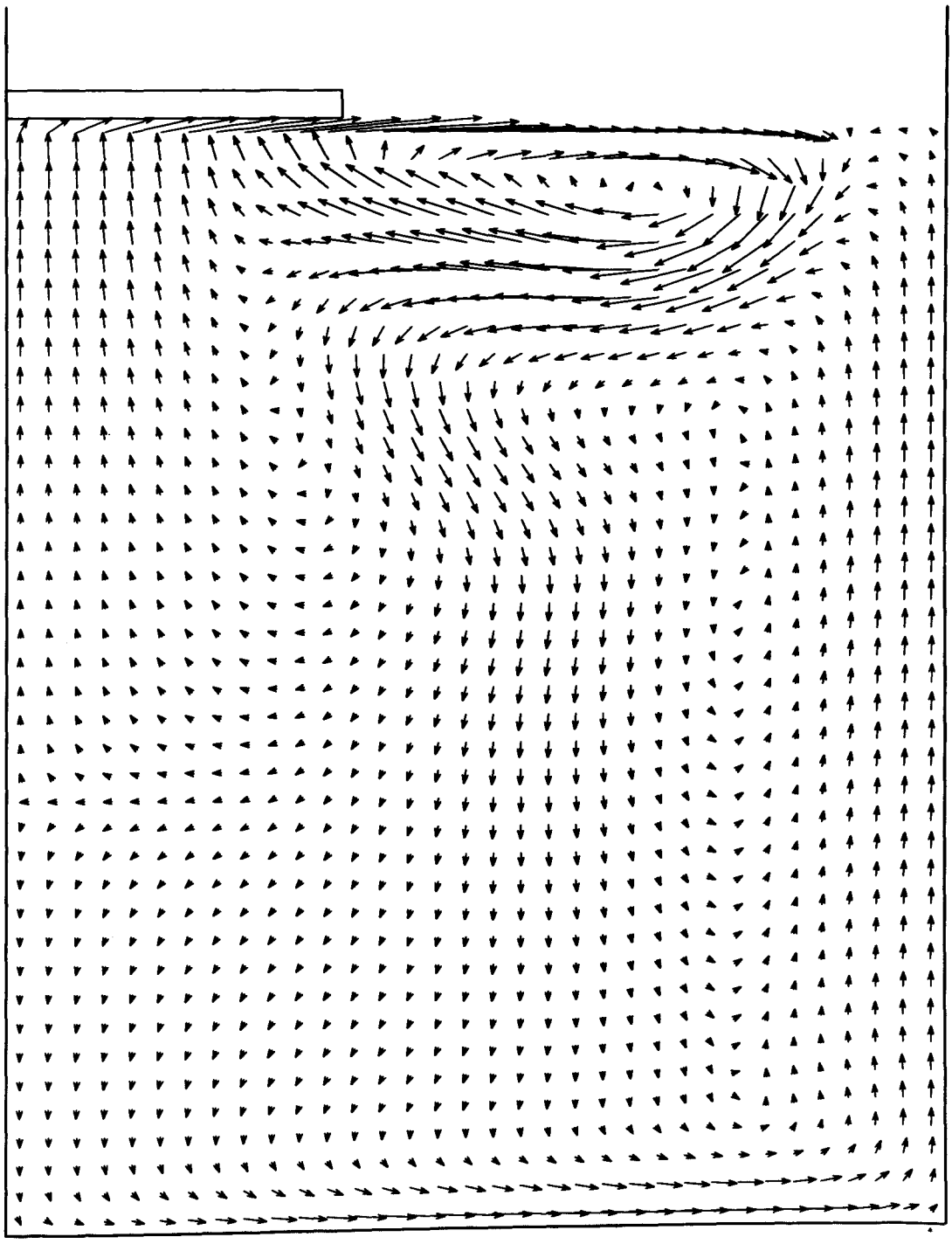

Fig. 16f : t = 62.123 s , v_{max} = 6.3E-1 cm/s

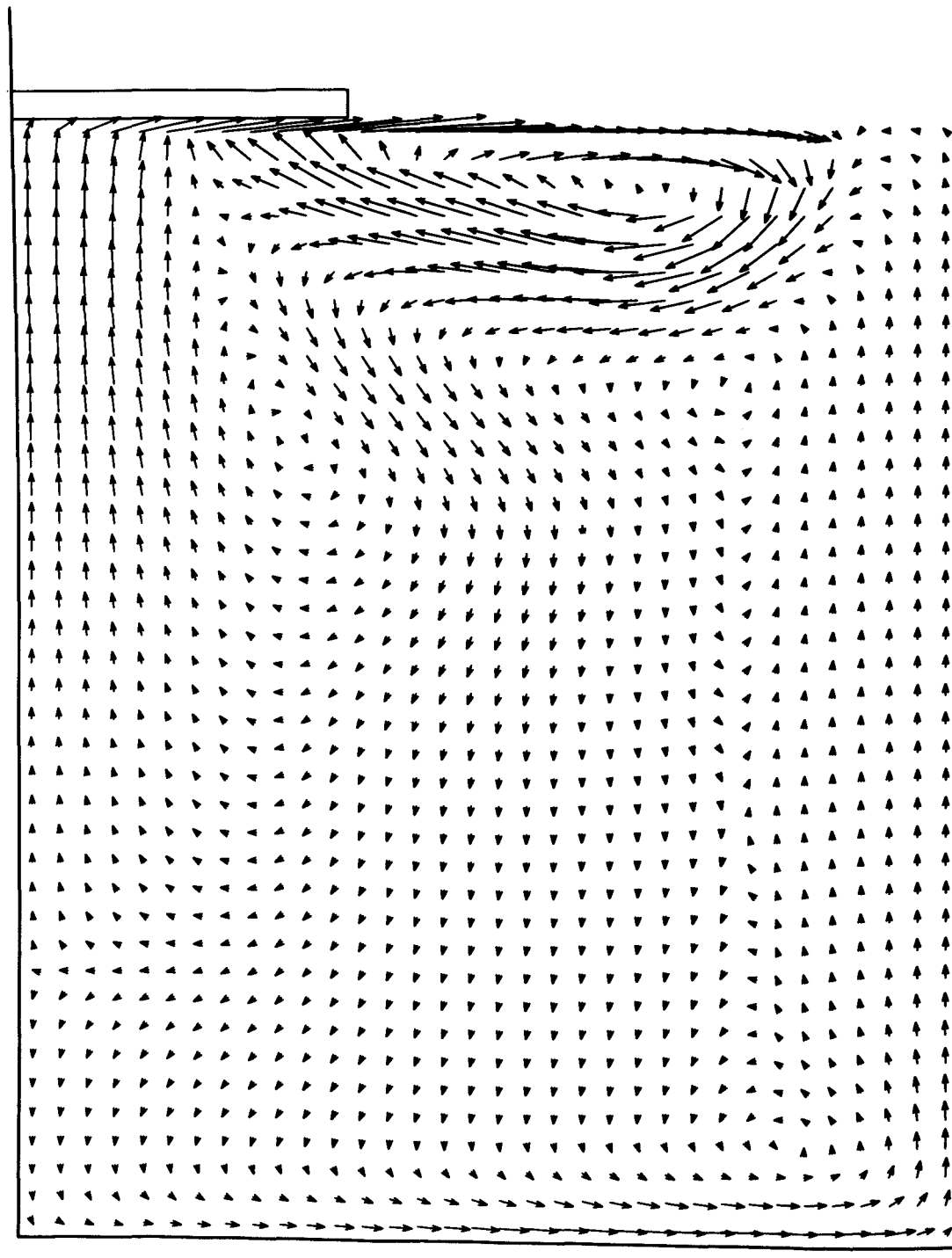

Fig. 17a : t = 2.0 s , v_{max} = 9.2E-1 cm/s

NUE : 0.005 cm^2/s

CRUCIBLE ROTATION : 1 rpm

CRYSTAL ROTATION : -50 rpm

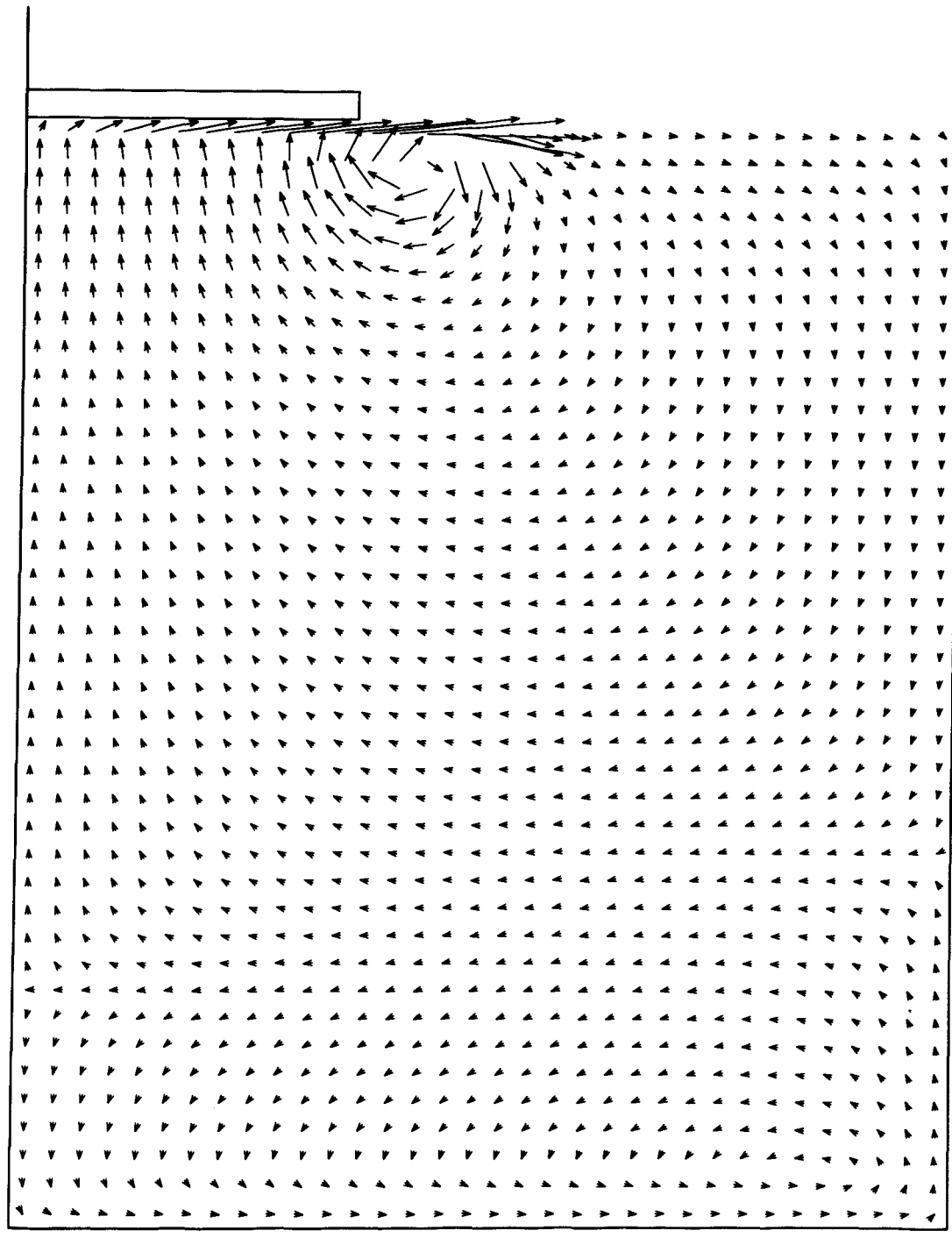

Fig. 17b : t = 15.0 s , v_{max} = 7.OE-1 cm/s

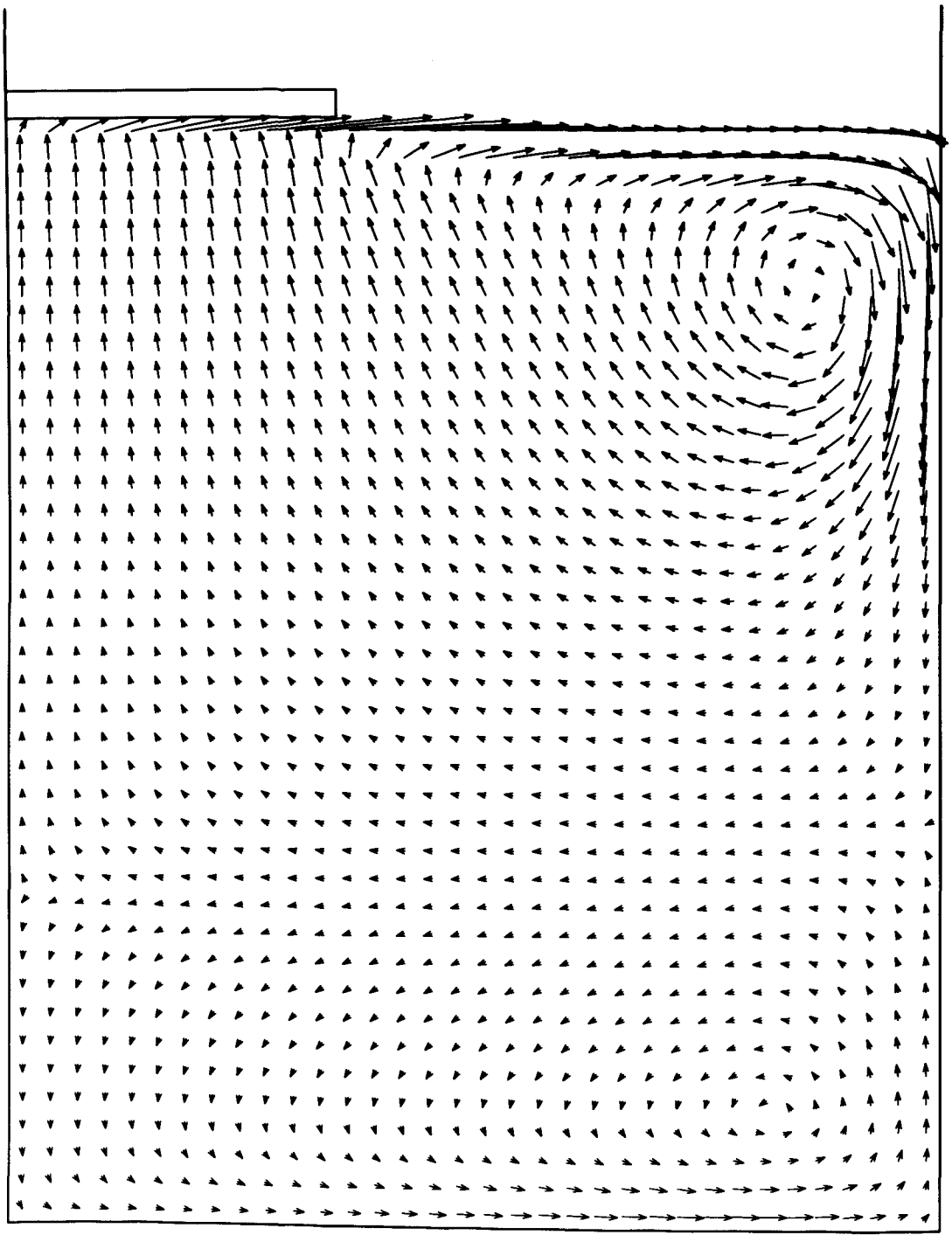

Fig. 17c : t = 30.0 s , v_{max} = 7.0E-1 cm/s

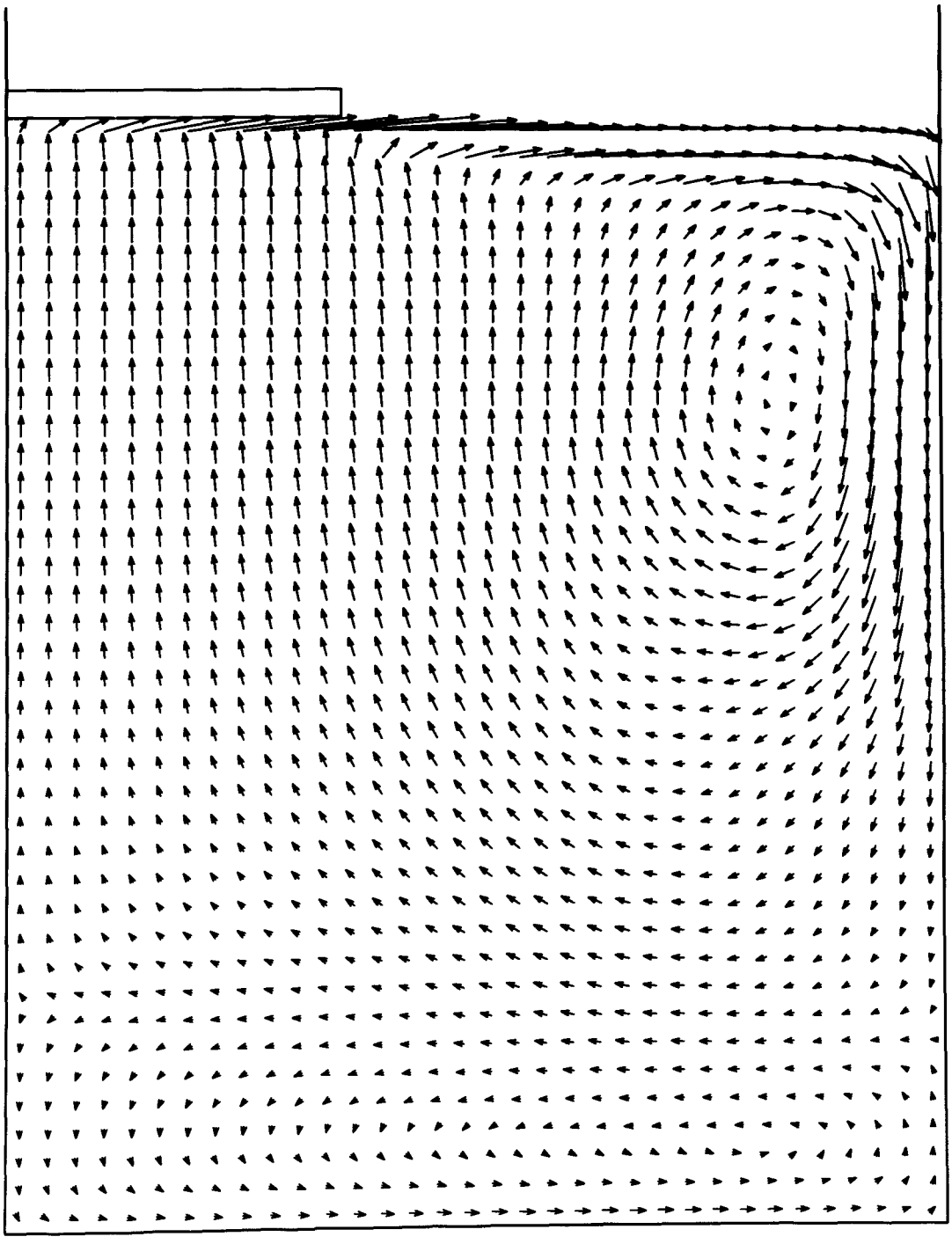

Fig. 17d : t = 40.0 s , v_{max} = 6.9E-1 cm/s

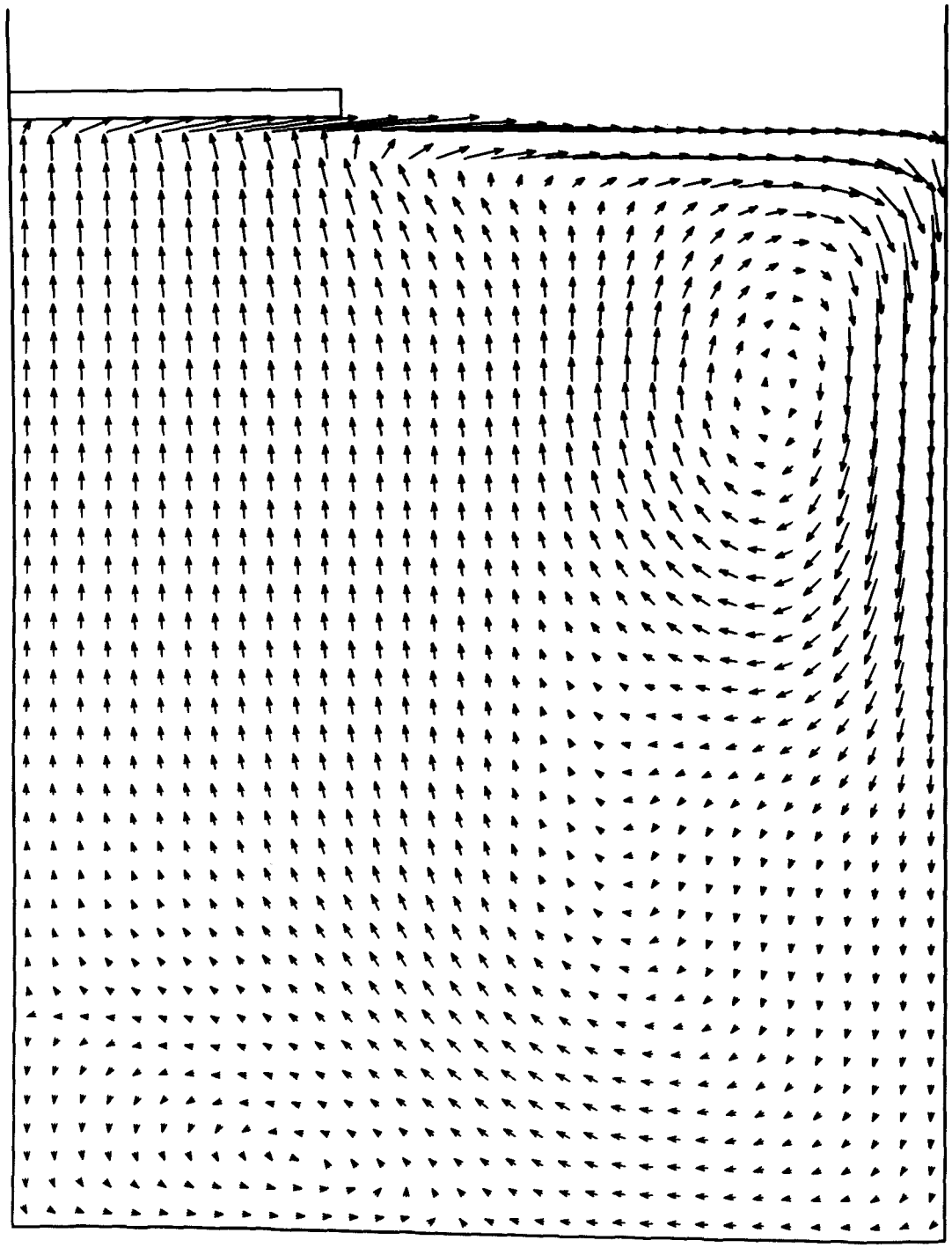

Fig. 17e : t = 50.0 s , v_{max} = 6.7E-1 cm/s

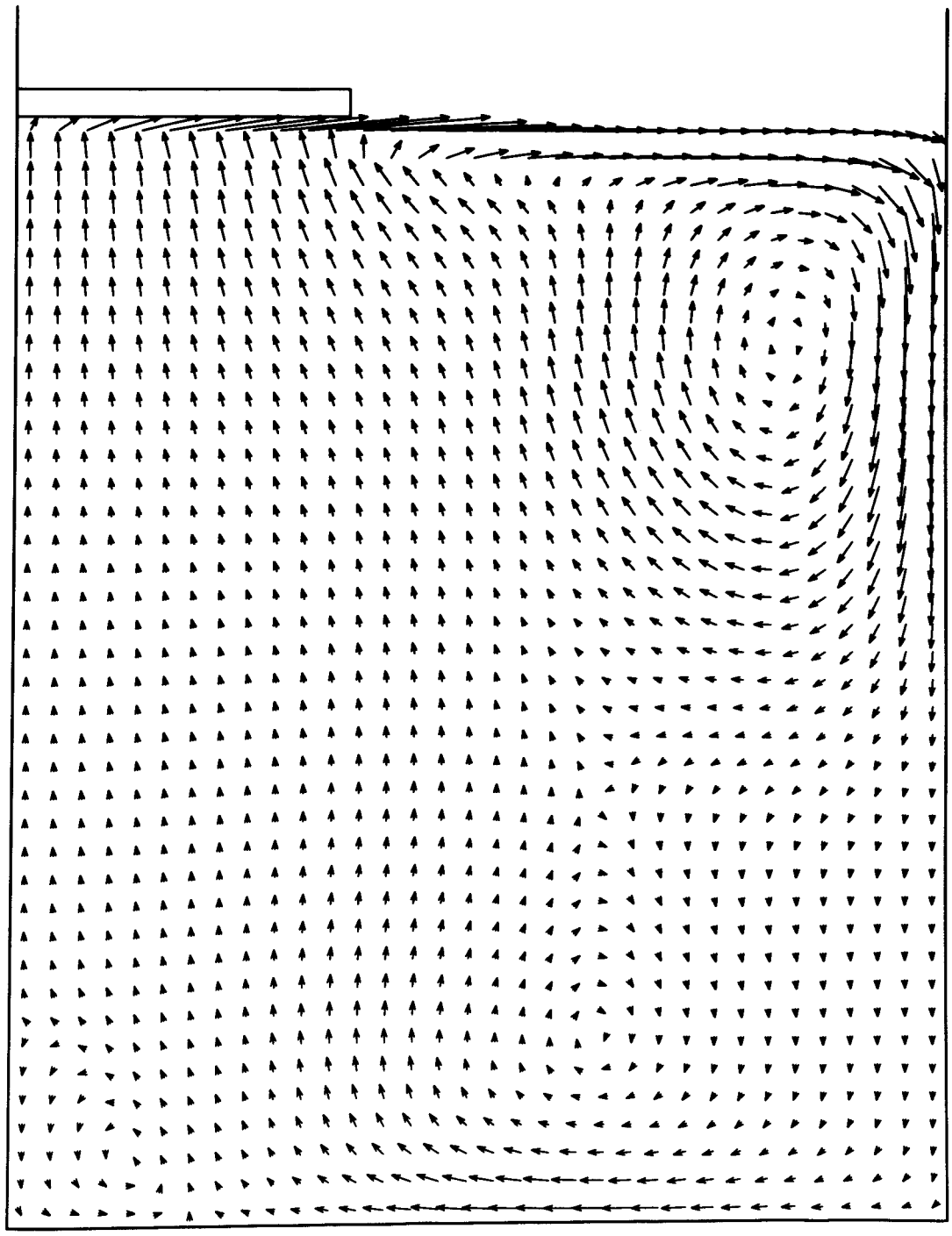

Fig. 17f : t = 60.0 s , v_{max} = 6.5E-1 cm/s

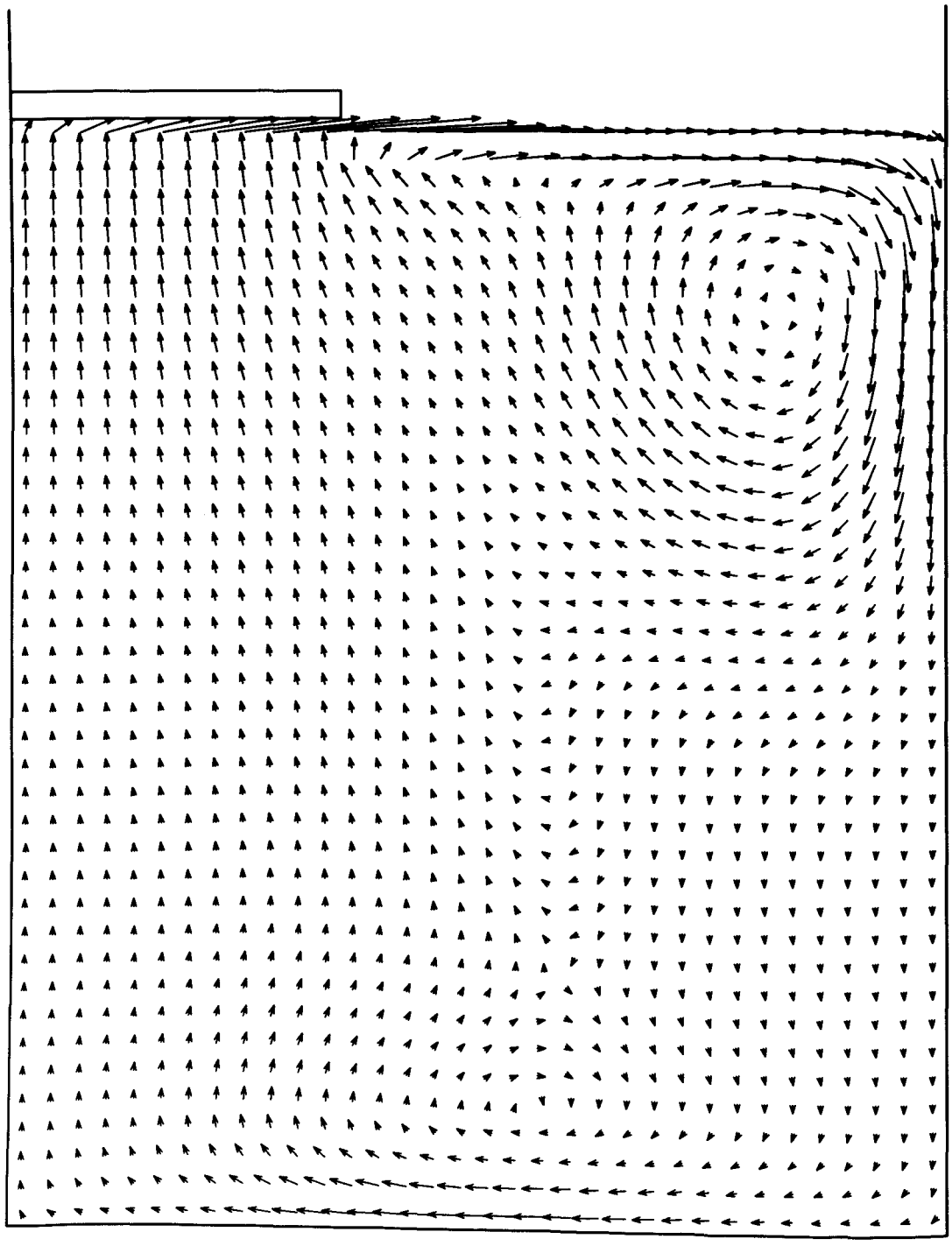

3.2.2. *ACRT Flux Growth*

This section is devoted to the low viscosity simulations of the ACRT arrangement described in section 3.1.2. In figs. 18a-k we present the flow patterns exhibited in the two acceleration modes in analogy to those in fig. 9 and figs. 23a-k, respectively. As in the case of moderate kinematic viscosity, the liquid reverses its flow direction with the change of the crucible rotation, where for low kinematic viscosity additional vortices develop in the stoppage phase. Altogether, ACRT seems to be an effective method to obtain optimum stirring of the melt independent of the kinematic viscosity.

Fig. 18a : t = 5.0 s , v_{max} = 4.4E0 cm/s

NUE : 0.005 cm^2/s

CRUCIBLE ROTATION : 20 : 0 rpm

TIME PERIOD : 10 s

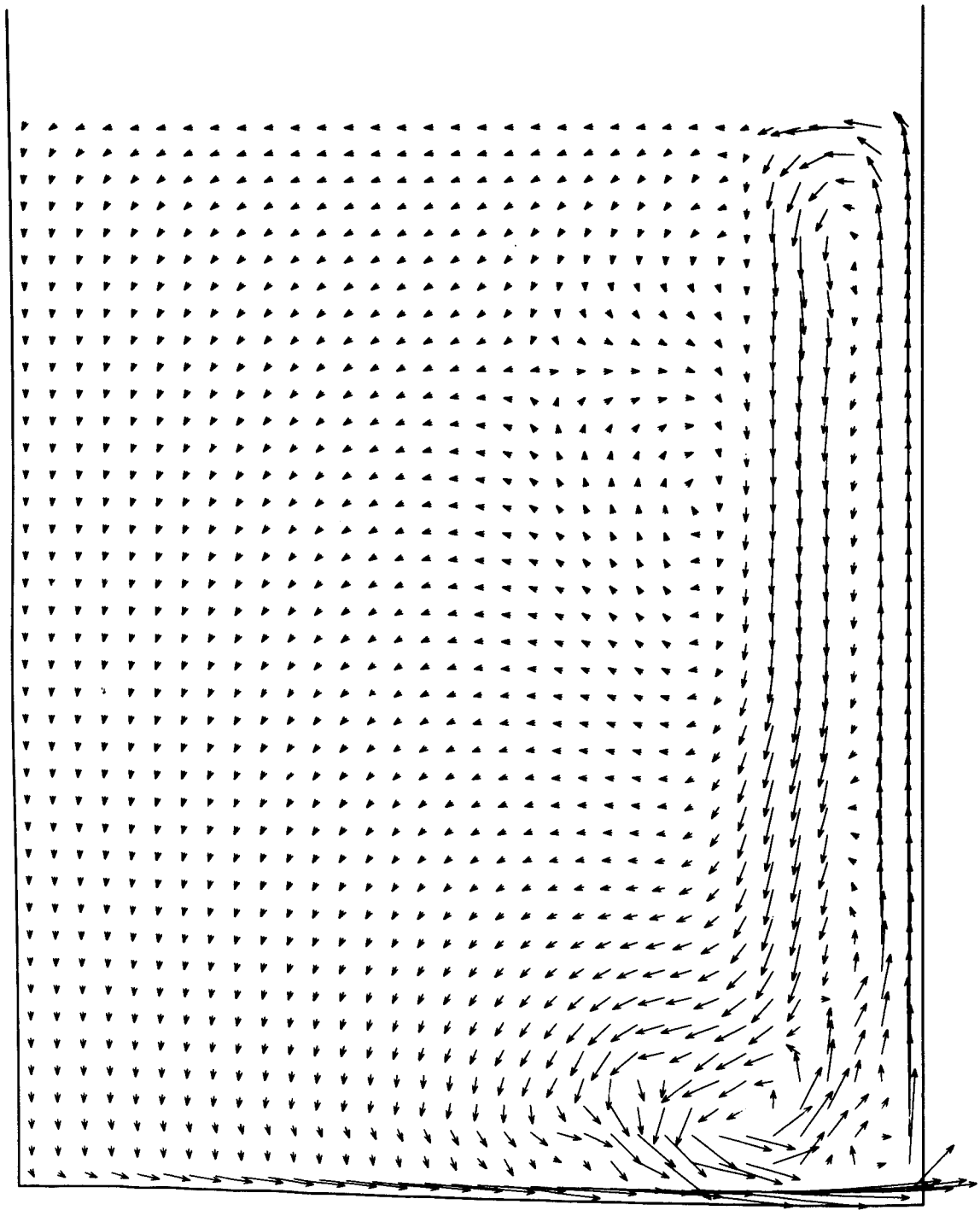

Fig. 18b : t = 10.0 s , v_{max} = 2.7E0 cm/s

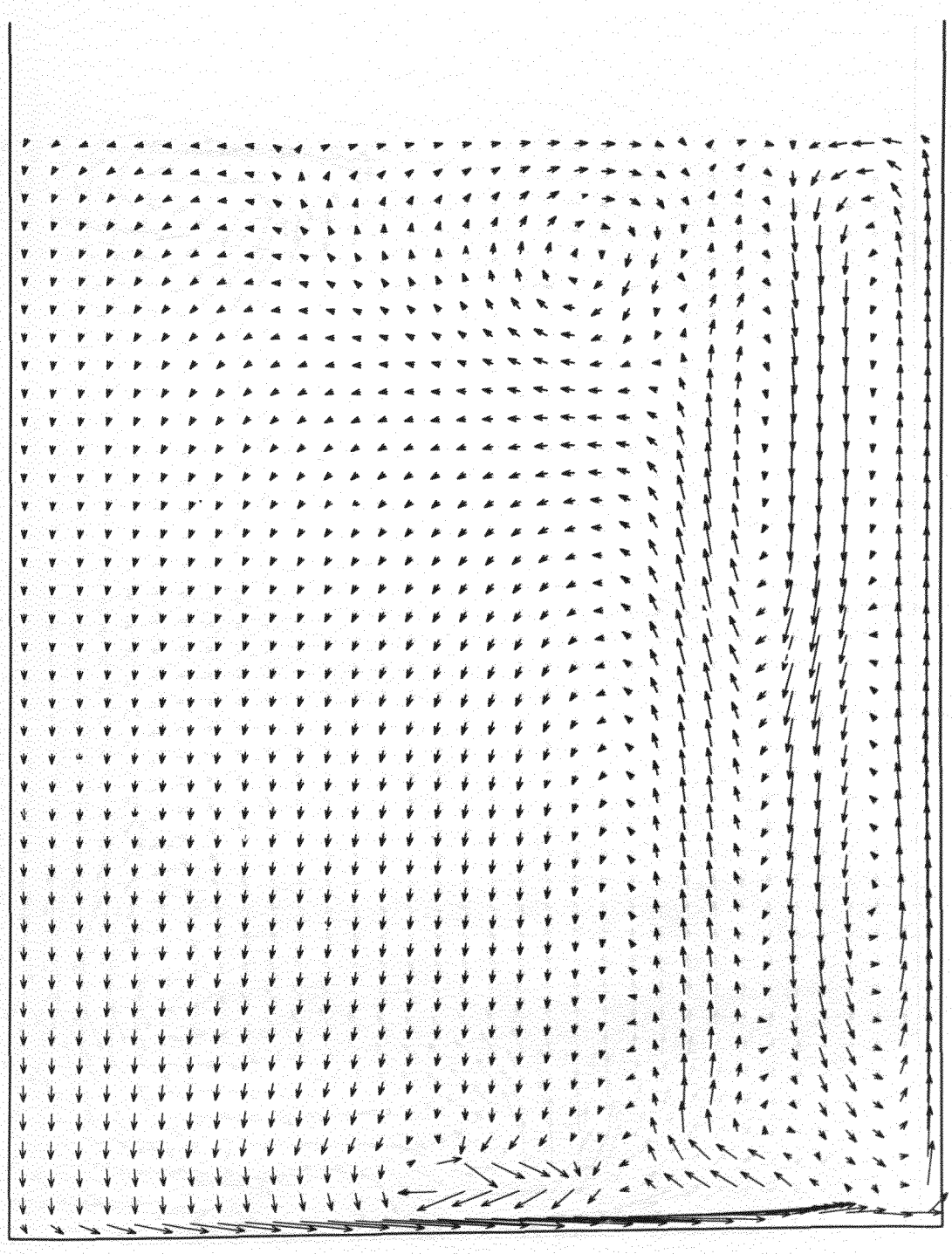

Fig. 18c : t = 11.0 s , v_{max} = 5.2E0 cm/s

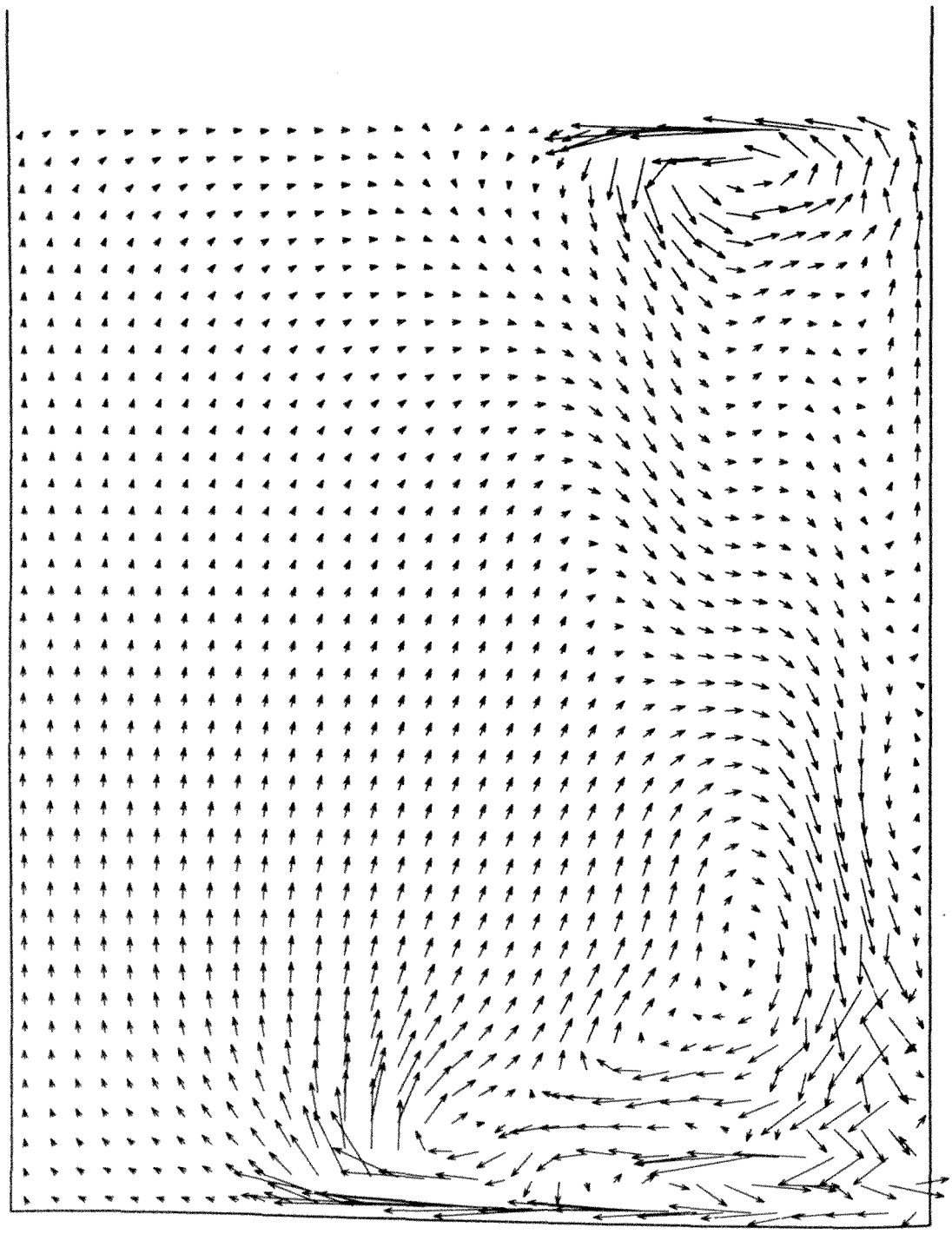

Fig. 18d : t = 15.0 s , v_{max} = 4.6EO cm/s

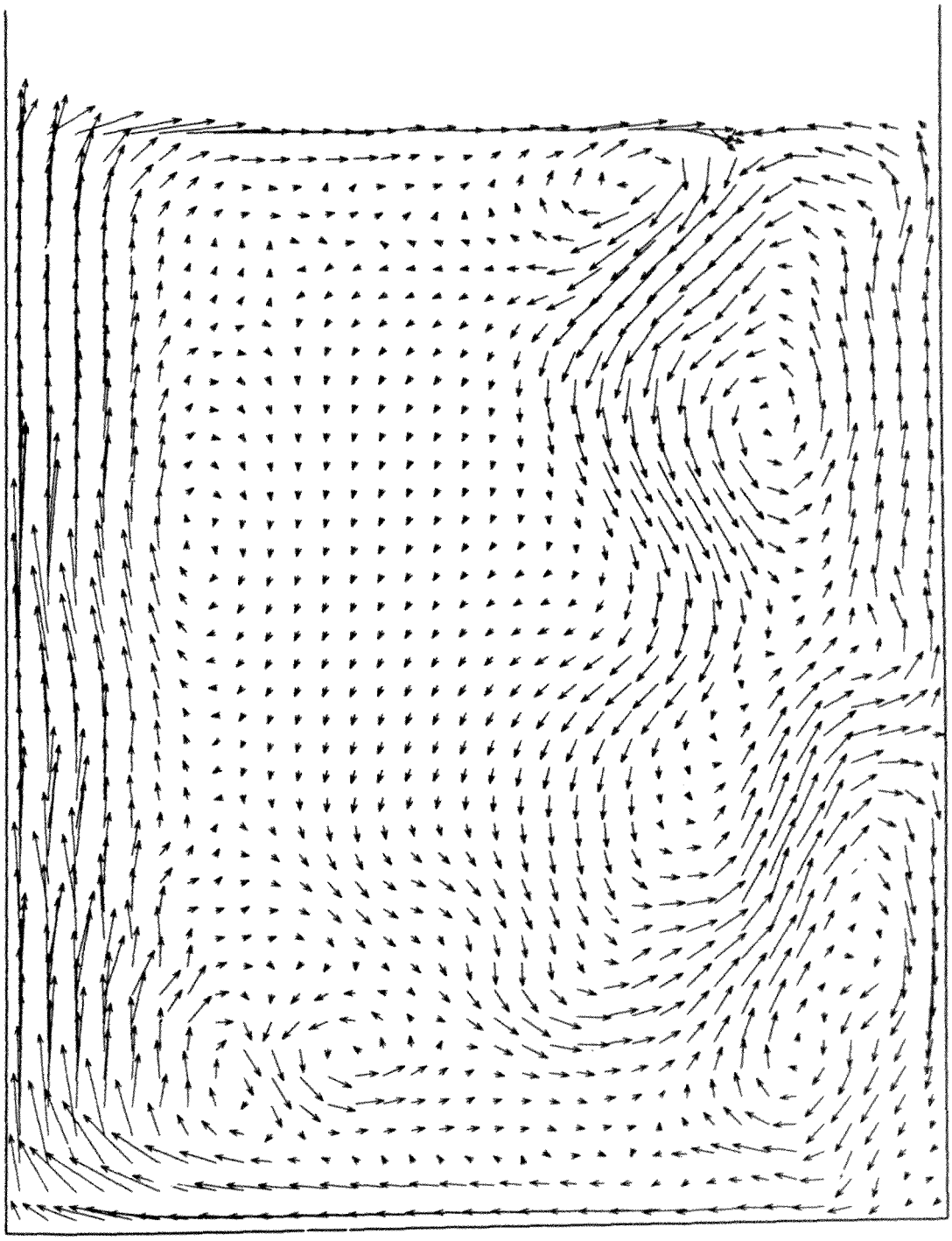

Fig. 18e : t = 20.0 s , v_{max} = 2.1E0 cm/s

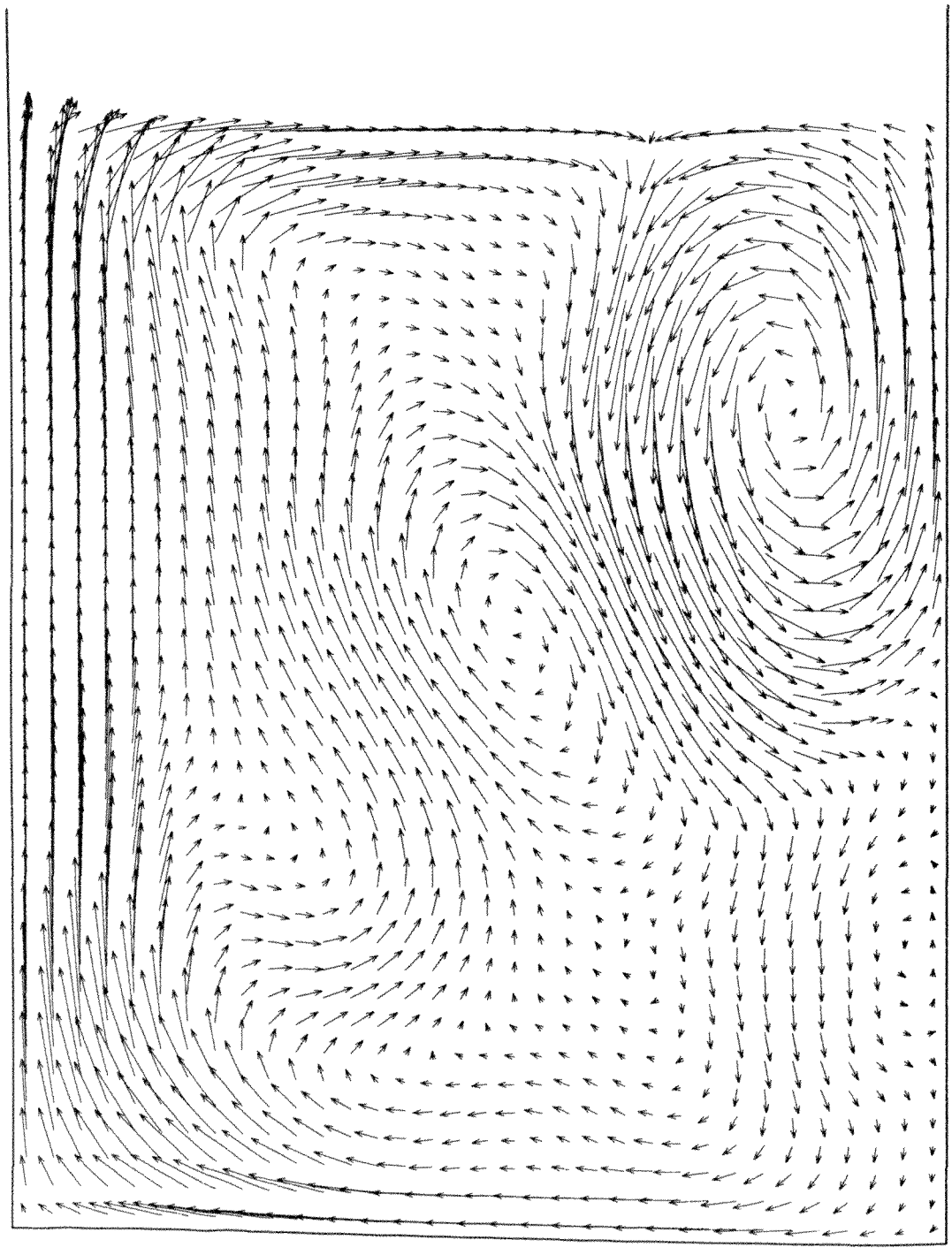

Fig. 18f : t = 21.0 s , v_{max} = 3.9E0 cm/s

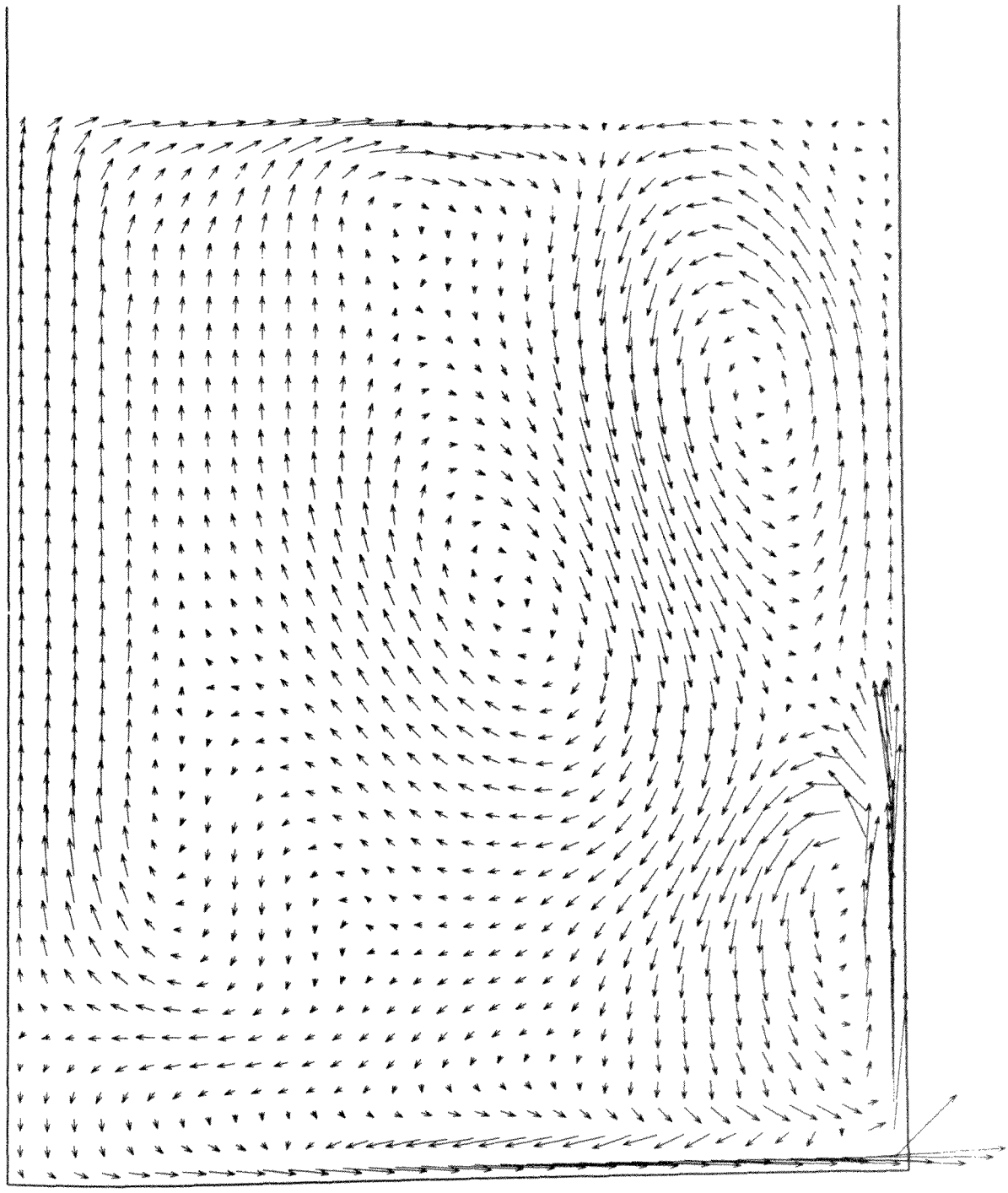

Fig. 18g : t = 25.0 s , v_{max} = 3.1EO cm/s

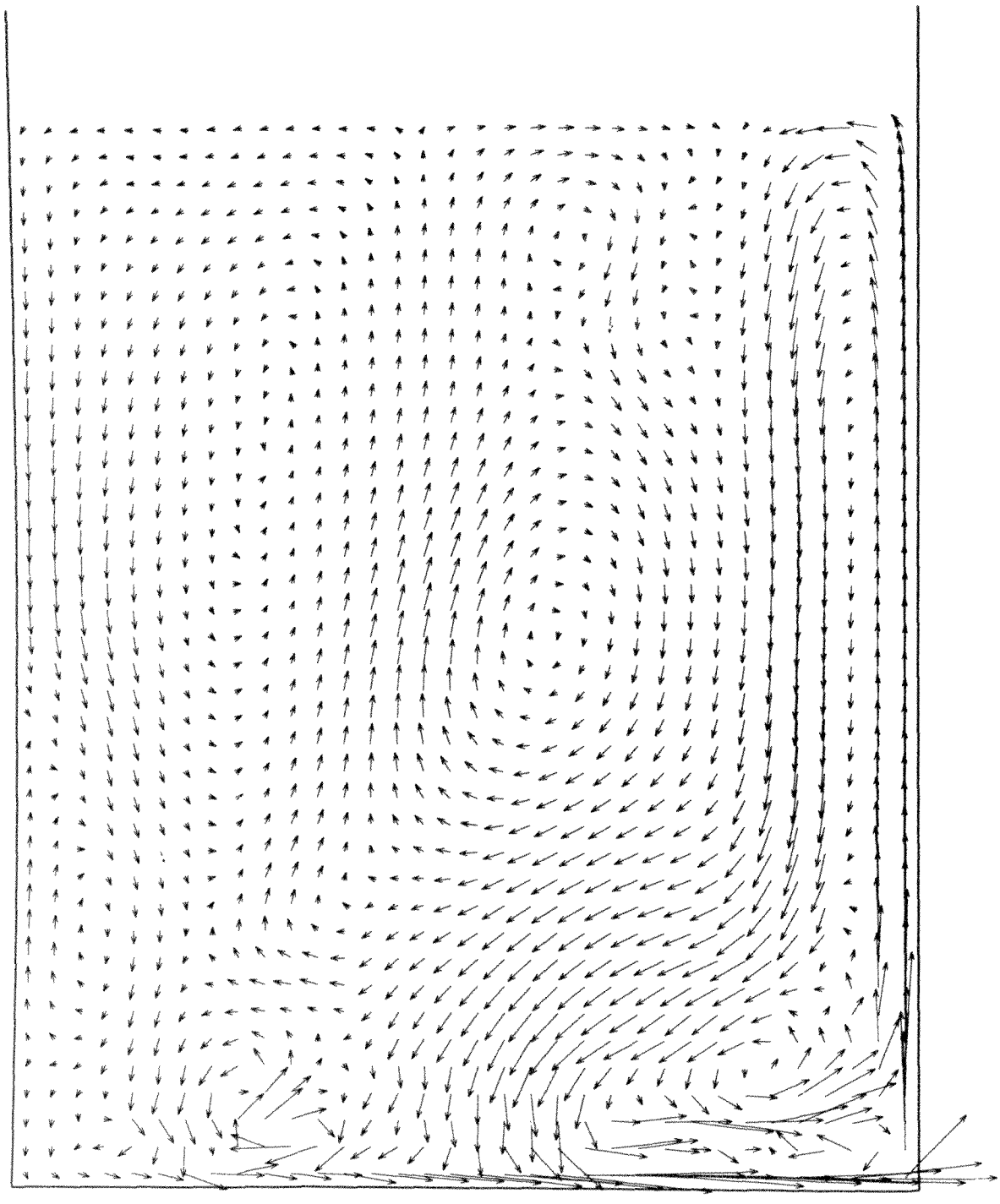

Fig. 18h : t = 30.0 s , v_{max} = 2.5E0 cm/s

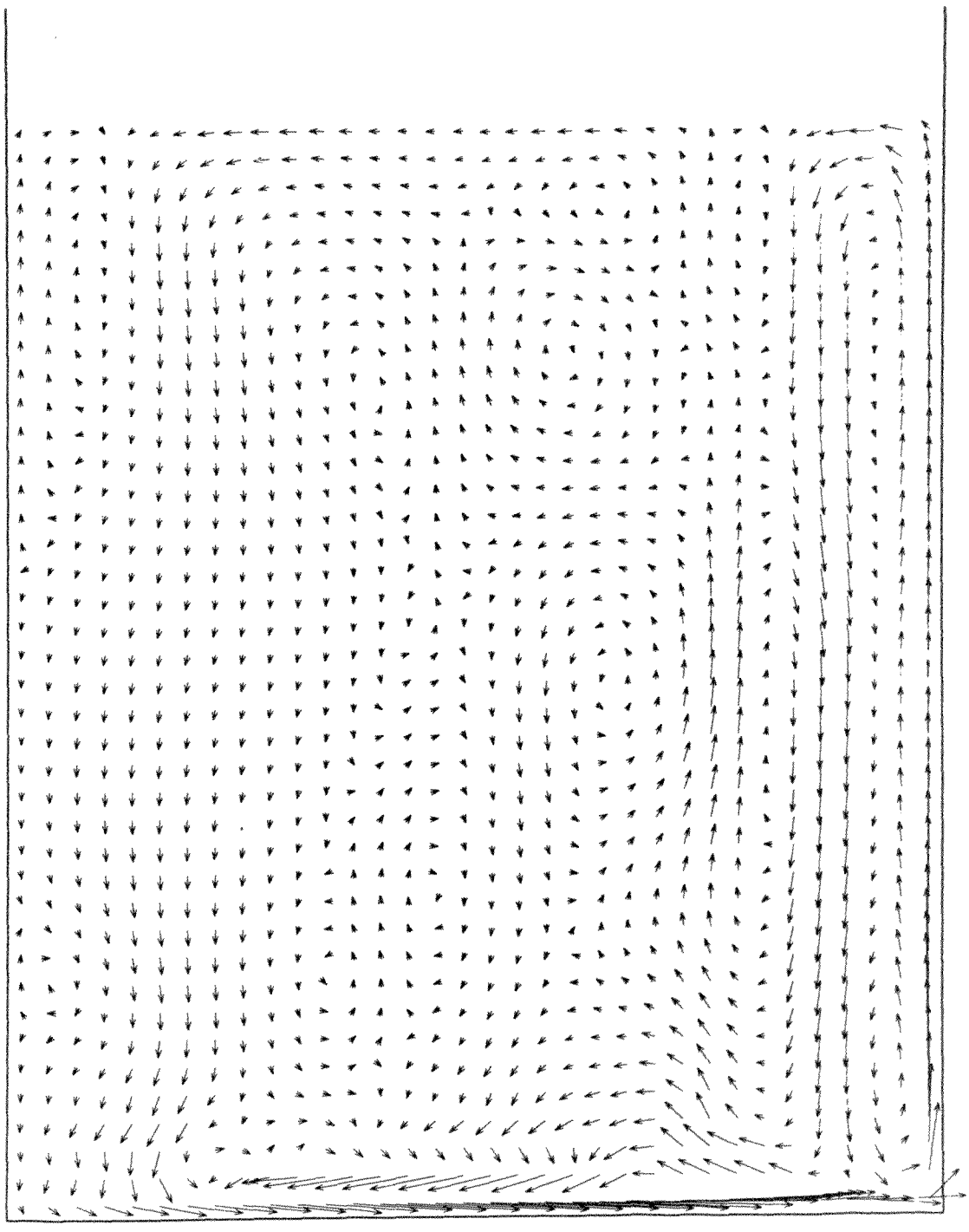

Fig. 18i : t = 31.0 s , v_{max} = 5.2E0 cm/s

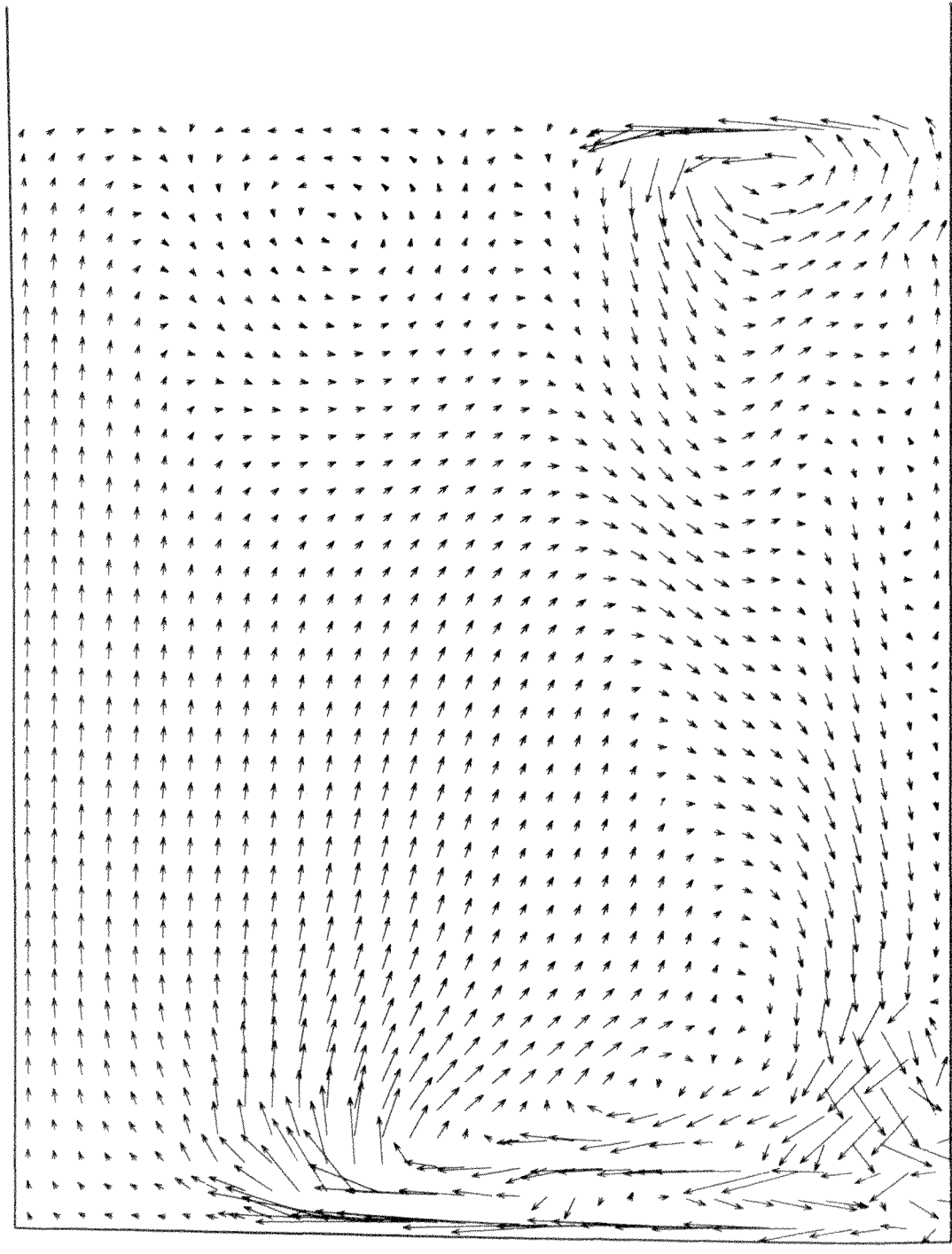

Fig. 18j : t = 35.0 s , v_{max} = 4.7E0 cm/s

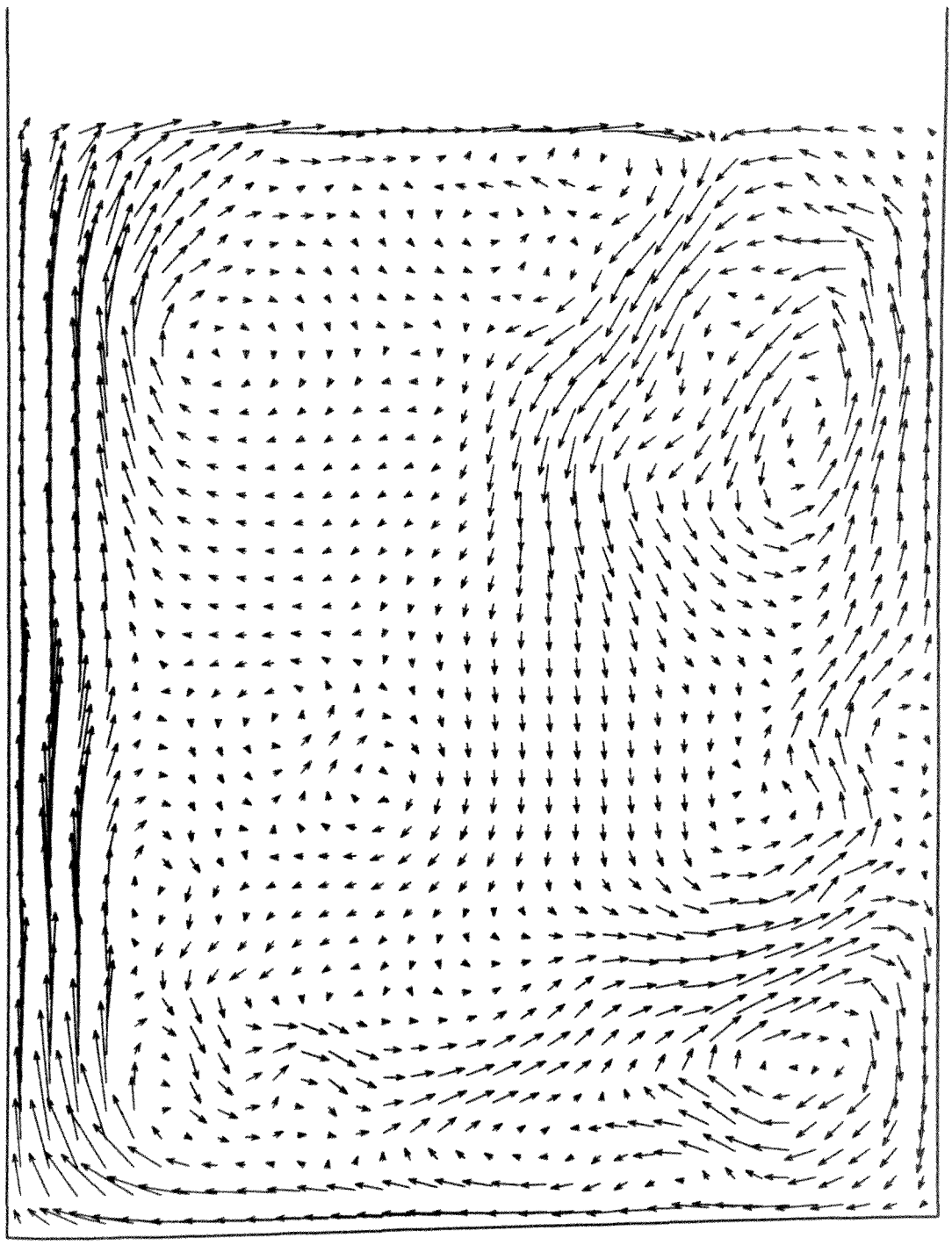

Fig. 18k : t = 40.0 s , v_{max} = 2.9E0 cm/s

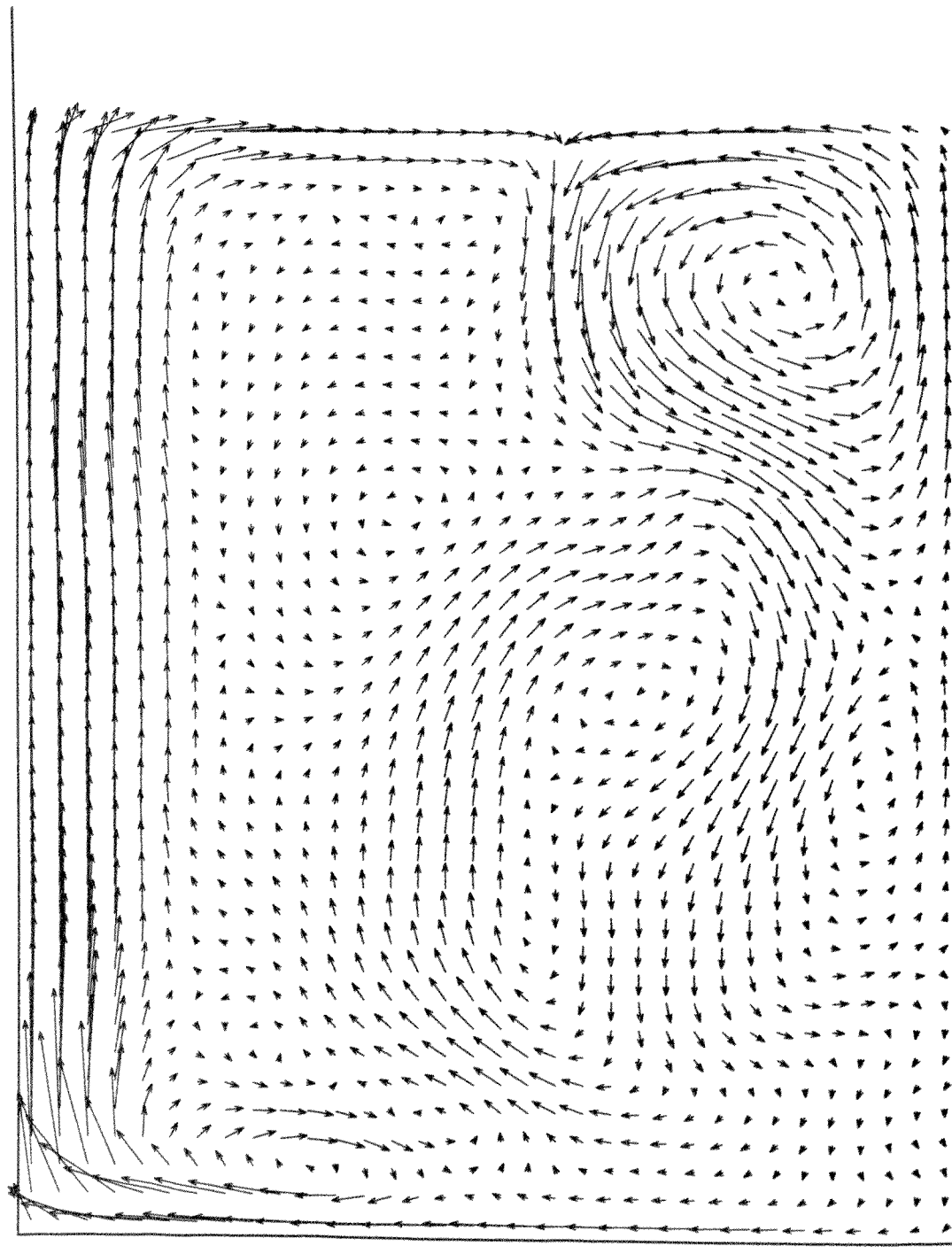

3.2.3. CACRT Czochralski Growth

Here we are concerned with the low viscosity analogues of the CACRT arrangements defined in section 3.1.3. Figs. 19a-g and 2oa-f show the flow patterns of the CACRT simulations with $\nu = o.oo5\ \frac{cm^2}{s}$ and a time period of 1o s (as in figs. 1o-11) for the counterrotational and the isorotational case, respectively. Figs. 21a-g and 22a-g differ from these simulations in the time period, which now has been increased to 2o s as in figs. 26-27 of the appendix. In the case of the low kinematic viscosity, the flow patterns for the counterrotational and the isorotational arrangements do not differ as significantly as in the moderate viscosity case of section 3.1.3. It always develops a Taylor-Proudman cell beneath the crystal in the acceleration phase, but deceleration of the crystal and crucible rotation destroys this cell and causes fluid flow from the bottom of the crucible along the axis of symmetry towards the crystal. The choice of the longer time period of 2o s seems to be more advantageous, because, in this case, the liquid is given more time to react on the varying crystal and crucible rotation rates. Moreover, the Taylor-Proudman cell beneath the crystal is a little greater in size for some time, and the suction effect of the crystal in the deceleration phase can be better exploited for the optimum stirring of the melt.

Fig. 19a : t = 10.0 s , v_{max} = 4.6E0 cm/s

NUE :	0.005 cm^2/s
CRUCIBLE ROTATION :	10 : 30 rpm
CRYSTAL ROTATION :	-40 : -80 rpm
TIME PERIOD :	10 s

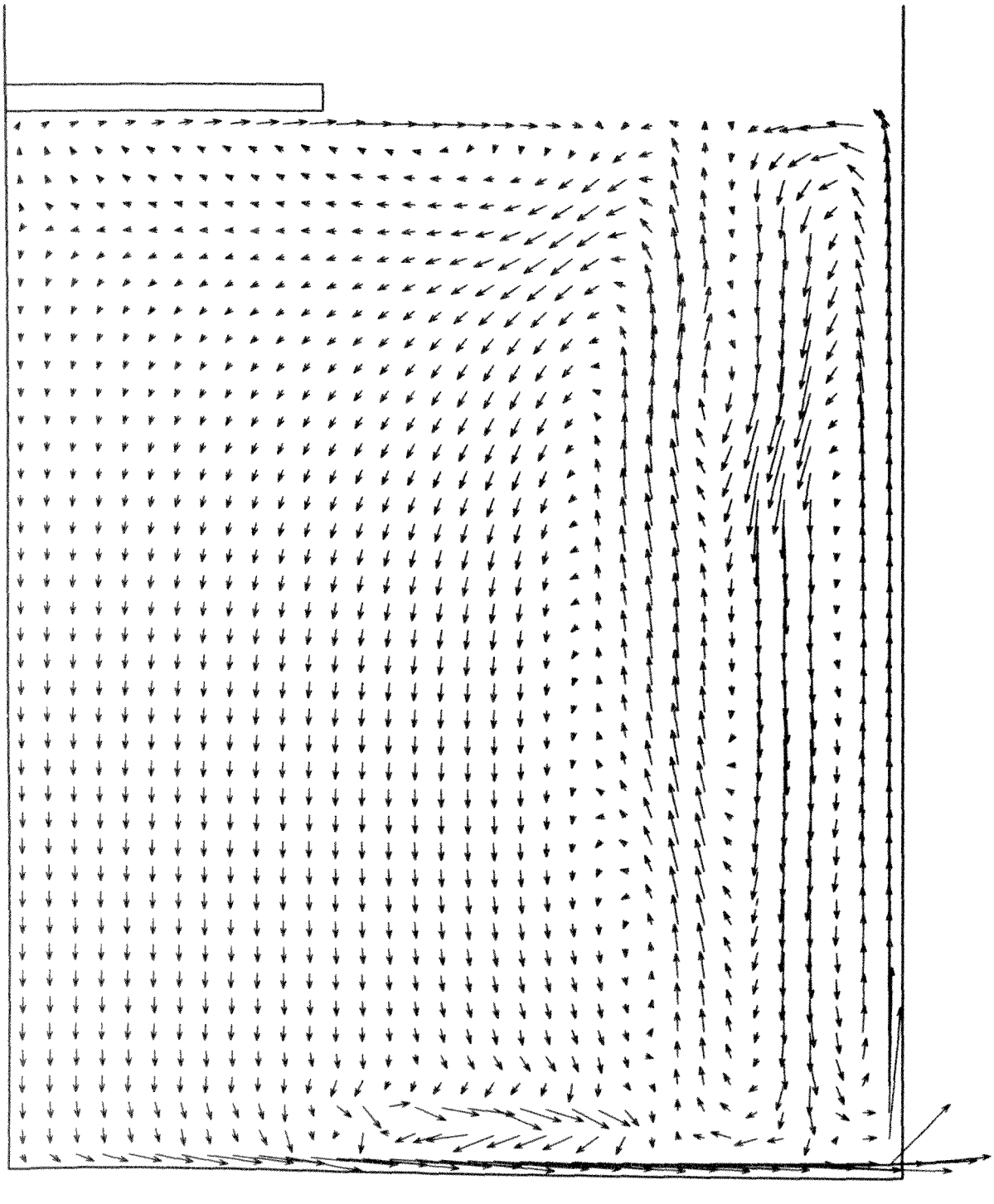

Fig. 19b : t = 11.0 s , v_{max} = 4.1E0 cm/s

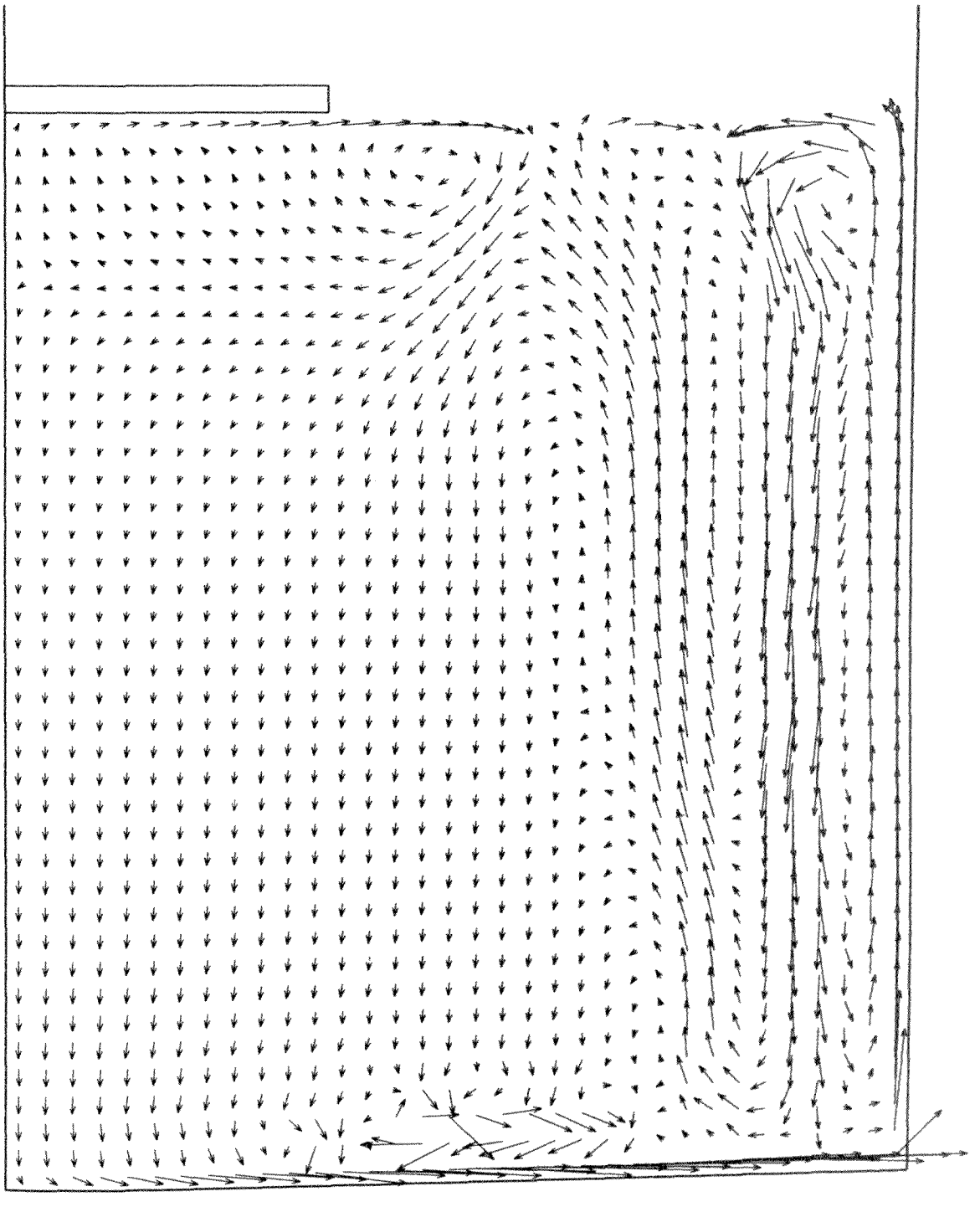

Fig. 19c : t = 15.0 s , v_{max} = 5.0E0 cm/s

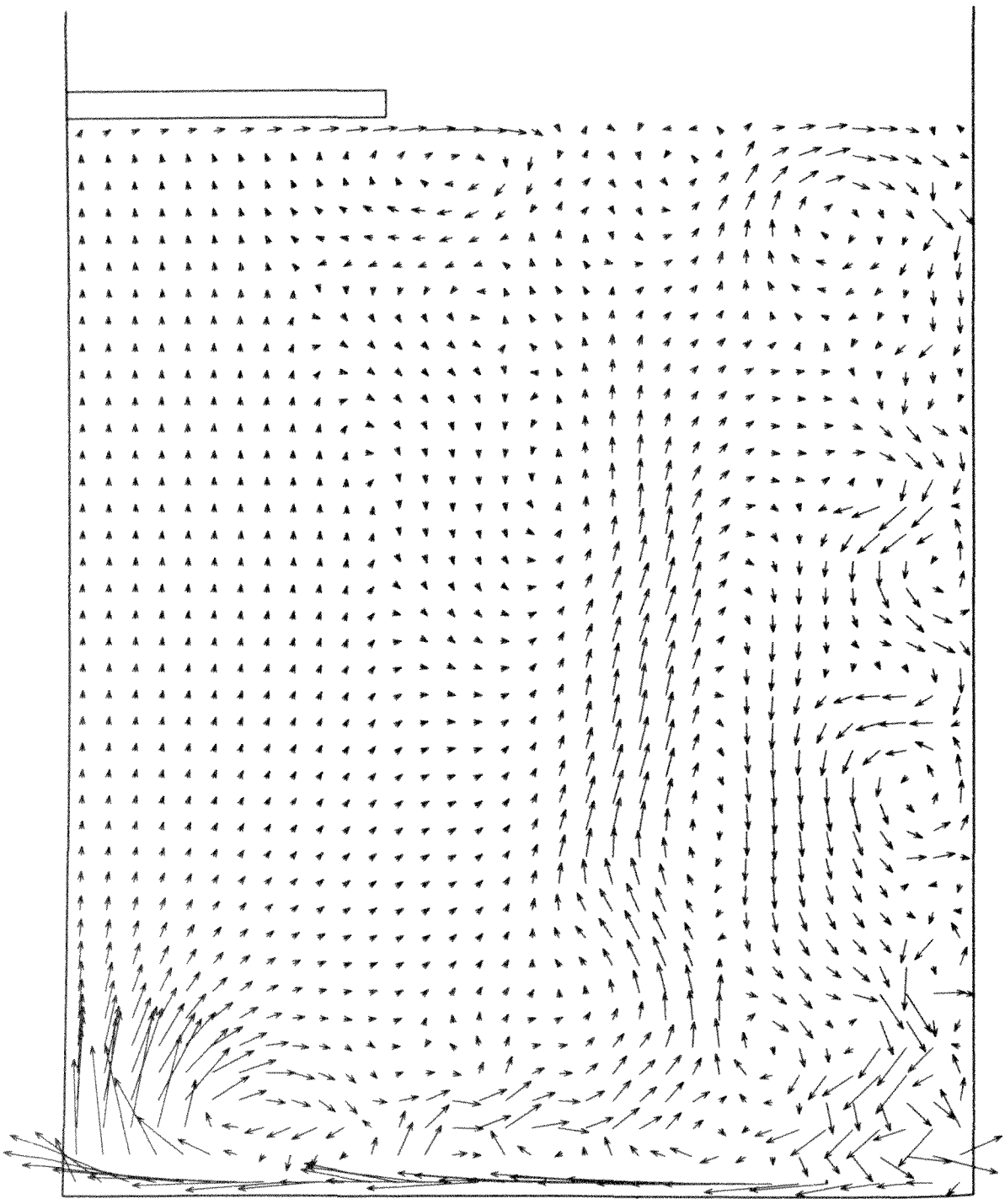

Fig. 19d : t = 20.0 s , v_{max} = 4.1E0 cm/s

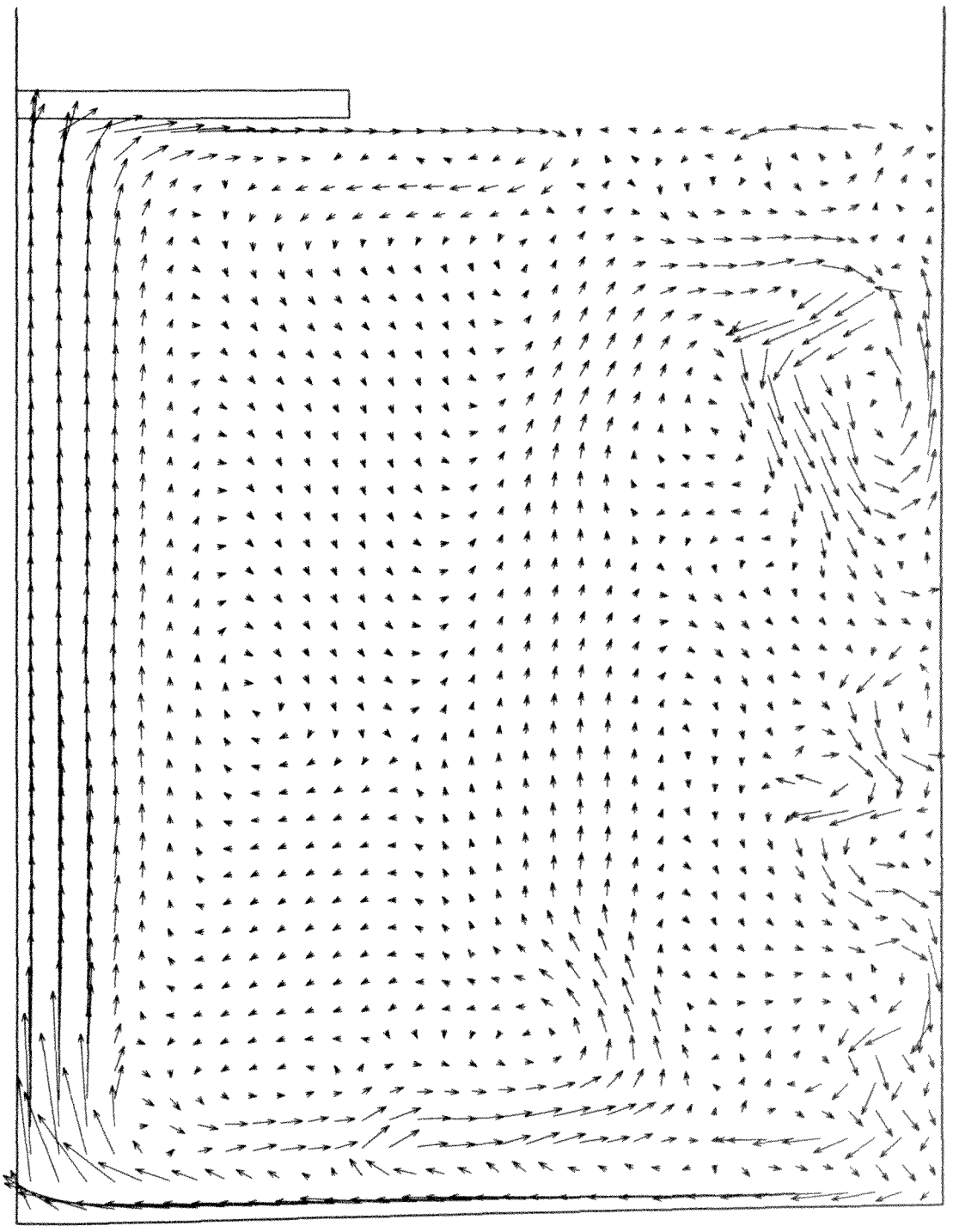

Fig. 19e : t = 21.0 s , v_{max} = 3.8EO cm/s

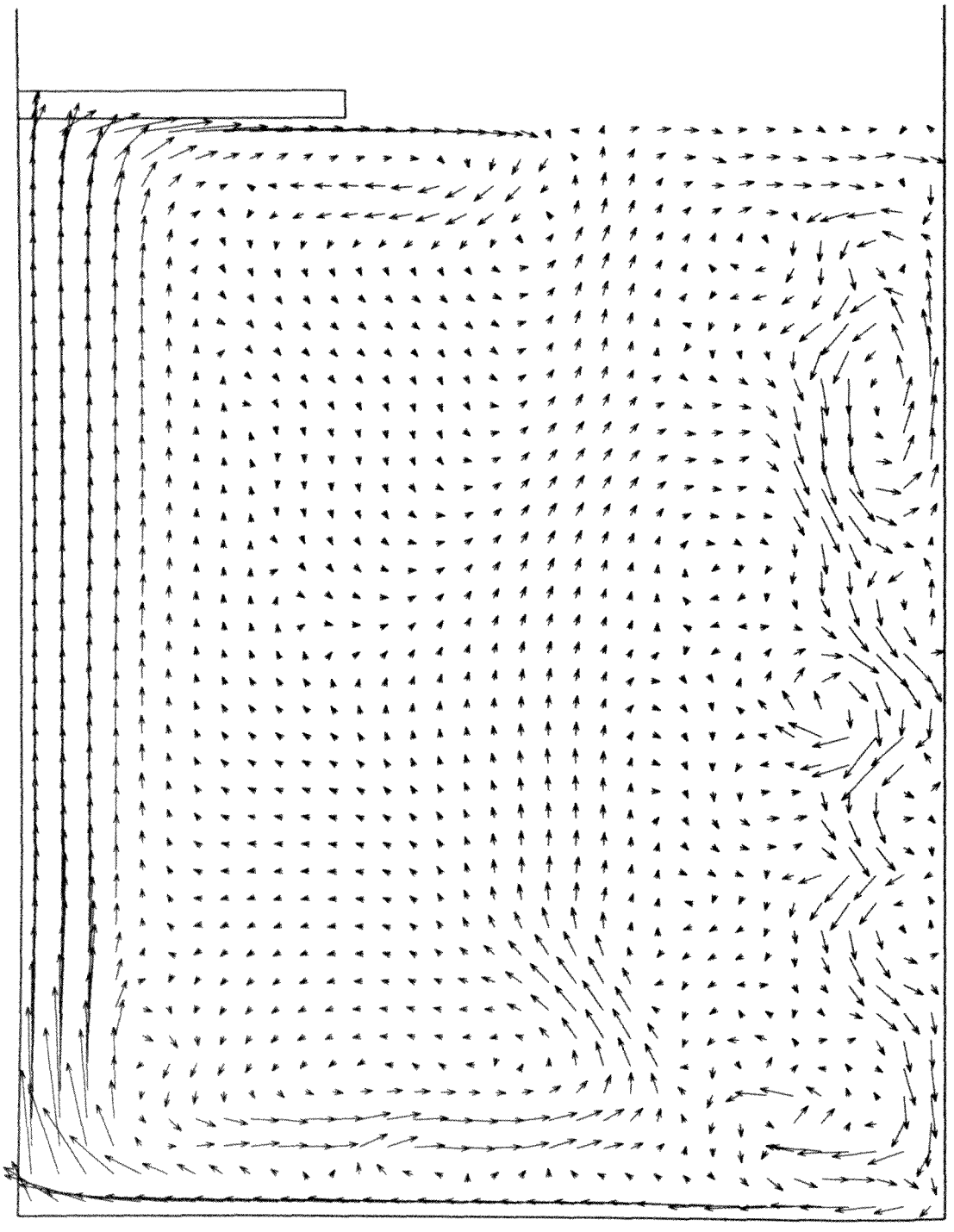

Fig. 19f : t = 25.0 s , v_{max} = 2.9EO cm/s

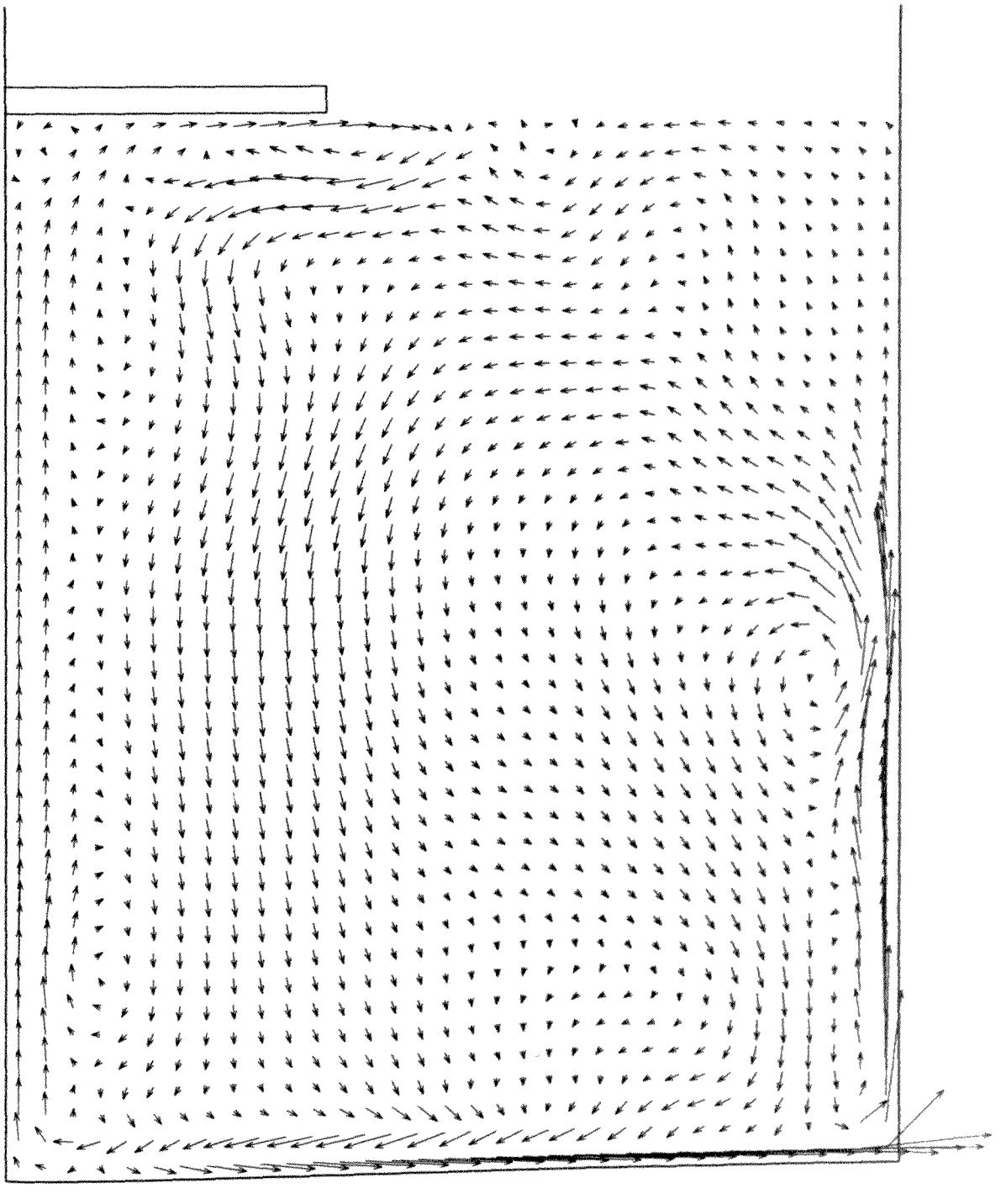

Fig. 19g : t = 30.0 s , v_{max} = 4.0E0 cm/s

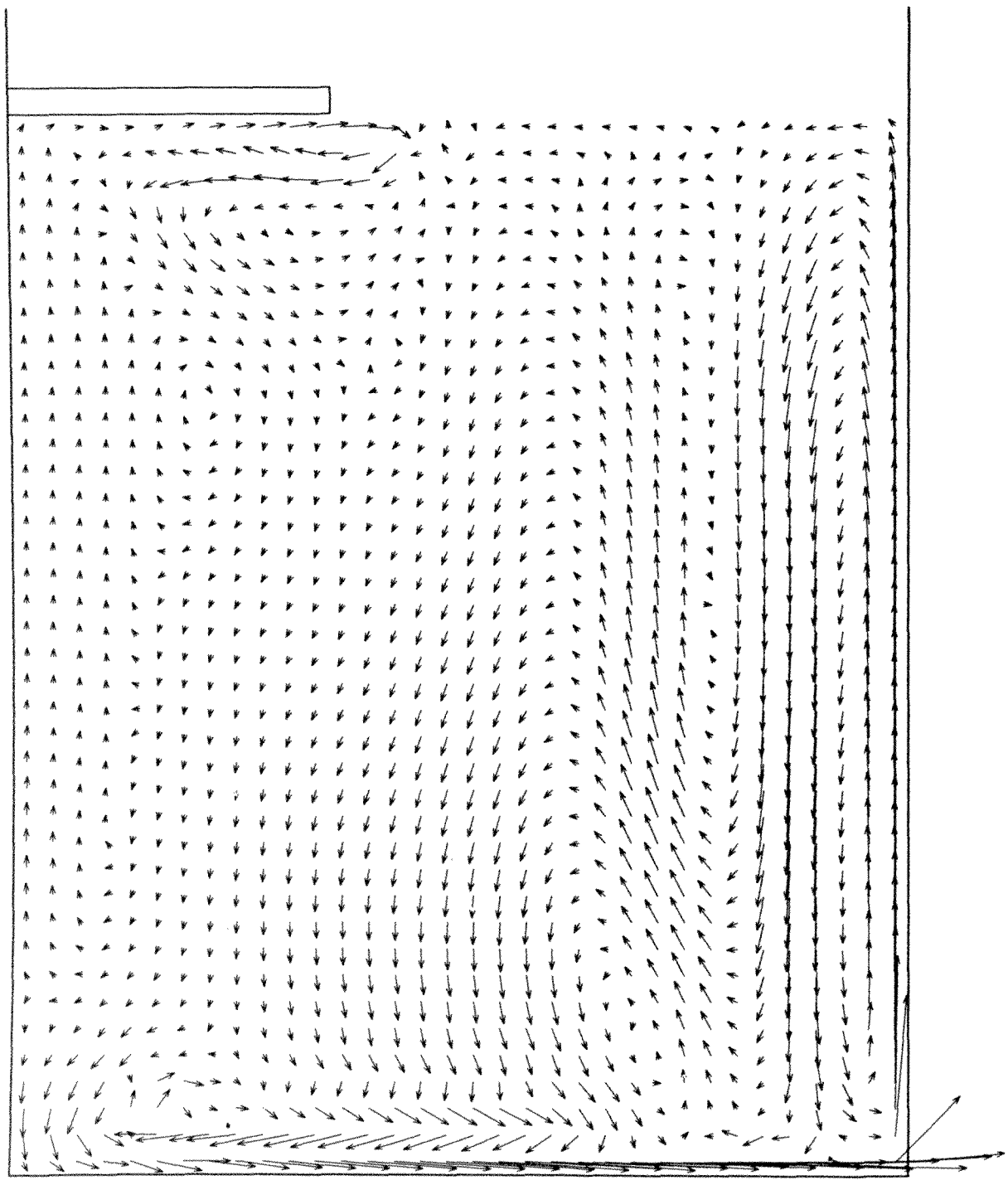

Fig. 2oa : t = 10.0 s , v_{max} = 4.6EO cm/s

NUE : 0.005 cm^2/s

CRUCIBLE ROTATION : 10 : 30 rpm

CRYSTAL ROTATION : 40 : 80 rpm

TIME PERIOD : 10 s

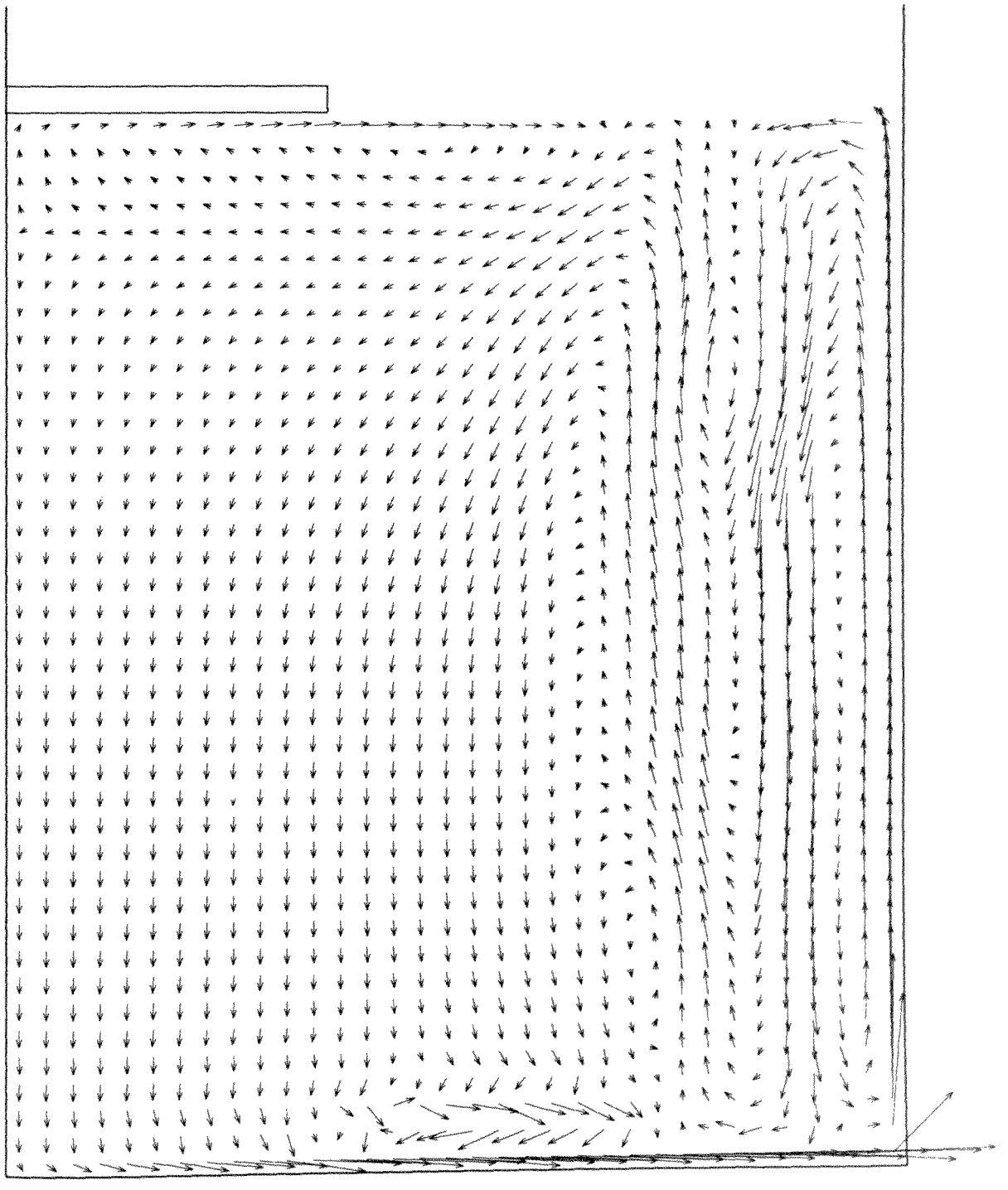

Fig. 2ob : t = 10.421 s , v_{max} = 4.5EO cm/s

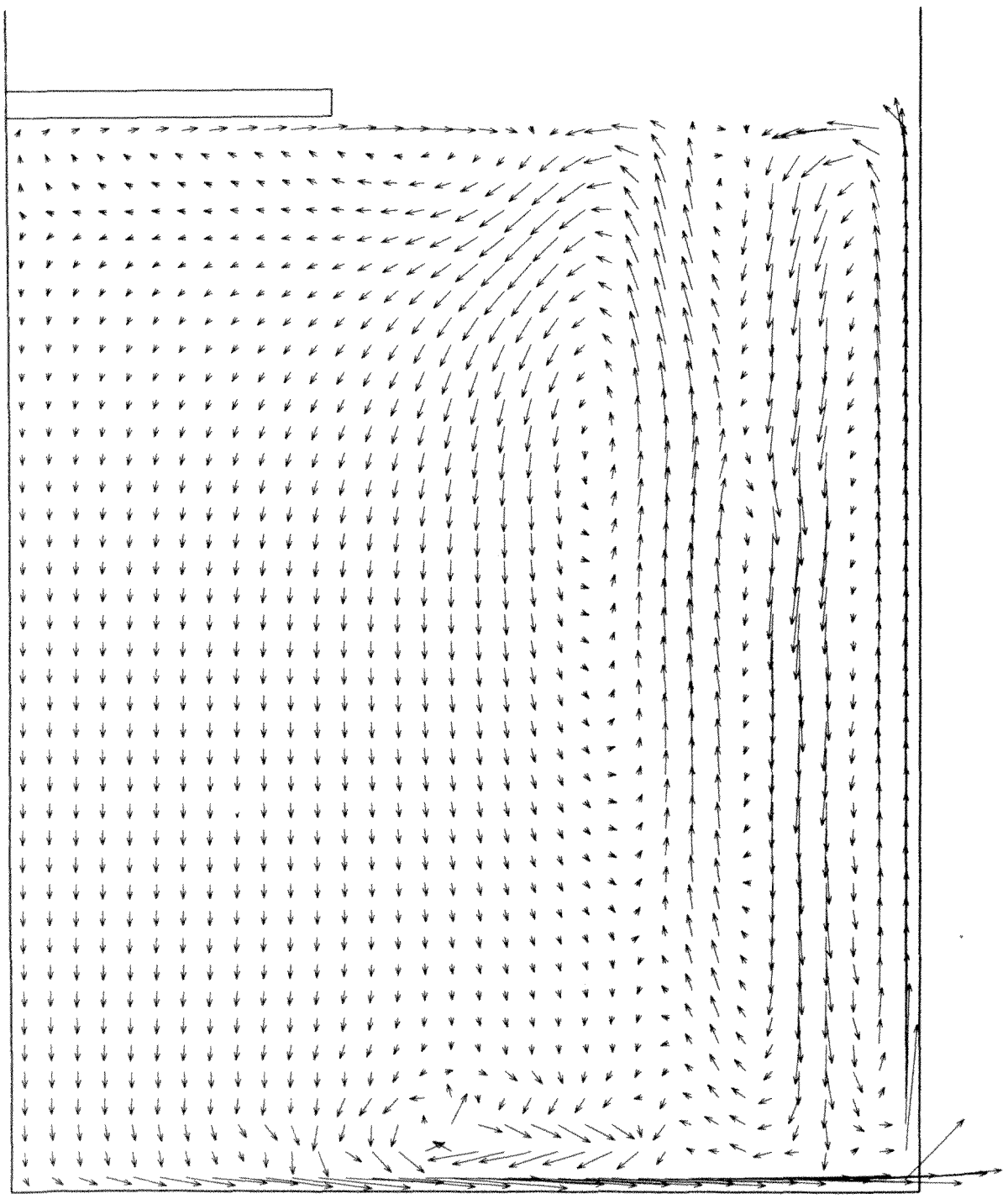

Fig. 2oc : t = 15.0 s , v_{max} = 6.5EO cm/s

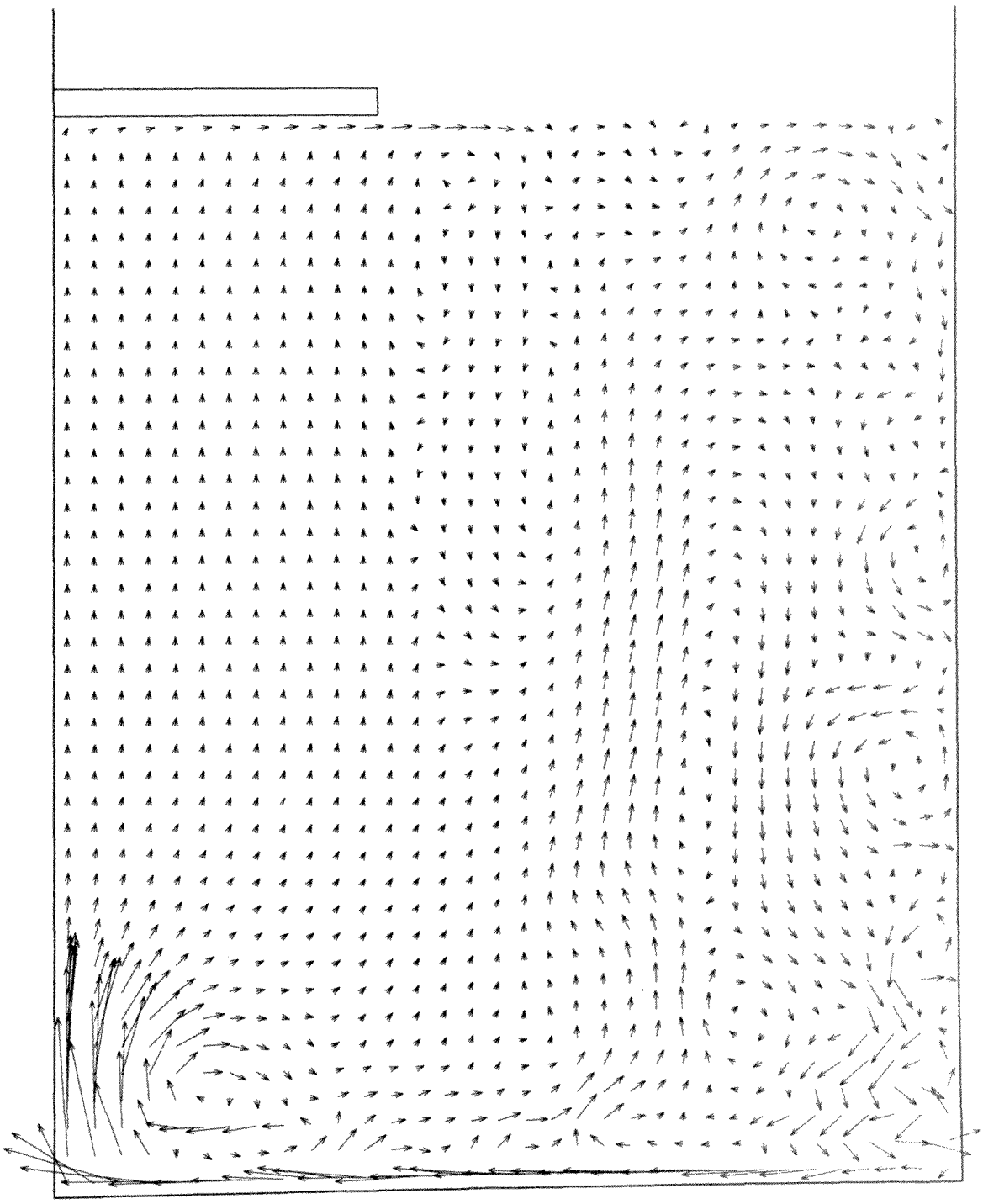

Fig. 2od : t = 19.831 s , v_{max} = 4.2EO cm/s

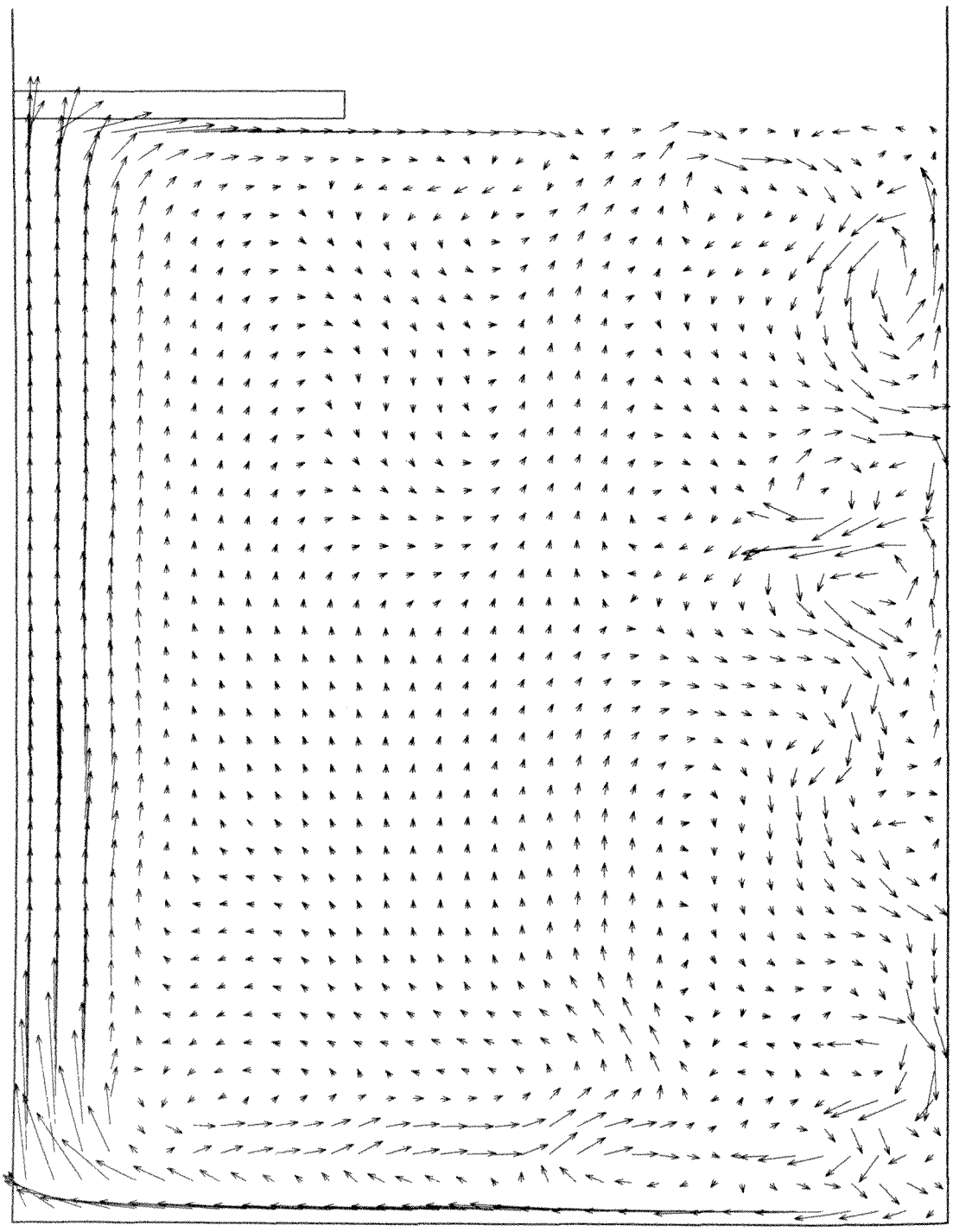

Fig. 2oe : t = 25.0 s , v_{max} = 2.7EO cm/s

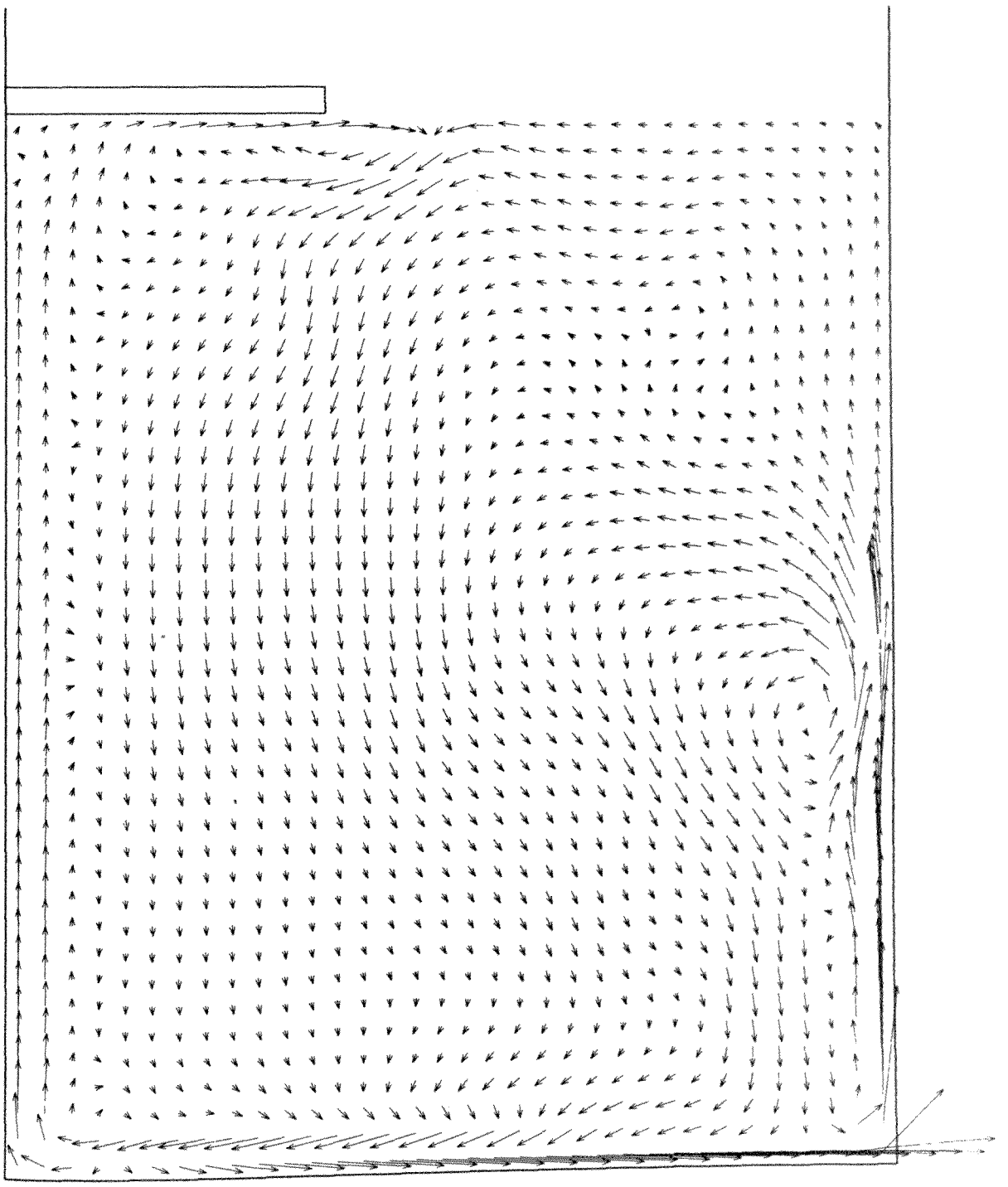

Fig. 2of : t = 30.0 s , v_{max} = 3.9EO cm/s

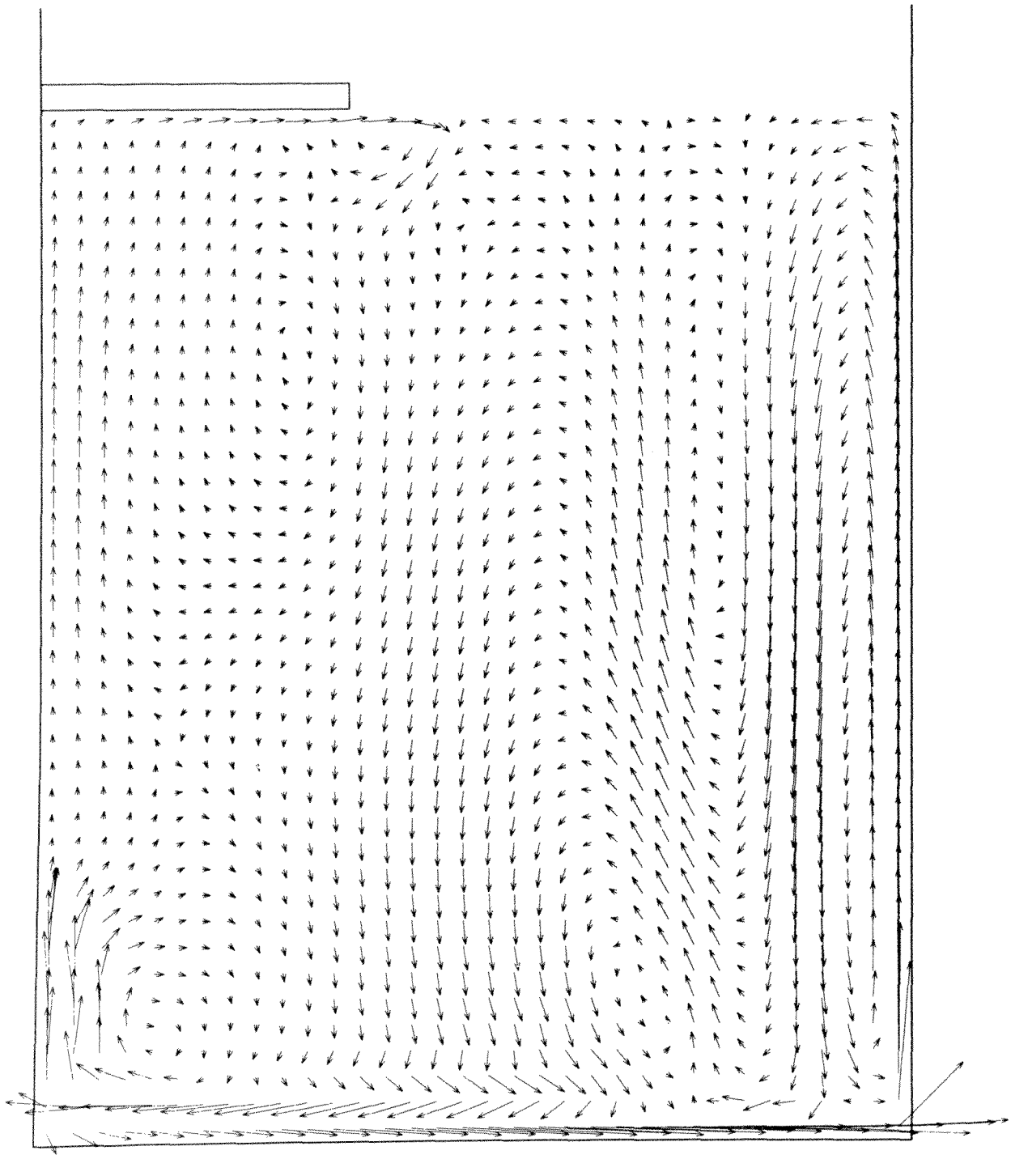

Fig. 21a : t = 5.0 s , v_{max} = 3.OEO cm/s

NUE : 0.005 cm^2/s

CRUCIBLE ROTATION : 10 : 30 rpm

CRYSTAL ROTATION : -40 : -80 rpm

TIME PERIOD : 20 s

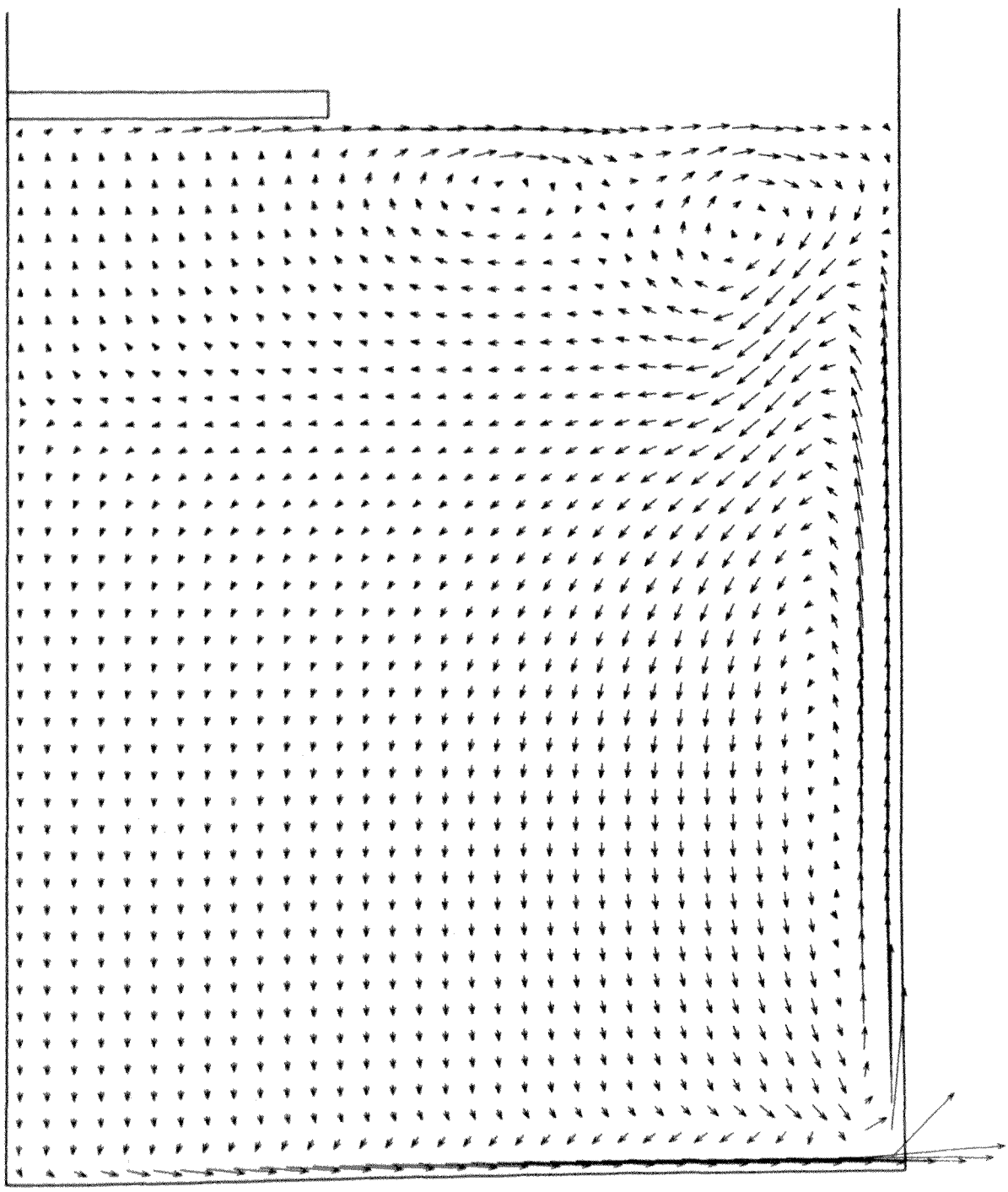

Fig. 21b : t = 15.0 s , v_{max} = 3.5EO cm/s

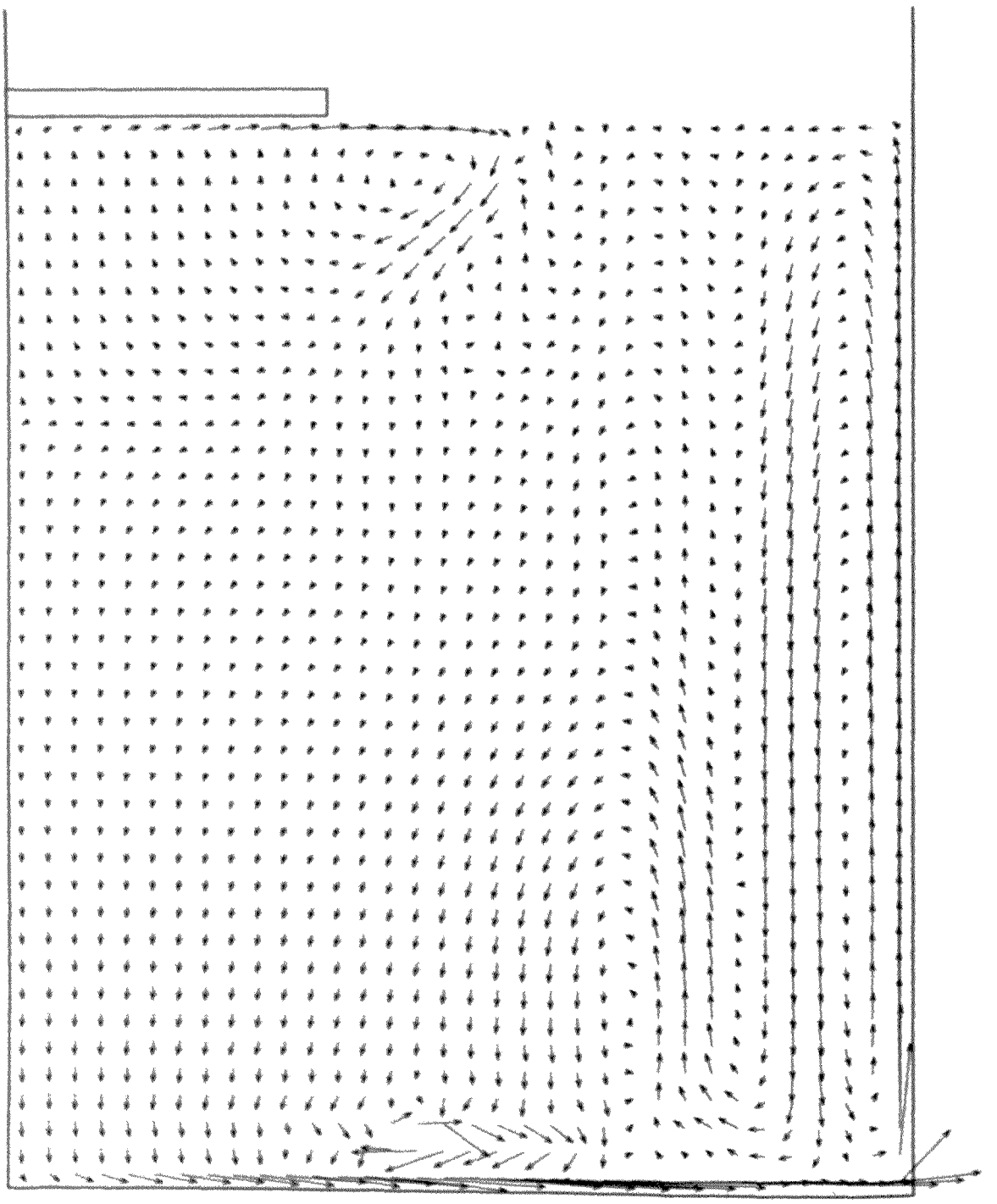

Fig. 21c : t = 20.0 s , v_{max} = 3.1E0 cm/s

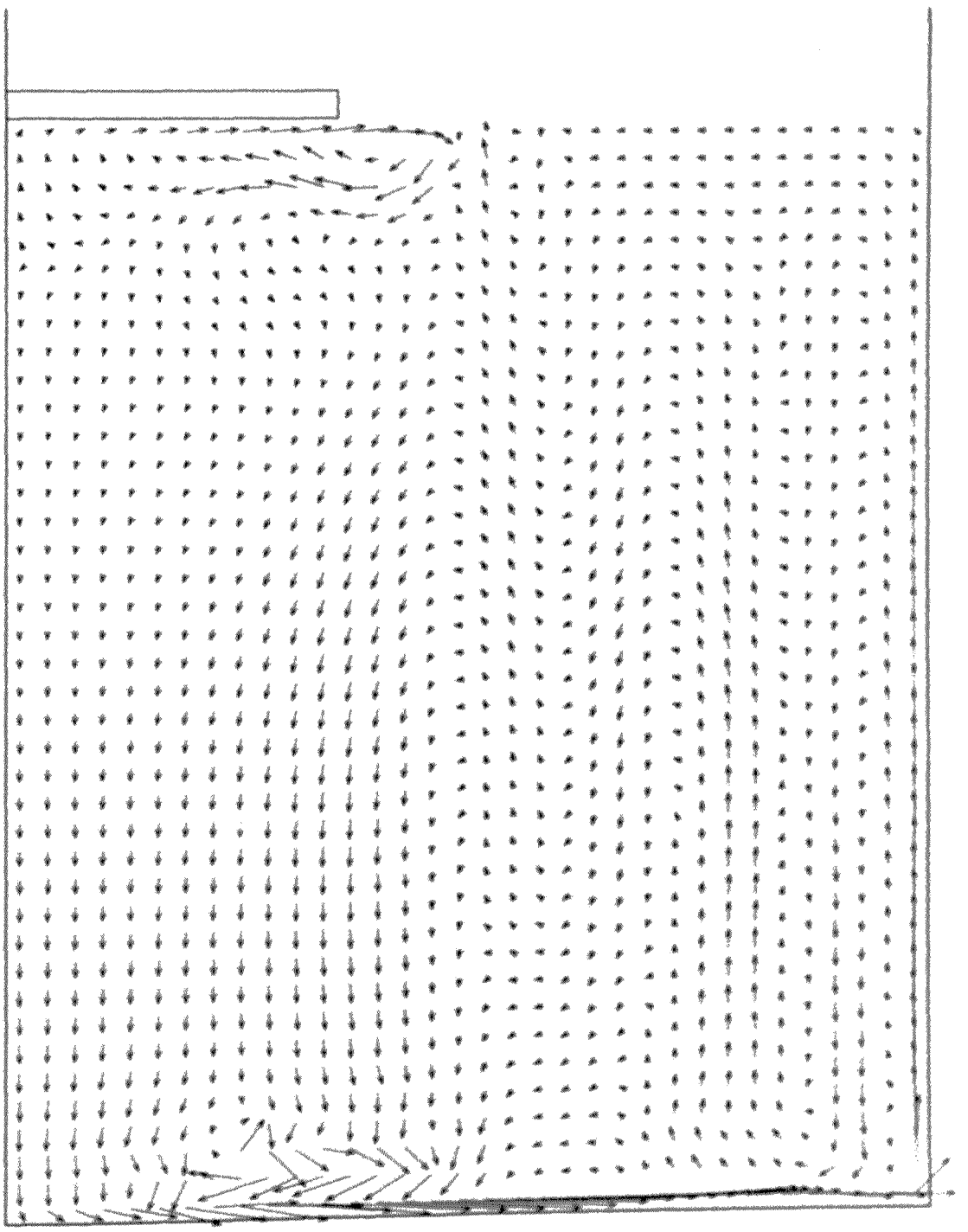

Fig. 21d : t = 21.0 s , v_{max} = 2.8EO cm/s

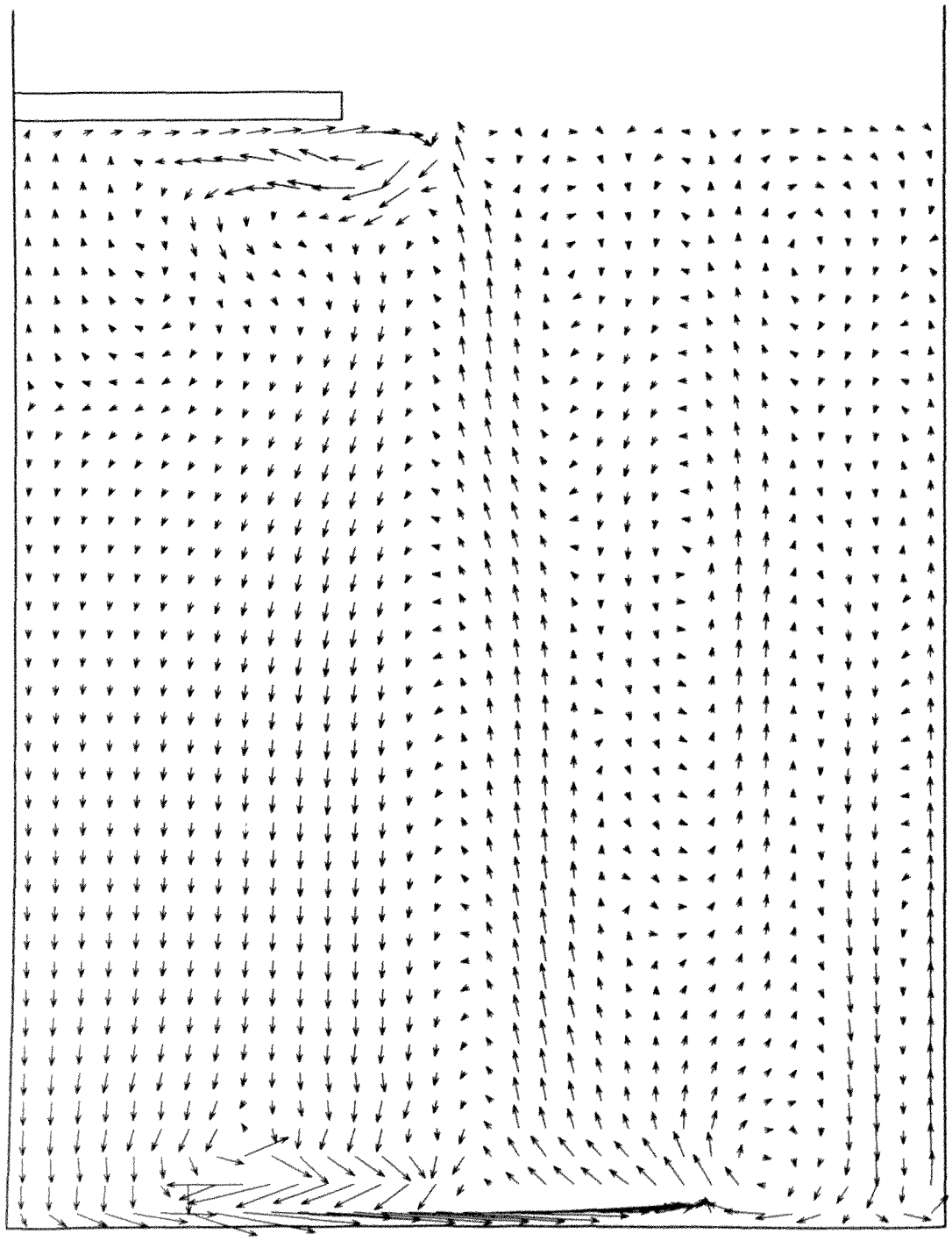

Fig. 21e : t = 25.0 s , v_{max} = 2.5EO cm/s

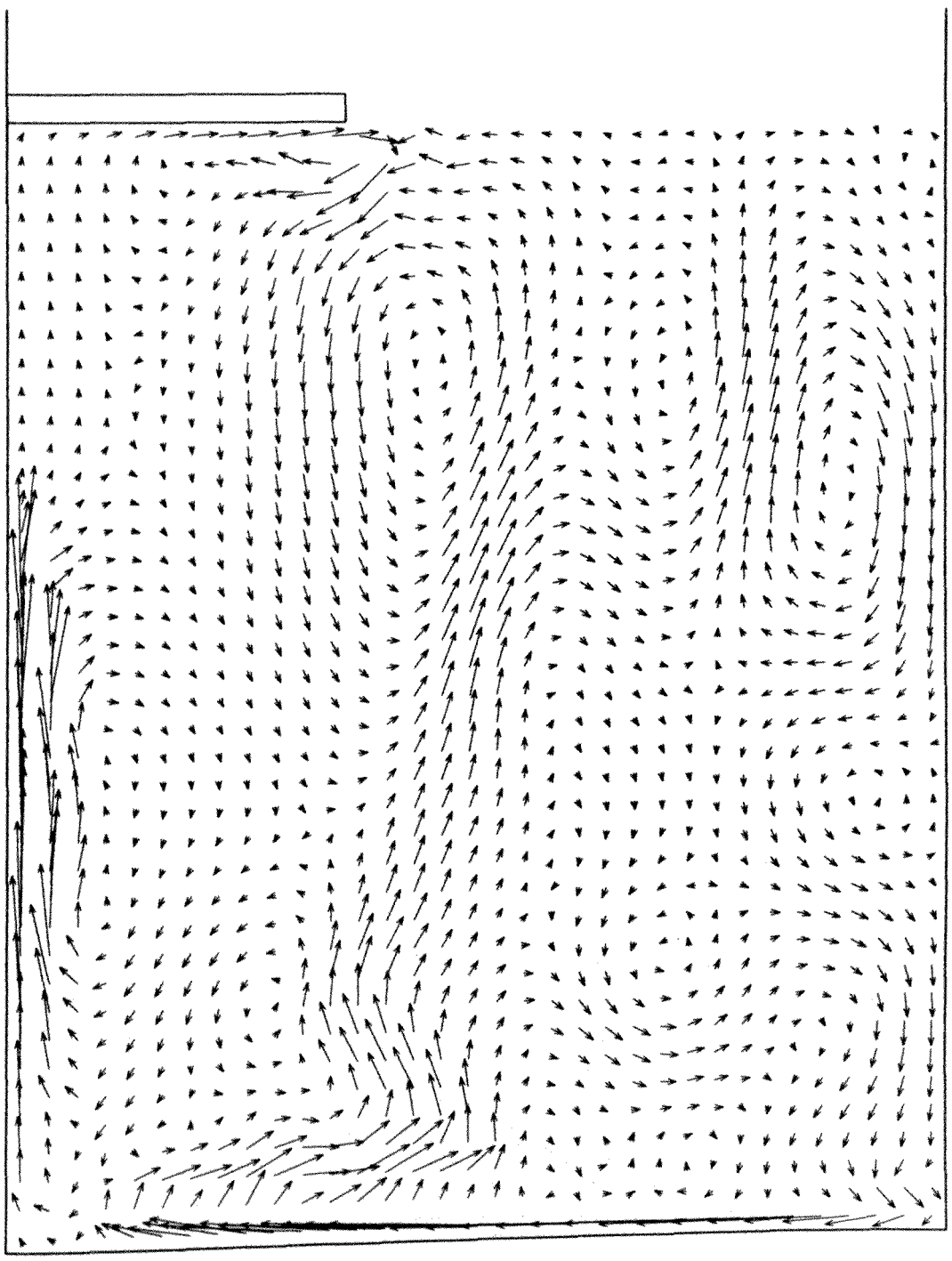

Fig. 21f : t = 35.0 s , v_{max} = 2.1EO cm/s

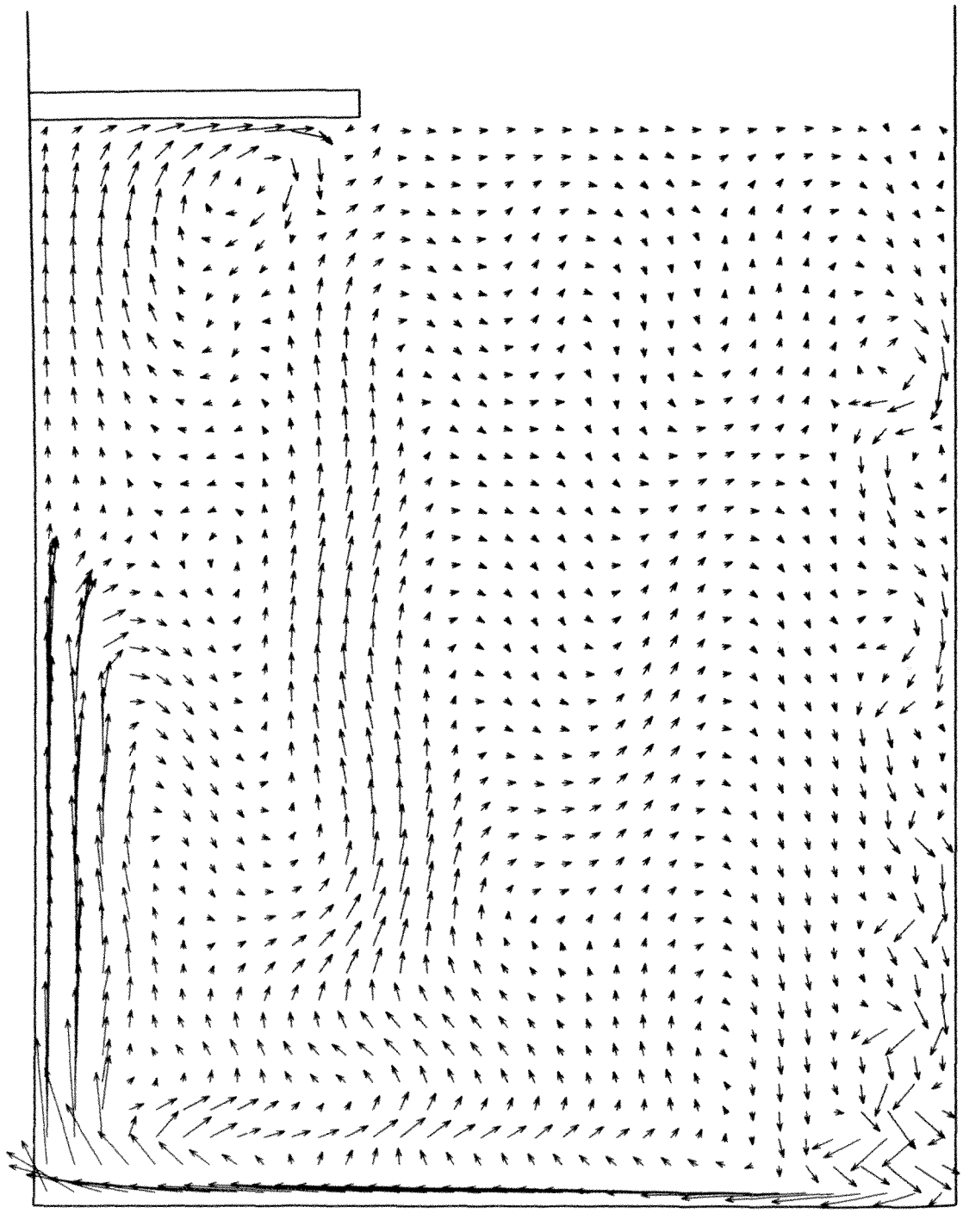

Fig. 21g : t = 40.0 s , v_{max} = 3.0E0 cm/s

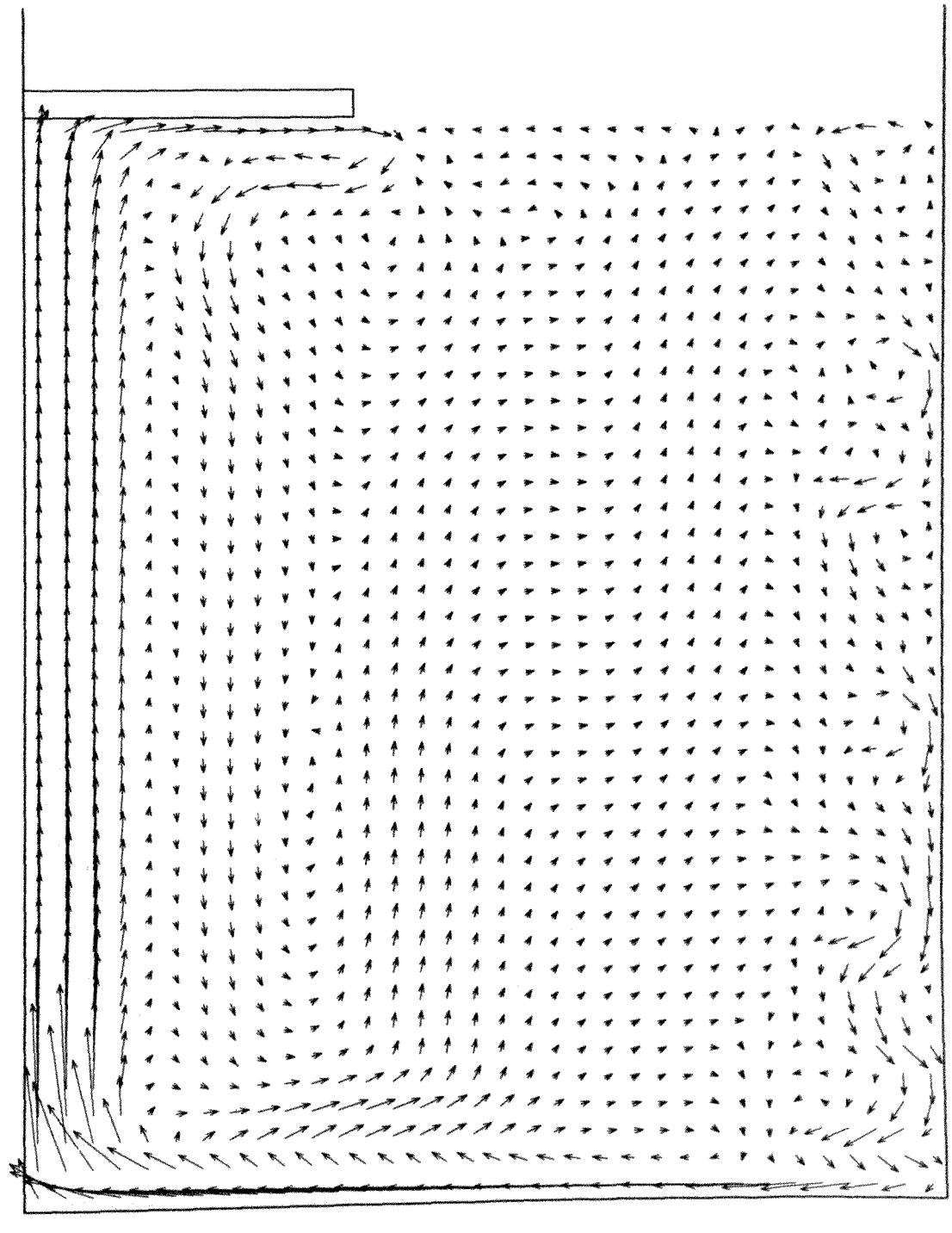

Fig. 22a : t = 5.0 s , v_{max} = 3.OEO cm/s

NUE : 0.005 cm^2/s
CRUCIBLE ROTATION : 10 : 30 rpm
CRYSTAL ROTATION : 40 : 80 rpm
TIME PERIOD : 20 s

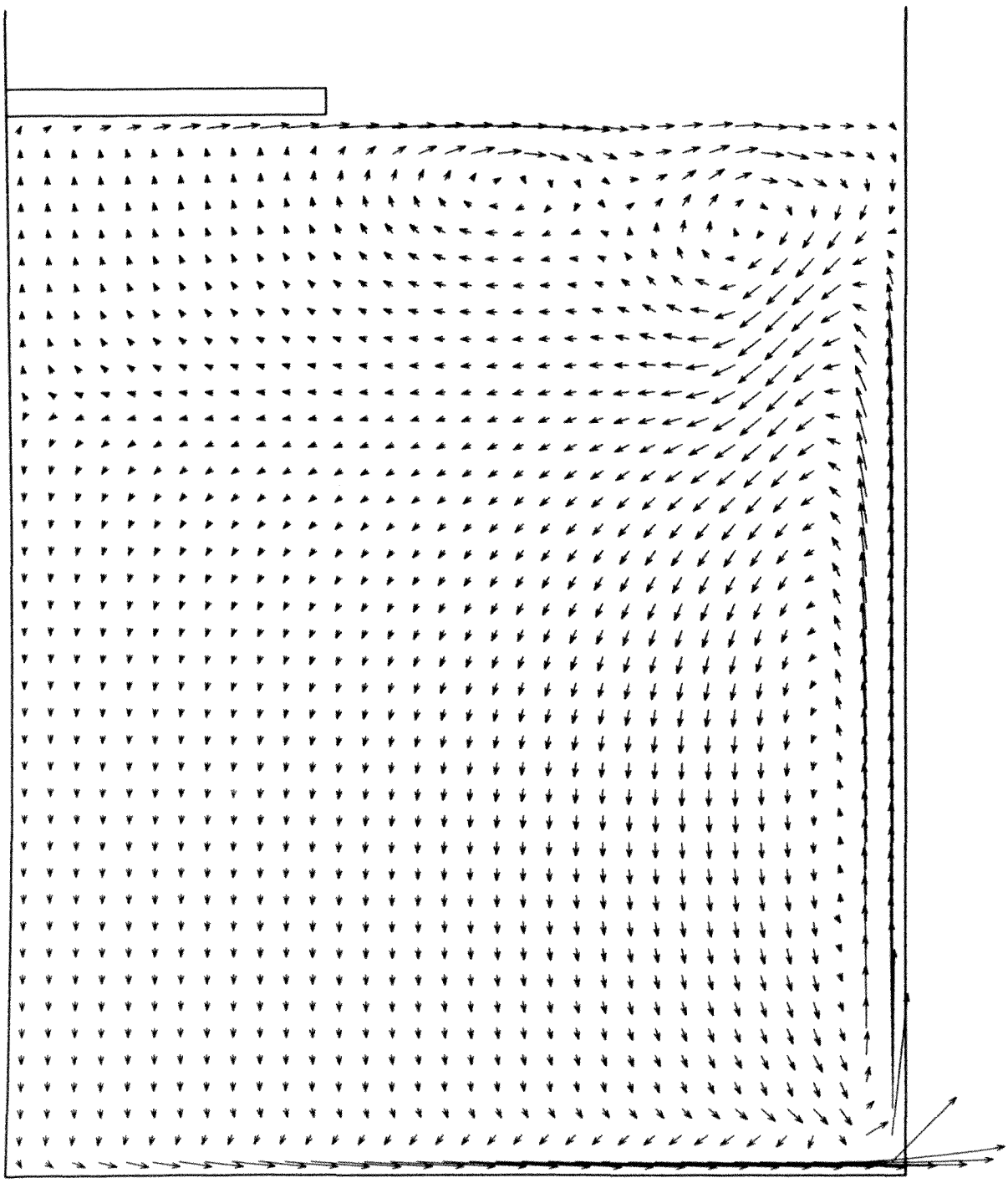

Fig. 22b : t = 15.0 s , v_{max} = 3.5EO cm/s

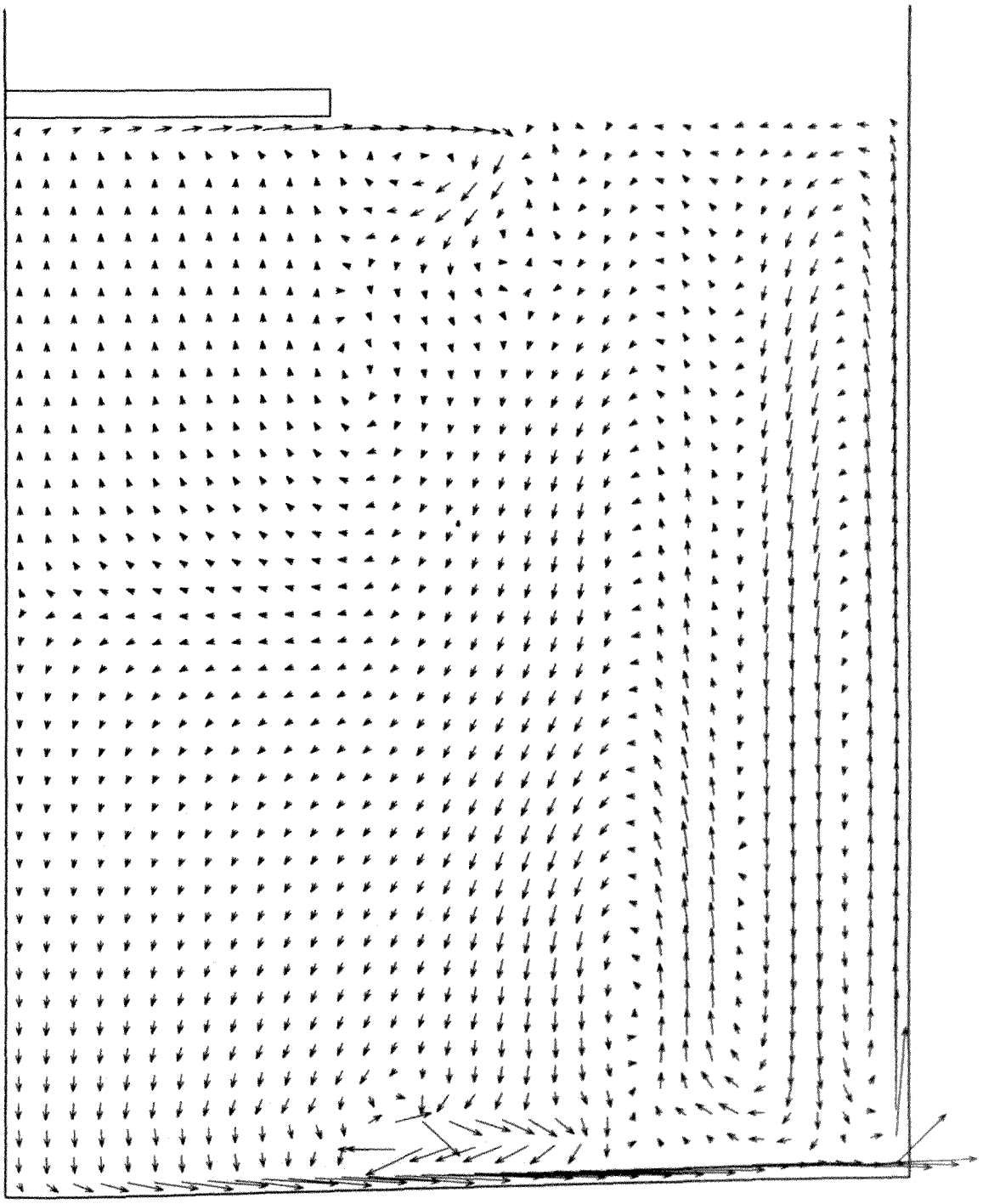

Fig. 22c : t = 20.0 s , v_{max} = 3.OEO cm/s

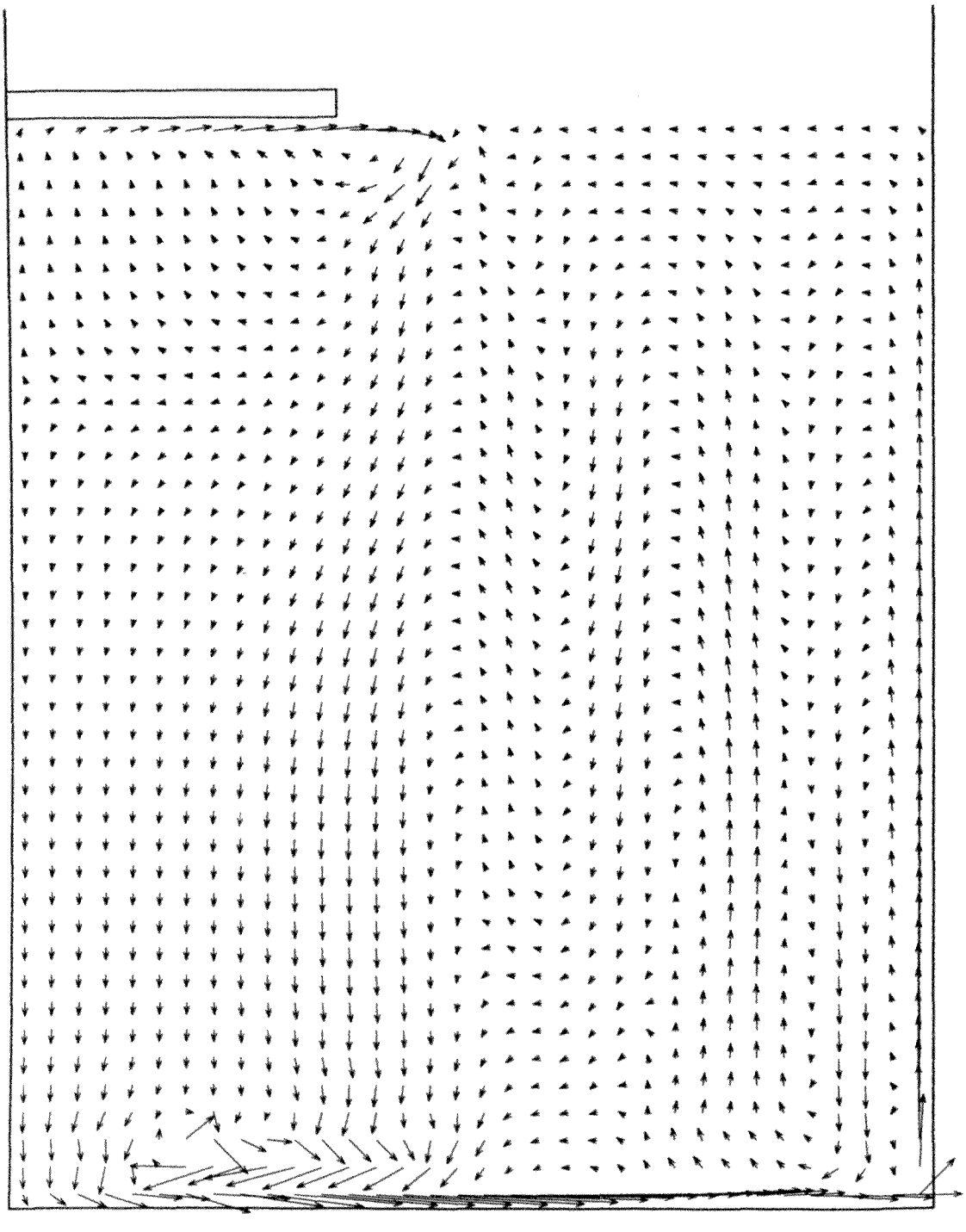

Fig. 22d : t = 21.0 s , v_{max} = 2.6EO cm/s

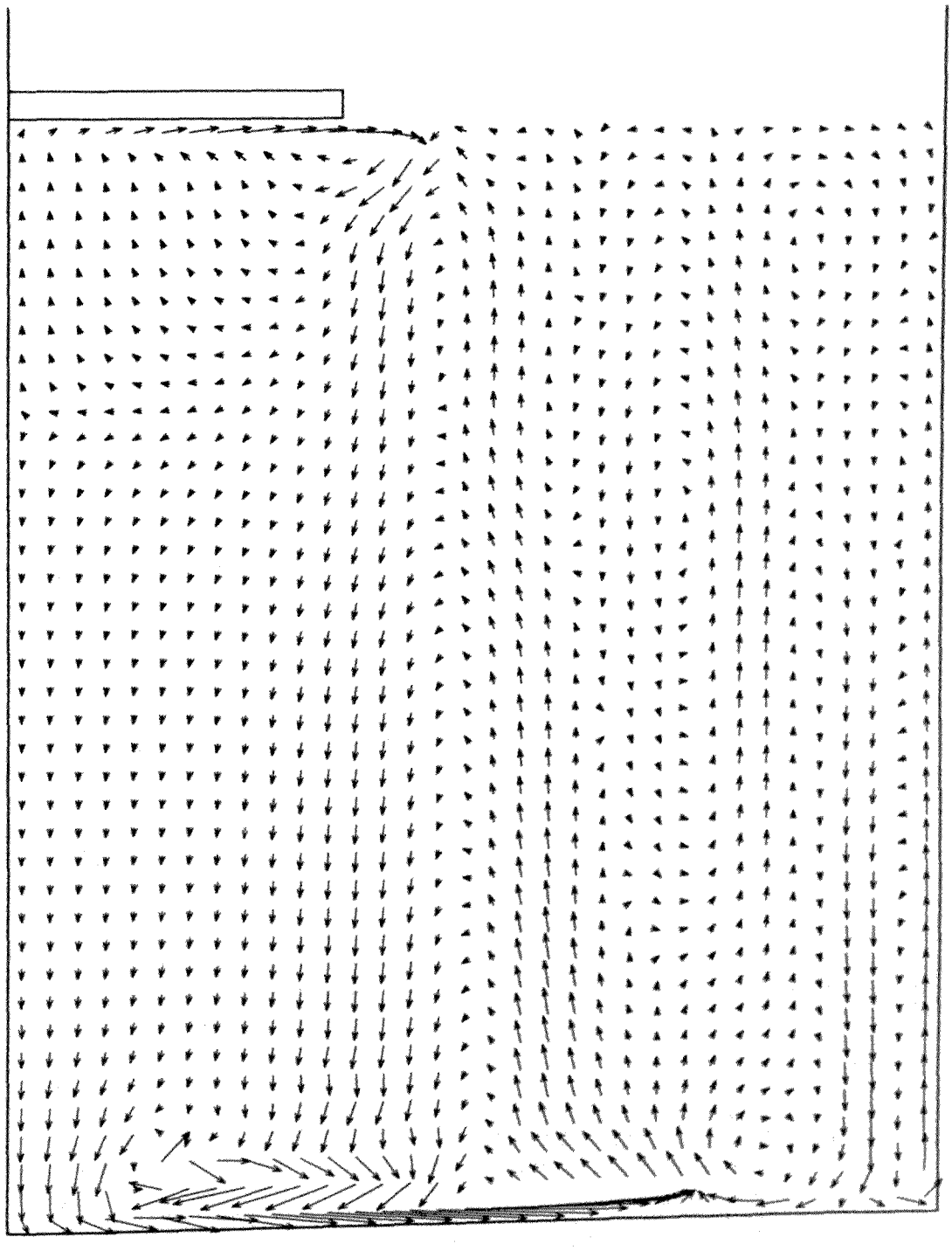

Fig. 22e : t = 25.0 s , v_{max} = 2.4E0 cm/s

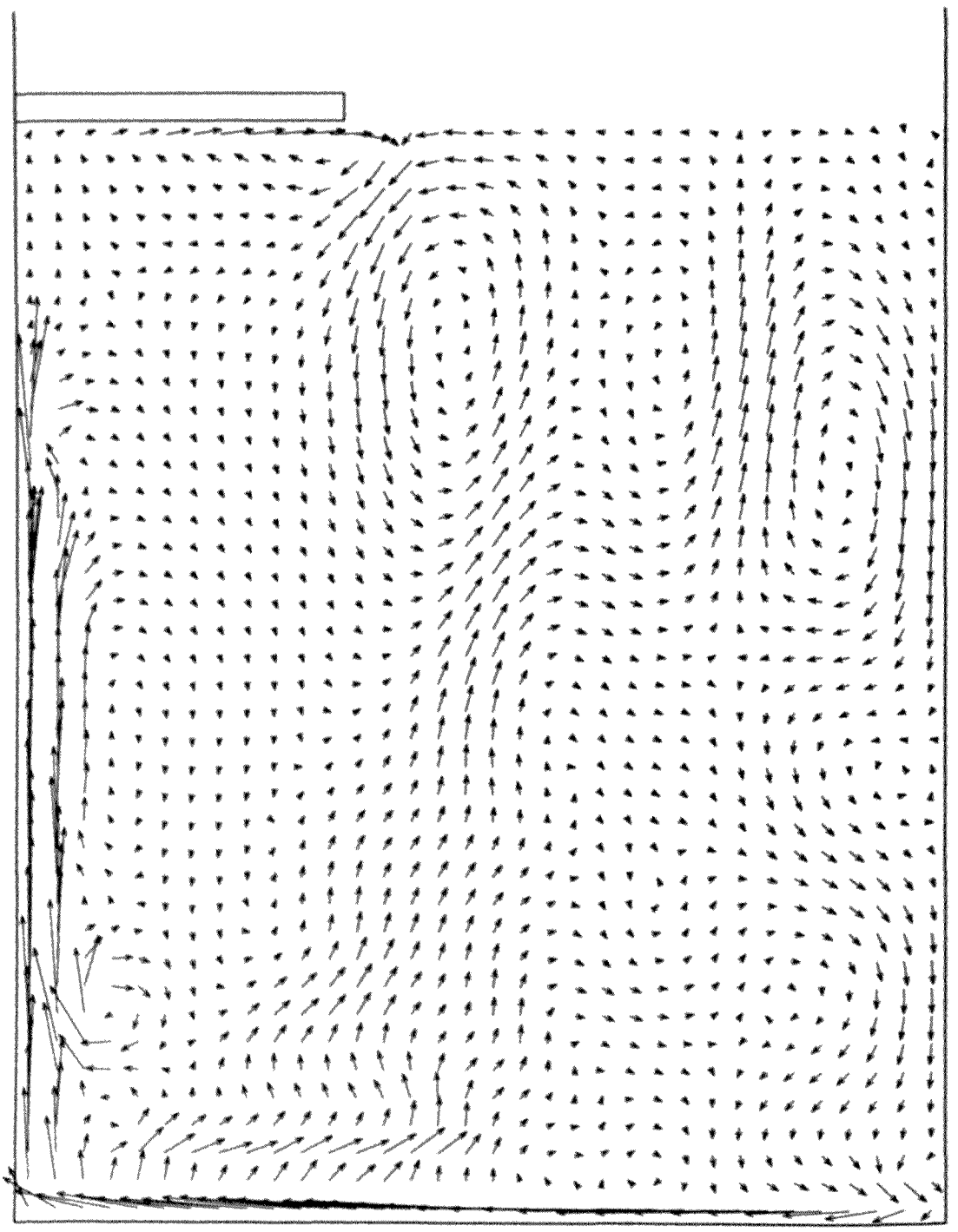

Fig. 22f : t = 35.0 s , v_{max} = 2.3E0 cm/s

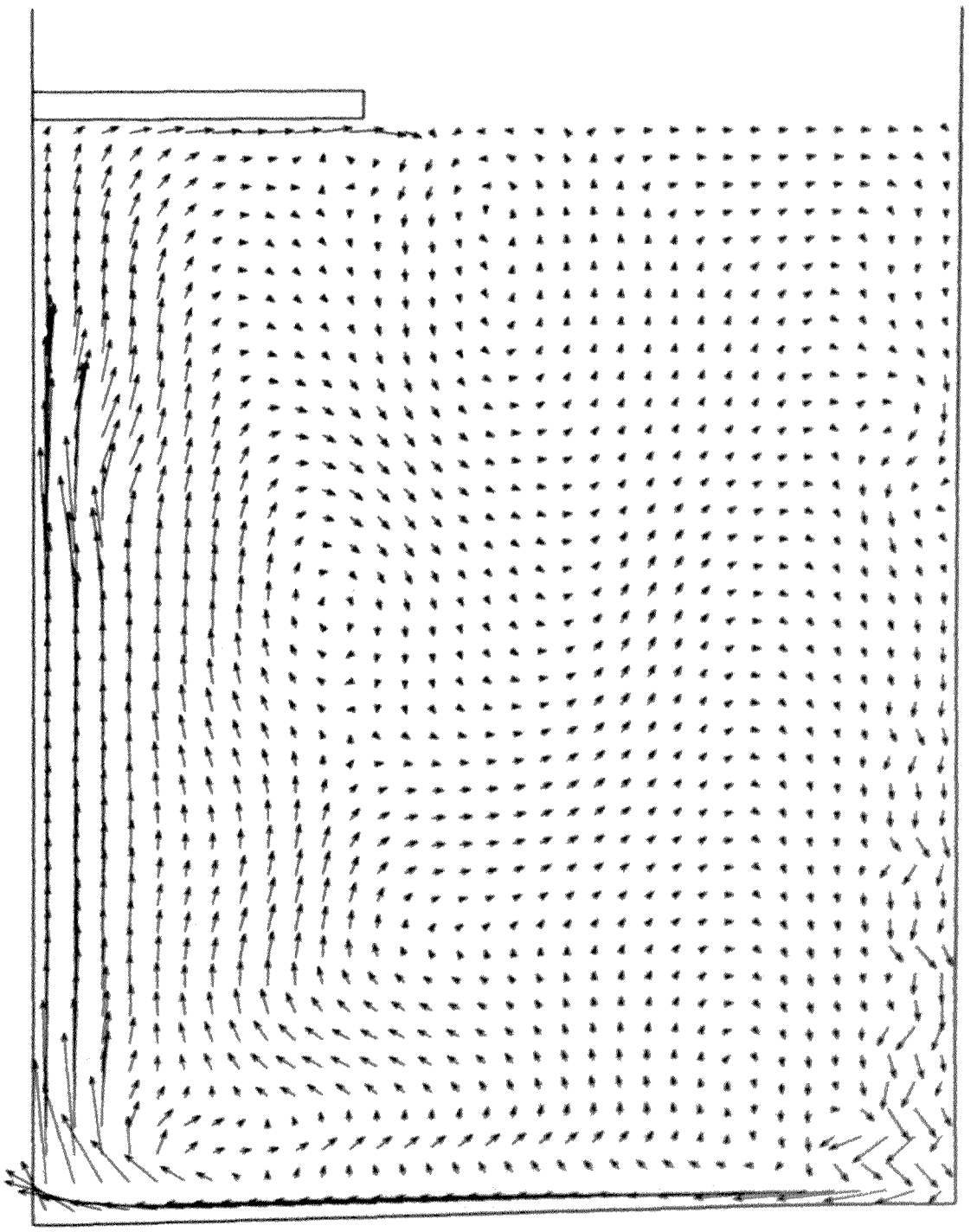

Fig. 22g : t = 40.0 s , v_{max} = 3.7E0 cm/s

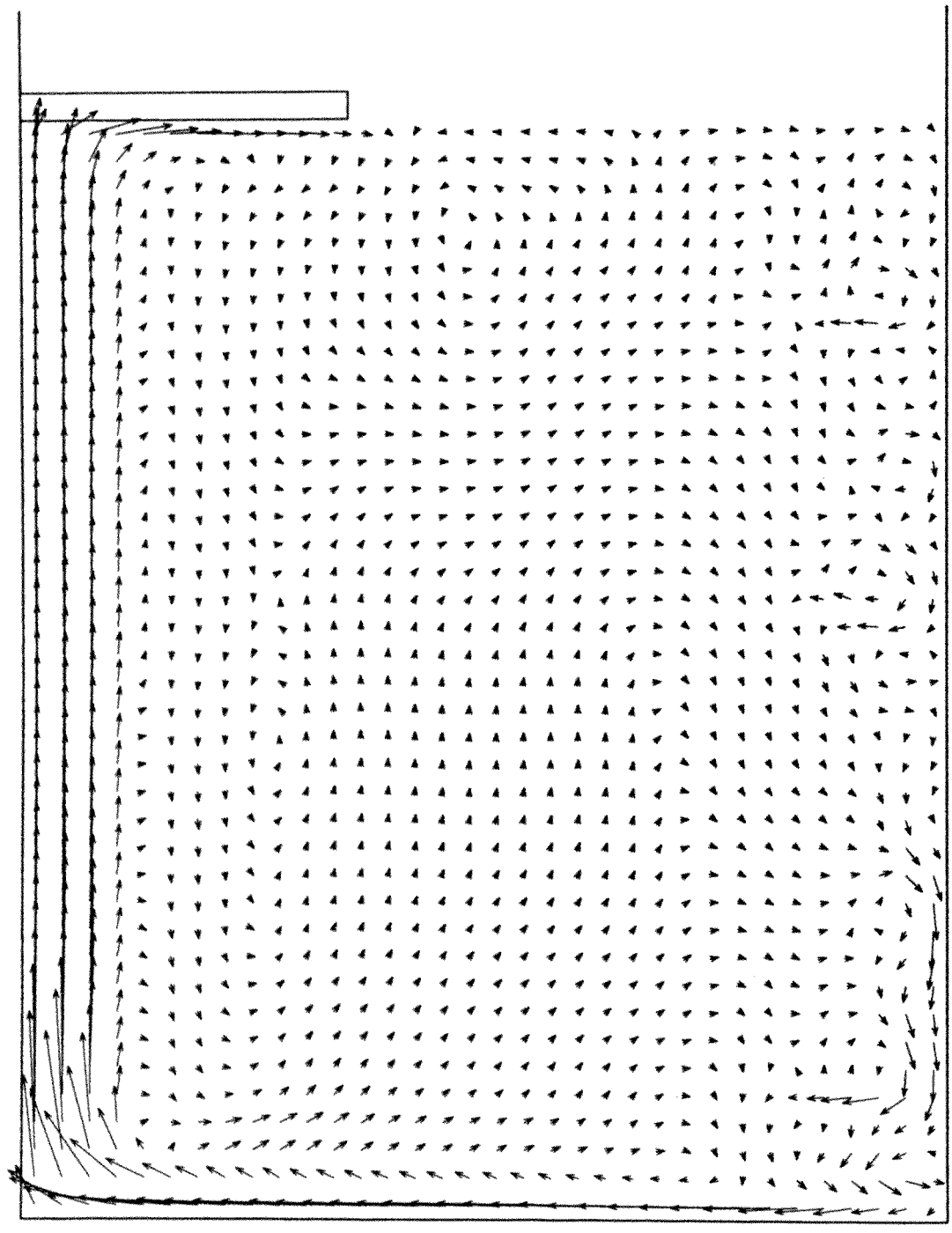

4. Conclusions

Within the scope of our present investigations of forced convection we should like to make the following inferences:

In the classical Czochralski crystal-growth process as well as in the ACRT arrangement and its application to the Czochralski method (CACRT), stagnation surfaces which prevent complete bulk liquid mixing in the crucible exist for most of the various angular velocities of the crystal and crucible commonly used in experiments. Practically speaking, non-mixing Taylor-Proudman cells are absent during the classical Czochralski crystal pulling only when the crucible rotation rate is very small compared to the crystal rotation rate. Especially, the present analysis has shown that the counter-rotational arrangement with crystal and crucible rotation of the same rate is the worst case in view of smooth stirring of the melt. Additionally, in practice one should pay more attention to the isorotational arrangement than up to now.

It should be pointed out that these statements are independent of the actual value of the kinematic viscosity of the liquid. Therefore the crystal grower has to be very careful in the selection of the various rotational rates.

ACRT has proved to be an effective method in order to achieve optimum stirring of the melt in the crucible. In the case of comparatively high kinematic viscosity, its application to the classical Czochralski method (CACRT) causes complete mixing of the melt only in the isorotational case when the non-mixing Taylor-Proudman cells vanish periodically, despite of

intuitive predictions which might have preferred the counter-rotational arrangement.

For low kinematic viscosity, however, CACRT seems to be an excellent technique in order to achieve total stirring of the melt independently of the relative rotational motion of crystal and crucible, as by all means the time period of acceleration and deceleration is much smaller than the transition time needed to reach the steady-state of the flow. Here the use of a relatively large time period for the alternation between acceleration and deceleration seems to be slightly preferable.

5. Outlook

Recently, we have started the simulation of free convective flow in the classical Czochralski crystal-growth process in order to study the flow patterns resulting from the superposition of free and forced convective fluid motion afterwards. Part 2 of this report will be concerned with these investigations.

Moreover, in the case of liquid copper, a detailed experimental analysis of the CACRT method based on the numerical results of the presented computer simulations is planned [1)].

Finally, as already mentioned before, we intend to investigate three-dimensional fluid flow, too, in order to examine whether there are similar non-axisymmetric flow patterns as described in [6].

---

1) A corresponding paper will appear in the near future.

6. References

[1] W.F. Ames, Nonlinear Partial Differential Equations in Engineering (Acad. Press, New York, 1963)

[2] A.A. Amsden and F.H. Harlow, The SMAC Method (Los Alamos Report LA-4370, 1970)

[3] J.R. Carruthers and K. Nassau, J. Appl. Phys. 39 (1968) 5205-5214

[4] R.K.-C. Chan and R.L. Street, J. Comput. Phys. 6 (1970) 68-94

[5] F.H. Harlow and J.E. Welch, The Physics of Fluids 8 (1965) 2182-2189

[6] R. Hide and C.W. Titman, J. Fluid Mech. 29 (1967) 39-60

[7] C.W. Hirt and J.P. Shannon, J. Comput. Phys. 2 (1968) 403-411

[8] N. Kobayashi and T. Arizumi, Japanese J. Appl. Phys. 9 (1970) 361-367

[9] N. Kobayashi and T. Arizumi, J. Crystal Growth 30 (1975) 177-184

[10] O.A. Ladyzhenskaya, The Mathematical Theory of Viscous Incompressible Flow (Gordon and Breach, New York, 1963)

[11] W.E. Langlois, J. Crystal Growth 42 (1977) 386-399

[12] W.E. Langlois and C.C. Shir, Computer Methods in Applied Mechanics and Engineering 12 (1977) 145-152

[13] B.D. Nichols and C.W. Hirt, J. Comput. Phys. 8 (1971) 434-448

[14] P.J. Roache, Computational Fluid Dynamics (Hermosa Publ., Albuquerque, N.M., 1972)

[15] H.J. Scheel, J. Crystal Growth 13/14 (1972) 560-565

[16] H.J. Scheel and H. Müller-Krumbhaar, J. Crystal Growth 49 (1980) 291-296

[17] H.J. Scheel and E.O. Schulz-Dubois, J. Crystal Growth 8 (1971) 304-306

[18] E.O. Schulz-Dubois, J. Crystal Growth 12 (1972) 81-87

[19] J.E. Welch and F.H. Harlow (et al.), The MAC Method (Los Alamos Report LA-3425, 1966)

[20] G.P. Williams, J. Fluid Mech. 37 (1969) 727-750

7. Appendix

The table below describes the following figures of this appendix:

Fig. No.	Analogue to Fig. No.	Arrangement of the Model	Description in the Text
23a-k	9,18a-k	ACRT	section 3.1.2 and 3.2.2 p. 31 and p. 75
24a-g	1o,19a-g	CACRT	section 3.1.3 and 3.2.3 pp. 31-33 and p. 87
25a-g	11,2oa-f	CACRT	section 3.1.3 and 3.2.3 pp. 31-33 and p. 87
26a-g	21a-g	CACRT	section 3.1.3 and 3.2.3 p. 33 and p. 87
27a-g	22a-g	CACRT	section 3.1.3 and 3.2.3 p. 33 and p. 87

Fig. 23a : t = 5.0 s , v_{max} = 1.8E0 cm/s

NUE : 0.06 cm^2/s

CRUCIBLE ROTATION : 20 : 0 rpm

TIME PERIOD : 10 s

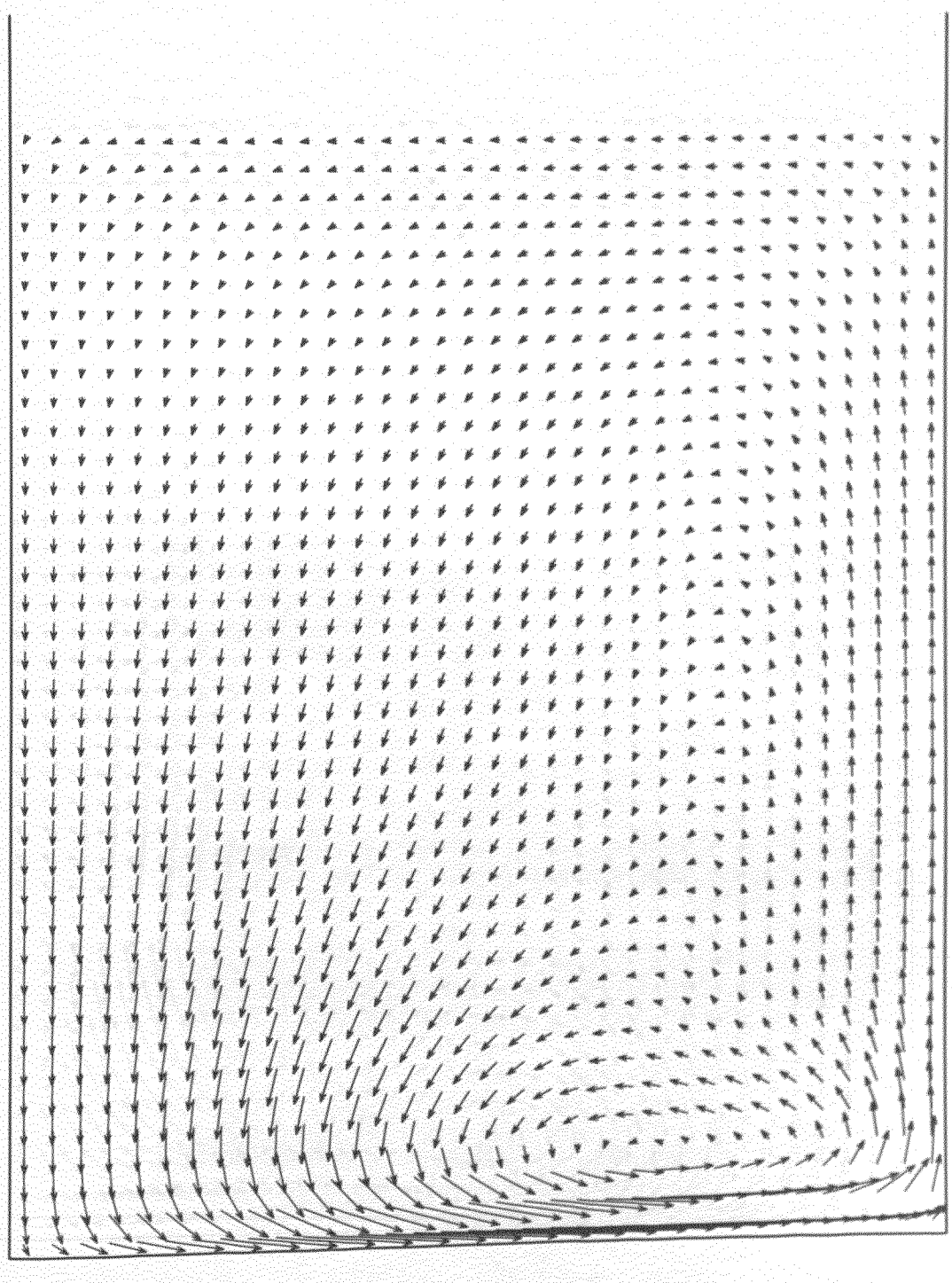

Fig. 23b : t = 10.0 s , v_{max} = 5.9E-1 cm/s

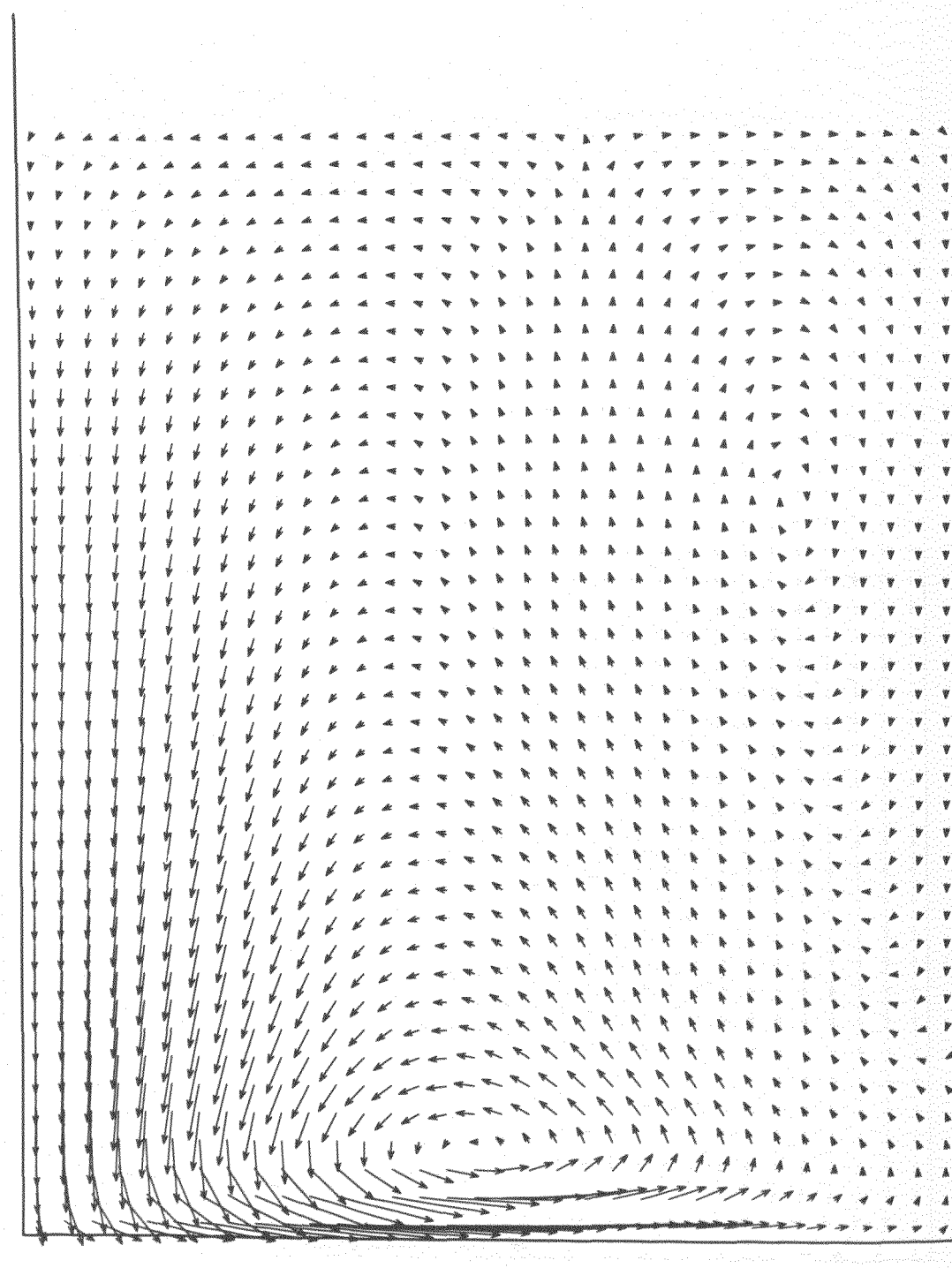

Fig. 23c : t = 11.0 s , v_{max} = 3.4E0 cm/s

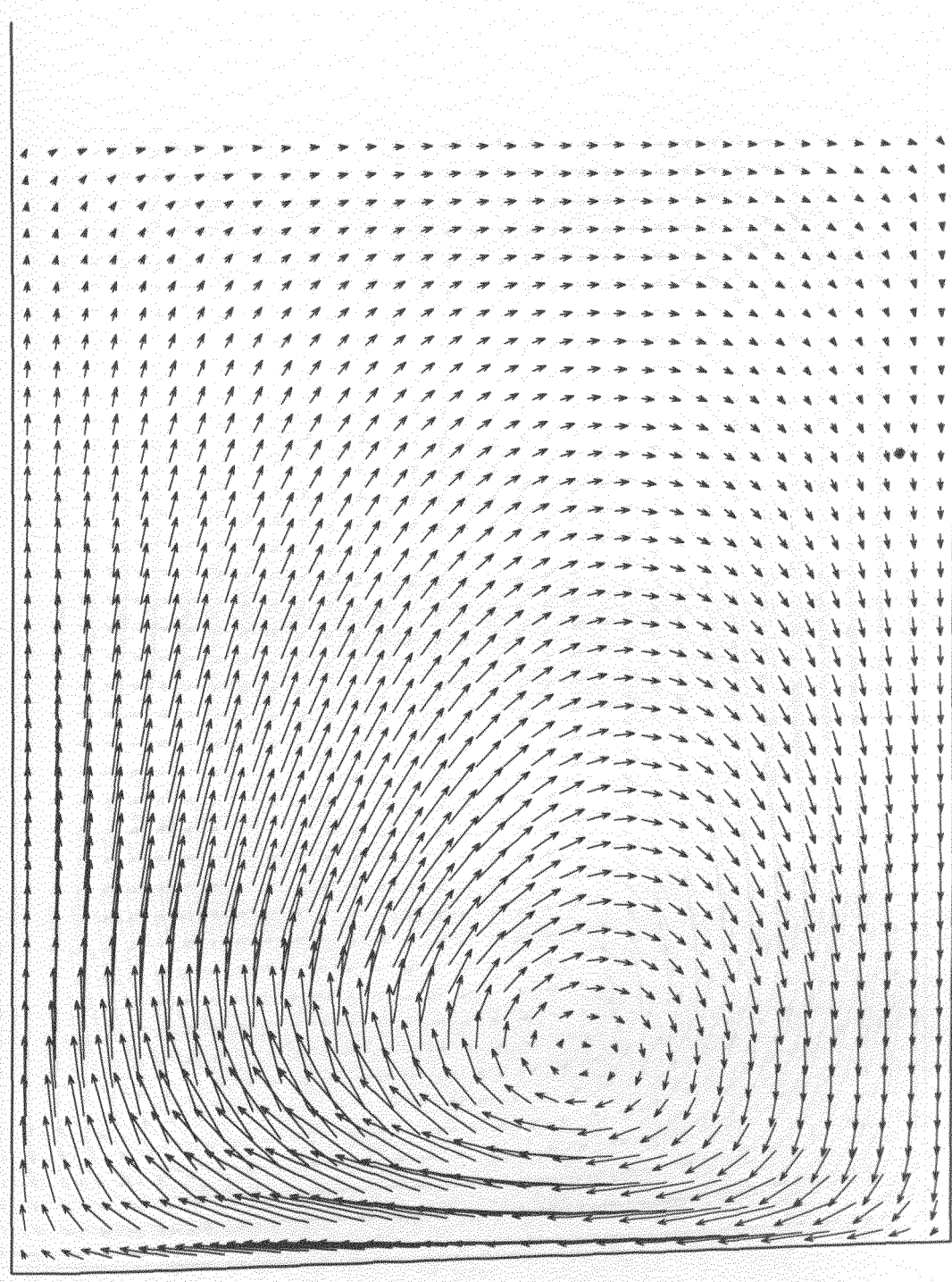

Fig. 23d : t = 15.0 s , v_{max} = 2.5EO cm/s

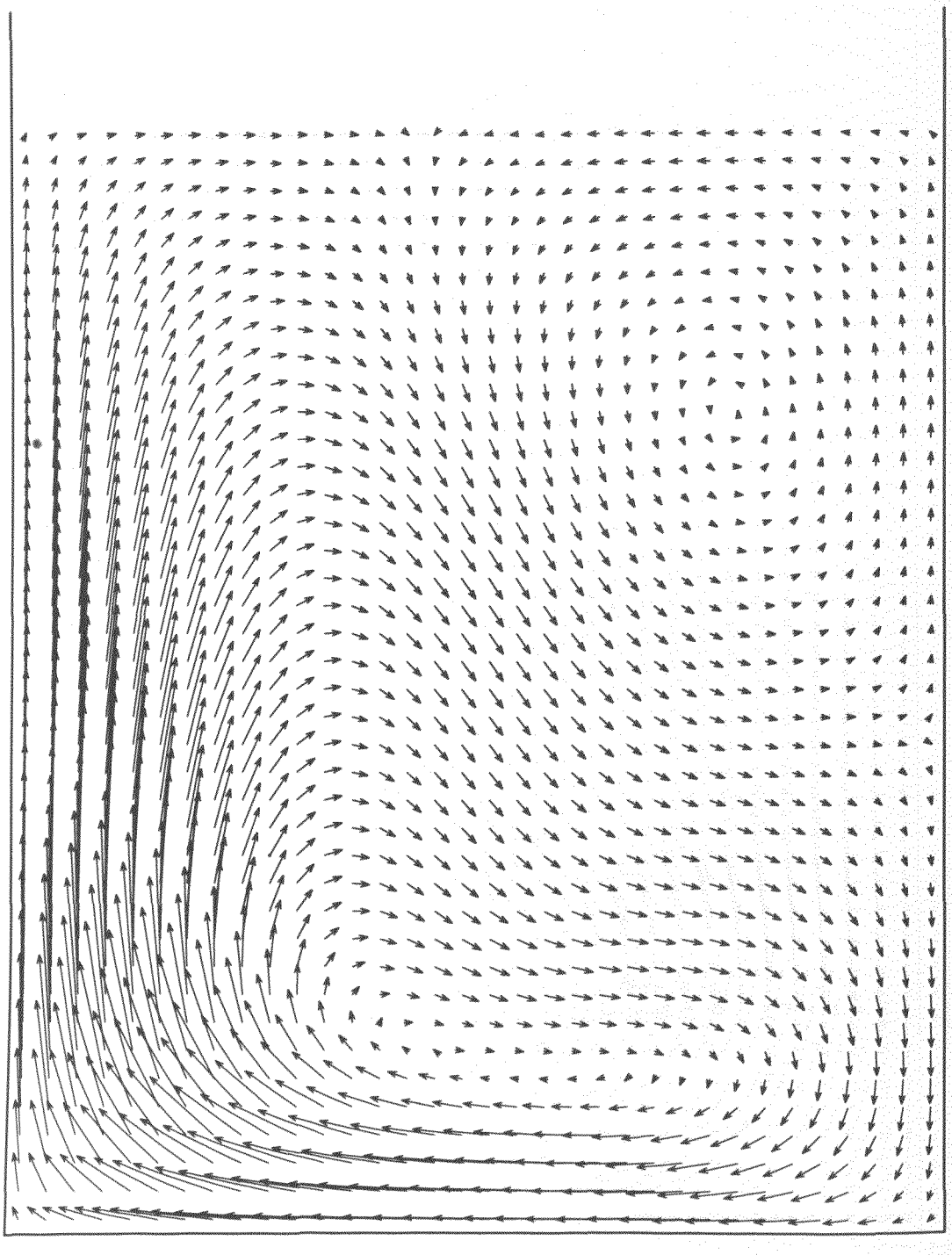

Fig. 23e : t = 20.0 s , v_{max} = 9.9E-1 cm/s

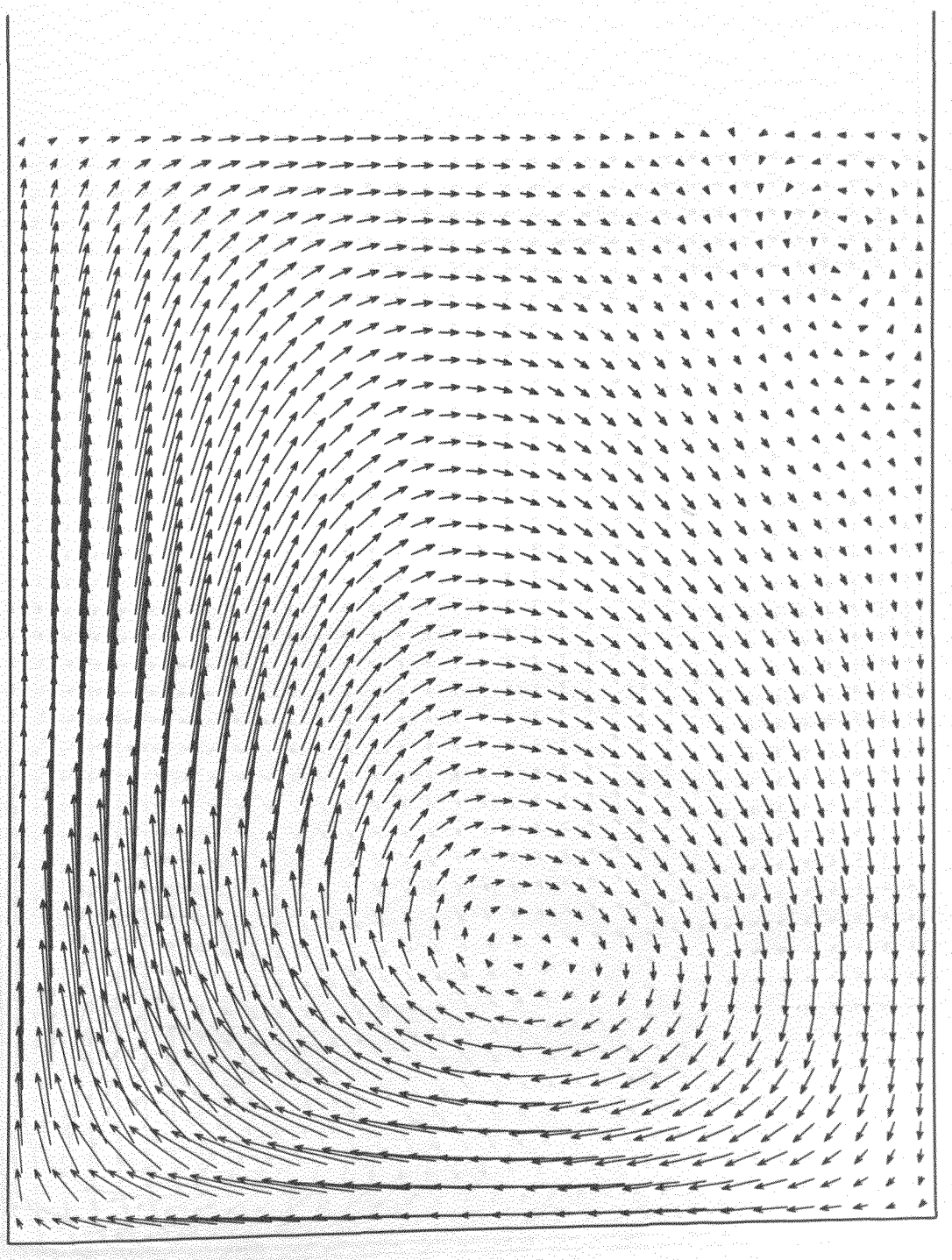

Fig. 23f : t = 21.0 s , v_{max} = 2.8EO cm/s

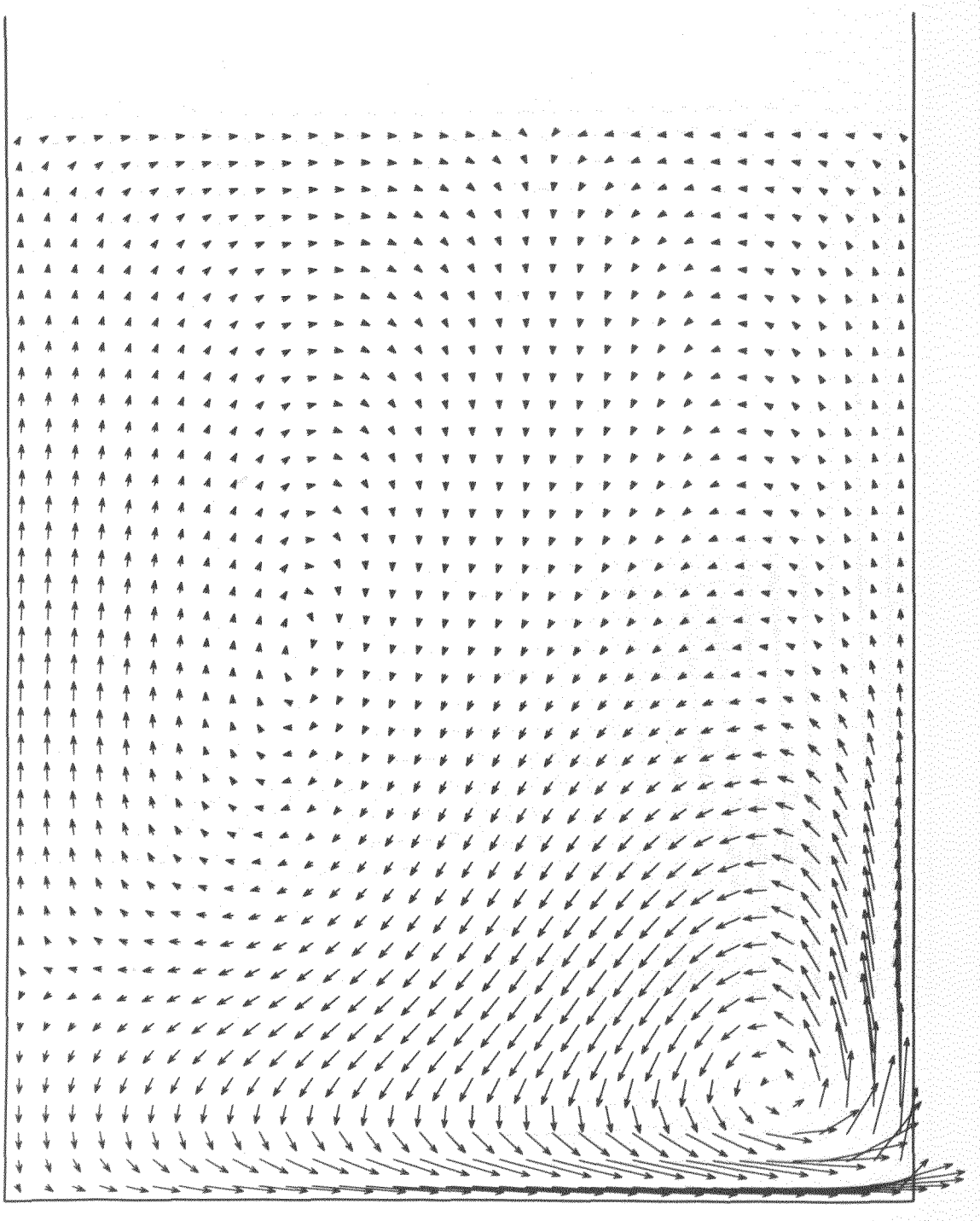

Fig. 23g : t = 25.0 s , v_{max} = 1.6EO cm/s

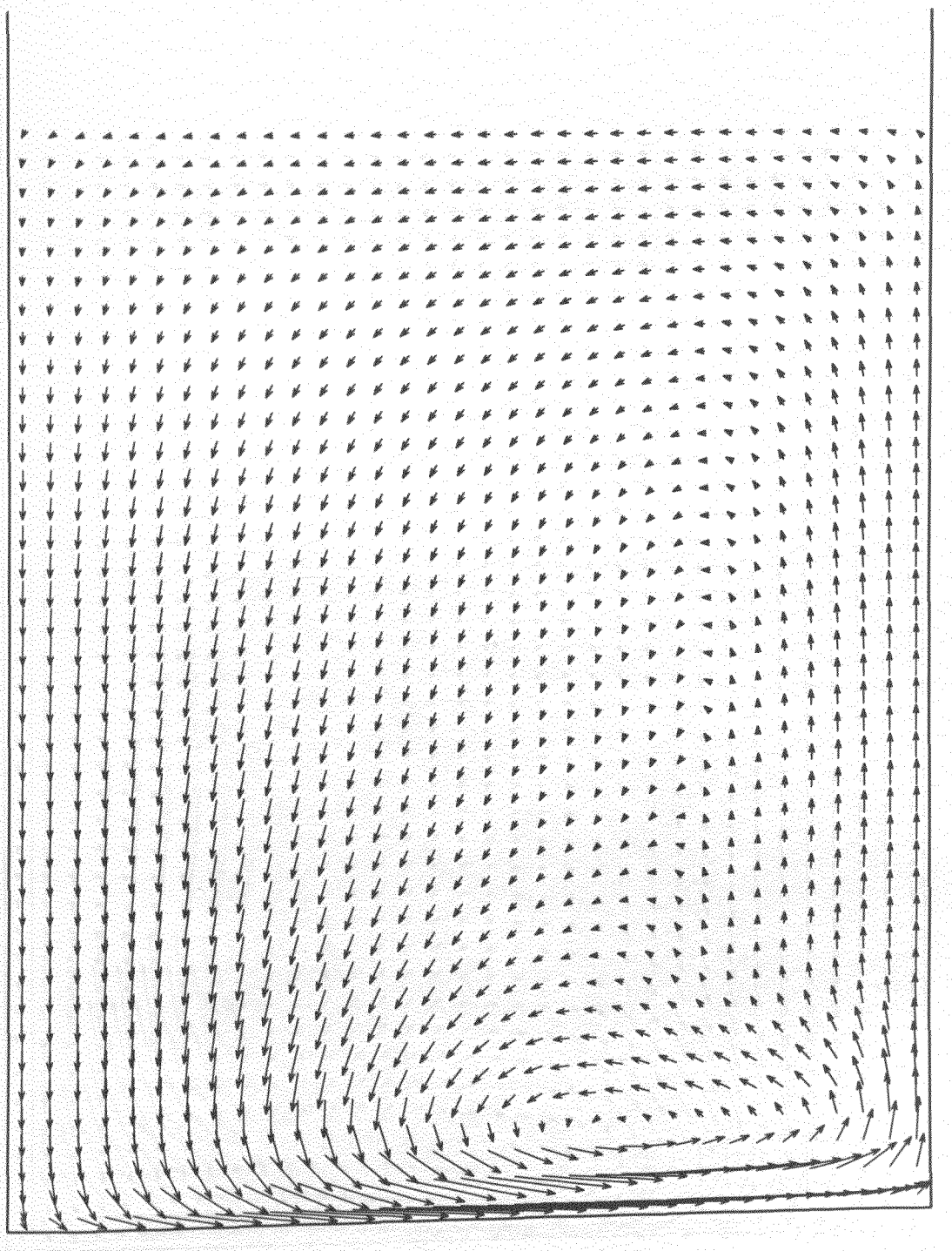

Fig. 23h : t = 30.0 s , v_{max} = 4.1E-1 cm/s

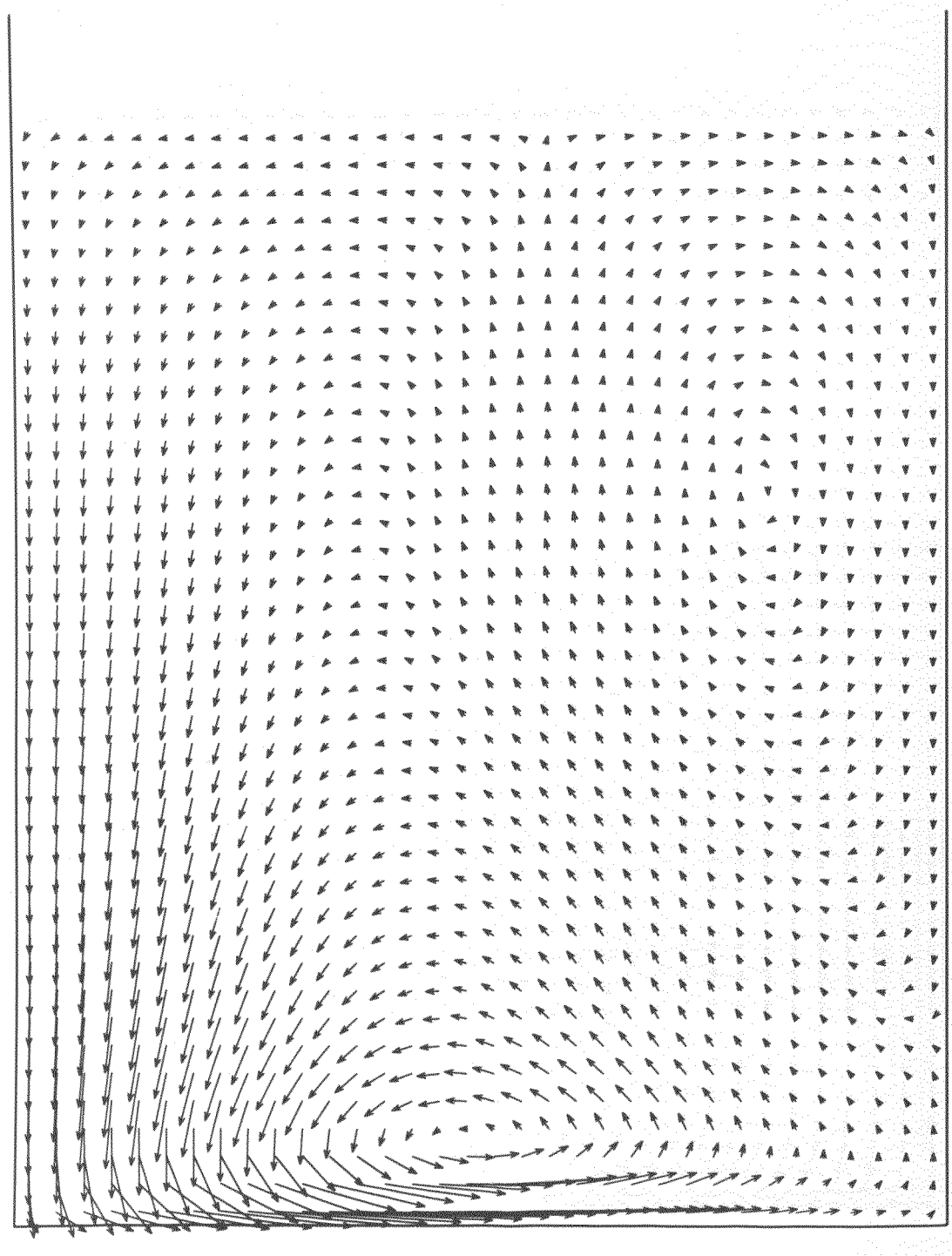

Fig. 23i : t = 31.0 s , v_{max} = 3.4E0 cm/s

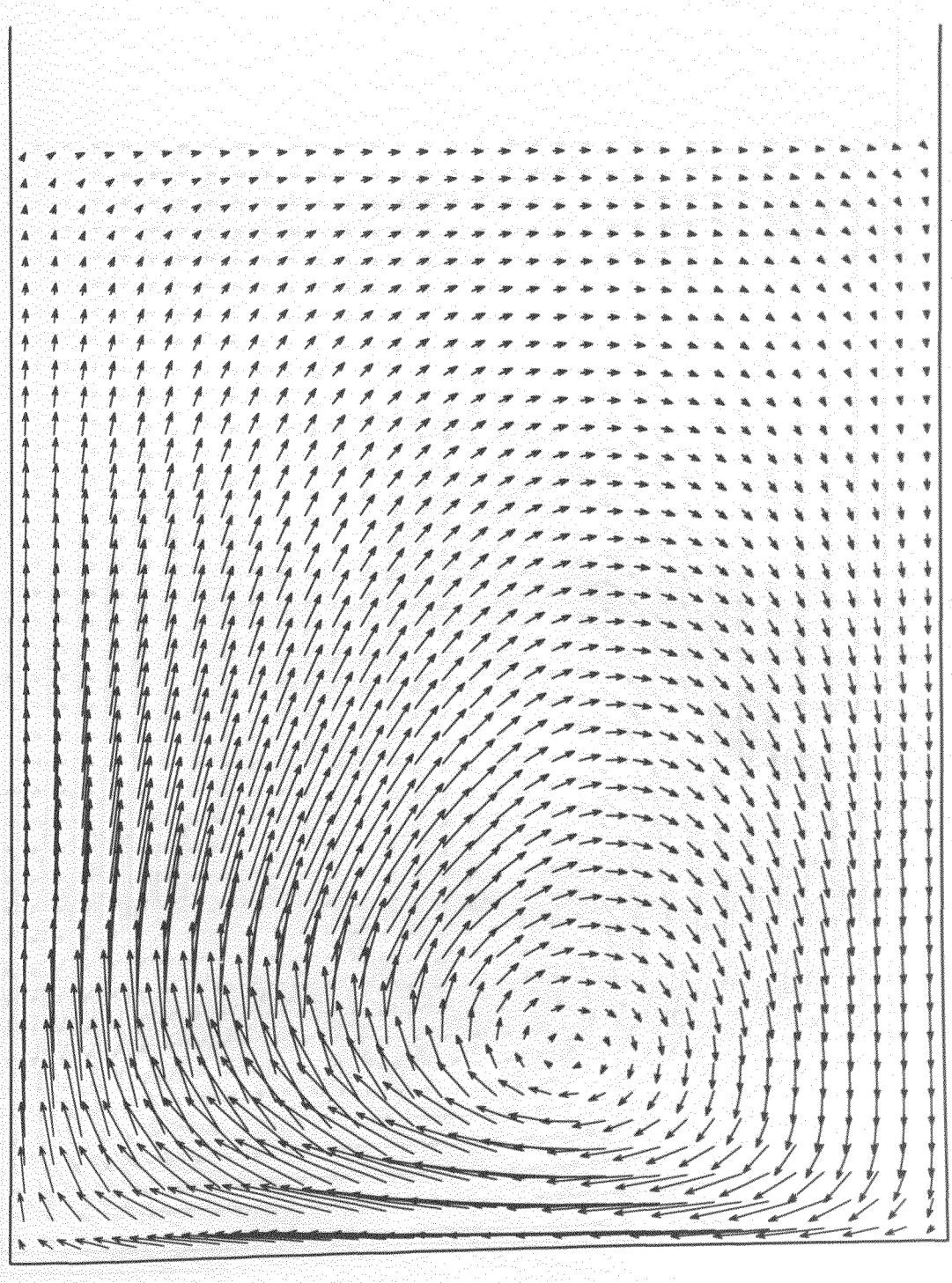

Fig. 23j : t = 35.0 s , v_{max} = 2.6E0 cm/s

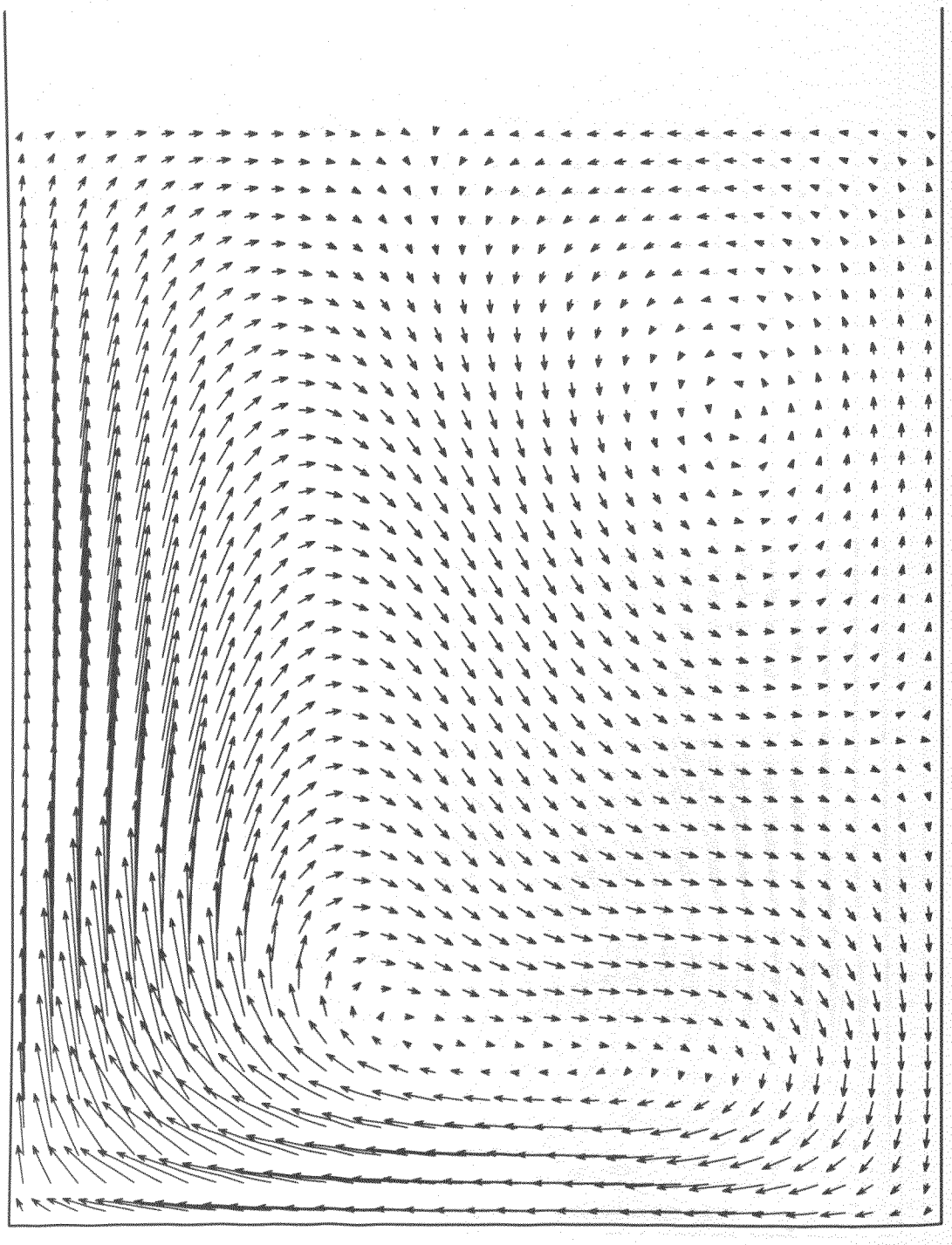

Fig. 23k : t = 40.0 s , v_{max} = 1.0E0 cm/s

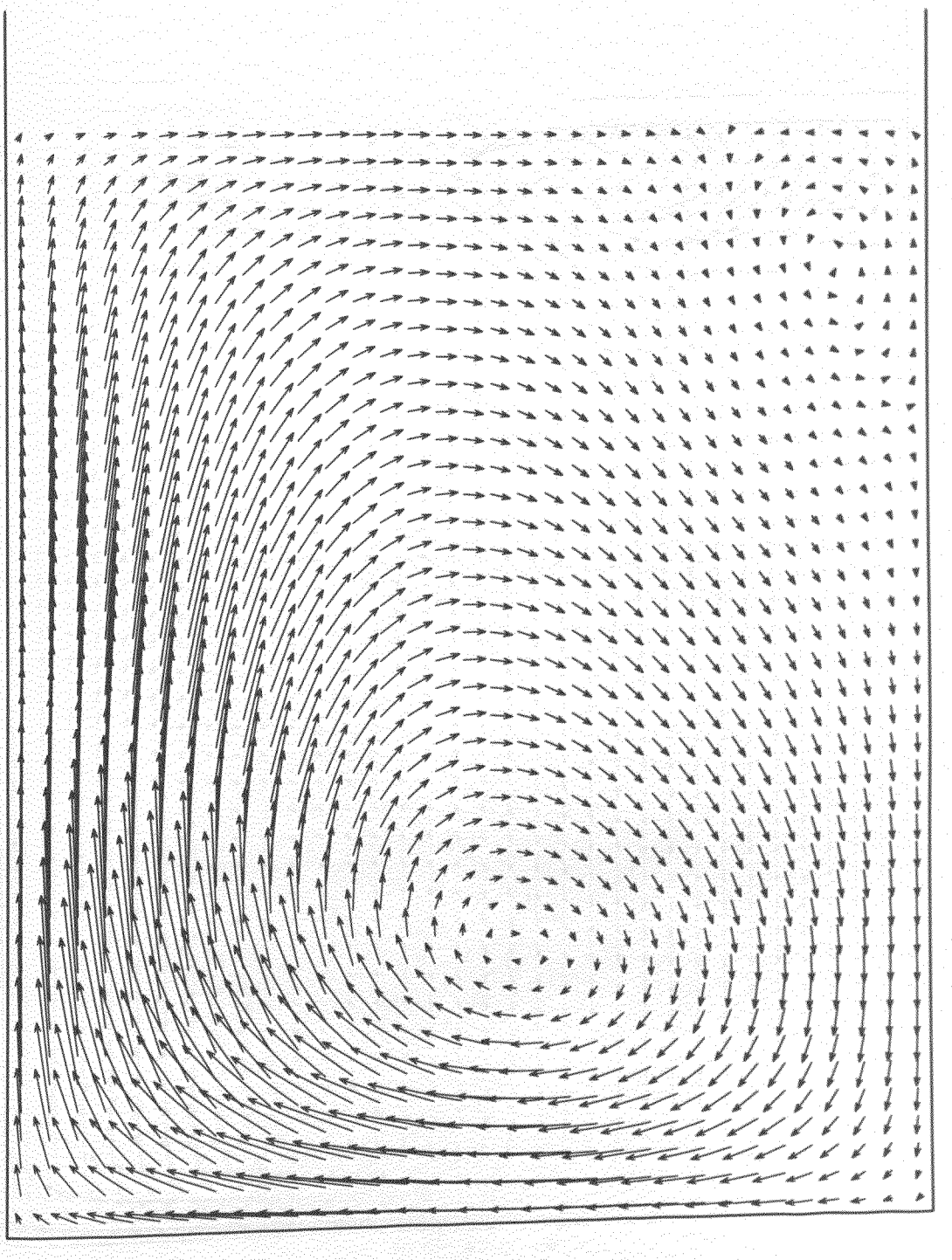

Fig. 24a : t = 10.0 s , v_{max} = 2.4E0 cm/s

NUE :	0.06 cm^2/s	
CRUCIBLE ROTATION :	10 :	30 rpm
CRYSTAL ROTATION :	-40 :	-80 rpm
TIME PERIOD :	10 s	

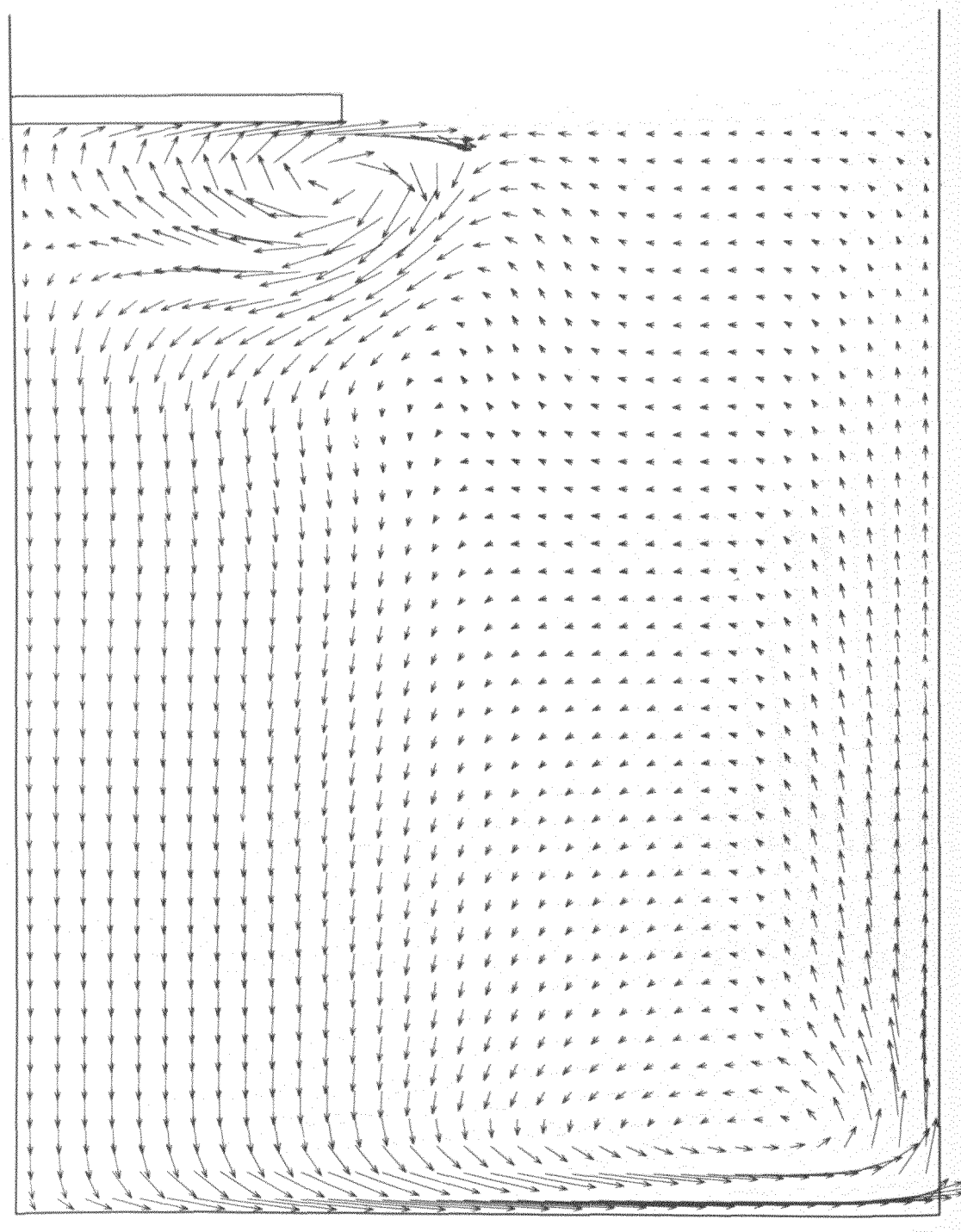

Fig. 24b : t = 11.0 s , v_{max} = 1.7E0 cm/s

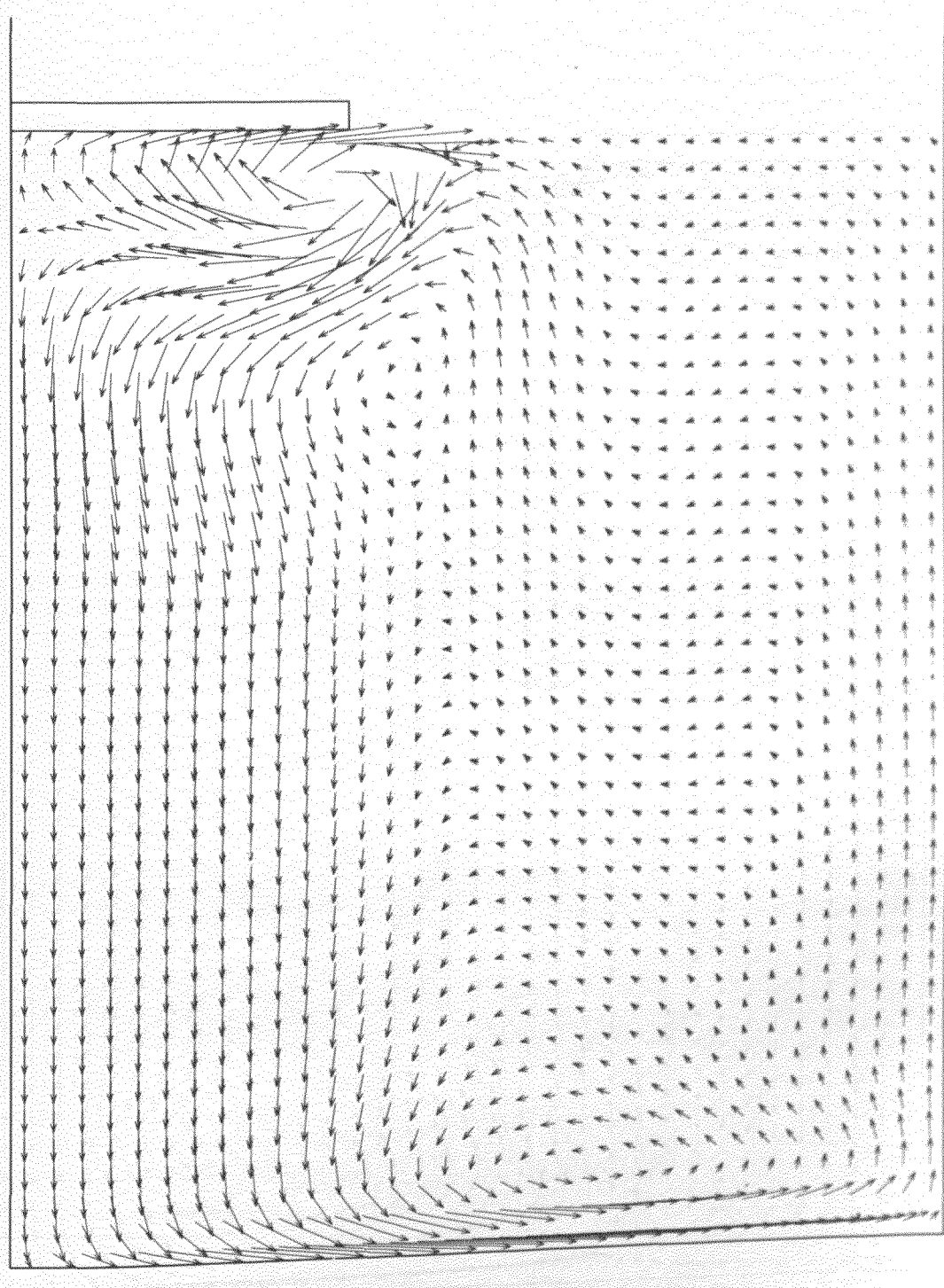

Fig. 24c : t = 15.0 s , v_{max} = 1.5E0 cm/s

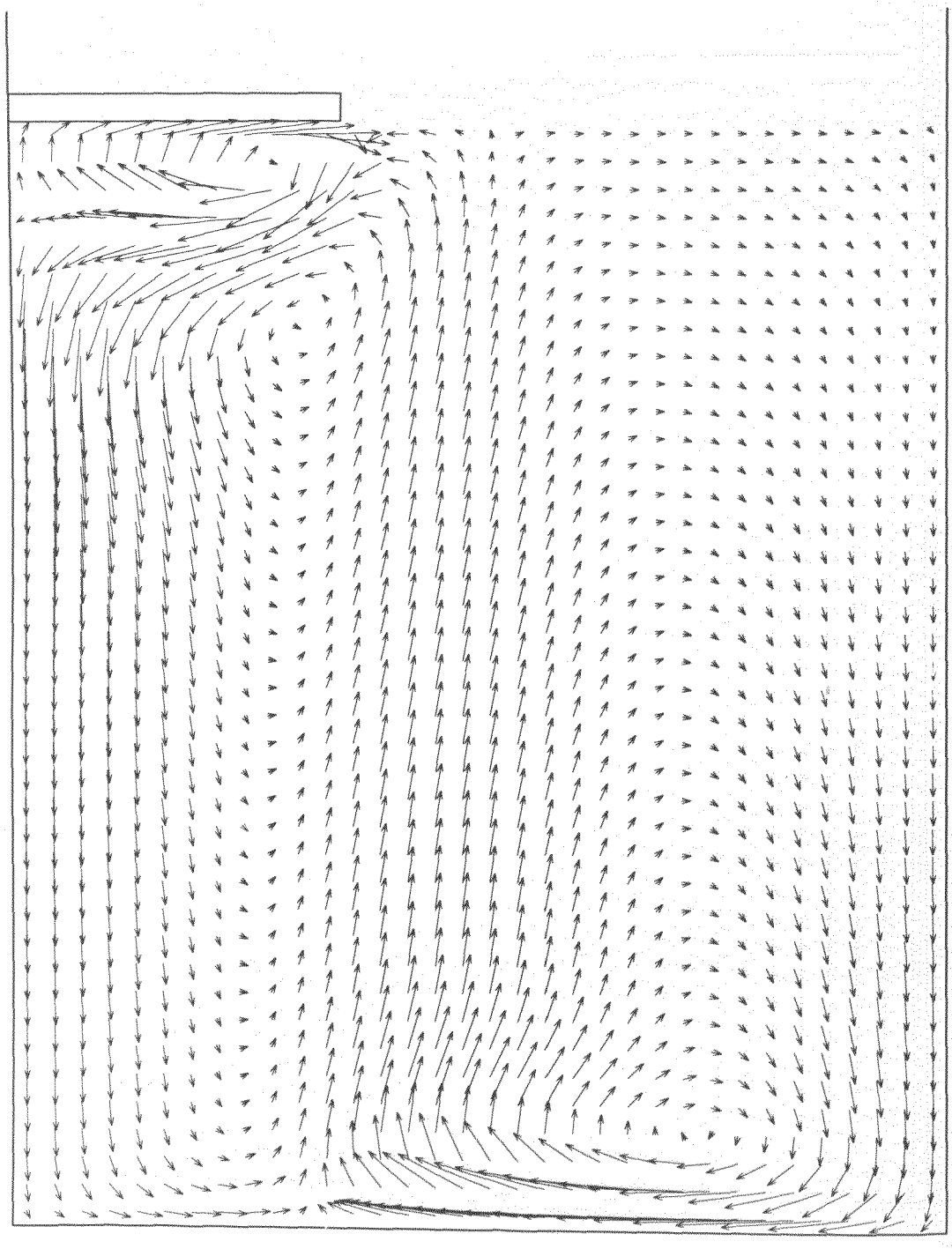

Fig. 24d : t = 20.0 s , v_{max} = 1.6E0 cm/s

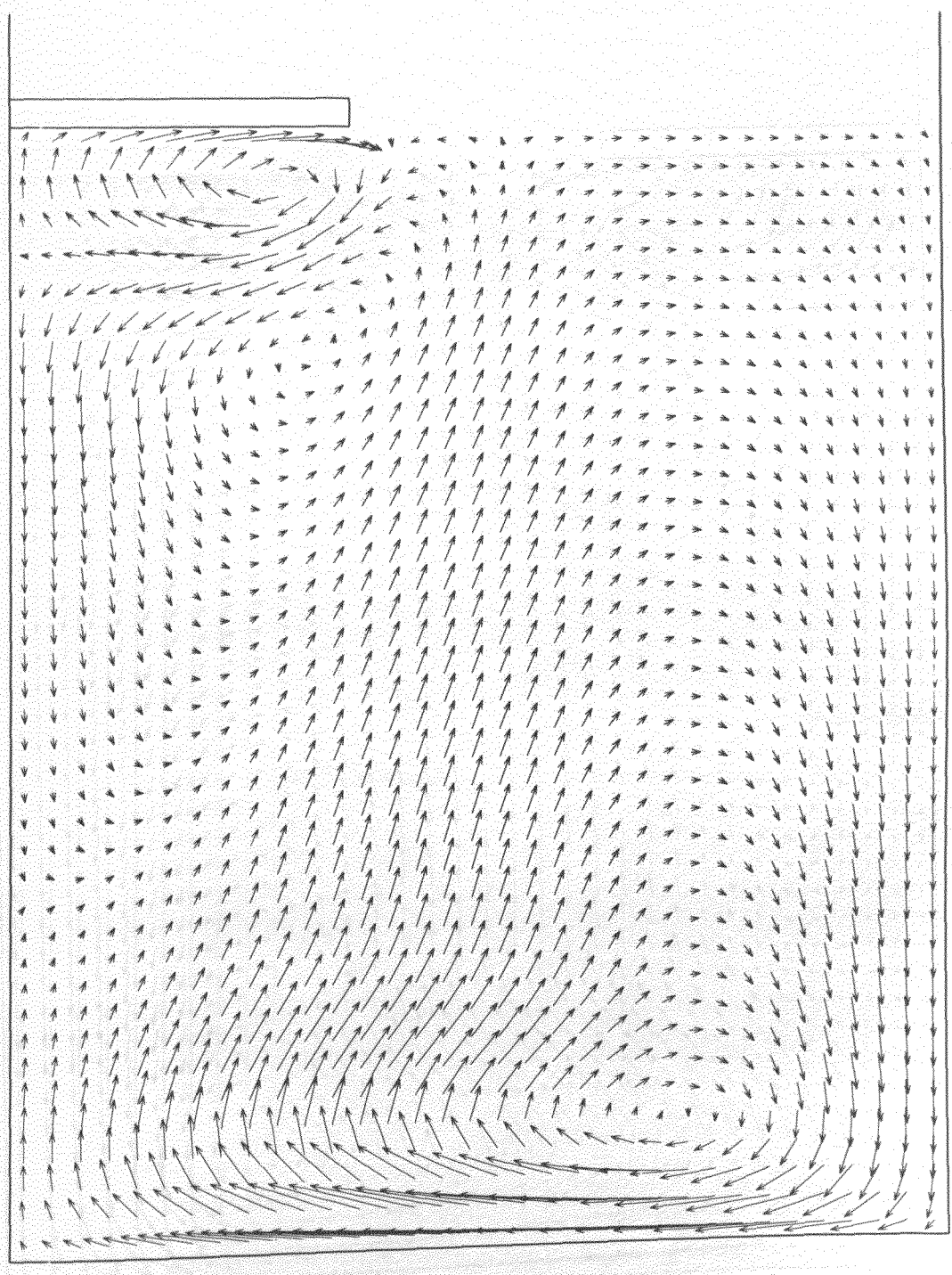

Fig. 24e : t = 21.0 s , v_{max} = 1.1E0 cm/s

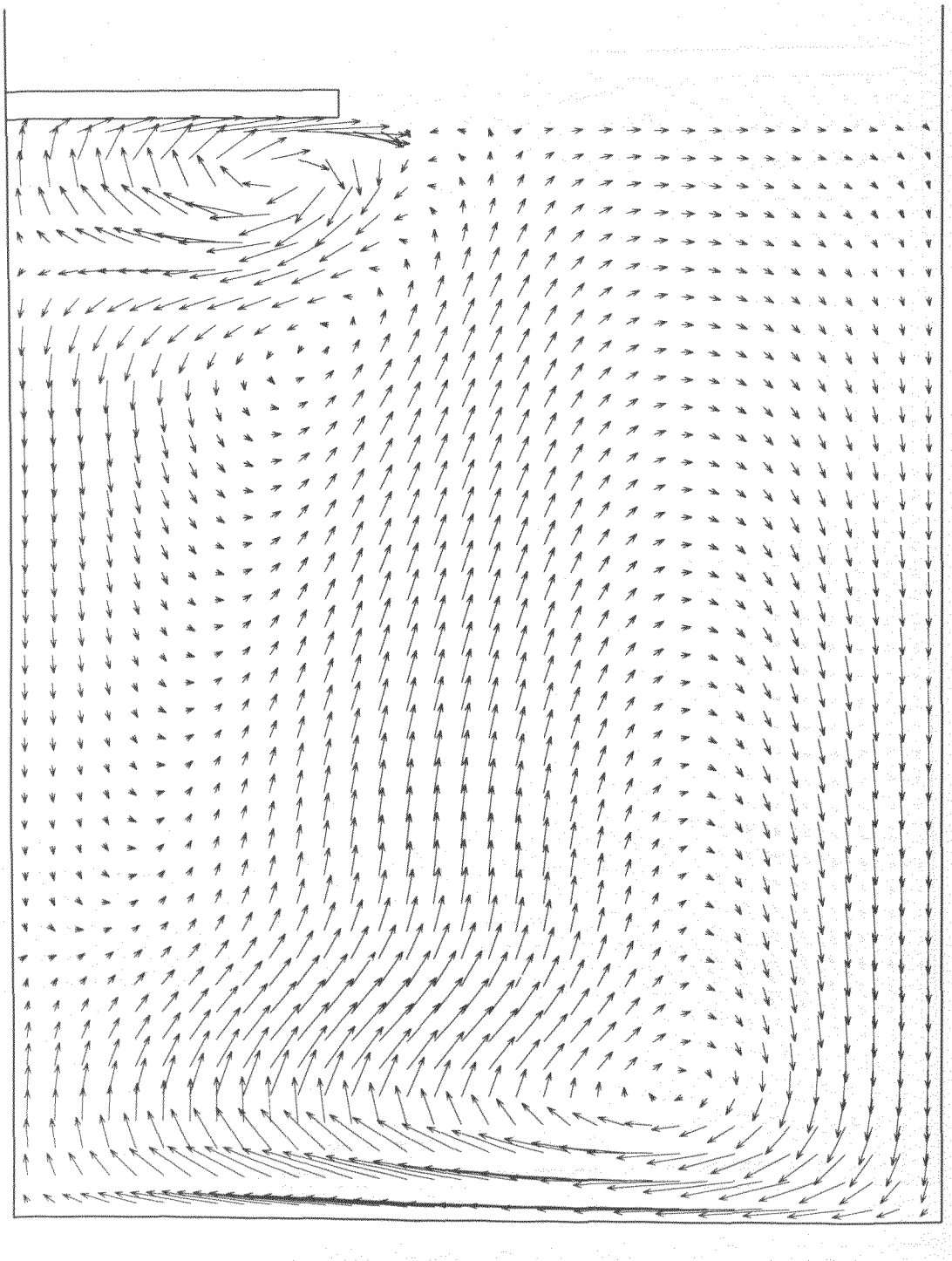

Fig. 24f : t = 25.0 s , v_{max} = 1.5E0 cm/s

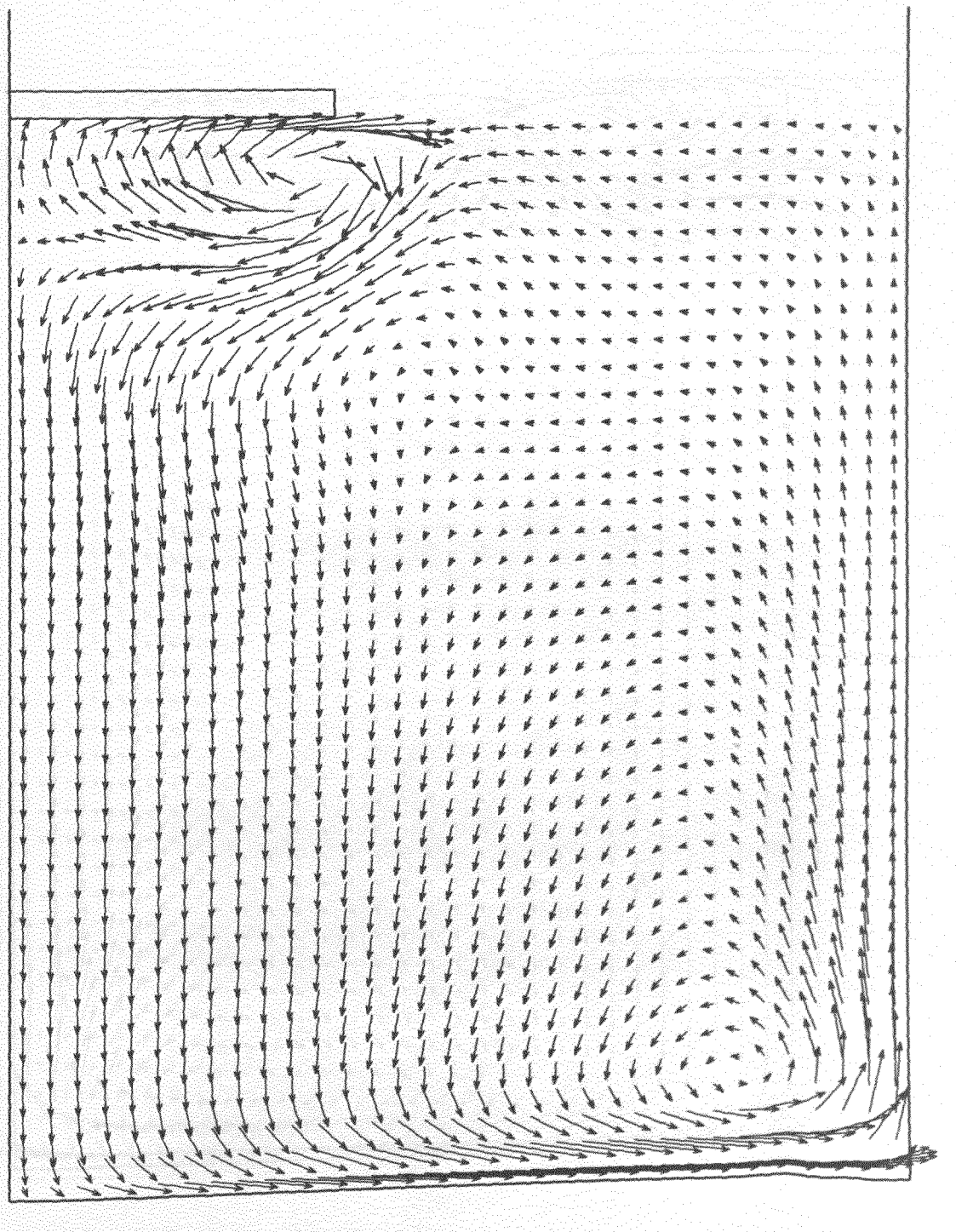

Fig. 24g : t = 30.0 s , v_{max} = 2.0E0 cm/s

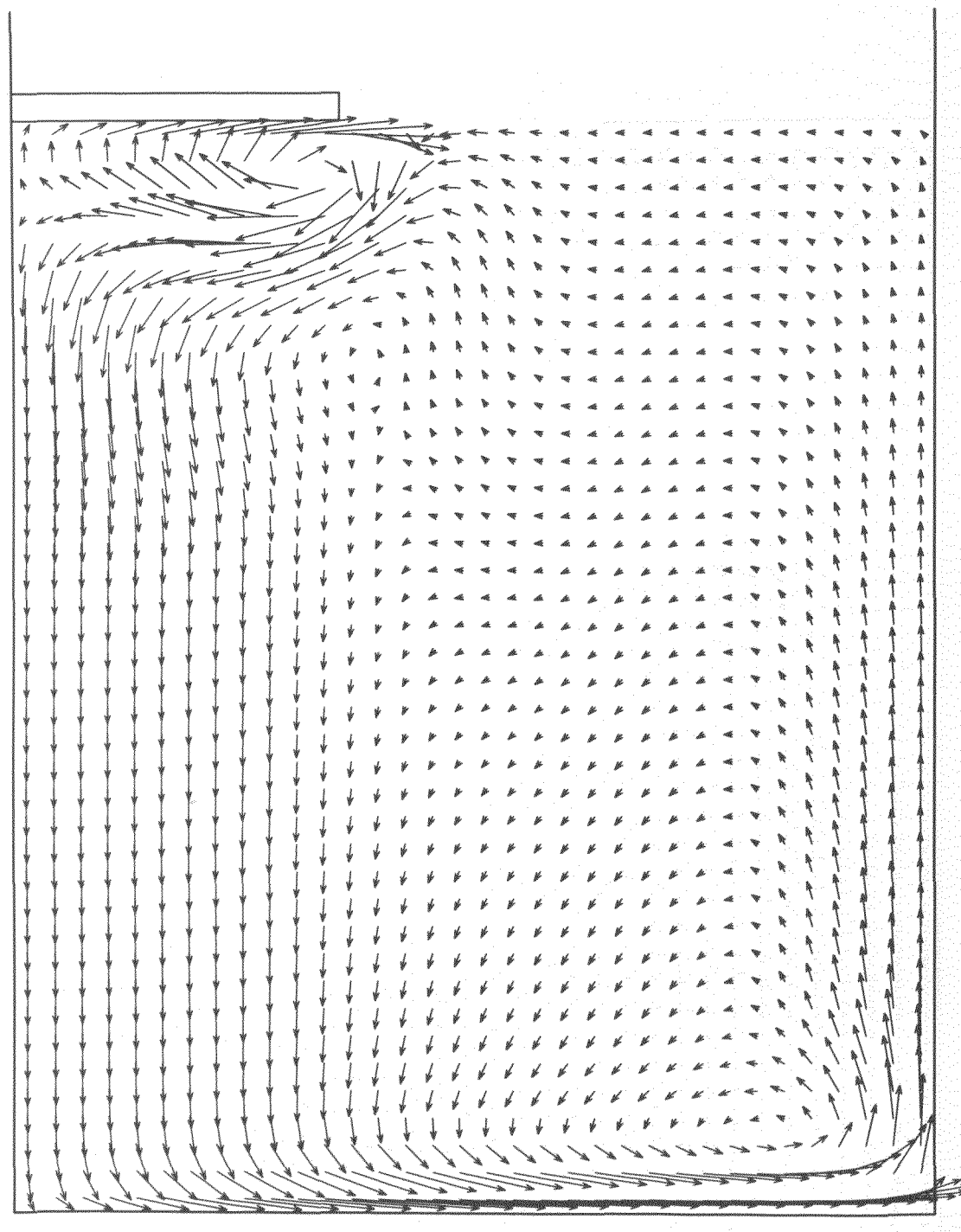

Fig. 25a : t = 10.0 s , v_{max} = 2.0E0 cm/s

NUE :	0.06 cm^2/s
CRUCIBLE ROTATION :	10 : 30 rpm
CRYSTAL ROTATION :	40 : 80 rpm
TIME PERIOD :	10 s

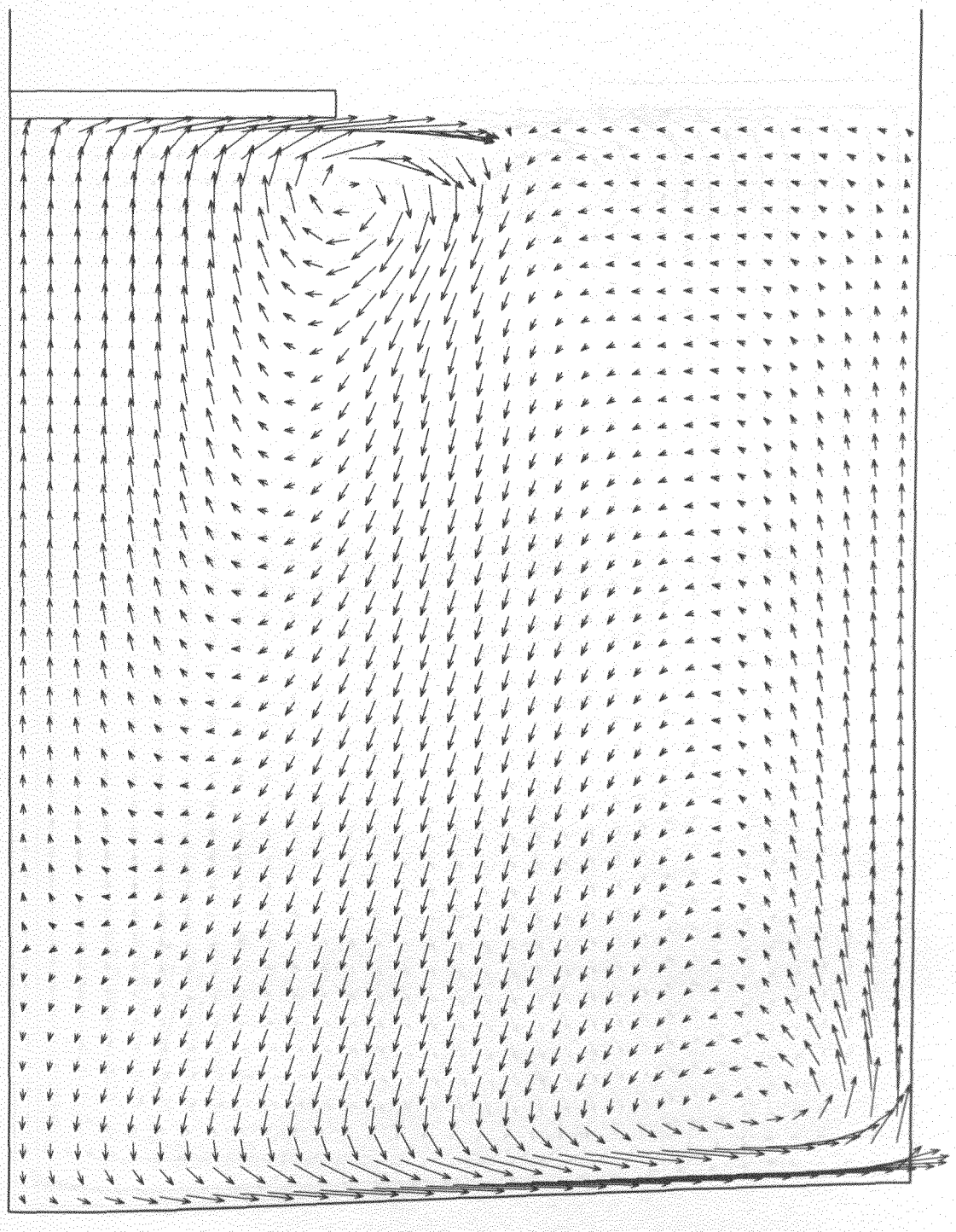

Fig. 25b : t = 11.0 s , v_{max} = 1.7EO cm/s

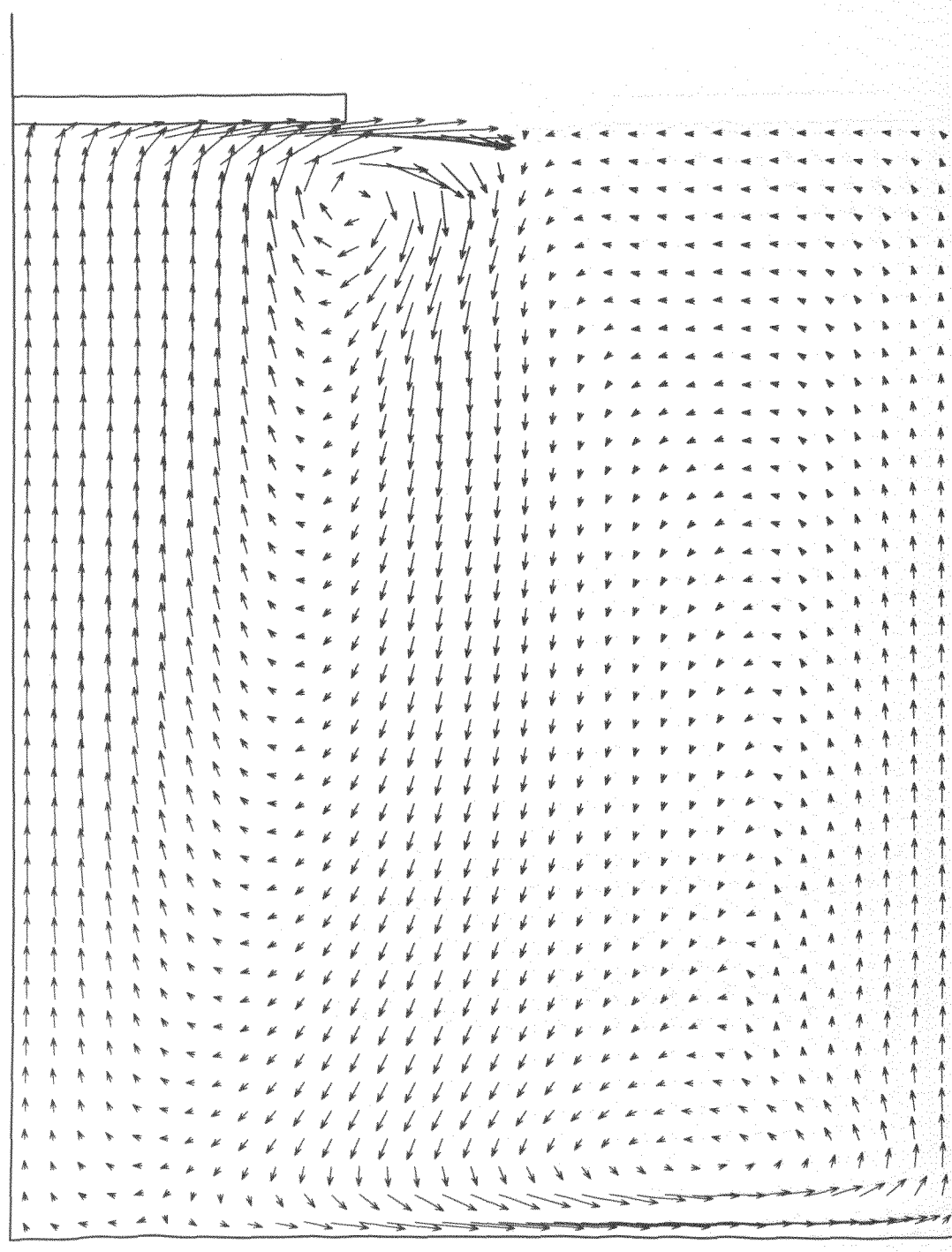

Fig. 25c : t = 15.0 s , v_{max} = 1.5E0 cm/s

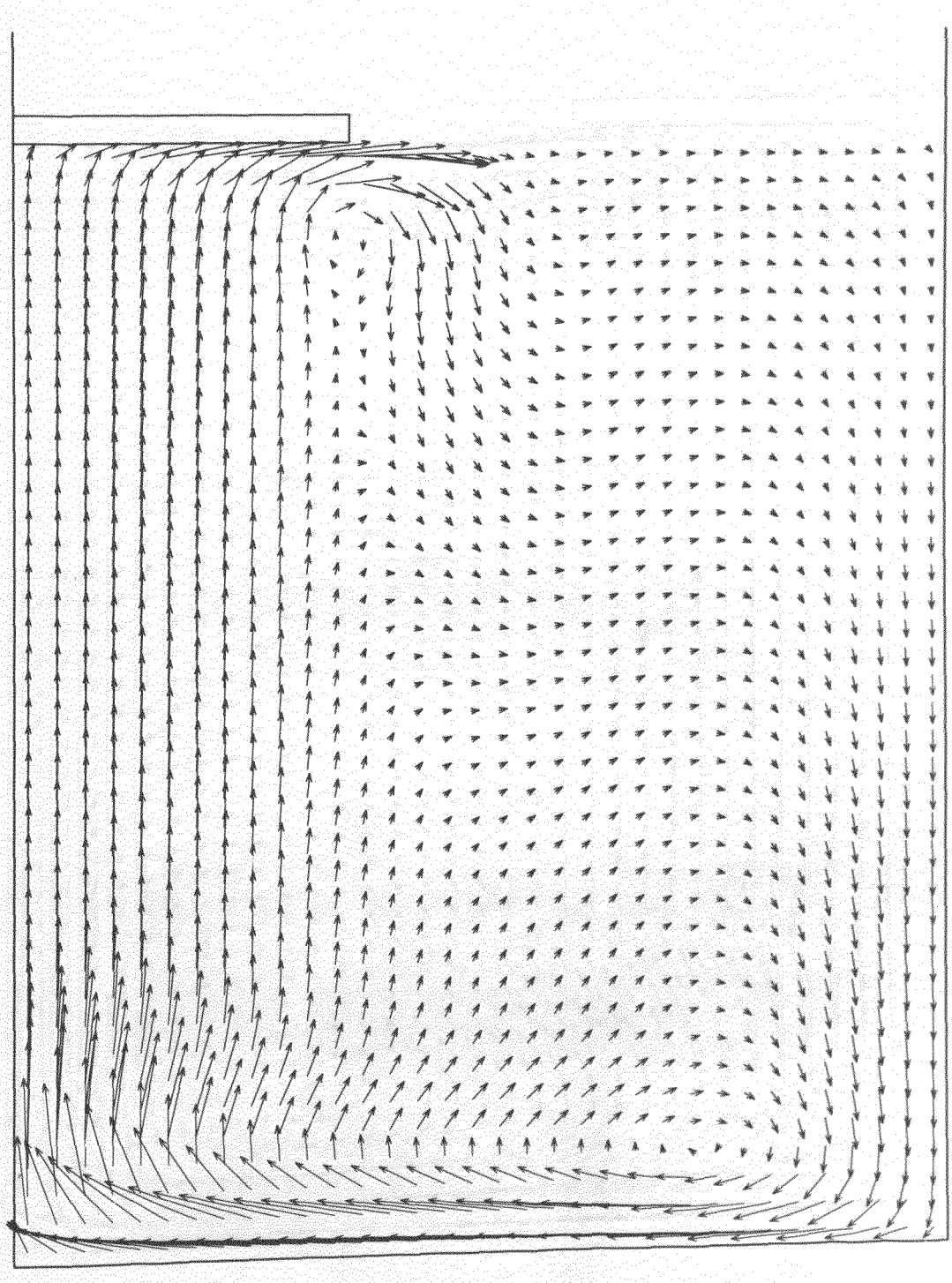

Fig. 25d : t = 20.0 s , v_{max} = 1.8E0 cm/s

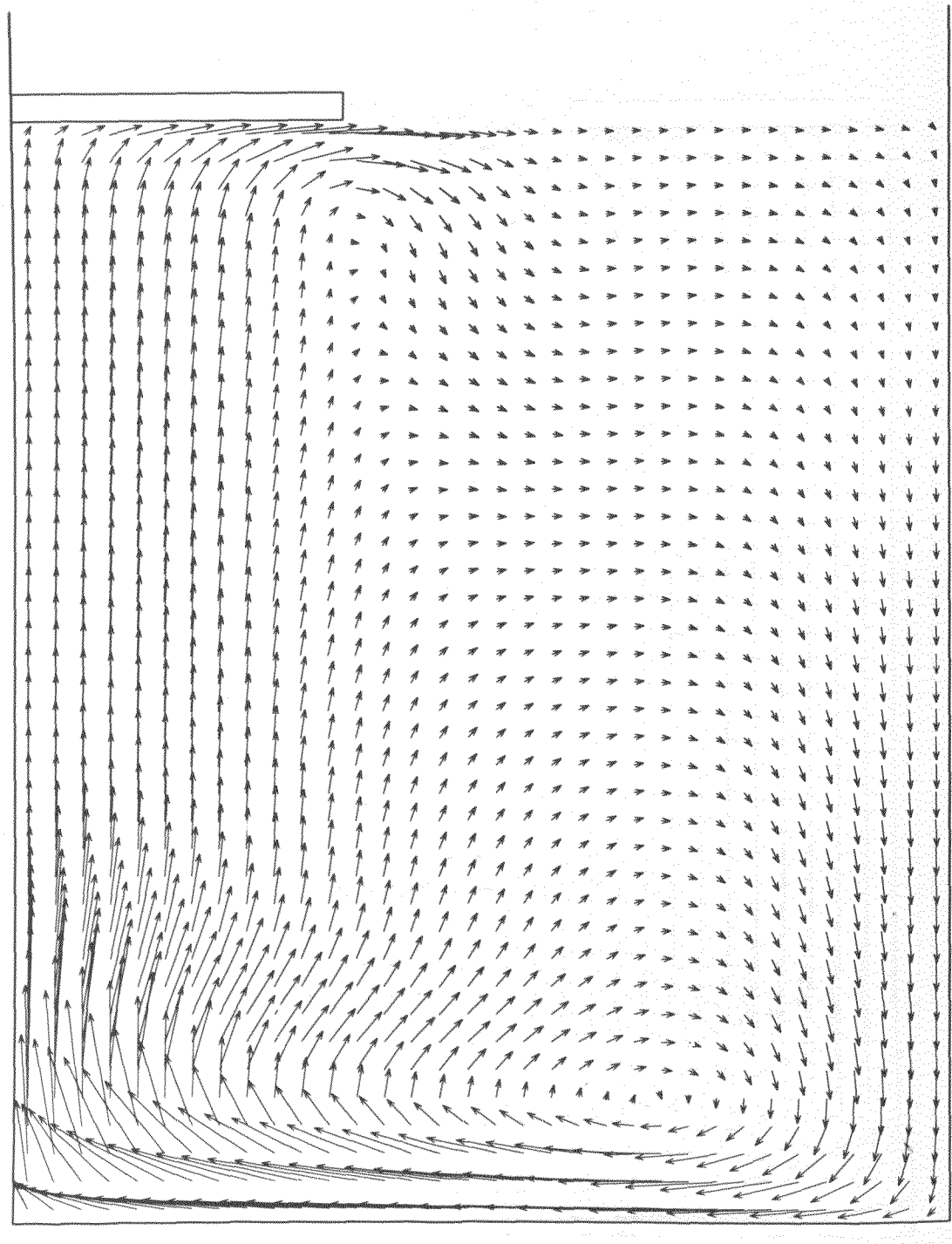

Fig. 25e : t = 21.0 s , v_{max} = 1.4E0 cm/s

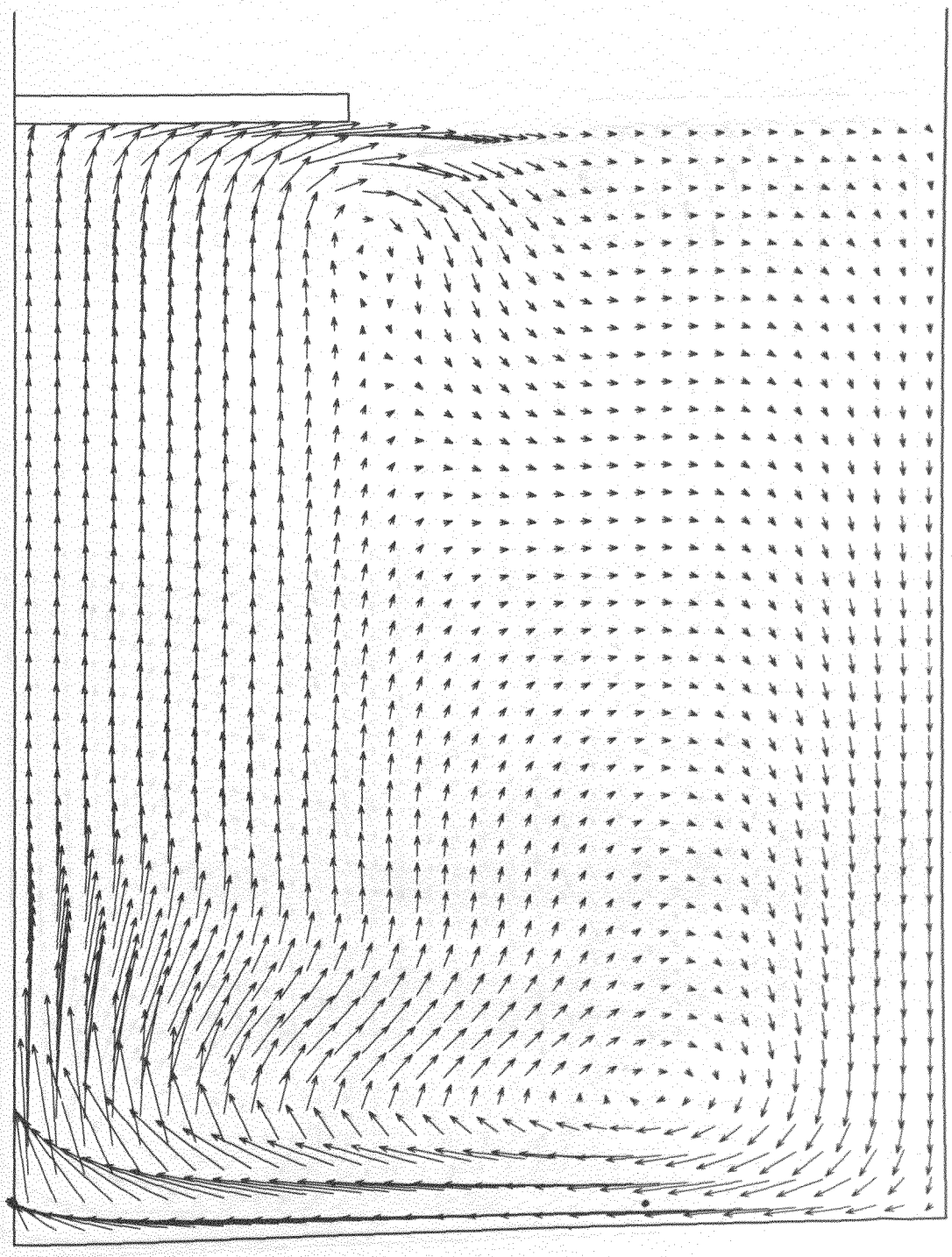

Fig. 25f : t = 25.0 s , v_{max} = 1.4E0 cm/s

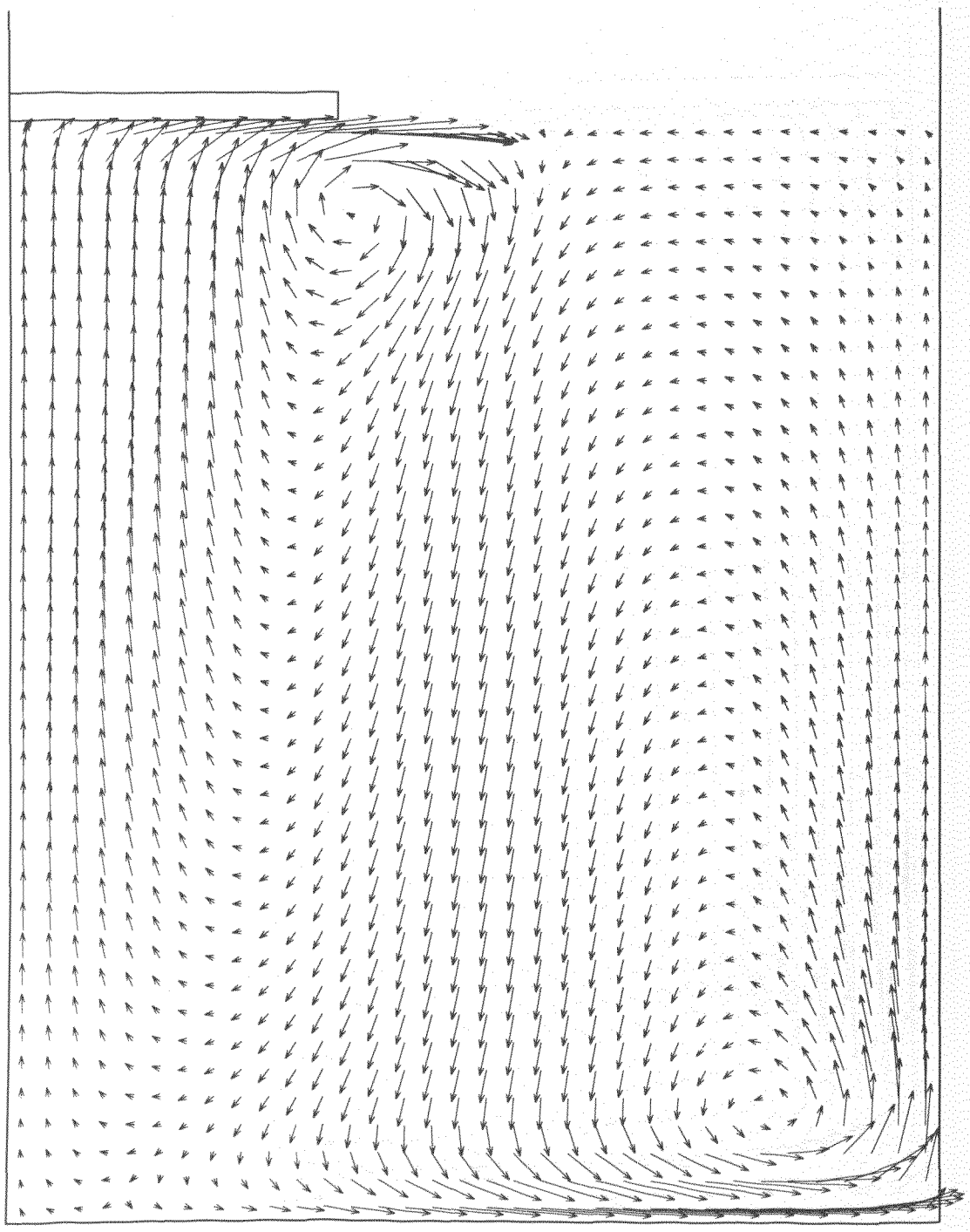

Fig. 25g : t = 30.0 s , v_{max} = 1.9E0 cm/s

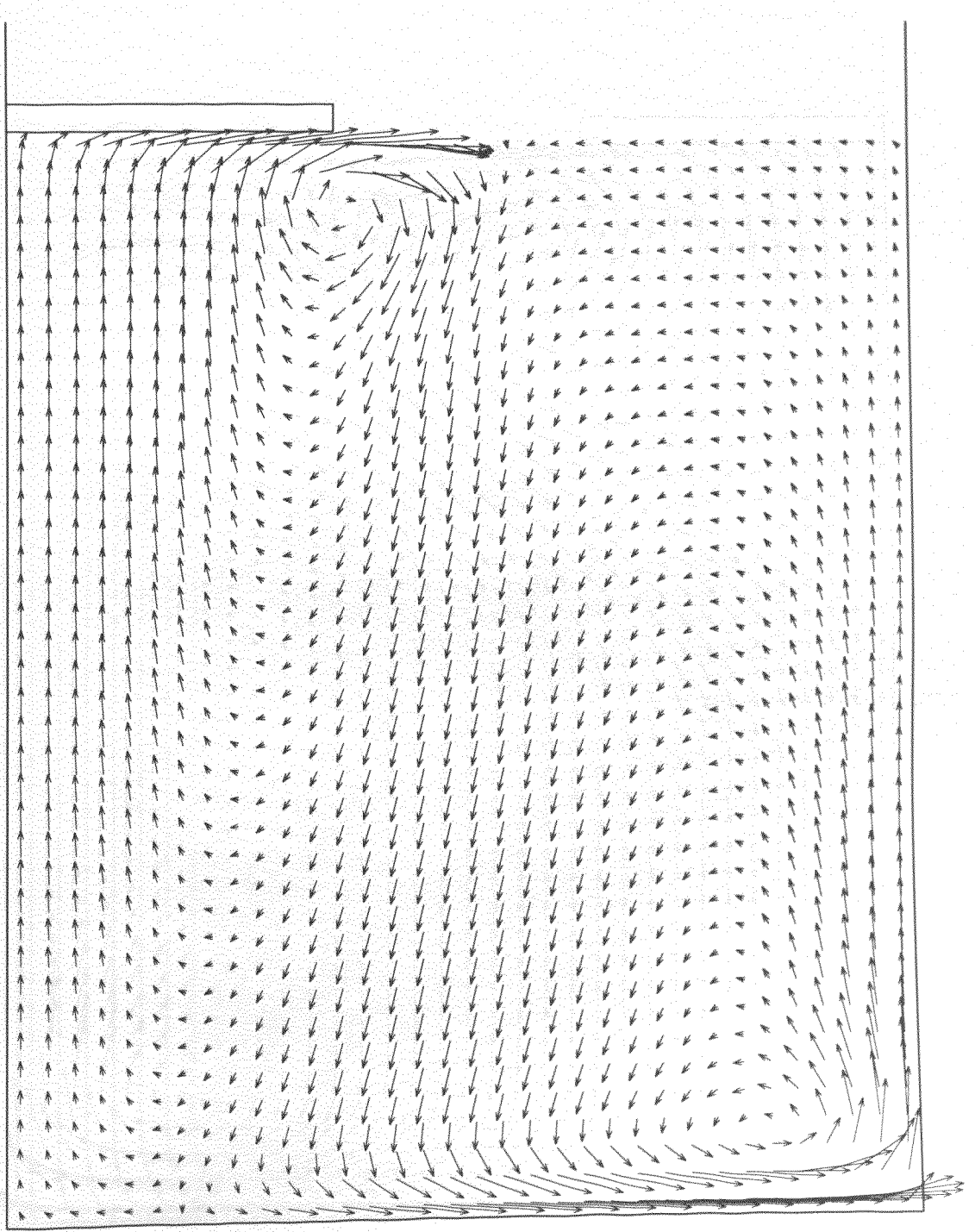

Fig. 26a : t = 5.0 s , v_{max} = 1.8E0 cm/s

NUE : 0.06 cm^2/s

CRUCIBLE ROTATION : 10 : 30 rpm

CRYSTAL ROTATION : -40 : -80 rpm

TIME PERIOD : 20 s

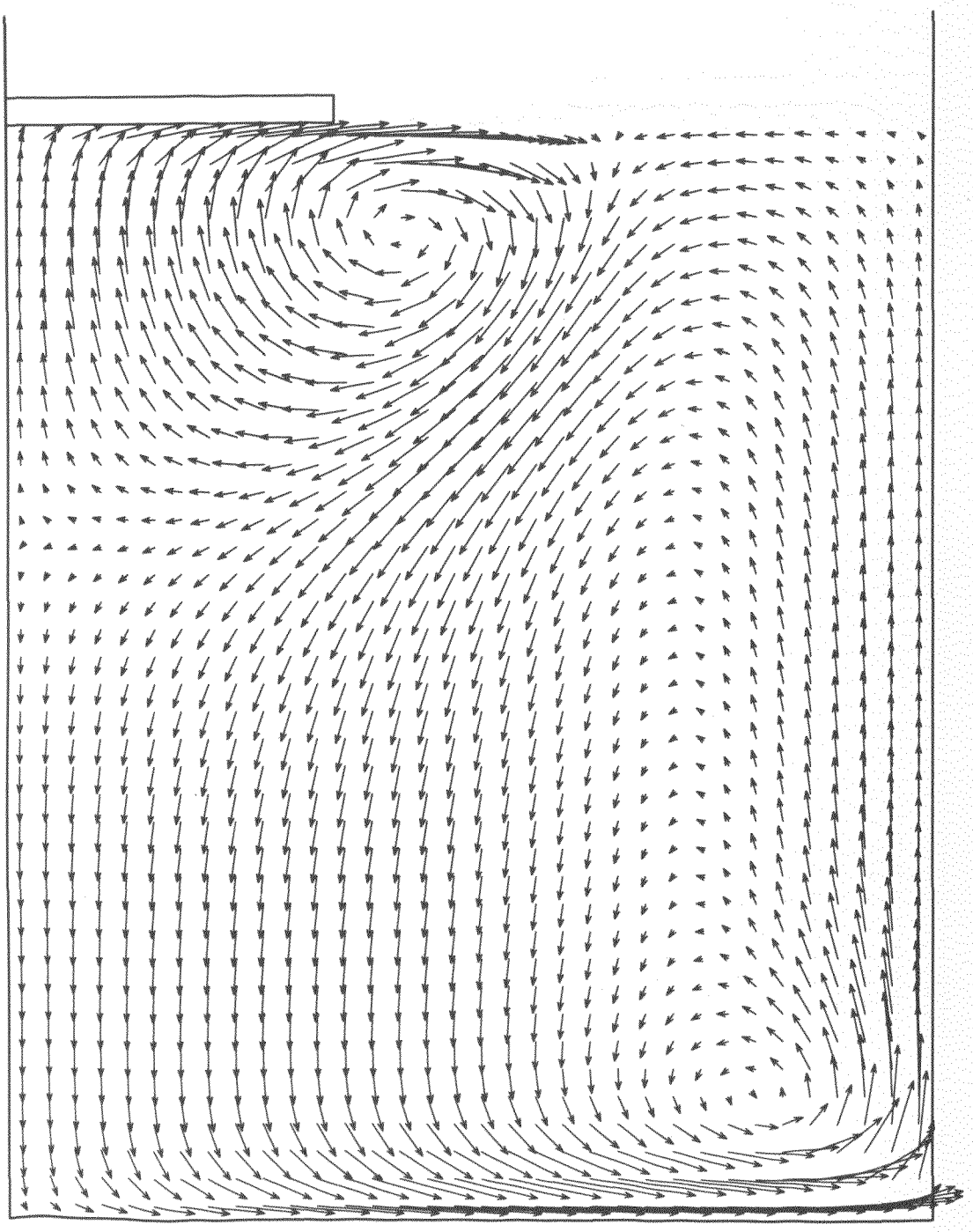

Fig. 26b : t = 15.0 s , v_{max} = 1.5EO cm/s

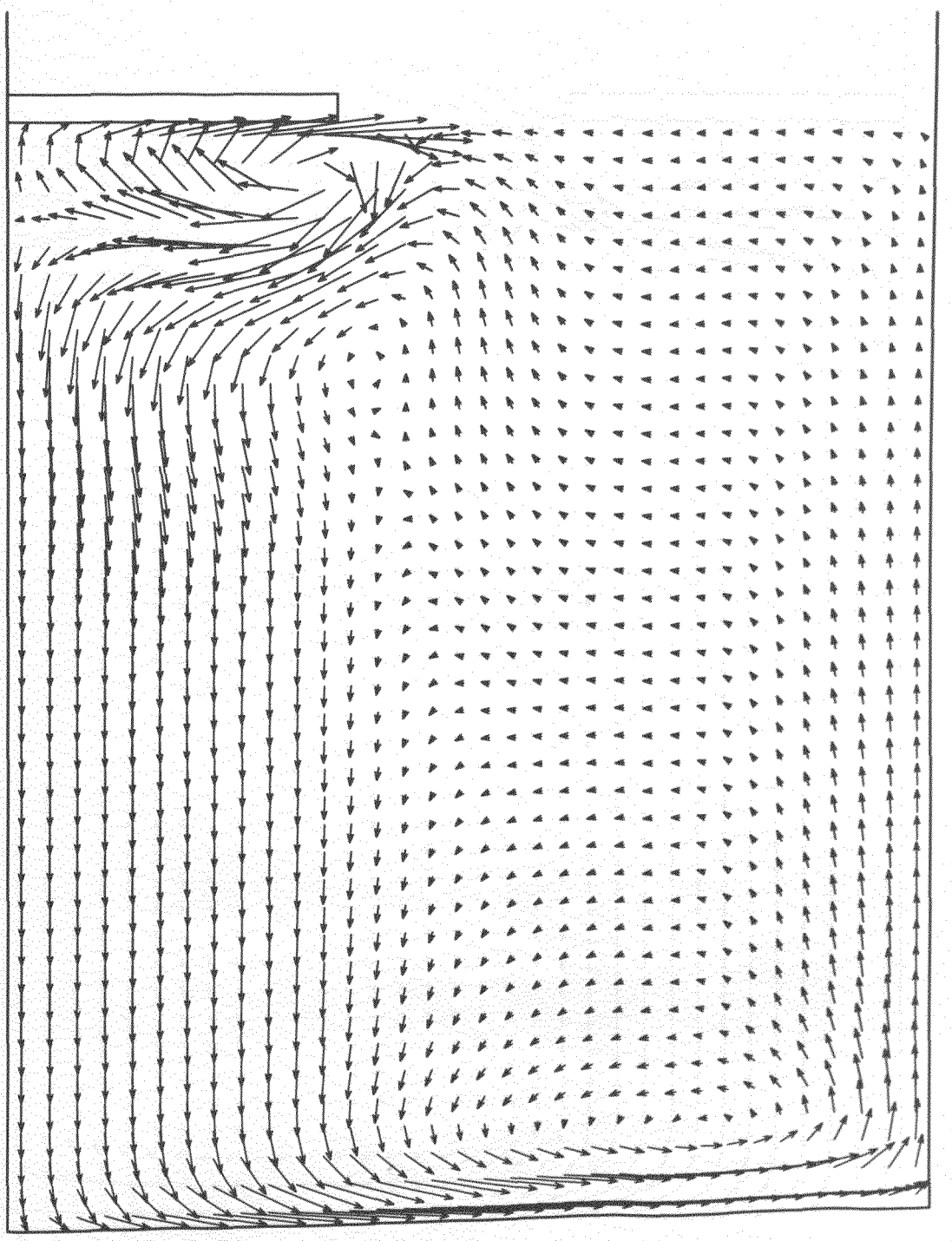

Fig. 26c : t = 20.0 s , v_{max} = 1.4E0 cm/s

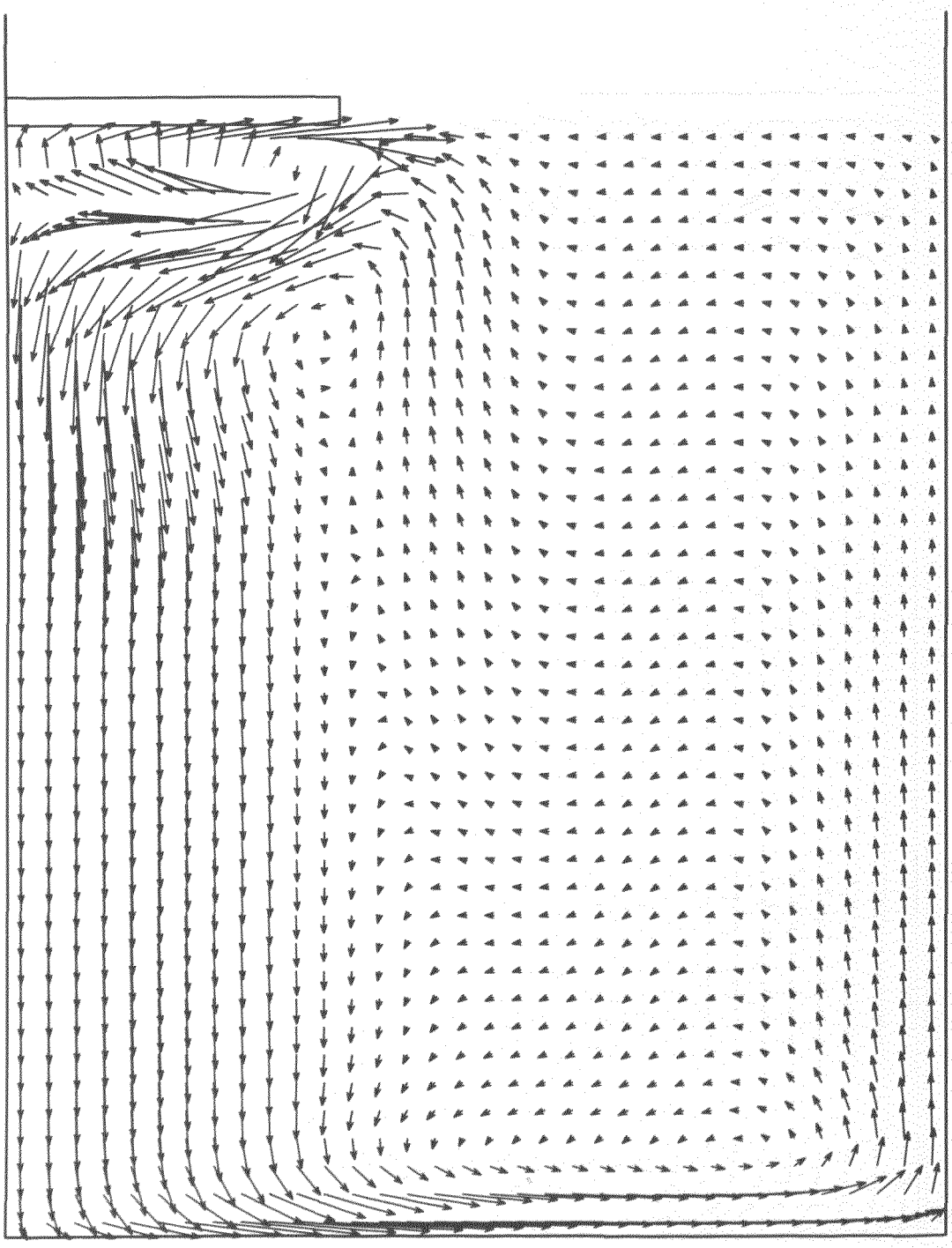

Fig. 26d : t = 21.0 s , v_{max} = 1.3EO cm/s

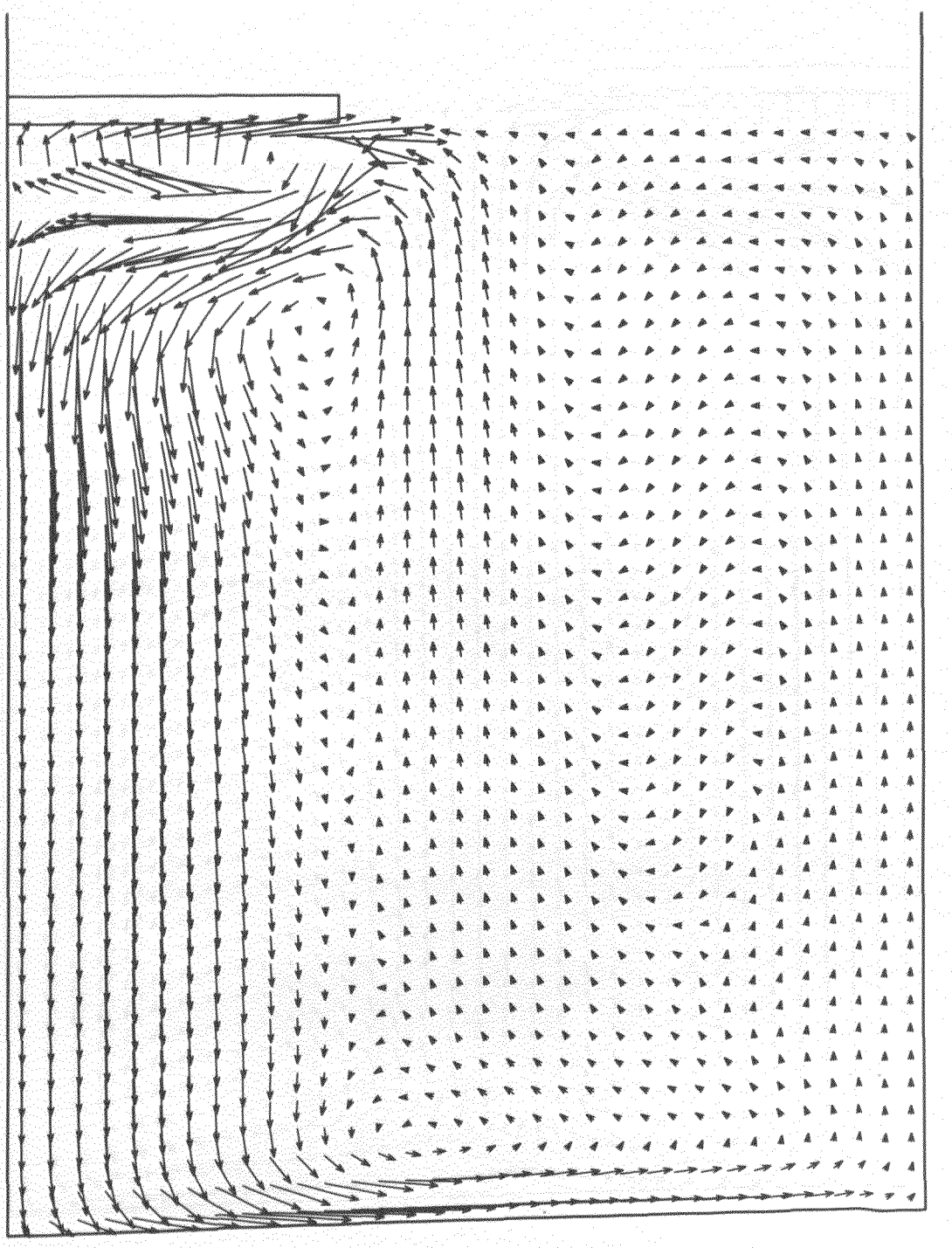

Fig. 26e : t = 25.0 s , v_{max} = 1.1EO cm/s

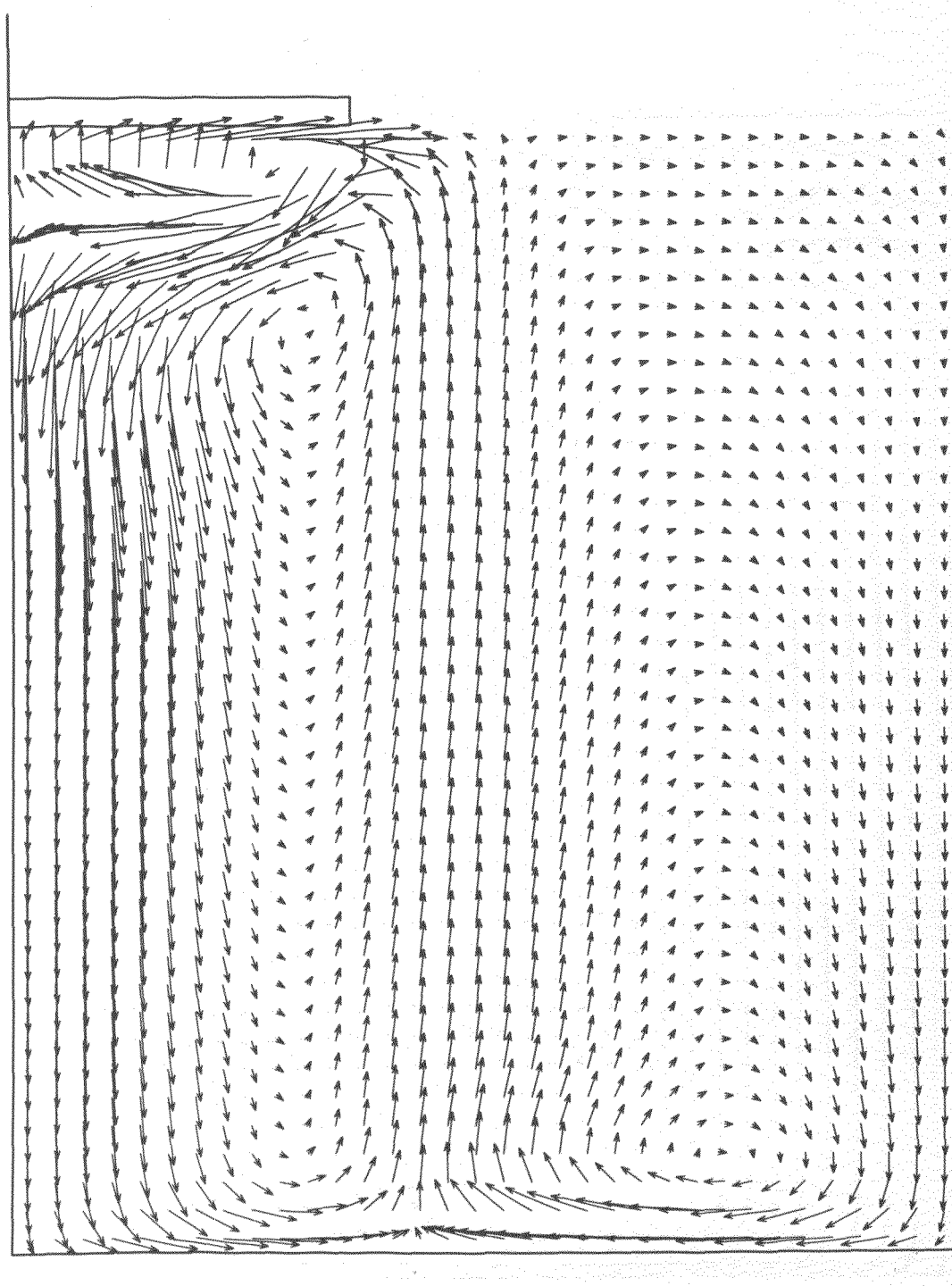

Fig. 26f : t = 35.0 s , v_{max} = 8.9E-1 cm/s

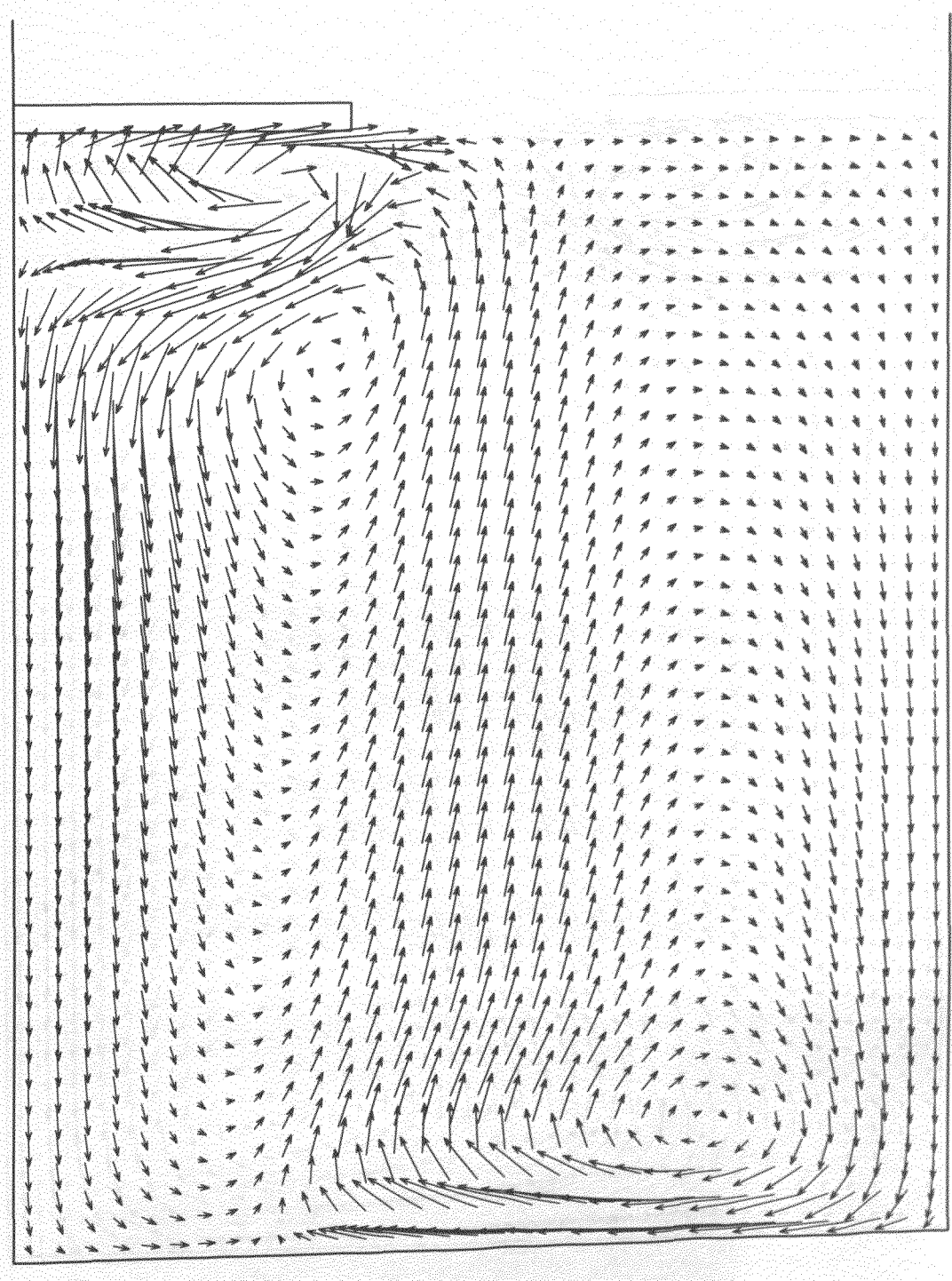

Fig. 26g : t = 40.0 s , v_{max} = 9.0E-1 cm/s

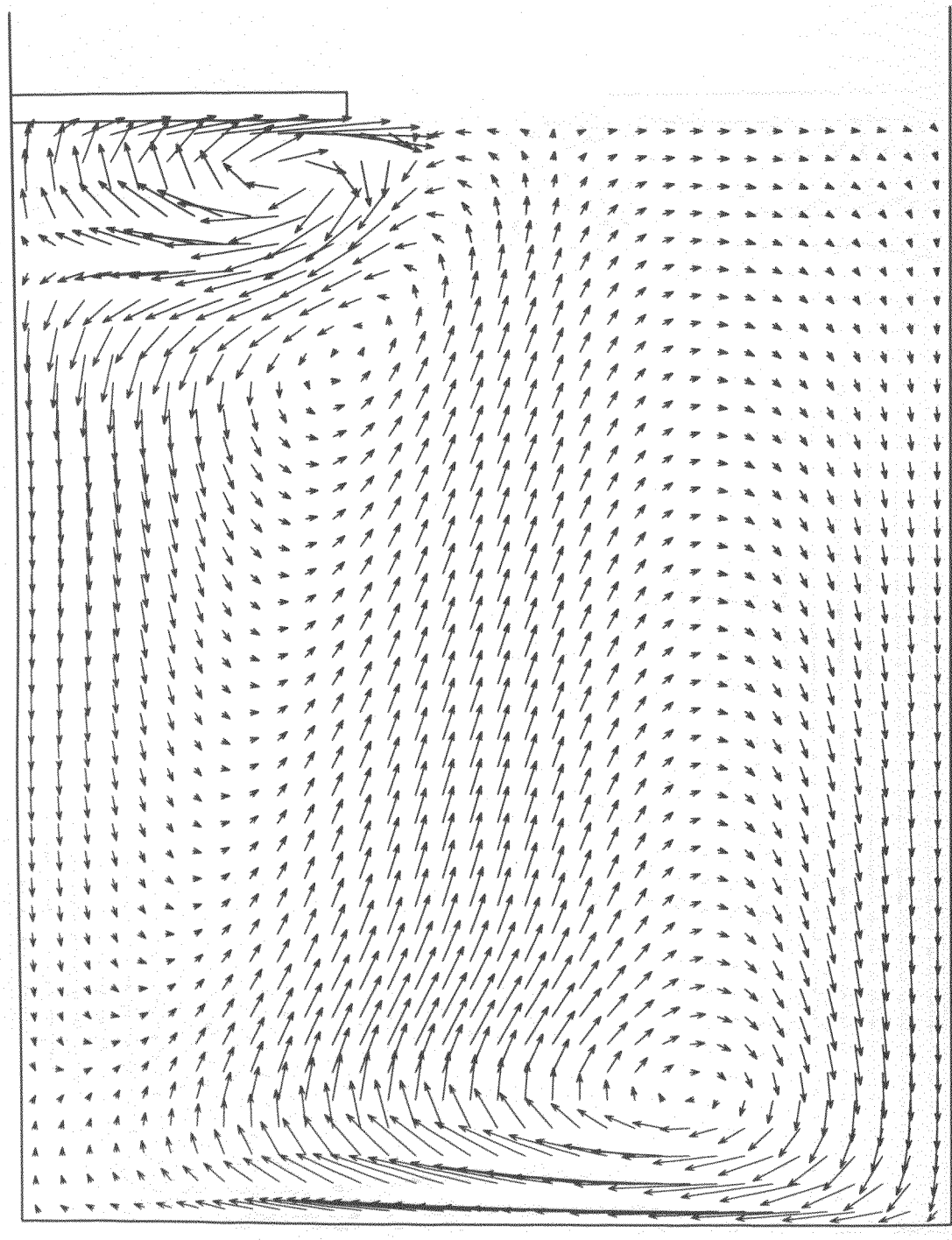

Fig. 27a : t = 5.0 s , v_{max} = 1.7E0 cm/s

NUE : 0.06 cm^2/s
CRUCIBLE ROTATION : 10 : 30 rpm
CRYSTAL ROTATION : 40 : 80 rpm
TIME PERIOD : 20 s

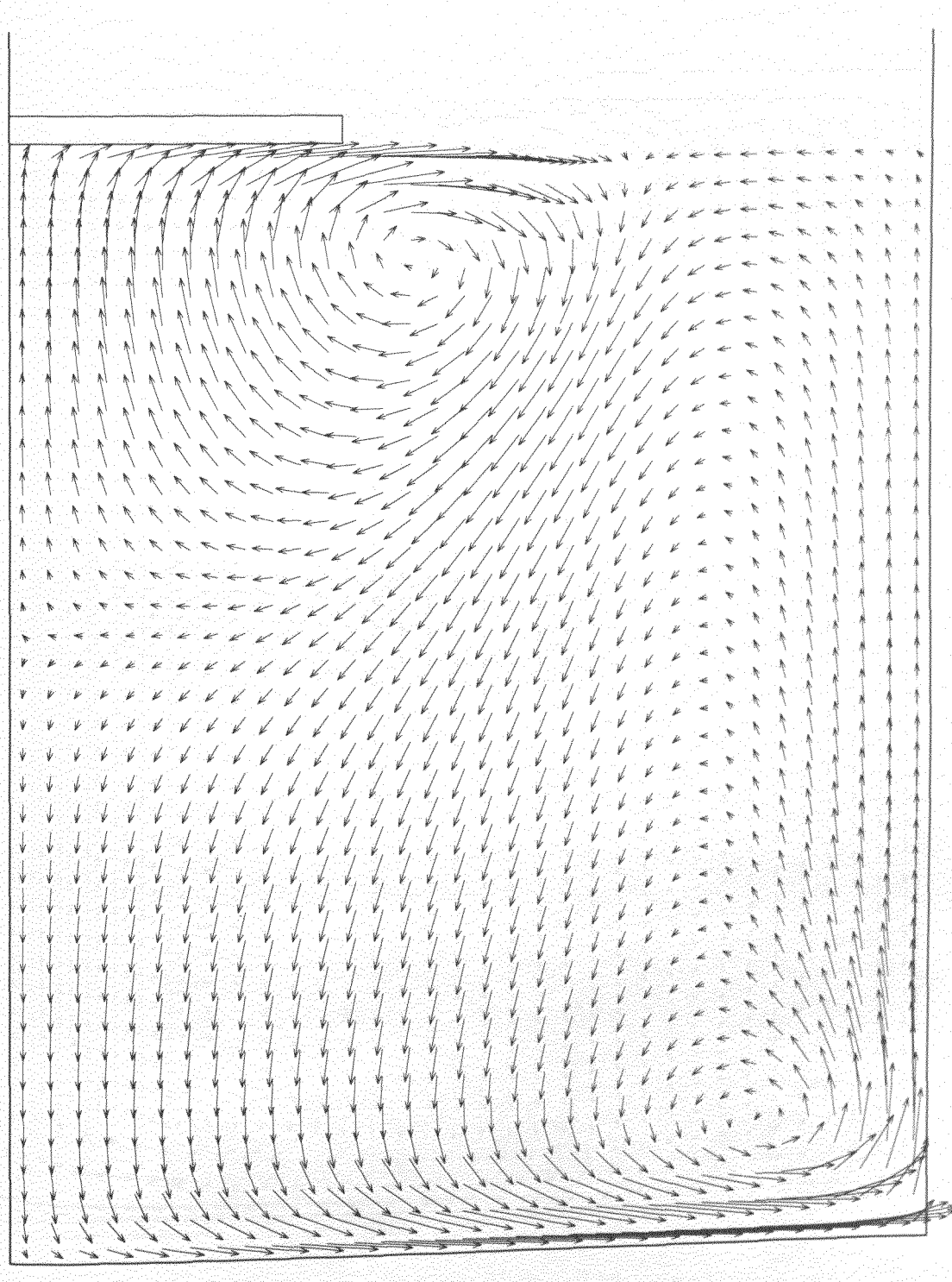

Fig. 27b : t = 15.0 s , v_{max} = 1.5E0 cm/s

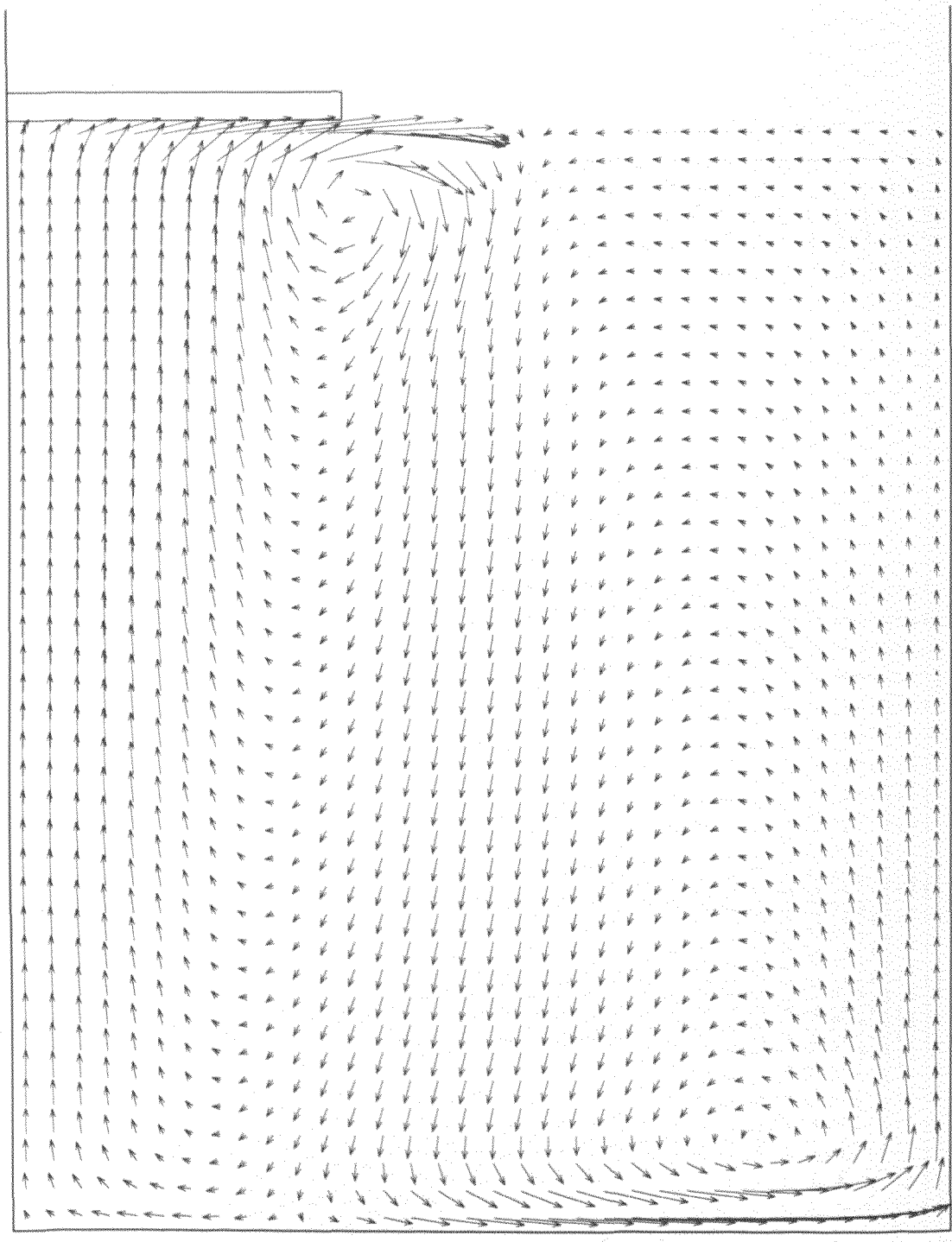

Fig. 27c : t = 20.0 s , v_{max} = 1.6E0 cm/s

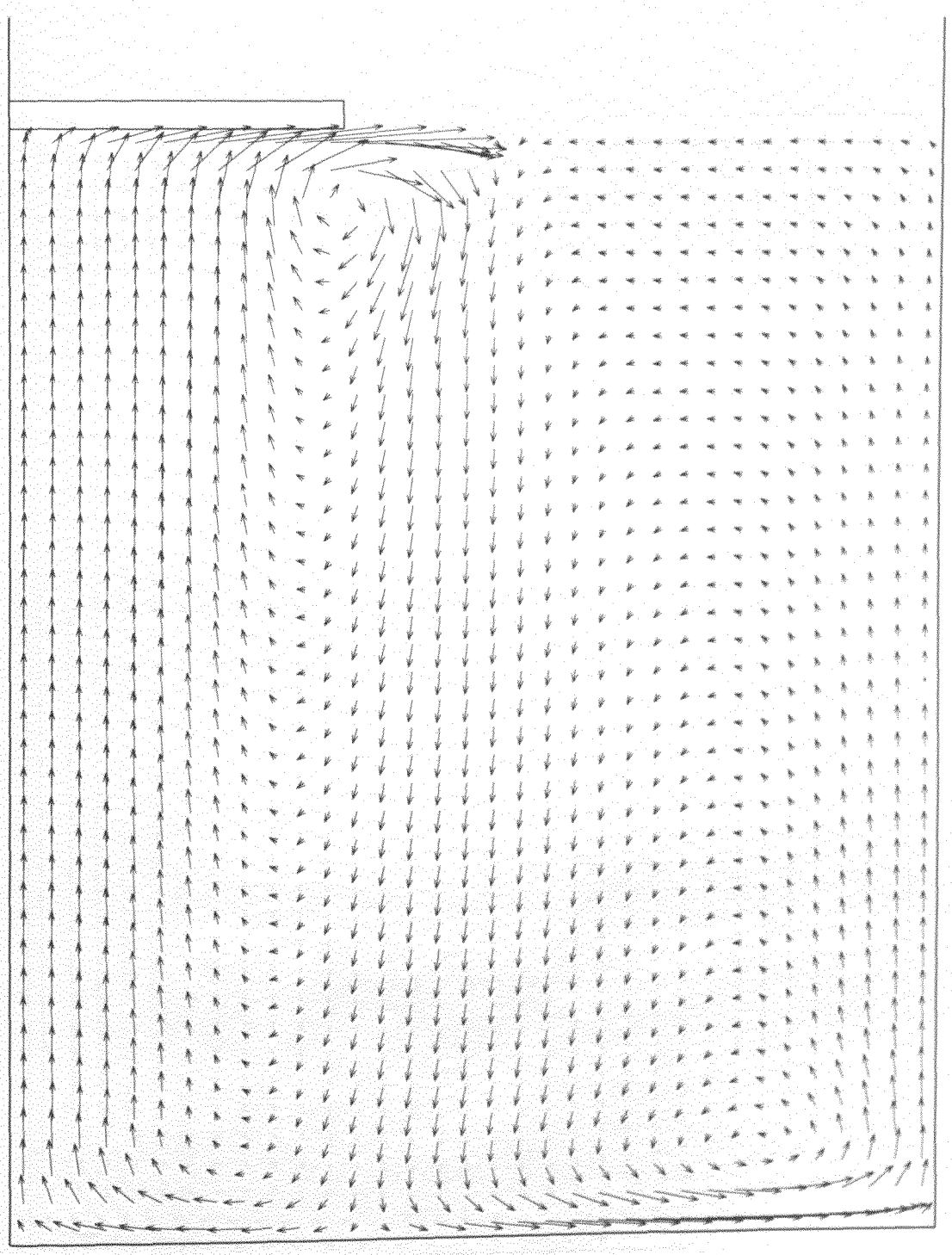

Fig. 27d : t = 21.0 s , v_{max} = 1.5E0 cm/s

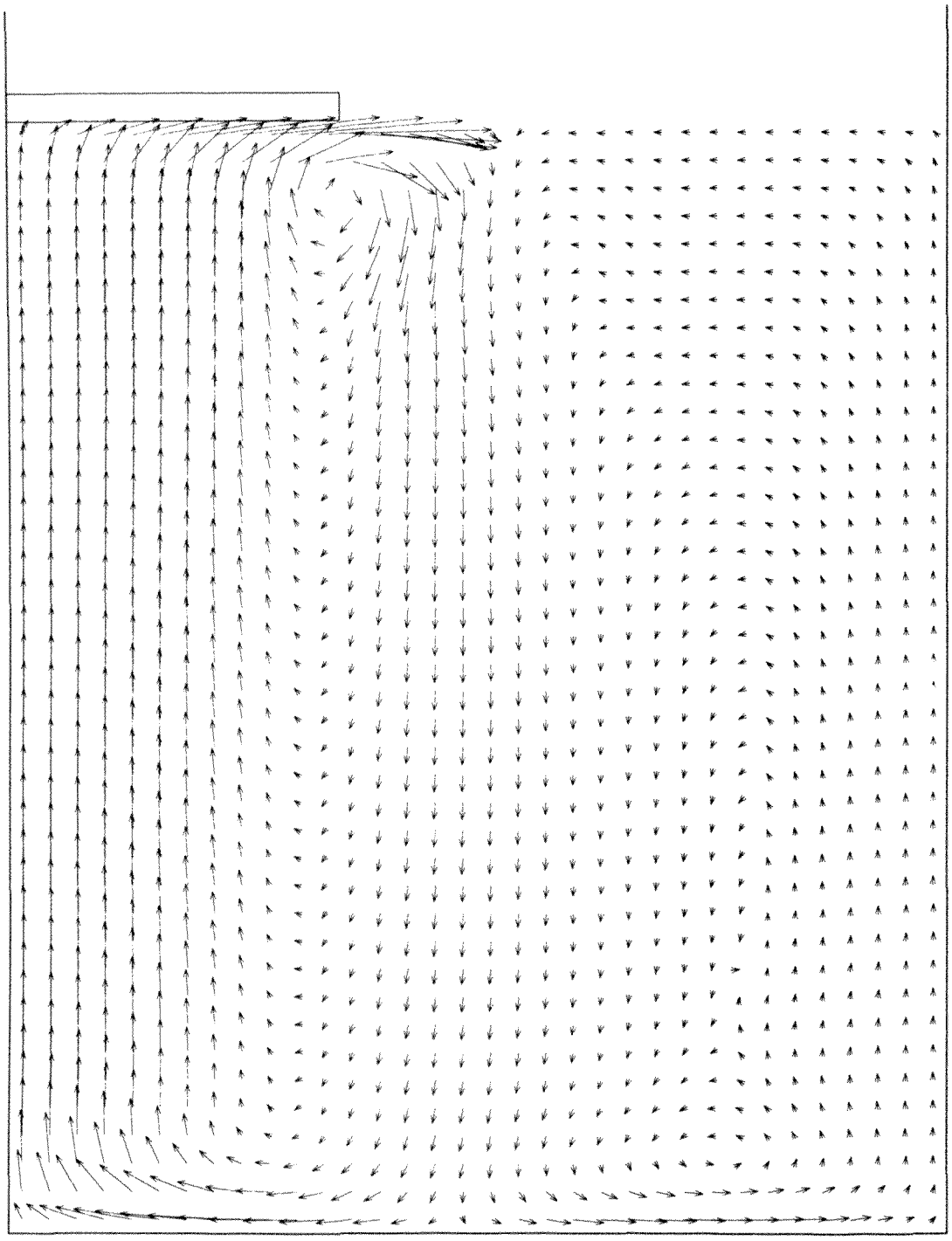

Fig. 27e : t = 25.0 s , v_{max} = 1.4E0 cm/s

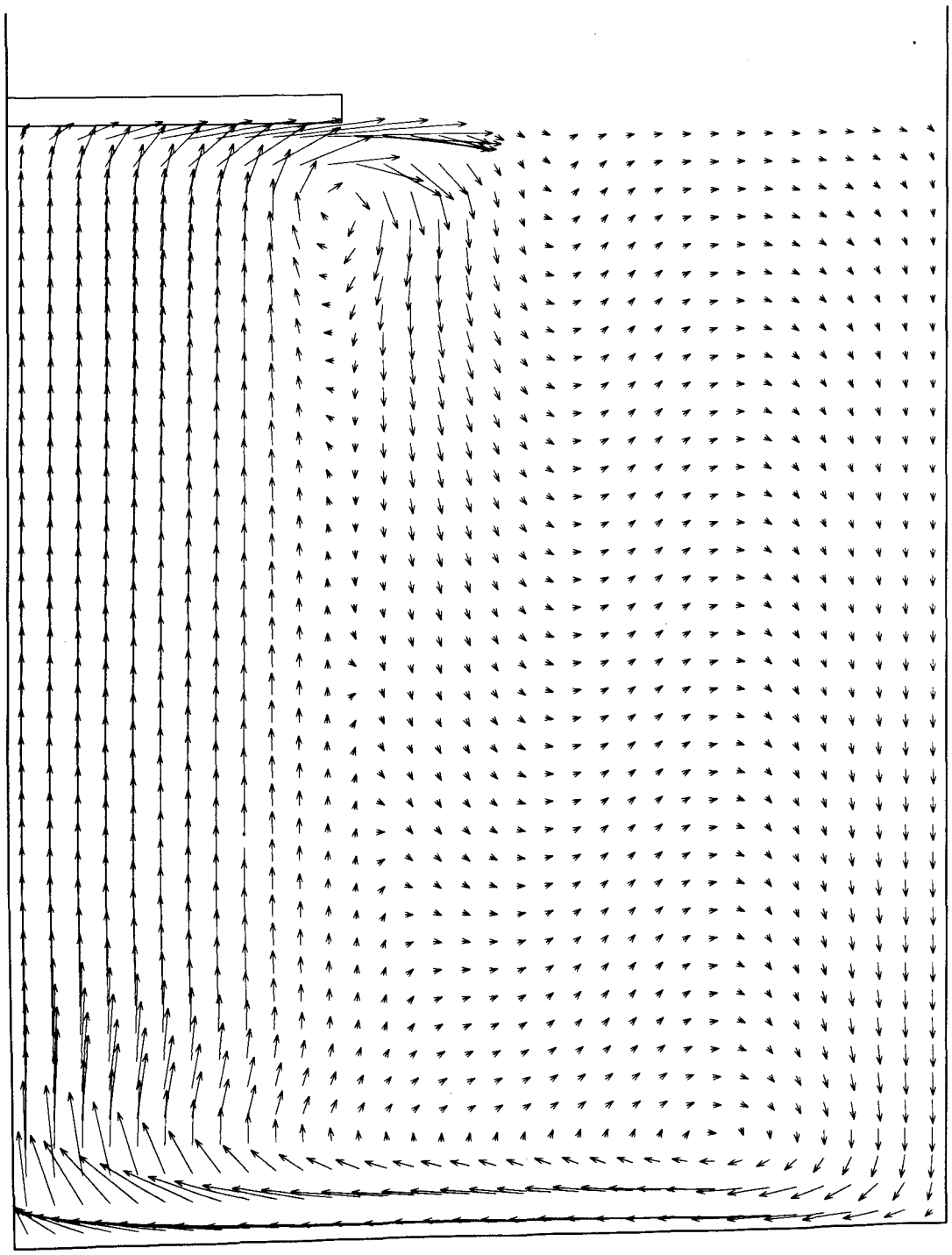

Fig. 27f : t = 35.0 s , v_{max} = 1.1E0 cm/s

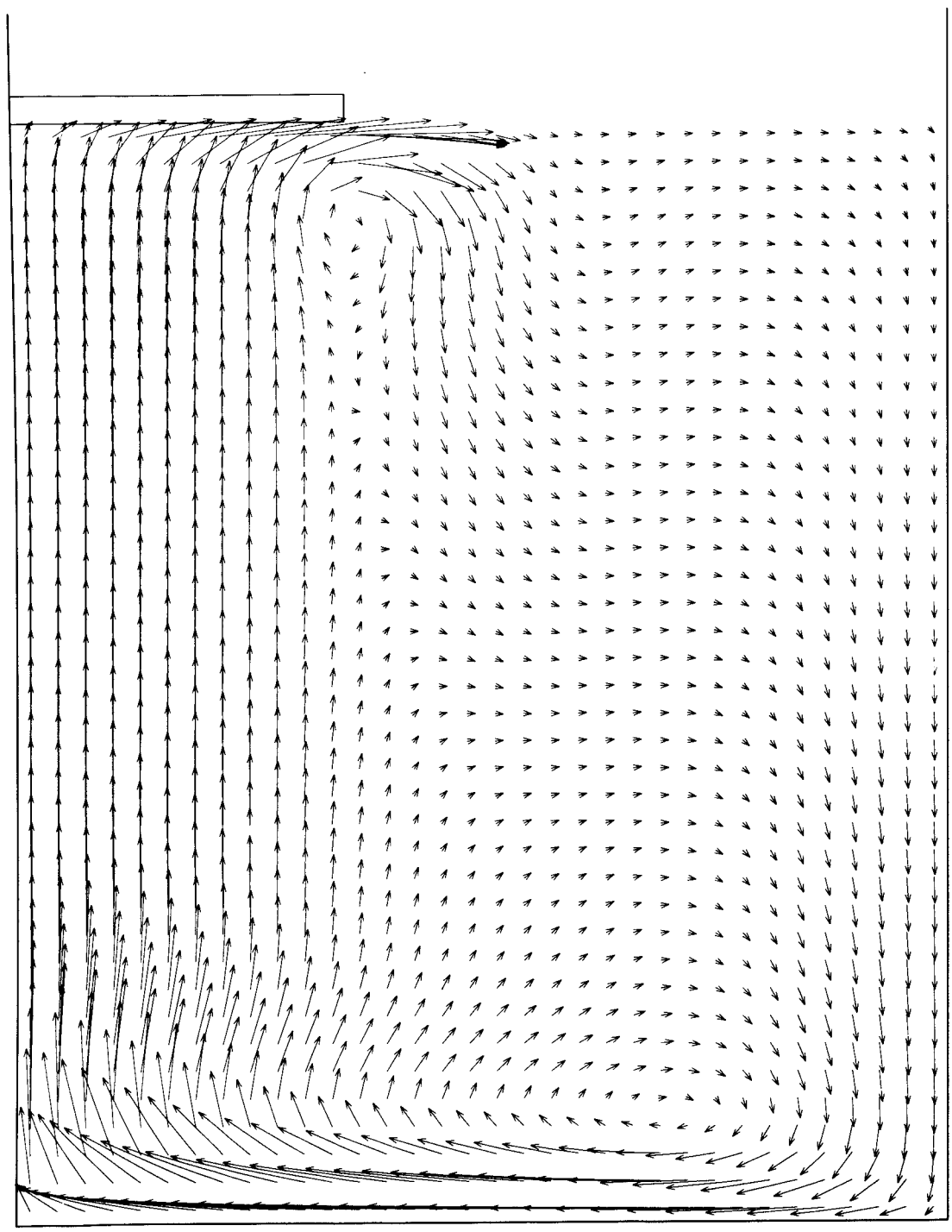

Fig. 27g : t = 40.0 s , v_{max} = 1.1E0 cm/s

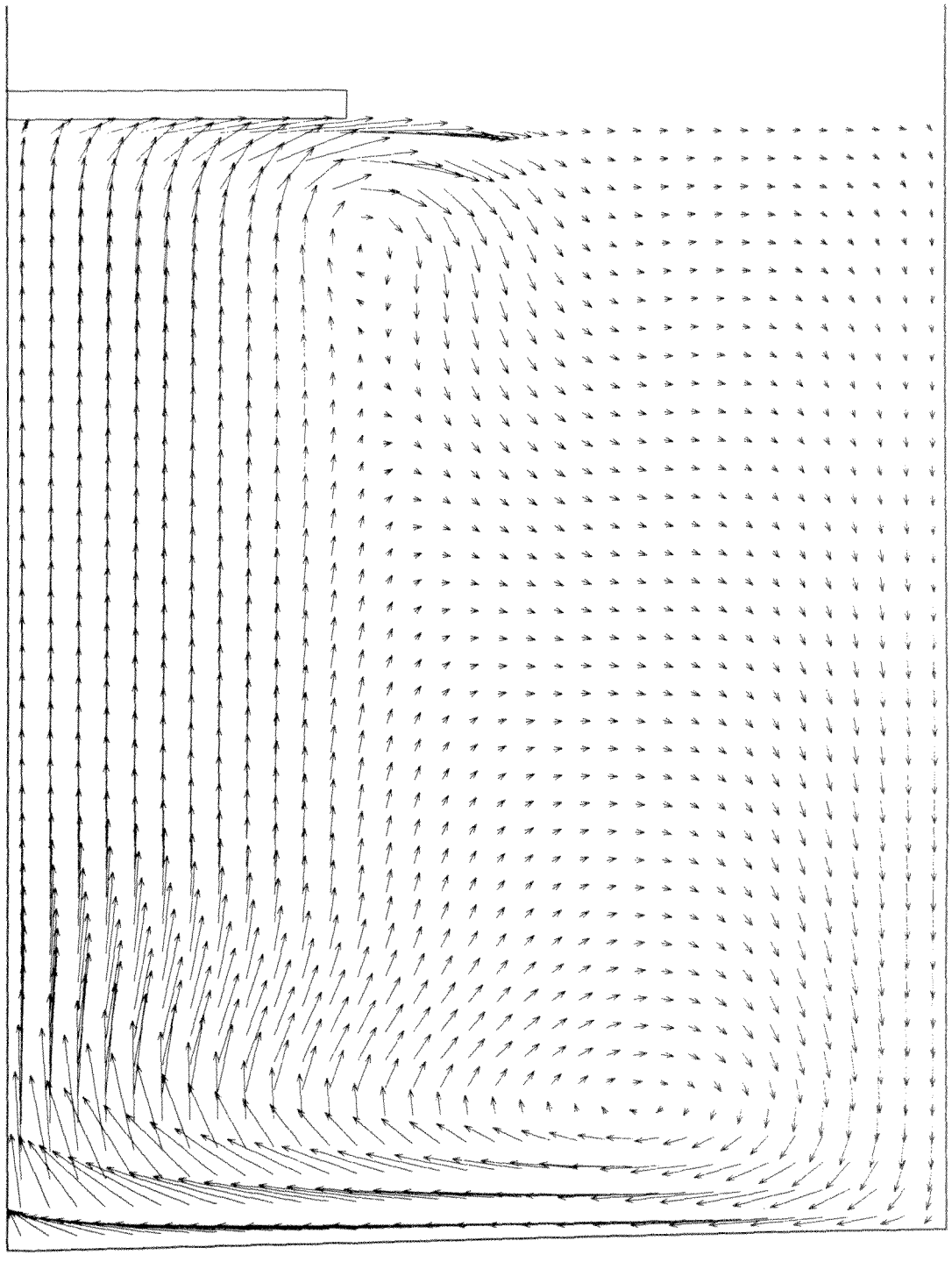

8. Acknowledgement

The digital simulations have been performed on the IBM 3o33 computer of the Zentralinstitut für Angewandte Mathematik (ZAM). We are very grateful to the director of ZAM, Dr. F. Hoßfeld, for his excellent support.

We also wish to thank Dr. K. Mika for his valuable critical remarks and helpful suggestions.

Moreover, the authors wish to express their gratitude to Frau M. Kötter for her care in typing this report.